

# Examination of severe thunderstorm outbreaks in Central Europe

A diploma thesis submitted to the  
INSTITUTE OF METEOROLOGY AND GEOPHYSICS,  
UNIVERSITY OF INNSBRUCK

for the degree of  
MASTER OF NATURAL SCIENCE

presented by  
HELGE TUSCHY

INNSBRUCK, SEPTEMBER 2009

*To Chris Broyles and Ed Andrade who fulfilled my dream  
in the tornado alley!*

*Wann und wo Helges Wetterleidenschaft begann ? Vielleicht trug er schon von Anfang an ein außergewöhnliches Wetter-Gen in sich.*

*Vielleicht war es aber auch der besondere Spaziergang (Helge war damals ungefähr 3 Jahre alt), an den wir Zwei uns später oft erinnerten: Nah am Wegrand blühten kleine, leuchtend blaue Blumen. ' Sieh mal' sagte ich, 'das sind Gewitterblümchen. Wenn du sie abpflückst, wird bald ein Gewitter aufziehen!' Meine Mutter, Helges Oma, hatte es mir so erzählt, als **ich** klein war. Inzwischen kannte ich den richtigen Namen der Blumen: Ehrenpreis! Ihn benutzte ich aber nicht, ich sagte **Gewitterblümchen**. Helge erzählte mir später, damals noch im treuen Glauben an die Allwissenheit seiner Mutter, dass er, wann immer er sie entdeckte, viele, sehr viele dieser Wetterblumen pflückte! Manchmal wirkte der versprochene Zauber, manchmal nicht!*

*Seine Leidenschaft für Wetter und die Faszination, die besondere Wettererscheinungen auf ihn ausüben, ließen jedoch nie nach - ganz im Gegenteil, wie sein Amerikabesuch 2002 und letztendlich seine Diplomarbeit beweisen ...*

*Eva Tuschy, die Mutter*



Auf Gewitterjagd im Jahre 2002: nördlich von Amarillo, Texas (USA).





# Abstract

The subject of this study is the research of deep and organized convection in parts of Europe with the mesoscale weather forecast model COSMO-DE from the DWD and observations. The first part of this thesis reveals a general overview about the dynamics and characteristics of different thunderstorm classes: the single cell, the multicell and the supercell, as well as the subspecies. Indices for thunderstorm forecasts are outlined including their application and weaknesses.

By means of model data from COSMO-DE and radar data from different parts of Europe, it is shown on the basis of different case studies what assists in the occurrence of organized convection, how well the weather model grasps the thunderstorm situations and what kind of use the thunderstorm forecast parameters have in the evaluation of the particular event. Five case studies were accomplished: a bow echo event over southern Germany (26 May 2009), an F4 tornado event in Hautmont, France (3 August 2008), a regional tornado outbreak in Poland (15 August 2008), a severe hailstorm case over southern Germany (22 August 2008) and finally a supercell event over southern Germany (23 June 2008). The following results are achieved by using COSMO-DE. The release of abundant instability in the lowest 3 km of the atmosphere, coupled to strong directional and speed shear in that layer favors tornado development. In case of thunderstorms, which line up and produce locally significant wind events, a strong speed shear in the lowest few kilometers is supportive, whereas strong wind shear in an unstable hail growth zone assists in severe hail events. It becomes clear that the use of the thunderstorm forecast parameters developed in the United States has to be applied carefully to the European cases. For example the magnitude of instability in most of the cases is less compared to those in America, which has an effect on the severe thunderstorm forecast parameters and their benefits.



# Zusammenfassung

Das der Studie übergeordnete Thema ist die Untersuchung von hochreichender, langlebiger Konvektion in Teilen Europas. Hierzu wird zunächst ein allgemeiner Überblick über die Dynamik und Merkmale der verschiedenen Gewitterklassen gegeben: die Einzelzelle, Multizelle und Superzelle, sowie deren zahlreichen Unterklassen. Neben dem Wetterphänomen 'Gewitter' werden auch die für die Gewittervorhersage entwickelten Indices behandelt und deren Nutzen wie auch Schwächen erörtert. Mit Hilfe von Modelldaten des mesoskaligen Wettervorhersagemodells des DWD 'COSMO-DE' und Radardaten aus verschiedenen Teilen Europas wird an Hand mehrerer Fallstudien gezeigt, was genau das Auftreten organisierter Konvektion ermöglicht, wie gut das Modell die Gewitterlagen erfasst und welchen Nutzen die Vorhersageparameter bei der Einschätzung der Situation haben. Die unter anderem mit COSMO-DE erzielten Ergebnisse bestätigen, dass reichlich Labilität in den untersten 3 km der Atmosphäre, gekoppelt mit starker Richtungs- und Geschwindigkeitsscherung des Windes mit der Höhe die Tornadoentwicklung begünstigen. Für linienhaft angeordnete Gewitter, die lokal signifikante Windereignisse erzeugen, ist eine starke Geschwindigkeitsscherung in den untersten Kilometern förderlich, während eine starke Windscherung im labil geschichteten Hagelwachstumsbereich Großhagelereignisse unterstützt. Es wird deutlich, dass die Benutzung der auf Nordamerika basierenden Gewitterparameter in einigen Fällen dank mangelnder Labilitätsfreisetzung in Europa keinen Nutzen für die Vorhersage und Einschätzung der zu erwartenden Gewitterlage bringen.



# List of abbreviations

$\Gamma$ .....	individual temperature lapse rate
$\gamma$ .....	environmental temperature lapse rate, $\gamma = -\frac{\partial T}{\partial z}$
$\Gamma_{dry}$ .....	dry-adiabatic temperature lapse rate: $\frac{g}{c_p}$
$\Gamma_{moist}$ .....	moist-adiabatic temperature lapse rate
$\nabla$ .....	$(\frac{\partial}{\partial x}, \frac{\partial}{\partial y}, \frac{\partial}{\partial z})$ : 3D gradient operator
$\nabla_h$ .....	$(\frac{\partial}{\partial x}, \frac{\partial}{\partial y})$ : horizontal gradient operator
$\omega$ .....	$\nabla \times v$ : <i>vorticity vector</i>
$\omega_h$ .....	horizontal vorticity vector
$\omega_{cw}$ .....	crosswise vorticity
$\omega_{sw}$ .....	streamwise vorticity
$\partial_i$ .....	Partial derivative
$\rho$ .....	density
$\theta$ .....	potential temperature
$\theta_e$ .....	equivalent potential temperature
$C_p$ .....	specific heat of dry air at constant pressure
$M_m$ .....	weight of a single molecule
$T_v$ .....	Virtual temperature
AGL .....	Above ground level
BRN .....	Bulk Richardson Number
BWER .....	Bounded weak echo region
CAPE .....	Convective Available Potential Energy
CAPPI .....	Constant altitude PPI
CCL .....	Convective Condensation Level
cf .....	confer (lat.) = vergleiche
CINH .....	Convective InHibition
dB .....	decibel
DCAPE .....	Downdraft CAPE
DMC .....	Deep Moist Convection
E .....	east
EH1 .....	Energy Helicity Index
EL .....	Equilibrium Level

EML .....	Elevated mixed layer
ESSL .....	European Severe Storms Laboratory ( <a href="http://www.essl.org">http://www.essl.org</a> )
ESTOFEX ...	European Storm Forecast Experiment ( <a href="http://www.estofex.org">http://www.estofex.org</a> )
FFD .....	Forward-flank downdraft
g .....	acceleration due to gravity
gpm .....	geopotential dekameter
h .....	hour
HRV .....	High Resolution Visible channel
Hz .....	Hertz: $1 \text{ Hz} = 1 \text{ s}^{-1}$
IR .....	InfraRed
k .....	Boltzmann Konstante: $k = 1.38 \times 10^{-23} \text{ J K}^{-1} \text{ molecule}^{-1}$
KI .....	K-Index
LCL .....	Lifted Condensation Level
LFC .....	Level of Free Convection
LHN .....	Latent heat nudging
LI .....	Lifted Index
MARC .....	Mid-Altitude Radial Convergence Signature
MCC .....	Mesoscale convective complex
MCS .....	Mesoscale convective system
MCV .....	Mesoscale convective vortex
MIRIAM .....	Mikroprozessorgesteuertes Registriersystem des Instrumentenamtes München
MLCAPE ....	Mean Layer CAPE
MUCAPE ....	Most Unstable CAPE
N .....	north
NCAPE .....	Normalized CAPE
NE .....	northeast
NW .....	northwest
NWS .....	National Weather Service
p .....	pressure
PCAPPI .....	Pseudo-Constant-Altitude Plan-Position Indicator
PPI .....	Plan position indicator
PRF .....	Pulse repetition frequency
RFD .....	rear-flank downdraft
RHI .....	Range-height indicator
S .....	south
SBCAPE .....	Surface Based CAPE
SCP .....	SUPercell Composite Parameter
SE .....	southeast

SI .....	Showalter Index
SPC .....	Storm Prediction Center, USA
SRH .....	Storm Relative Helicity
SRH-1 .....	Storm Relative Helicity from 0-1km
SRH1 .....	Storm Relative Helicity in the 0-1km layer
STP .....	Significant Tornado Parameter
SW .....	southwest
SWEAT .....	Severe WEATHER Threat index
T .....	Temperature
TI .....	Thompson-Index
TT .....	Total-Totals index
TVS .....	Tornado vortex signature
USA .....	United States of America
UTC .....	Universal time coordinated
v .....	(u, v,w): 3D velocity vector
VAD .....	Velocity-azimuth display
VIS .....	VISible channel
VIS .....	VISible
W .....	west
WBZ .....	Wet-Bulb Zero level
WER .....	Weak echo region
WV .....	Water Vapor





# Contents

<b>Dedication</b>	<b>2</b>
<b>Abstract</b>	<b>5</b>
<b>Zusammenfassung</b>	<b>7</b>
<b>List of abbreviations</b>	<b>8</b>
<b>Contents</b>	<b>11</b>
<b>1 Introduction</b>	<b>17</b>
1.1 Motivation . . . . .	17
1.2 Goals and outline of the thesis . . . . .	19
<b>2 Numerical model, weather radar and data</b>	<b>21</b>
2.1 Overview . . . . .	21
2.2 Brief overview of COSMO-DE . . . . .	21
2.3 Weather radar . . . . .	25
2.3.1 Brief history of radar meteorology . . . . .	25
2.3.2 Radar basics . . . . .	26
2.3.2.1 Reflectivity . . . . .	28
2.3.2.2 Pulse repetition frequency, folding and the Nyquist interval . . . . .	29
2.3.3 Doppler velocity . . . . .	30
2.3.4 Polarimetric radar . . . . .	31
2.3.5 POLDIRAD at the DLR . . . . .	36
2.3.5.1 ZDR . . . . .	37
2.3.5.2 LDR . . . . .	38
2.3.6 Measurements by the polarimetric radar and the display . . .	39
2.3.6.1 Mesocyclone and TVS . . . . .	42
2.3.6.2 Weak echo region and bounded weak echo region . .	43
2.3.6.3 Hook echo . . . . .	43

2.3.6.4	Mid-Altitude Radial Convergence (MARC) . . . . .	46
2.4	Data from the National Meteorological Institutes . . . . .	46
<b>3</b>	<b>Deep moist convection and severe thunderstorm parameters</b>	<b>55</b>
3.1	Deep moist convection . . . . .	55
3.1.1	Definition of deep moist convection and the thunderstorm spectrum . . . . .	55
3.1.1.1	Single cell . . . . .	56
3.1.1.2	Multicell storms . . . . .	57
3.1.1.3	Supercell . . . . .	58
3.2	Different types of organized, deep moist convection . . . . .	59
3.2.1	The supercell . . . . .	59
3.2.1.1	Definition and the classification . . . . .	59
3.2.1.2	Internal structure . . . . .	60
3.2.1.3	V-notch, cold-U and the close in warm area . . . . .	63
3.2.1.4	Classic supercell . . . . .	64
3.2.1.5	Low precipitation supercell, (LP) . . . . .	65
3.2.1.6	High precipitation supercell, (HP) . . . . .	65
3.2.2	Severe hailstorm . . . . .	66
3.2.3	The bow echo . . . . .	67
3.2.3.1	The rear inflow jet . . . . .	70
3.2.4	Mesoscale convective systems . . . . .	73
3.2.4.1	The wake depression . . . . .	75
3.2.4.2	The derecho . . . . .	77
3.2.4.3	Mesoscale convective complex, MCC . . . . .	78
3.2.4.4	Mesoscale convective vortex, (MCV) . . . . .	80
3.3	Severe thunderstorm parameters and their (dis)advantages . . . . .	81
3.3.1	Basic surface . . . . .	82
3.3.2	Thermodynamic fields . . . . .	83
3.3.2.1	Convective available potential energy . . . . .	84
3.3.3	Wind shear . . . . .	94
3.3.3.1	Anvil-layer storm relative wind (9-11km) . . . . .	95
3.3.3.2	Mid layer storm relative wind (4-6 km) . . . . .	96
3.3.3.3	Low-level shear (boundary layer-1km) . . . . .	97
3.3.3.4	Storm relative vorticity . . . . .	97
3.3.3.5	Storm relative helicity . . . . .	101
3.3.3.6	Storm motion . . . . .	107
3.3.3.7	ID method . . . . .	110
3.3.4	Composite indices . . . . .	112

3.3.4.1	Energy helicity index . . . . .	112
3.3.4.2	Vorticity generation parameter, VGP . . . . .	113
3.3.4.3	Significant tornado parameter, STP and the Super-cell composite parameter, SCP . . . . .	113
3.3.4.4	Bulk Richardson number . . . . .	114
3.3.4.5	K-index . . . . .	115
3.3.4.6	Thompson index . . . . .	117
3.3.4.7	Severe weather threat index, SWEAT . . . . .	117
3.4	Severe thunderstorms in Europe . . . . .	117
3.4.1	Short review about European severe thunderstorm research . . . . .	117
3.4.2	Ingredients for severe thunderstorm outbreaks in Europe . . . . .	119
3.4.2.1	Elevated mixed layer, EML . . . . .	120
<b>4</b>	<b>Case studies</b>	<b>123</b>
4.1	Calculation of a few selected parameters . . . . .	123
4.2	Choice of events and verification . . . . .	123
4.3	Case studies . . . . .	124
4.3.1	26 May 2009: Bow echo, Southern Germany . . . . .	124
4.3.1.1	Overview . . . . .	124
4.3.1.2	Synoptic-scale overview and mesoscale discussion . . . . .	125
4.3.1.3	COSMO-DE performance . . . . .	134
4.3.2	3 August 2008: F4 tornado in Hautmont, France . . . . .	137
4.3.2.1	Overview . . . . .	137
4.3.2.2	Synoptic-scale overview and mesoscale discussion . . . . .	137
4.3.2.3	COSMO-DE performance . . . . .	146
4.3.3	15 August 2008: Regional tornado outbreak, Poland . . . . .	148
4.3.3.1	Overview . . . . .	148
4.3.3.2	Synoptic-scale overview and mesoscale discussion . . . . .	148
4.3.3.3	COSMO-DE performance . . . . .	158
4.3.4	22 August 2008: Severe hailstorm, south Germany . . . . .	159
4.3.4.1	Overview . . . . .	159
4.3.4.2	Synoptic-scale overview and mesoscale discussion . . . . .	159
4.3.5	23 June 2008: Supercell thunderstorm over southern Germany . . . . .	169
4.3.5.1	Overview . . . . .	169
4.3.5.2	Synoptic-scale overview and mesoscale discussion . . . . .	169
<b>5</b>	<b>Conclusions and outlook</b>	<b>179</b>
	<b>Bibliography</b>	<b>182</b>

<b>Acknowledgments</b>	<b>197</b>
<b>Curriculum Vitae</b>	<b>201</b>

# Chapter 1

## Introduction

### 1.1 Motivation

Thunderstorm! A word which comprises the allure, the danger and the total complexity of the weather ever since humans have populated the earth. The same mixture of fascination and scientific interest in this phenomenon brought the author of this thesis to this topic. Many people wonder how thunderstorms can influence someone in such an intense way that he dedicates his life to thunderstorm research. The answer cannot be delivered here on the paper but has to be answered on a field at night, when a huge thunderstorm updraft gets illuminated by a bright moon with lightning flashes quivering out of this cloud, accompanied by a deep, plowing thunder or the marvelous structure of a rotating updraft with various cloud sculptures in the sky. The other aspect however is the scientific part. With respect to thunderstorm forecasts, a lot has been achieved, but it can be seen on everyday's forecast that by far not all aspects of thunderstorm dynamics are understood or even discovered. An increase in technology and computer capacity, which allows scientists to amend numerical models with higher resolution, complex model physics and the assimilation of new observation and remote sensing data has caused an appreciable progress mainly in the short and medium range forecasts. However, small-scale phenomena like summer-time thunderstorms are still not resolvable and predictable (Hohenegger and Schär 2007) due to the coarse mesh-grid of the models or the simple fact that convection is still parameterized in the global models (although mesoscale models like *The Weather Research and Forecasting model*, (Michalakes et al. 2001) or the *CO*nsortium for *S*mall-Scale *MO*deling, *COSMO-DE 2.2* now resolve convective processes). The weakness of models results from the failure in the prediction of initiation or correct track forecasts. Human weather forecasters are therefore still

needed with the knowledge about the dynamics of thunderstorms, what they need for organization and where and when they will occur. This need of knowledge is enforced by the fact that thunderstorms pose a significant hazard to the economy (e.g. airport or agriculture) and to the chattels, which is highlighted for example in the following declaration of AIR Worldwide Corporation (AIR)<sup>1</sup> for the United States: *In the U.S., annual aggregate losses from severe thunderstorms have, on average, accounted for more than half of all insured catastrophe losses since 1990. In 2006 they accounted for nearly 90% of all such losses. Billion dollar occurrence losses are no longer uncommon.* Lightning, hail, hurricane-force wind gusts, tornadoes and flash flooding are all serious threats, which can occur everywhere, where thunderstorms are possible. This thesis outlines thunderstorms, which are well known in producing the most serious damage and ought to give an understanding about the complete spectrum of thunderstorms, but also the current level of knowledge how to use the data for the preparation of thunderstorm forecasts and warnings.

The beginning of thunderstorm interest can be tracked back into the time, when people were able to consign information to the posterity by pictures or letters. The interest and ability for thunderstorm research however can be traced back to the time, when appropriate instruments were invented like the weather radars in the early part of the 20<sup>th</sup> century. Major step points in the use of radar for thunderstorm forecasts were the detection of a certain reflectivity pattern on radar, on 9 April 1953 by the Illinois State Water Survey, North America and on 9 July 1959, Wokingham (England) (Browning and Ludlam 1962), which accompanied long-lasting and damage producing thunderstorms. This also was the cornerstone for the beginning of detailed studies of the different thunderstorm spectra like the (Byers and Braham Jr. 1949) thunderstorm project, how they behave in certain environmental conditions and what the dynamic looks like inside those thunderstorm clouds. Whereas the research on organized convection kept going in the United States throughout the 20<sup>th</sup> century, the primary interest in supercells and tornadoes in Europe was carried out mainly by two people, *Alfred Wegener* and *Johannes P. Letzmann*, between 1917 and 1940. However the interest in this subject disappeared mainly for historical reasons and it was not until the sixties and seventies, when the interest in tornado and organized thunderstorm research emerged again. Nevertheless, even nowadays, the knowledge of the dynamics of thunderstorms and its behavior reveals major differences in Europe due to the different technical settings, restrictions due to politics or the local interest of the weather service (e.g. specialized in topics about climatology, hydrology or satellite meteorology). A more detailed review about previous research is presented in the respective sections.

---

<sup>1</sup><http://www.airworldwide.com/>

## 1.2 Goals and outline of the thesis

Various severe thunderstorm events occurred over central Europe in the past few years. Some occurred in the typical environment, where long - lived and organized thunderstorms are common, and others occurred in an environment, where both the behavior and the strength were not expected. The goal of this thesis is to present an outline about the current knowledge about thunderstorms, including their dynamics and different degrees of organization. The second goal is to apply that knowledge to case studies of severe thunderstorm forecasts. A combination of polarimetric radar data from the DLR, high resolution weather forecast model data from the DWD (COSMO-DE) and remote sensing data was used to address the second goal.

In chapter 2, an overview about the numerical model and data is presented. The polarimetric Doppler radar of the DLR and the mesoscale weather forecast model COSMO-DE are described with additional information how to interpret certain radar signatures, which are important for thunderstorm forecast. In chapter 3, a detailed discussion is provided about the definition of deep convection and categorization. Indices commonly used for thunderstorm forecasts are introduced in chapter 3. Finally, in chapter 4, case studies are presented, where the current knowledge of severe thunderstorm forecasting is used to explain and handle five severe thunderstorm events in different regions of Europe.





# Chapter 2

## Numerical model, weather radar and data

### 2.1 Overview

Numerical weather prediction is a direct approach to weather forecasting, in which the physical laws, governing the atmosphere are integrated from an initial state (Shuman 1978). Next to the increasing computer capacity and therefore ameliorated numerical simulations, remote sensing data like satellite data also increases the accuracy of weather forecast models. This chapter provides an overview about the numerical model COSMO-DE in section 2.2. Then, the weather radar in general will be introduced from the basics to the modern polarimetric radar of the DRL in section 2.3. Finally, the specific data is discussed in section 2.4, which was used for this thesis.

### 2.2 Brief overview of COSMO-DE

The COnsortium for Small-Scale MOdelling, COSMO, was formed in October 1998 and is composed of various members, including the National Weather Services of Germany (DWD), Switzerland (MeteoSwiss), Italy (USAM), Greece (HNMS), Poland (IMGW), Romania (NMA) and Russia (ROSHYDROMET). The members actuate their own versions of COSMO, whereas the German version was used for this study. The main task of this consortium is to develop, improve and maintain a non-hydrostatic limited-area atmospheric model, which can be used both for operational and for research applications by the members of the consortium. In this work, COSMO-DE was used for studying the synoptic and mesoscale conditions on the case study days. This mesoscale model is an advancement of the 'Lokal-Modell Kürzestfrist', formerly known as (LMK) and amends the 'Globales Modell', (GME)

(grid mesh roughly 40 km) and the 'Lokal-Modell Europa', LME (grid mesh roughly 7 km and now known as COSMO-EU) since spring 2007 with a grid mesh of 2.8 km. For operational applications, COSMO is nested in the global model GME of DWD. Hence, COSMO-EU data is driven by the global model GME, or expressed differently, the GME data are assimilated on the COSMO-EU grid. DWD uses an own assimilation run for COSMO-DE (impelled by the data of the COSMO-EU run) from which the forecasts are started. The latent heat nudging (LHN) is still active for the first hour of the forecast. The analysis of atmospheric fields is done with the nudging-based data assimilation. In COSMO-DE, nudging is performed towards direct observations (Schraff and Hess 2003) and can be seen in Fig. 2.1. The location of the observation, the influence of the observation on a certain grid

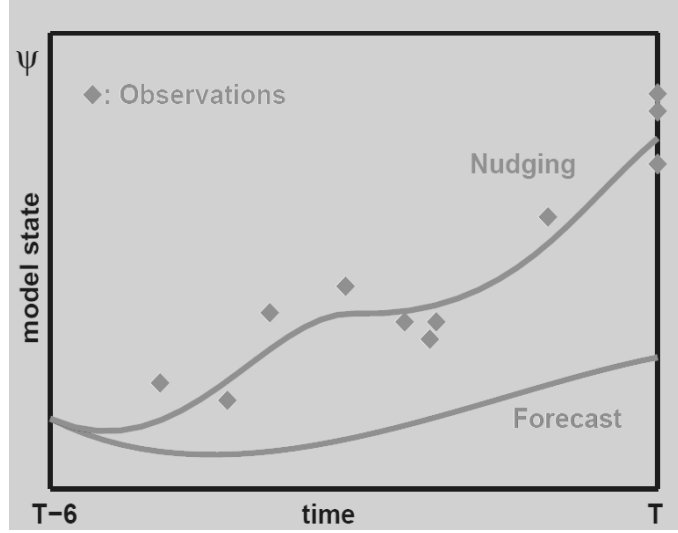


**Figure 2.1:** Conceptual illustration of nudging (Schraff and Hess 2003).

point and other weightings are considered by the introduction of a relaxation term into the model equations, where the tendency for the prognostic variable  $\psi(x,t)$  is given by:

$$\frac{\partial}{\partial t}\psi(x,t) = F(\psi,x,t) + G_\psi \cdot \sum_{k_{obs}} W_k(x,t) \cdot [\psi_k^{obs} - \psi(x_k,t)] \quad (2.1)$$

$F$  denotes the model dynamics and physical parameterizations,  $\psi_k^{obs}$  the value of the  $k^{th}$  observation influencing the grid point  $x$  at time  $t$ ,  $x_k$  the observation location,  $G_\psi$  a constant called nudging coefficient and  $W_k$  an observation-dependent weight. An *observation increment* is called the difference between an observed and model value. The so-called nudging-equation describes a continuous adaption of the model values towards the observed values during the forward integration of the model, which has an exponentially behavior when neglecting the dynamics and physics with

further assumptions (adapted from Schraff and Hess (2003)). This can be seen in Fig. 2.1. The factor  $W_k$  determines the weights, given two different observations at a specific grid point. The weight of a single observation depends on many differences, highlighted in:

$$W_k = \frac{w_k}{\sum_j w_j} \cdot w_k \quad (2.2)$$

$$w_k = w_t \cdot w_{xy} \cdot w_z \cdot \epsilon_k \quad (2.3)$$

where  $\epsilon_k$  is the quality of the observation and the horizontal ( $w_{xy}$ ), vertical ( $w_z$ ) or temporal ( $w_t$ ) difference between the observation and the target grid point.

Another assimilation method is the assimilation of radar data with the help of the latent-heat-nudging (LHN). A relationship between the observed quantity and the prognostic variables of the forecast model has to be established before assimilating any observed data into a numerical model. This is particularly difficult for the precipitation due its complex behavior. A variety of processes occur from the first formation of cloud droplets until the arrival at the ground, with phase changes and collisions. Latent heat is released by condensation and freezing and evaporative cooling and melting remove energy from the environment. That is what is considered with the LHN. A relation between the rain rate  $R$  and the latent heat release  $\Delta(L_H)$  and therefore a certain temperature change  $\Delta T$  was established:

$$R(l_g) \propto \int_{l_0}^{l_g} \Delta L_H(l) dl \quad (2.4)$$

where  $l$  is an arbitrary path, a precipitation particle takes from its formation at  $l_0$  to the ground  $l_g$ . The LHN now takes the assumption that the whole path  $l$  is run through within one single model column and one single time step. The rain rate at the surface grid point is proportional to the vertical integral of latent heat release in the column above this point. The modeled latent heat profile is then scaled according to the ratio of observed and modeled rain rates. The model produces rain rates, closer to the observed one as it responds to the adapted heat release (The information is adapted from Stephan et al. (2008) and Leuenberger (2005)). An assimilation method for radar reflectivity and satellite data into COSMO-DE is also presented in Sokol (2008).

The main reason for the implementation of the Lokal-Modell (LM) was the too large grid-spacing, operational numerical weather prediction-models had in the past. A lack of information was present at smaller scale, like the meso- $\gamma$  scale (500 m to 5 km). Therefore, the general goal of COSMO was the prediction of the evolution of the atmospheric flow in such small scales. In COSMO-DE, a grid-spacing of 1 to 3 km is used, so deep moist convection and associated feedback mechanisms with large scale motions can be resolved explicitly. Additional operational applications are planned with COSMO, but the resolution of deep convection is the most important

fact for this thesis. In the following, the COSMO-DE is presented, as this model domain was used for the case studies.

The project COSMO-DE of the DWD began in July 2003 and ran for 3 years. COSMO-DE prepares forecasts up to 18 h in advance with the aforementioned meso- $\gamma$  resolution (horizontal mesh grid width is 2.8 km). The model domain comprises Germany, Switzerland, Austria and parts of the neighboring states, preparing 21-h forecasts 8 times a day at 00, 03, 06, 09, 12, 15, 18 and 21 UTC (see Fig. 2.2). It has  $421 \times 461$  grid points in the horizontal and 50 vertical model levels. The lowest level is 10 m AGL with the uppermost model level being roughly at 34 hPa or 21.5 km AGL .

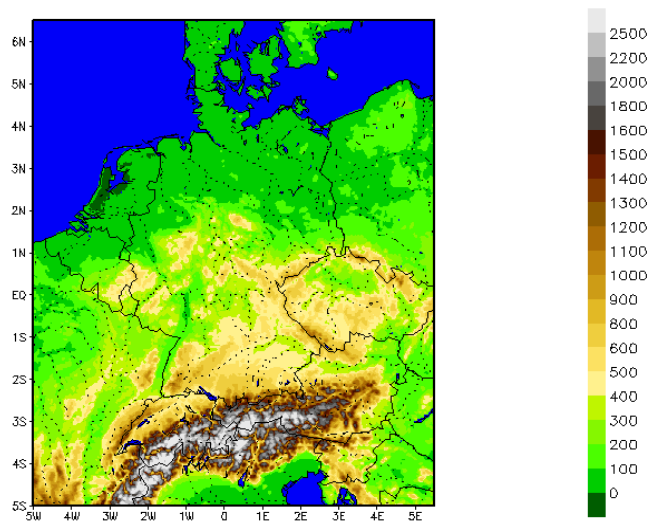


**Figure 2.2:** The domain of COSMO-DE and the orography (height in m). Adopted from [http://www.cosmo-model.org/content/tasks/operational/dwd/default\\_de.htm](http://www.cosmo-model.org/content/tasks/operational/dwd/default_de.htm)

Significant modifications were done with the physical parameterization. The parameterization for convection was stopped completely.

For this thesis, only forecasts of COSMO-DE were used. Dependent on the time, when the severe thunderstorm events occurred, either 00 UTC or 12 UTC forecasts were used:

- 26 MAY 2009 ... **period:** 00 UCT - 21 UTC ... **forecast:** every 15 minutes with the COSMO-DE domain
- 22 AUGUST 2008 ... **period:** 00 UCT - 21 UTC ... **forecast:** every 15 minutes with the COSMO-DE domain
- 15 AUGUST 2008 ... **period:** 00 UCT - 21 UTC ... **forecast:** every 15 minutes with the COSMO-DE domain

- 03 AUGUST 2008 ... **period:** 12 UCT - 21 UTC ... **forecast:** every 15 minutes with the COSMO-DE domain
- 23 JUNE 2008 ... **period:** 00 UCT - 21 UTC ... **forecast:** every 15 minutes with the COSMO-DE domain

The dynamical formulation of the COSMO-DE is based on the COSMO-Model (Doms and Schättler (2002); Steppeler et al. (2003)). It is a non-hydrostatic, fully compressible model in advection form. Instead of the leap-frog time integration and the second-order centered differences as applied so far in the larger-scale applications of the COSMO-Model, COSMO-DE uses a two-time-level integration scheme based on the Runge-Kutta method of third order for the prediction of the 3 Cartesian wind components  $u$ ,  $v$ ,  $w$ , the pressure perturbation  $p'$  from a hydrostatic base state and the temperature perturbation  $T'$  (Stephan et al. 2008). COSMO-DE is not the only mesoscale model as most of the members also have their own version of COSMO. At MeteoSwiss for example, the COSMO-2 is running with a resolution of 2.2 km since February 2008. The COSMO-IT has been running since October 2007 with a resolution of 2.8 km at USAM in Rome. More information about COSMO can be found on the main COSMO page<sup>1</sup>.

## 2.3 Weather radar

### 2.3.1 Brief history of radar meteorology

At the beginning a short review about radar meteorology in general is given before concentrating on the scientific radar at the DLR. This summary cannot do full justice to that episode where radar data was included into the meteorological service step by step but it ought to sketch the most important events, which mark the advancement to a separate branch in the field of meteorology. The information about radar meteorology in general is mainly based on Hitschfeld (1986) and Rinehart (1991). Radar meteorology has its beginning in the early thirties and forties of the 20<sup>th</sup> century. The leaders in this new sector were Germany, the USA and England, which made their first experiences with the backscattering of electromagnetic waves during the war. The radar meteorology itself had its beginning in the late thirties when Sir Robert Watson-Watt noticed a shower cloud on his very high frequency radar. This event fell just in the time period, when J.Randall and H.Boot invented the magnetron in 1939, which was used as 'transmitting tube'. The first thunderstorm was tracked by David Atlas on the 20 February 1941 along the south coast of New England. In 1943 scientists looked for a

---

<sup>1</sup><http://www.cosmo-model.org/>

correlation between the strength of the precipitation and the rate of backscattering from the hydrometeors, which could be seen on the radar screen. In 1947, the first reflectivity factor (Z) - rain rate (R) relation<sup>2</sup> was described and just one year later, the Marshall-Palmer exponential drop-size relation was published. The fifties were the decade when radar meteorology was more and more practiced in different parts of the world, like Japan and the Soviet Union. Doppler capabilities were added in the fifties and polarization in the seventies. Today, radar meteorology is a large field. Weather radar conferences, which started in 1947 with a small group, now attract hundreds of people from all over the world.

As for severe thunderstorms, the breakthrough began with the recognition of a persistent and well structured hook echo on 9 April 1953 by the Illinois State Water Survey. On that day Mr. Donald Staggs, an electrical engineer, detected that signal during his preparations for a field campaign later-on and continued to follow the storm for some more time. One of those radar images (Fig.2.3) is included below and displays a persistent hook echo with an attenuation notch due to strong rain and hail.

A nice summary about this event can be found in the internet<sup>3</sup>, with more radar images and data of that day. Another date to remember is 9 July 1959, as a strong hailstorm in Wokingham (England) was studied by radar (Fig.2.4). During those measurements the hailstone trajectories were evaluated so this became the first event when the streamline pattern of an organized thunderstorm, probably a supercell, was recognized. Both examples are just the most prominent ones aside from numerous other observations during that time frame.

### 2.3.2 Radar basics

The word *RADAR* is an acronym for *radio detection and ranging* and was coined in the early forties. It is a detecting system, which uses electromagnetic waves to identify altitude, direction or range of an object. The radar itself was developed in the thirties, before the Second World War began. (Fig. 2.5) explains the basics of a radar. In blue the transmitted signal in form of microwaves or radio waves with a pulse power of roughly  $10^5$  Watt. Those waves travel with the speed of light and are in phase when emitted. During the passage of the troposphere, the signal interacts with various objects like the topography (ground clutter), aircrafts or the rain producing clouds. However also the atmosphere itself has an impact on the direction, the signal takes. When the radar beam encounters an object,

---

<sup>2</sup>note of the author: Z-R is the relation of reflectivity to rainfall intensity

<sup>3</sup>[http://chill.colostate.edu/w/CHILL\\_history](http://chill.colostate.edu/w/CHILL_history)

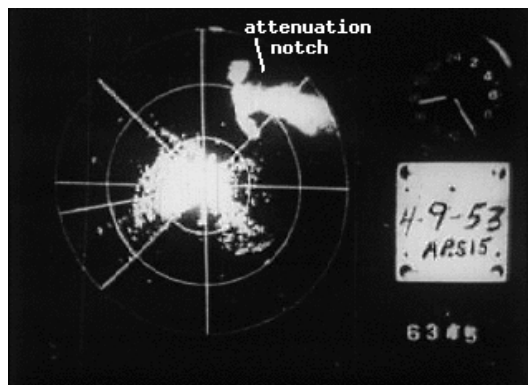


**Figure 2.3:** 9<sup>th</sup> April 1953, first radar image of a pronounced hook echo, displayed as a PPI.

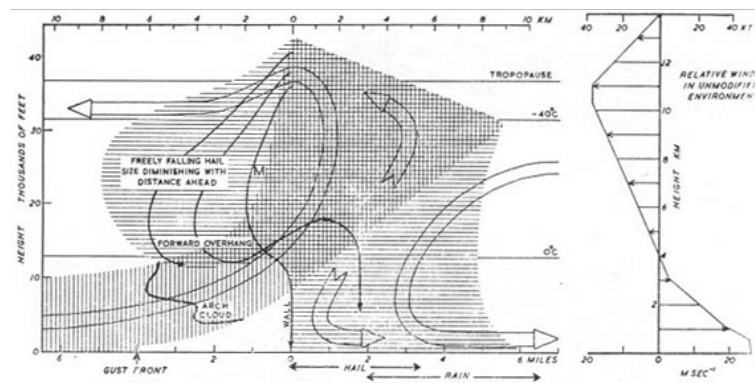


**Figure 2.4:** 9<sup>th</sup> July 1959 Wokingham hailstorm in England.

it is scattered in all directions and therefore also back to the transmitter. For a monostatic radar (as sketched in Fig. 2.5), the backscattered signal is received by the very radar. The signal then has to be amplified because the backscattered signal is very weak, in the order of  $10^{-14}W$ . Hence the range of power between the transmitter and receiver is in the order of 19. However, the ability to detect such a weak signal allows the radar to find objects, which would not be found with different signals, like sound for example.

The radar is a very useful tool to detect objects like airplanes but also to allow measurements in a volume, when the radar beam is filled out completely by the measured object (for example rain). Two perspectives are important when working with a radar: **elevation** and **azimuth**. The elevation is the angle between a horizontal plane and an aslope upward tilted line, which is displayed with the angle  $\phi$  in Fig. 2.5. The azimuth encloses the angle on an horizontal plane, when we spin around in a clockwise manner for example, so it is also called an angle which encloses different geographical directions ( $0^\circ$  is north and  $180^\circ$  south).

The radar, which was described is called an *impulse radar*. To be able to assess

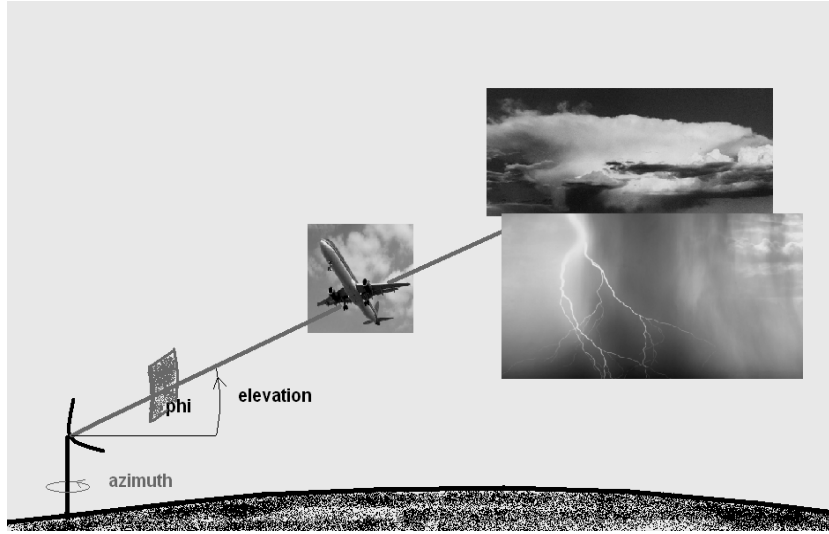


**Figure 2.5:** A sketch about the functionality of a radar.

the magnitude of backscattered energy from a point target, the following equation is used:

$$P_r = \frac{(P_t G)}{(4 \pi R^2)} \sigma \frac{A_e}{(4 \pi R^2)} \quad (2.5)$$

The radar equation states that the received signal power  $P_r$  has to be of sufficient strength for detection in order to detect a target of radar cross section  $\sigma$  at a given distance  $R$  using a radar with average transmit power  $P_t$ , antenna gain  $G$  and effective area of the receiving antenna  $A_e$ .  $A_e$  can be expressed as  $\frac{G\lambda^2}{4\pi}$ .

In meteorology however, the targets which have to be detected are so extensive that they fill out the radar beam completely. For those targets, the radar equation for volume targets is as follows:

$$P_r = \frac{(P_t G^2 \lambda^2 \theta_0^2 h)}{(1024 \ln(2) \pi^2 R^2)} \Sigma_{vol} \sigma_i \quad (2.6)$$

where  $h = c \cdot \tau$ ,  $c$  is the speed of light,  $\tau$  the pulse duration,  $A_e = \frac{G\lambda^2}{4\pi}$ ,  $R$  the distance from the radar,  $P_t$  the transmitted energy and  $P_r$  the received energy,  $\sigma$  the radar cross section and  $\theta$  the half-width of the radar cone. With the knowledge of what is in the 'volume' of the radar cone, one can evaluate the rain-, snow- or hail-rate.

### 2.3.2.1 Reflectivity

The most basic parameter in radar meteorology is the *reflectivity*. It can be expressed as:



$$z = \sum_{Vol} D_i^6 \quad (2.7)$$

The amplitude of the backscattered signal is very weak, so amplification of the signal is needed (a logarithmic one with the unit: dBZ). The reflectivity depends heavily on the diameter of the precipitation particle but also on the number of particles in the observed volume. A rough guide line for Z is between 10 and 40 dBZ for rain, up to 40 dBZ for soft hail and 55 dBZ and more for large hail.

### 2.3.2.2 Pulse repetition frequency, folding and the Nyquist interval

Radars are very useful and also reliable tools in observing and forecasting thunderstorms. The structure of certain reflectivity patterns is a hint on specific severe thunderstorms like a hook shaped echo, which indicates the possibility of rotation in this storm or a sharp reflectivity gradient along the leading edge of a mesoscale convective system which points to strong convergence and a mature system. However, Doppler velocity data helps to assess the wind field in those storms and therefore highlights the degree of organization in addition to the basic reflectivity data. A short overview about the most important radar patterns is given in respect to organized, severe thunderstorms.

Before elaborating certain Doppler velocity patterns one has to keep in mind a few constraints for radar measurements, which make the final interpretation sometimes quite difficult. The first one is the so called *Doppler dilemma*:

$$v_{max} \times r_{max} = \frac{c\lambda}{8} \quad (2.8)$$

$v_{max}$  is the unambiguous velocity or Nyquist velocity

$$v_{max} = \frac{PRF\lambda}{4} \quad (2.9)$$

and  $r_{max}$  the maximum range a radar signal can travel:  $r_{max} = \frac{c}{2PRF}$ . PRF is the shortcut for *pulse repetition frequency* and describes the frequency of the transmission of each pulse.  $v_{max}$  states that in order to detect high velocities, high wavelengths have to be used. The Doppler dilemma is the fact that both  $v_{max}$  and  $r_{max}$  have PRF once in the denominator and once in the nominator. Solving both equations for PRF and equating these, one obtains equation 2.8. The right hand side of the equation is constant for a given radar, so for large  $v_{max}$  one has to choose a small  $r_{max}$  and vice versa. As meteorologists want to measure high wind speeds also in a long distance, the solution would be to work with longer wavelengths

$\lambda$ , but this means bigger and more expensive radars, which is not the best way to solve the problem. Therefore meteorologists have to work with that dilemma, which manifests itself in both range and velocity aliasing (*folding*). *Second-trip echoes* are generated, when a radar beam detects a thunderstorm beyond  $r_{max}$ , so the radar displays the signal at a distance of  $(r - r_{max})$ . It is sometimes hard to distinguish second-trip echoes, especially when other thunderstorms are present nearby the radar station but there are a few possibilities to detect those. One is a more wedge-like appearance, which points to the radar whereas real storms reveal a more circular or irregular appearance and they do not necessarily know where the radar is situated. Another hint is the compressed height, which would not be expected with storms, which have high reflectivity.

Velocity folding is another complicating factor for meteorologists, when evaluating a Doppler image. Whenever a target exceeds  $v_{max}$  the velocity gets aliased or folded by a velocity, the *Nyquist interval velocity*. Any velocity, exceeding  $+/- v_{max}$  is converted into that interval. Depending on the magnitude of the aliased region, one is able to detect a folded area quite easily due to an abrupt change in velocities. For example if a storm moves towards the radar much faster than  $v_{max}$ , the storm's center would reveal an area with strong outbound values, surrounded by strong inbound values. Dependant on the range of the velocity measurements (e.g. POLDIRAD uses  $+/- 16 \frac{m}{s}$ ), numerous foldings can occur, which makes it sometimes difficult to tell the true velocity at a given range. More detailed discussions can be found in radar books and papers to that topic, like Doviak and Zrnic (1984), Jing and Wiener (1992) and Holleman and Beekhuis (2002).

Although mainly the most serious cases are recognized, attenuation of a radar signal can be a serious problem facing meteorologists and hydrologists due to the fact that in heavy rain or hail events, reflectivity information can be completely lost from large portions of a radar scan. The attenuation depends on the spectrum of droplets, which gets sampled in a radar beam. Another factor is the consistence of the hail, as wet hail forces a much higher attenuation than dry hail or sleet. Various corrections were proposed (Rahimi et al. 2005) but the adjustment is hard to accomplish as the property of the particles is not well known so one has to be careful when interpreting a signal behind a strong shower or thunderstorm.

### 2.3.3 Doppler velocity

Another useful characteristic is the *Doppler effect*. This effect was forecast by Christian Doppler already in 1842 and is widely used in meteorology, especially for severe thunderstorm forecast. The reason for this effect depends on the following

equation:

$$\lambda \cdot f = c \quad (2.10)$$

where  $\lambda$  is the wavelength,  $f$  the frequency and  $c$  the speed of light. The Doppler effect is a modification of the measured frequency as either the transmitter or the target or both move with different speed and direction against each other. In meteorology, the transmitter is stationary in general with the target moving towards, away or parallel to the radar. If the target approaches the radar, then the frequency increases and the opposite occurs, when the target departs from the radar. The meteorologist is interested in this product to assess the wind direction, how well the model did in forecasting the wind field but also to detect rotation in thunderstorms. In general, movements towards the radar (inbound) are colored in 'cold' colors, like blue, whereas movements away from the radar (outbound) are colored in 'warm' colors, like red. An example can be seen in Fig. 2.11 with the radar placed at Dodge City or in the upper left corner of this radar image.

### 2.3.4 Polarimetric radar

A general overview about polarimetric radar research is conducted in this chapter. Most of that information is taken out of the National Severe Storms Laboratory polarimetric radar research manuscript <sup>4</sup> but also rounded by Rinehart (1991) and the documents of the lecture *Einführung in die Radarmeteorologie* by Dr. Martin Hagen. A polarimetric radar differs from conventional radars in respect to the transmitted radio waves, which have both horizontal and vertical orientations. This new technique allows meteorologists not only to assess the vertical and horizontal dimensions of the cloud but also to improve the estimation of rain and snow rates, hail distribution and rain/snow transition zones like the bright-band. Like the other impulse radars it transmits short pulses of radio waves at a very high pulse repetition frequency (PRF) and in between it receives the backscattered signal from scatterers and hydrometeors. The signal is received by the antenna and everything gets analyzed by the radar signal processor. In addition to that, the ability to estimate the Doppler frequency shift enables those radars to measure the motion of cloud droplets and precipitation particles in radial range. Those radars are so called *Doppler radars* and they are able to determine the wind speed with that attribute.

Despite the frequency shift there are more possibilities how cloud and precipitation

---

<sup>4</sup><http://www.cimms.ou.edu/schuur/radar.html>

particles can interact with the radar's power and phase, including the following:

- ★ Backscattering

- ★ Propagation

Backscattering is a quite complex function of shape, density and size of the particle ensemble. It refers to the process of radio waves, which become influenced by precipitation particles and cloud droplets, which reflect just a fraction of the overall power back to the radar. Propagation on the other hand refers to the process, where precipitation particles as a whole modify the power and the phase of a transmitted signal in forward direction. All those effects accumulate as the signal advances through the cloud and the absorbed energy results in a decrease of power, also known as **attenuation**. There are more complicating facts when using a radar like the illuminated area becoming larger during the time as the very focused beam broadens and becomes more diffuse. More complicating factors for radar measurements and the analysis of the results include:

- ★ *ground clutters* like natural obstacles (e.g. hills and trees) or man-made obstacles like buildings, which block parts of the radar beam and cause an artificial high power return

- ★ the highly non-linear nature of the relationship between the size and the power return and the fact that just the smallest drops keep a spherical appearance

Let us now concentrate on the question, what is exactly meant by the term *polarization*. Radio waves are composed of a series of oscillating electric and magnetic fields, which are orthogonal to each other. Polarization itself just describes *the direction of orientation of the electric field wave crest*. Thus an horizontal polarized wave yields an electric field crest which is oriented in horizontal direction with respect to the magnetic field wave crest, which is aligned in vertical direction. Vice versa for the vertical polarization. The operating mode of a polarimetric radar is therefore just a constant switch between the horizontal and vertical polarization with each successive pulse. Due to the transmission of two polarizations of radio waves, those radars are sometimes referred to as **dual-polarization radars**. The fact that both horizontal and vertical pulses are emanated, informations on the size, shape and density of hydrometeors may be estimated. There are quite a few variables measured by the polarimetric radar. A few of them will be listed below but a more detailed explanation is carried out in the next section:

- reflectivity
- differential reflectivity for drop shape assessment

- correlation coefficient to detect a mixture of precipitation types
- linear depolarization ratio

Now the radar product for linear H/V polarization is discussed in more detail. As mentioned earlier, the polarization of the emitting radar beam at POLDIRAD changes between each pulses from vertical to horizontal to vertical and so on and numerous pulses from one polarization are averaged to increase the accuracy. Radar meteorologists use the so called *scattering matrix*<sup>5</sup> to define the dimensions of the reflectivity measurements. The following products can be achieved, whereas the first index describes the polarization of the received radiation and the second index the polarization of the emitted radiation:

- $Z_{hh}$  means outgoing waves are polarized horizontal and incoming waves are polarized horizontal.
- $Z_{vv}$  means outgoing waves are polarized vertical and incoming waves are polarized vertical.
- $Z_{vh}$  means outgoing waves are polarized horizontal and incoming waves are polarized vertical.
- $Z_{hv}$  means outgoing waves are polarized vertical and incoming waves are polarized horizontal.

A short example ought to show why it is important to know how to work with different polarizations. When following a raindrop during its free fall, a change of its shape can be recognized, as the raindrop tends to flatten out somewhat. Therefore the drop reveals a shape, which is wider horizontally than vertically. Hence it is of interest to work with a radar, which measures with horizontal polarization for

---

<sup>5</sup>Definition of the scattering matrix:

$$\begin{bmatrix} E_h^s \\ E_v^s \end{bmatrix} = \begin{bmatrix} S_{hh} & S_{hv} \\ S_{vh} & S_{vv} \end{bmatrix} \begin{bmatrix} E_h^i \\ E_v^i \end{bmatrix} \quad (2.11)$$

with  $E^i$  the incoming wave and  $E^s$  the emitting one, V=vertical and H=horizontal

maximizing the rainfall detection. Not just the shape of the precipitation differs in a cloud, but also its consistence (e.g. ice, rain, snow), which can be used to get a unique insight into the cloud with a polarimetric radar. In this thesis just the most used tools of the POLDIRAD are discussed, which includes the differential reflectivity (ZDR) and the linear depolarisation ratio (LDR). One of the most interesting aspects in the meteorological forecast is the discrimination between rain and hail, especially for aviation and agricultural applications. Hail detection began in the late 1950s, using a single polarized radar with techniques based on reflectivity measurements, which is described in more detail in Vulpiani et al. (2007) and Cook (1958). With the development of the radar polarimetry, the  $Z_{DR}$  became the most used and studied parameter for hail detection and was published in many papers, like Bringi et al. (1984), Geotis (1962) and Illingworth et al. (1986). Hail has an isentropic radar appearance even if the hailstone is oblate. The reason for that was found by Knight and Knight (1970) in the 70s with the tumbling being the main reason for the more spherical appearance in the radar. In Europe, nearly all weather radars operate at C-band as bands higher than S-band can result in strong attenuation effects. Nowadays, algorithms for correction are evaluated, especially for the polarimetric radars. However, mixed phase regions still pose a problem, which causes erratic measurements or estimations regarding hail or rain dispersal in a thunderstorm cloud. A more detailed explanation can be found in radar books like Zrnica and Doviak (2006) and on the radar page of the National Severe Storms Laboratory (NSSL)<sup>6</sup>.

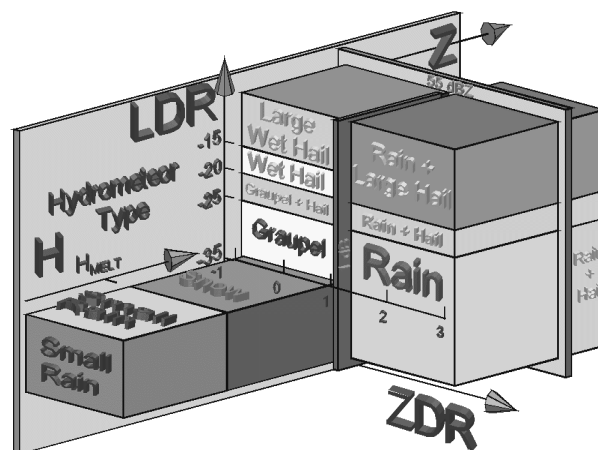


**Figure 2.6:** Classification according to Höller (1998). ZDR is the differential reflectivity, LDR the linear depolarization ratio,  $z$  the reflectivity and  $H$  the height above ground.

<sup>6</sup><http://www.nssl.noaa.gov/divisions/radar/radpubs.php>

In (Fig. 2.6), H.Höller compiled a classification for hydrometeors with the help of ZDR, LDR,  $z$  and the height of 0°C mainly for thunderstorms. Higher LDR values for example hint on potential hail and the same for higher  $z$ -values, where 55 dBZ act as the threshold, where hail becomes increasingly likely.

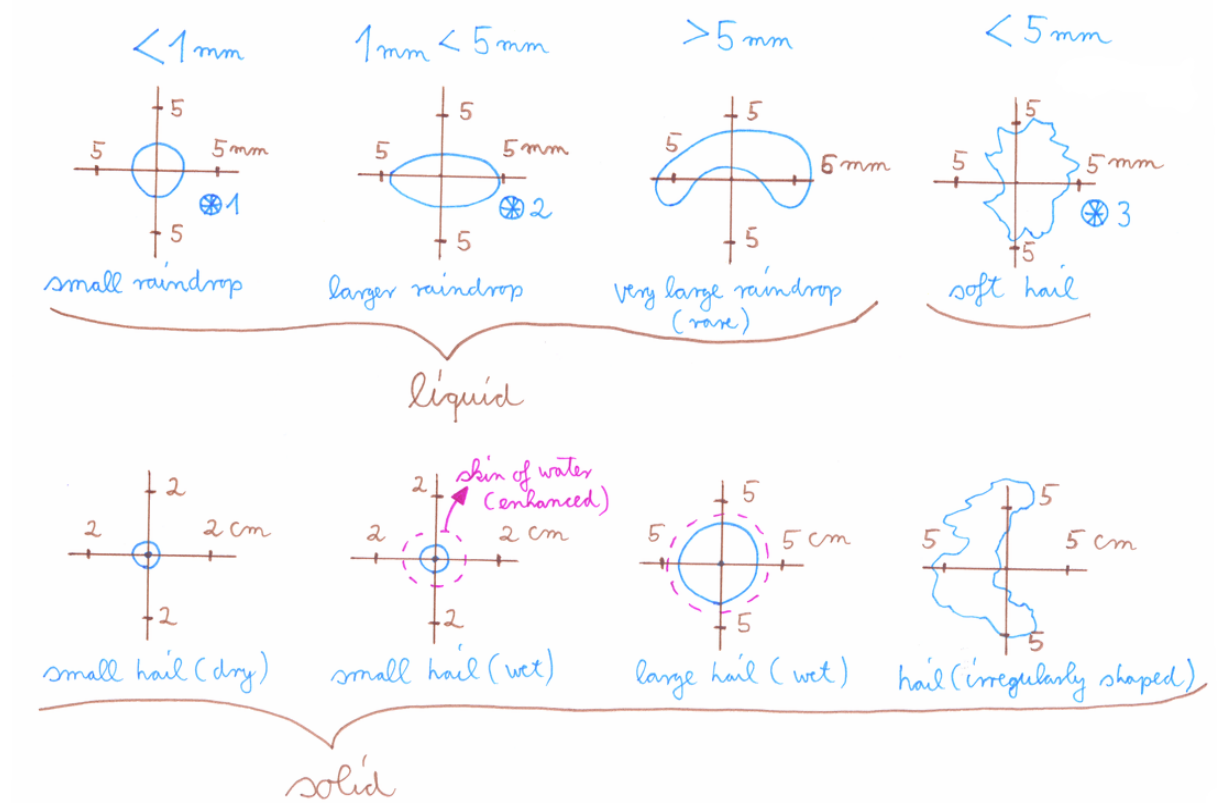


**Figure 2.7:** An overview about the shape of liquid and compact particles.

In (Fig. 2.7) an overview is given about how the shape and constitution influence the backscattered pulse. The liquid part is sketched first. The diameter of the rain drop increases from the left to the right.

★ 1): Very small droplets with a diameter of less than 1 mm remain round due to the limited contact surface. The raindrop remains symmetric and one expects:  $Z_{hh} = Z_{vv}$  with a low  $Z_{vh}$ .

★ 2): When increasing the diameter to 5 mm, the shape of the raindrop becomes oblate due to the increasing contact surface.  $Z_{hh} > Z_{vv}$  with a low  $Z_{vh}$

The raindrop even grows larger in size (in rare cases up to 8 mm in diameter), but raindrops that large tend to bisect themselves with two small droplets being the end result.

★ 3): Soft hail is of the same size, but compact. In general, the shape of soft hail is very irregular and complex.  $Z_{hh} > Z_{vv}$  with an higher  $Z_{vh}$  compared to the liquid particles.

Thereafter, hail in different sizes, shapes and constitutions causes quite complex backscattered signals. For example hail, surrounded by a thin water film, causes different LDR and ZDR compared to dry hail. Also the shape of the hail becomes increasingly complex as the hailstone grows. Another characteristic for hail is the tumbling movement of the hydrometeor. Finally, snow causes very low LDR values and also low reflectivity values. Snowflakes reveal a very complex shape.

### 2.3.5 POLDIRAD at the DLR

The polarimetric Doppler weather radar at the DLR operates for research since 1986 in cooperation between the 'Institut für Physik der Atmosphäre, (IPA)' and the 'Institut für Hochfrequenztechnik und Radarsysteme' at the DLR. Two main research fields are covered which include the cloud physics and the mesoscale meteorology. Another reason for the necessity to operate a polarimetric radar is the fact that cloud system models are not able to handle such aspects simultaneously. Therefore, parameterization is the only solution, which is used for example for hydrodynamical flow patterns, turbulence, entrainment or the more detailed microphysics. Hence verification is needed to prove how reliable those parameterizations are. The radar is not only used to understand the dynamics and microphysical structures of clouds but also to distinguish between the different precipitation types and size distribution. In cooperation with the DLR (IPA), numerous studies like the Convective and Orographically-induced Precipitation Study (COPS) 2007, CLEOPATRA (21 July 1992) or LINOX (15 July - 2 August 1996) were carried out mainly for thunderstorm research, but also to get a better insight into frontal systems and extensive and long-lived squall lines. In addition to the use of Doppler velocity data one is able to explore the wind fields throughout those features. In accord with another monostatic Doppler radar (e.g. Hohenpeißenberg) an entire three-dimensional flow field in an area with precipitation can be determined.

POLDIRAD measures many useful real time data (only for research) like

★ reflectivity factor

★ differential reflectivity



- ★ linear and circular depolarisation ratio
- ★ Doppler velocities and Doppler spectral width

Two types of receivers work parallel. The first one is for 'power products' like the reflectivity, differential reflectivity and linear and circular depolarisation ratio. The other product is a phase product like Doppler spectral width. POLDIRAD is a C-band radar with  $1^\circ$  beamwidth at azimuth and elevation. The radar is able to scan a range of 120 km or 300 km with a resolution of 300 m or 750 m respectively. Right now the radar operates with an accuracy of roughly 1dB for power measurements and  $1 \text{ m s}^{-1}$  uncertainty is present when using phase measurements like the radial velocity. Further informations are listed in Schroth et al. (1988).

### 2.3.5.1 ZDR

A new polarization method has proved useful over the past years, which is called the differential reflectivity (ZDR), which was tested by Seliga and Bringi (1976). In this scheme, the radar transmits and receives a pulse of horizontally polarized radiation and it processes the preserved echo. Then the next impulse is transmitted and received but now a vertically polarized signals is used. This switch between vertically and horizontally polarized pulses continues and therefore  $Z_{DR}$  can be written as:

$$Z_{DR} = 10 \log \left( \frac{\langle z_{hh} \rangle}{\langle z_{vv} \rangle} \right) \quad (2.12)$$

with the following units:  $z = \text{mm}^6 \text{m}^3$  or  $Z = \text{dBZ}$ . The units of ZDR is dB.

The final degree of  $Z_{DR}$  depends on the shape of the particle, its orientation and behavior during the free fall. This method serves for the identification of horizontal oriented precipitation particles. It is noteworthy that falling raindrops vary their shape, sometimes feature nearly perfect shaped spheres for small droplets to more flattened drops, when the diameter reaches 3 mm or more. Pruppacher and Beard (1970) found that the deformation of drops of sizes  $0.5 \text{ mm} < r_0 < 4.5 \text{ mm}$  was linearly related to the drop size with  $r_0$  being the equivalent radius of a drop. When using a large, flattened drop for example, one gets higher returns at horizontal polarization compared to the vertical one, so  $Z_{DR}$  for large droplets has slightly positive values (up to 5 dB), whereas smaller, more spheric drops have a  $Z_{DR}$  next to 0 dB. Europe is situated in a climate region, where precipitation development is heavily bound to the ice phase, so mixed precipitation, hail and sleet

are all present in deep convective thunderclouds. Hail can be recognized with the  $Z_{DR}$ , but it is helpful to check the reflectivity maps in the area of interest as both, light rain with small raindrops and hail have a  $Z_{DR}$  near 0 dB. Hail, especially large one exhibits erratically shaped surfaces, so hailstones do not fall with a preferred orientation but tumble as they fall. Hence in a single pulse volume of a radar, random orientations of the hailstones preponderates with roughly as many oriented vertically as horizontally so that polarization effects cancel. A rough guide line for the  $Z_{DR}$  is 0 to 5 dB for rain, around 0 for soft hail and the same for hail. Another effect, which ought to be mentioned is the *differential attenuation* when a polarized radar beam crosses an area with heavy rain. Due to the shape of the droplets, the horizontal signals get attenuated significantly compared to the vertical signal. Therefore, the  $Z_{DR}$  has negative values behind an area with strong precipitation.

### 2.3.5.2 LDR

The other parameter is the linear depolarisation ratio (LDR), which is derived as follows:

$$LDR = 10 \log_{10} \left( \frac{z_{vh}}{z_{hh}} \right) \quad (2.13)$$

with the following units:  $z$  in  $mm^6 m^3$  or  $Z$  in dBZ. LDR has the units dB.

The definition of the LDR is the following: The ratio of the power received in the orthogonal or cross-polarized channel to that received in the transmission or copolarized channel of a dual-channel radar, when a linearly polarized signal is transmitted.<sup>7</sup> The final magnitude of LDR depends on the shape of the particles, their orientation and their behavior during the free fall. LDR serves as a useful tool to detect the bright band region, where various phase changes occur. In this area, melting particles acquire a more asymmetric shape and wobble around. Hailstones are also not perfectly spherical and their tumbling motions cause some of the backscattered radiation to contain a small signal component that is polarized orthogonally to the incident radar pulse. A rough guide line for the LDR is smaller than -30 dB for rain, -25 to -30 dB for soft hail (very wet hail has values up to -25 dB) and -25 dB up to -15 dB or higher for hail. Ground clutters for example result in a strong depolarization, which is also present during the forward scattering of radiation. Hence, the LDR has to be handled with care when the radar beam passed through an area where strong depolarization took place as the linear part of the

---

<sup>7</sup><http://amsglossary.allenpress.com/glossary/search?id=linear-depolarization-ratio1>

polarization has weakend significantly. This is the case for sure during the passage of strong hail cores. The reason for the LDR being negative is because of the main component of the linearly polarized, backscattered signal from hydrometers has the same polarization as the transmitted one, so the LDR yields a value less than unity or a negative decibel quantity<sup>8</sup>. More details are published in Aydin et al. (1986).

### 2.3.6 Measurements by the polarimetric radar and the display

A myriad of informations can be achieved by polarimetric radar measurements but just those will be mentioned, which play a grave role in this thesis. The first and the most widespread used display is the *plan position indicator*, PPI, which is a map-like format with the radar in the center. Numerous *range marks* or *range rings* indicate the distance and for fixed-site installations, north is at the top. This so called panorama-display is achieved by rotating the radar 360° around the radar site at a fixed elevation. Dependant on what the forecaster exactly needs, this measurement can be repeated at the same or at different elevations. One has to keep in mind that the radar beam continues to move upwards through the atmosphere and experiences refraction caused by the atmosphere. Therefore a PPI is not exactly a plane but a cone of more or less upward bent curves. The reader is referred to radar books like Rinehart (1991) for more detailed informations.

Another kind of useful display is the *range height indicator*, RHI. An example can be seen in Fig. 2.8. Measurements have to be done at a constant azimuth but

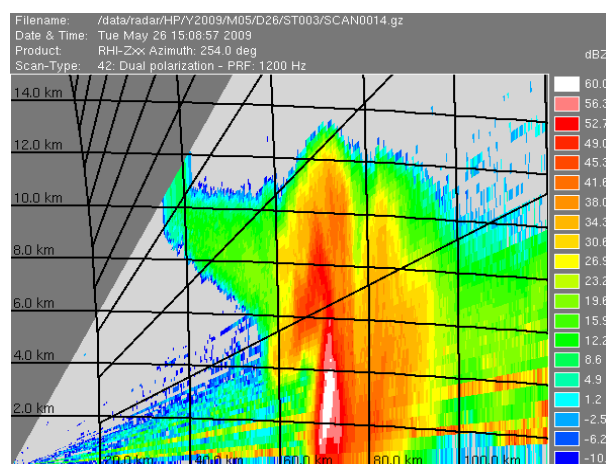


**Figure 2.8:** An example of the RHI product from POLDIRAD (26 May 2009).

different elevation angles. As it is the case in the PPI display, the horizontal axis is

<sup>8</sup>[http://www.chill.colostate.edu/w/CSU\\_CHILL](http://www.chill.colostate.edu/w/CSU_CHILL)

again the distance from the radar with the vertical axis sampling the height above the radar. This product is just used in special studies for the scientific operating mode. It is useful in detecting more pronounced features in a cloud like the bright band or bounded echo regions. A combination of both, PPI and RHI however is a very helpful tool in the interpretation what is going on inside a thunderstorm.

When drawing up PPIs with different elevations another product can be achieved, which is called *constant altitude plan position indicator*, CAPPI. It solves the disagreeableness, which was mentioned before, where PPIs do not represent a flat plane. Therefore one interpolates those PPI measurements on a constant height and therefore it is possible to determine the reflectivity on a specific height. This was first carried out by the **Stormy Weather Group** at the McGill University in Montreal and it was composed of data from each angle that is at the height requested for the cross-section.<sup>9</sup> However there are a few constraints also with that product like the unavailability of data at some distance, depending on the height of the CAPPI. Beyond that distance, a CAPPI displays the data from the lowest PPI. Another weakness can be seen when scrolling through the different CAPPI heights, where one is able to see that the PPI zones become smaller the higher we want to create our CAPPI. A sketch can be found in Fig. 2.13.

Another option is the use of the *Pseudo CAPPI* (PCAPPI). If we want to display a PCAPPI-2000 m for example, one gets the problem that at short range, even the highest radar beam is lower than the 2000 m. So the values are taken from the highest elevation. Thereafter one follows the 2000 m height by interpolation before the opposite problem arises in the long range. The lowest radar beam is higher than 2000 m and therefore the values are taken from the lowest elevation. A sketch can be found in Fig. 2.14. The final display is called *maximum constant altitude plan position indicator*, MAXCAPPI. To get a product like this, one has to project the maximum value out of a vertical column onto a horizontal plane and the result is a two dimensional display of the radar volume scan.

The *velocity/azimuth display* (VAD) vertical wind profile (VWP) shows wind velocities at various altitudes above the surface and provides the forecasters near realtime wind data for that specific spot. It is a time series of the horizontal wind at specific heights above the radar and provides valuable insight into meteorological phenomena like the frontal structure or the movement of moisture. Wood (2008) explained in more detail how the measurements of the Doppler velocity along a circle at constant range look like in this case during the approach of hurricane Katrina in 2005.

The VAD is a volume scan product, which samples the horizontal wind at

---

<sup>9</sup>Gematronik

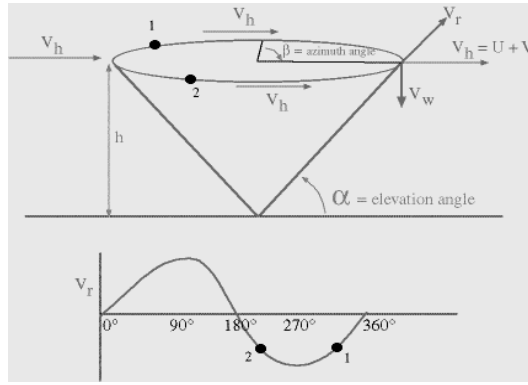


**Figure 2.9:** The calculation of a Velocity Azimuth Display.  $\alpha$  is the elevation angle and  $\beta$  the azimuth.  $v_h$  is the wind velocity with  $V_r$  and  $v_w$  the horizontal and vertical component.  $h$  is the height AGL.

specific heights above the radar. At the DLR, Oberpfaffenhofen, PPI scans at an elevation of  $20^\circ$  are used to cover various heights with just one scan. The wind velocity, here called  $v_h$ , can be divided into a horizontal and vertical term,  $v_r$  and  $v_w$  respectively and is composed of the U and V wind component (see Fig.2.9)<sup>10</sup>.  $v_r$  is retrieved by the following formula:

$$v_r = (U \sin \beta + V \cos \beta) \cos \alpha + v_w \sin \alpha \quad (2.14)$$

where  $\alpha$  is the elevation angle and  $\beta$  the azimuth angle. A wind field is examined, which varies approximately linear in the horizontal scale across the region and the wind components can be considered, including the divergence and deformation of the horizontal wind and the vertical motion. The wind component u and v are assumed to be constant in time over the observed period (1 min). With  $\beta$  resolving  $0^\circ - 360^\circ$  and  $\alpha$  being fixed, a volume scan is done, sampling the lowest 5-10 km.  $v_w$  is assessed to zero, so Fig. 2.14 modifies to

$$v_r = (U \sin \beta + V \cos \beta) \cos \alpha \quad (2.15)$$

Now just two samples have to be done and the U and V component can be calculated. The Doppler velocity has its maximum value in the downwind direction and its minimum in the upwind direction (hence on storm relative velocity products, the wind blowing towards the radar has negative values and positive ones, if it leaves the radar station). The wind velocity appears as the amplitude of the sine curve. In some products available on the internet, a different color code is used to indicate the reliability of the wind data in respect of the number of scatterers,

<sup>10</sup><http://apollo.lsc.vsc.edu/classes/remote/>

which are available at the particular azimuth and elevation. Scatterers must be present, otherwise no VAD can be generated despite clear air echoes next to the radar (often seen as a ring around the radar on the screen). Another source of information is the absence of data suggesting few scatterers, which is an indication of drier air. However the main power of a VWP product is the ability to easily recognize the structure of fronts, the strength of thermal advection but of capital importance, supervising the strength of jets. This is a nice nowcast tool due to the ability for forecasters to compare the strength of the wind field with various model data so that one is aware of any over-/underestimation of the model wind field. Houze (1994) and especially Browning (1968) treat this topic in more detail.

### 2.3.6.1 Mesocyclone and TVS

Certain Doppler velocity patterns indicate how well organized a thunderstorm is and allow forecasters to increase the lead time for severe thunderstorm warnings. A well known phenomenon, which can be seen in velocity data is the mesocyclone. The term *mesocyclone* was first coined by Fujita in 1963, who made the following interpretation of a mesocyclone: *A mesolow which is found to accompany a definite circulation pattern is called a mesocyclone* (Fujita 1985a). It took more than twelve years for the term to become more prominent in the severe weather forecasting community as Burgers and Lemmon presented Doppler velocity analyses of mesocyclones (Lemon et al. 1977). In the early eighties, one could find the following description: *First the entire thunderstorm updraft begins to rotate; the spinning column of rising air, 10 to 20 kilometers in diameter, is called a mesocyclone.* (If it goes on to generate a tornado, which the majority of mesocyclones do not, it is called a tornado cyclone, ref. to Fujita (1984)). Doswell III. and Burgess (1993) came up with a definition, which is valid until nowadays: **The mesocyclone is a deep, persistent cyclone** whereas *deep* means a significant fraction of the depth of the cumulonimbus cloud in which the circulation is embedded (several kilometers). *Persistent* refers to the convective time scale, defined by the time it takes for an air parcel to rise from within the inflow layer of the updraft to the anvil outflow (a few tens of minutes). This kinematic-dynamic approach is just one possibility to distinguish and detect supercells. The dispersal and strength of the precipitation is also a nice tool to separate different supercell categories. On a Doppler radar, the mesocyclone has quite a unique feature composed of a strong velocity couplet. Enclosed, two different images of a mesocyclone can be found, one emerged from a computer simulation and the other one featuring a real event (Fig. 2.10 and Fig. 2.11).

The main characteristic is a tight vorticity couplet with strong inbound and outbound velocities. Depending on the geometry of the radar beam, the location of the beam relative to the mesocyclone and the distance of the mesocyclone from the radar, not more than one or two pixels are occupied. Those pixels reveal intense radial velocities and one can expect that the velocity data gets folded in this region, which is the basic principle of the rotation algorithm, called *tornado vortex signature*, *TVS*. If a TVS is detected, the presence of a strong mesocyclone is indicated and tornadogenesis can occur or is imminent. The term TVS is somewhat deceptive in respect of what is detected by the radar as tornadoes itself are too small in most of the cases, so just the persistent mesocyclone is caught by the radar beam. In addition, not just the strength of the gate-to-gate shear (inbound and outbound velocities) determines the magnitude of the TVS but also the size and depth of the TVS and the strength of any surrounding mesocyclone. For tornado forecasting, just those can be forecast, which are closely connected to a rotating updraft, so gustnadoes or fairweather waterspouts cannot be detected.

#### 2.3.6.2 Weak echo region and bounded weak echo region

The weak echo region (WER) (Chisholm 1973) and the bounded weak echo region (BWER) are closely connected to the same mechanism and are indicators of strong updrafts. A WER evolves as intense upward motions are present in the updrafts core and water droplets or hail fail to form due to the very limited time they have during the ascent. Dependent on the strength of the updraft, this void of scatterers can extend well upward and eventually becomes bounded at all sides by much stronger reflectivities. The reason for that is the rapid growth of water droplets and hail, which develop during their rapid rise through the updraft core. They now exit the updraft and encircle the updrafts core as they fall back toward the earth. This feature is now called a BWER and serves as an indicator that the storm transitioned into a severe and organized thunderstorm. An example is shown at Fig. 2.8.

#### 2.3.6.3 Hook echo

Probably the most well known and notable feature is the hook echo, which is an indicator for rotating and probably tornado producing thunderstorms. It was first identified in the early fifties (9 April 1953, (Stout and Huff 1953)) although Van Tassel (1955) is given credit for coining the term. In the history of the research of the hook echo many different findings were published, like a 'wall of echo' at the

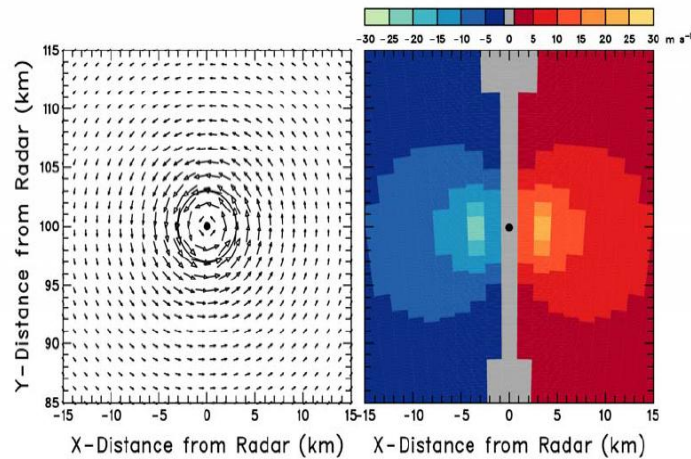


**Figure 2.10:** The Doppler velocity pattern (right) corresponds to a mesocyclone (left) that has peak tangential velocities of  $25 \text{ m s}^{-1}$  at a radius of 3 km from the circulation center (black dot). The radar is situated to the south. Adapted from: <http://www.nssl.noaa.gov/papers/dopplerguide/>

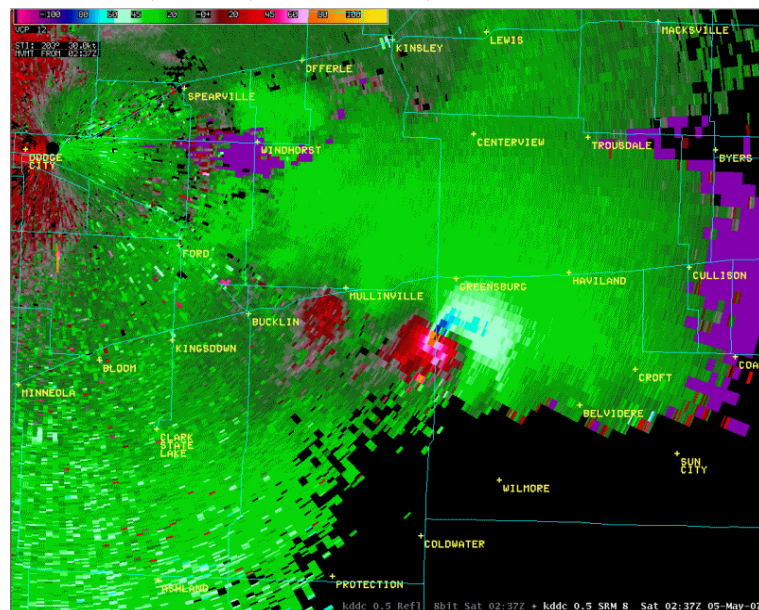


**Figure 2.11:** This image was taken from the NOAA National Weather Service radar station in Dodge City, Kansas on 7 May 2007 that was operating in Doppler mode. (Adopted from the National Weather Service). The radar is positioned in the upper left corner of this image. Green and blue is inbound and red and orange the outbound velocity. One of the strongest mesocyclones ever observed is just about to enter Greensburg.



southern edge of the hook (Browning and Donaldson 1963) or a 'circular echo' on the tip of a hook echo, called *asc* (Garrett and Rockney 1962). Another important aspect during the research of that feature was the appearance of a region with anticyclonic vorticity on the opposite side of the hook echo, which was studied closely by Brandes (1978) and Brandes (1984). In 1982, Fujita and Wakimoto (1982) even documented an anticyclonic tornado within the region of anticyclonic vertical vorticity although the origin of that phenomenon was not well understood. Many theories were established about the evolution of the hooked shaped appendix although the majority came up with similar results. The first explanation was developed in the late fifties by Fujita. He thought that the advection of precipitation from the rear of the main echo around the tornado cyclone and the updraft would cause the hook (Fujita 1958). This was confirmed by Brandes (1981) and also in three-dimensional numerical simulations by Klemp and Ray (1981). During the research of this feature, many different shapes were recognized, like a spiral shaped echo or a doughnut shaped hook (Fujita 1973), as well as hooks that morphed from one shape into another. This makes it sometimes very difficult for forecasters to detect a hook echo. Therefore, velocity data is an irreplaceable tool. Another interesting finding is the false hook echoe in Switzerland (Houze et al. 1993). Those hooks are placed on the right sides of left moving storms with respect to the storm motion. This feature is therefore not associated with the updraft region, but is associated with the downdraft region of anticyclonical rotating storms. The main reason for the continuing interest in this feature is its relevance for tornado forecasting. The National Weather Service considers the presence of a hook echo as sufficient to justify issuing a tornado warning. However, despite the fact that strong rotation is present and a supercell may be ongoing, many other ingredients play a role in tornadogenesis at lower levels, so despite a more or less enhanced possibility for tornado development, no coercive tornado report has to be expected. In fact, Sadowski (1969) documented a quite low false alarm rate of about 12% during his study when issuing tornado warnings due to the appearance of an hook echo but a worse result was received during other campaigns. Forbes (1975) finally presented nice statistics of a major tornado outbreak on 3 - 4 April 1974 in the US, which for example showed that tornadoes associated with hook echoes tend to be stronger, or that hook echoes appeared roughly 30 min ahead of the tornado formation. A weakness of this study was the limited time-frame of just one day.

To summarize, hook echoes are an indicator for well-organized thunderstorms and often signal the presence of a mesocyclone. They frequently precede tornado development, but many hook echoes occur without subsequent tornado activity. An example is shown in Fig. 4.35 a.

#### 2.3.6.4 Mid-Altitude Radial Convergence (MARC)

Another important pattern in the Doppler velocity fields is the *Mid-Altitude Radial Convergence (MARC)* velocity signature (Przybylinski 1995), (Schmocker et al. 1996) and (Funk et al. 1996). This signature is a precursor of severe to damaging wind events, bound to the passage of organized mesoscale convective systems or bow echoes. A more detailed understanding of the dynamics of mesoscale convective systems or bow echoes is required and therefore just the basic mechanisms will be explained here in this chapter. The region of interest is the deep convergence zone along the updraft and downdraft interface, highlighting intense convergence with an average depth of 10 km. If the eastward moving storm is west of a radar, strong outward velocities indicate the downstream tilted updraft current but also the front to rear flow. On the other hand, inbound velocities indicate the mesoscale rear inflow jet, which penetrates towards the deep convergence zone. The MARC is therefore just a close coupling of inbound and outbound velocities at mid-altitudes with values  $> 22 \text{ m s}^{-1}$ . Once radial velocity differentials reach such values, the potential for severe straight line winds increases. A sketch is presented in Fig. 2.12.

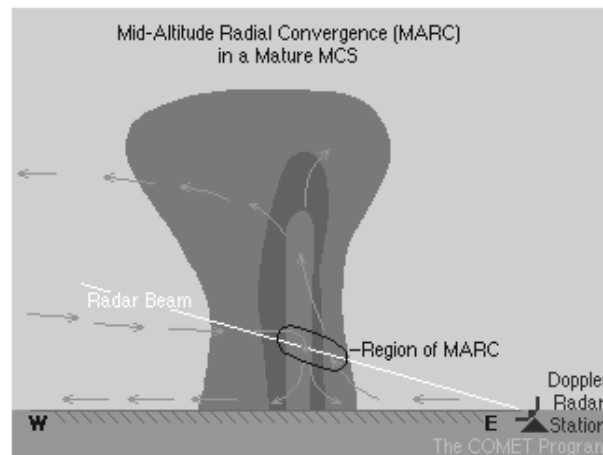


**Figure 2.12:** Mid-altitude radial convergence signature, COMET Program (<http://www.comet.ucar.edu/>). The different grey colors represent the precipitation area with increasing intensity towards the center of the thunderstorm, the white line the radar beam and the arrows the trajectories, a parcel would take.

## 2.4 Data from the National Meteorological Institutes

The intent of this work is to cover not only parts of south Germany, where excellent radar data is available, but to include other parts of Europe where frequent severe

thunderstorm events occur, too. It was therefore a necessity to get in contact with nearby weather services where significant severe thunderstorm events occurred during the past 1-2 years. Several meteorological institutes supplied radar imagery, high-resolution satellite data and surface data for the case studies. Both the data and institutions are listed below:

- **Deutscher Wetterdienst**

★ High resolution 'Mikroprozessorgesteuertes Registriersystem des Instrumentenamtes München' (MIRIAM) data with the following parameters:

- air temperature (accuracy  $0.1^{\circ}\text{C}$  within the past 10 minutes)
- dewpoint temperature (accuracy  $0.1^{\circ}\text{C}$  within the past 10 minutes)
- wind direction (accuracy in tens degree within the past 10 minutes)
- wind speed (accuracy  $0.1 \text{ ms}^{-1}$  within the past 10 minutes)
- maximum wind speed (accuracy  $0.1 \text{ ms}^{-1}$  within the past 10 minutes)
- amount of precipitation (accuracy  $0.1 \text{ mm}$  within the past 10 minutes)

- **Czech Hydrometeorological Institute (CHMI) in cooperation with EUMETSAT**

The data products can be divided into the CHMI Radar Department and the Remote Sensing Branch (SATELLITE DEPARTMENT). First the radar data, which were received (Basic Operational Radar Products). At the CHMI, digital radar measurements began in 1993 with the following radar products, generated from volume data every 10 minutes:

- Maximum reflectivity in ground and side views
  - \* Intensity levels (dBZ): 16 (from 4 to 60 dBZ )
  - \* Horizontal resolution :  $2 \times 2 \text{ km}$  up to max range of 256 km
  - \* Vertical resolution :  $1 \text{ km}$  up to height of 14 km
  - \* The geographical projection is gnomonic with the center at Prague-Libus

In addition, advanced operational radar products were provided (Advanced Operational Radar Products). New radar processing and visualization was done at the CHMI since 2001, generating operational radar products every 10 minutes:

- PPI - constant elevation radar reflectivity field
- CAPPI (constant altitude radar reflectivity field: 1-14 km with 0.5 km vertical step)
- Maximum reflectivity in ground and side views
- ETOP - Echo top heights

- VIL - vertically integrated liquid
  - \* Intensity levels (dBZ): 256 (from -32 dBZ with the 0.5 dBZ step)
  - \* Horizontal resolution :  $1 \times 1$  km up to max range of 256 km
  - \* Vertical resolution : 0.5 km up to height of 14 km
  - \* The geographical projection is gnomonic with the center at Prague-Libus

Data were also received by the Remote Sensing Branch (SATELLITE DEPARTMENT).

- RGB-airmass:

AIRMASS includes information from the split water vapour channels and ozone channel. It identifies airmass and gives indications of atmospheric dynamics (jet streams, stratospheric intrusions (proxy for potential vorticity)) in the middle-upper troposphere. At the same time it gives an overview on the accompanying cloud system. The following color codes are used:

- \* red: the moisture content at roughly 700-400 hPa and 500-200 hPa levels, approximated by brightness temperature differences of split WV channels
- \* green: the proxy for total  $O_3$  content distinguishing between  $O_3$ -rich polar and  $O_3$ -poor (sub) tropical air mass, using brightness temperature difference between  $9.7 \mu\text{m}$  ( $O_3$  channel) and  $10.8 \mu\text{m}$
- \* blue: mid/upper-level moisture content profile provided by brightness temperature at  $6.2 \mu\text{m}$

MET9 RGB-air mass composite (ref. to EUMETSAT: air mass is an RGB composite based upon data from infrared and water vapour channels from Meteosat Second Generation, MSG). It is designed and tuned to monitor the evolution of cyclones, in particular rapid cyclogenesis, jet streaks and PV (potential vorticity) anomalies. Due to the incorporation of the water vapour and ozone channels, its usage at high satellite viewing angles is limited. The air mass RGB is composed from data from a combination of the SEVIRI<sup>11</sup> water vapor (WV)6.2, WV7.3, infrared (IR)9.7 and IR10.8 channels ). This information was adopted from Roesli et al. (2006).

- RGB-129

RGB color composite of AVHRR with the following bands: 1,2 and 9

---

<sup>11</sup>MSG Spectral Response Characterisation (SEVIRI). A detailed explanation can be found at: [http://www.eumetsat.int/Home/Main/Access\\_to\\_Data/Meteosat\\_Image\\_Services/SP\\_1123237865326?l=en](http://www.eumetsat.int/Home/Main/Access_to_Data/Meteosat_Image_Services/SP_1123237865326?l=en)

- RGB-108-BT

RGB color composite of AVHRR with the following bands: 1,0 and 8. In addition to that, the color enhanced brightness temperature (200-240 K) is overlaid.

- HRV

The High Resolution Visible (HRV) channel provides measurements with a resolution of 1 km (brightness temperature, VIS/IR combination for the Czech Republic and for Europe). The high resolution satellite data was available for the following regions: Czech Republic, central Europe and Europe with the following products:

- \* brightness temperature
- \* VIS / VIS-IR combination and WV
- \* MSG1\_RSS (Meteosat Rapid Scanning: The MSG satellites normally scan the full Earth disc every 15 minutes. By scanning a smaller area scans can be conducted more frequently. If only a third of the Earth disc is scanned, it takes a third of the time to scan the area - in this case every 5 minutes instead of every 15 minutes (EUMETSAT).

- further satellite data with different RGB combinations, for example for convective forecasts (RGB-STORM)

- **Institute of Meteorology and Water Management, Poland**

- ★ Satellite images from METEOSAT in channel IR 10.8  $\mu\text{m}$  for Europe and HRV for Poland. HRV is a channel on Meteosat-8 with a broad spectral response providing 1 km resolution beneath the satellite (also called *satellite sub-point*)

- ★ Lightning data products from the detection system PERUN for Poland. The data was forwarded with 60 minutes pro map. The time of each lightning event is marked by 6 colors.

- ★ Radar data from the radar network POLRAD (using the standard version of software, called RAINBOW, produced by the Gematronik GmbH ([www.gematronik.com](http://www.gematronik.com))). The following products were used:

- CAPPI (Fig. 2.13).

The CAPPI algorithm calculates the desired product for the selected height. Data is present for the areas L2 and L3 whereas L1 and L4 have no data and can't be filled. Within areas L2 and L3 the data are derived by a distance weighted mean of the corresponding range bins of the

neighbouring higher and lower elevations, here El3 and El2 for area L2 and El2 and El1 for area L3 (Gematronik GmbH). A few technical details:

- \* Displayed range is 25 - 400 km
  - \* Layer height is 0 - 18 km (height of horizontal cut above mean sea level)
  - \* Displayed dynamic range for Z is -31.5 to 95.5 dBZ, 0 to 70  $\text{ms}^{-1}$  for the velocity with an uncertainty of  $\pm 0.1 \text{ ms}^{-1}$  and finally the rain rate with 0.1 to 500  $\text{mm h}^{-1}$
- PCAPPI (Fig. 2.14)
- The inner area L1 is filled with data, originated from the upper most elevation El2. The outer area L4 is filled with data, originated from El1, which is the lowest elevation in this example. In the middle part of the Pseudo-CAPPI layer - areas L2 and L3 - the data are derived by a distance weighted mean of the corresponding range bins of the next higher and lower elevations, here El2 and El1. Therefore, the data of area L2 are more influenced by El2 values, whereas area L3 is more influenced by El1 values. The technical details are the same like the CAPPI product (Gematronik GmbH).
- SRV (storm relative velocity)
- The Storm Relative (mean radial) Velocity product is used to show local radial velocity values relative to a moving storm.
- \* Displayed dynamic range is 30  $\text{ms}^{-1}$
- HSHEAR (horizontal shear)
- The HSHEAR product takes a velocity volume data set as input and displays shear values for a single, curvature corrected Cartesian layer. The change of the wind velocity in north-south direction and in east-west direction is calculated and added to find the value of the horizontal shear. The HSHEAR product can be generated from any multiple elevation scan. The output values are scaled to  $(\text{m s}^{-1}) \text{ km}^{-1}$ .
- \* Displayed range is 25 - 400 km
  - \* Layer height is -6 - 18 km below and above mean sea level
  - \* Displayed dynamic range is 0 to 70  $\text{ms}^{-1} \text{ km}^{-1}$

- Institut Royal Météorologique, (IRM)

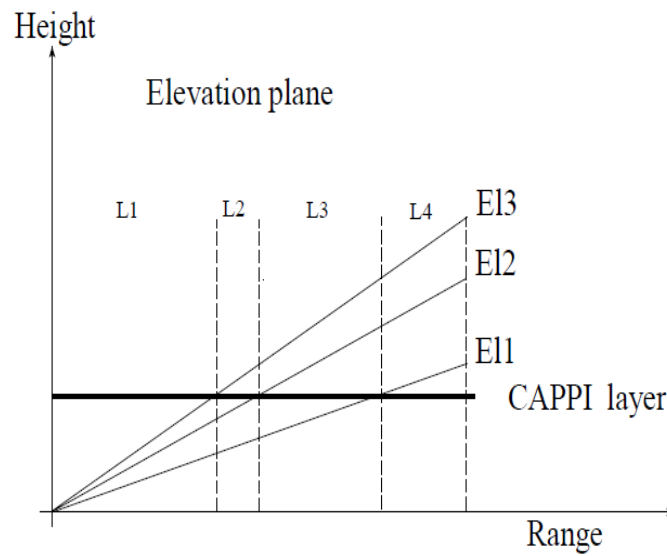


**Figure 2.13:** A sktech, how the CAPPI is produced. Adapted from Gematronik GmbH (<http://www.gematronik.com/products/radar-components/rainbowR-5/>)

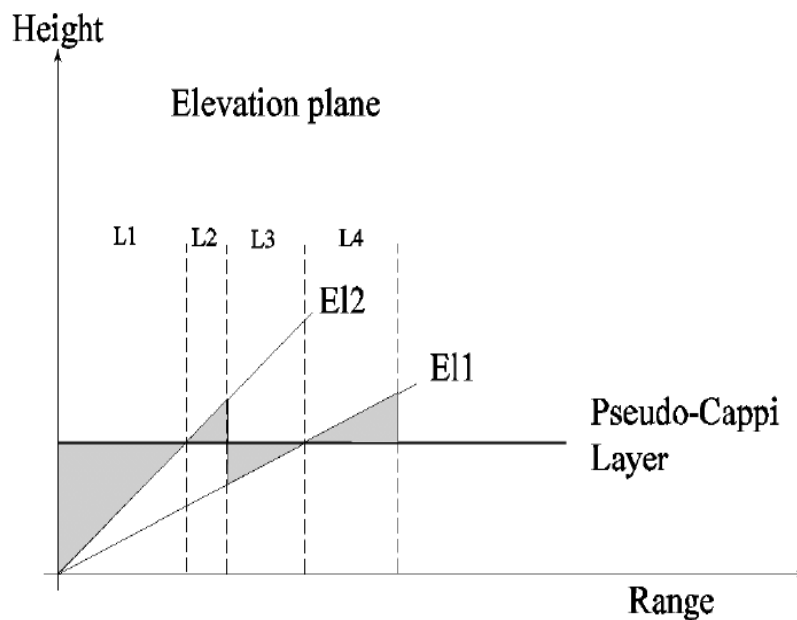


**Figure 2.14:** A sktech, how the PCAPPI is produced. Adapted from Gematronik GmbH (<http://www.gematronik.com/products/radar-components/rainbowR-5/>)



The data of two different radar station was supplied. The meteorological radar of the IRM is situated in *Wideumont*, in the province of Luxembourg. The second radar of the meteorological weather service 'Belgcontrol' is situated at *Zaventem*. The maximum range of those radars is 240 km although for precipitation measurements, a range of 100 km is used. The radar images are produced every 5 minutes. Numerous products were provided:

- CAPPI (constant altitude PPI) with a pulse repetition frequency of 1200 Hz, a range of 120 km and resolution of 0.333 km
- Belgian composite
- a PCAPPI for velocity data (PCAPPI(V)) with the following technical details:
  - dual PRF velocity unfolding (Holleman and Beekhuis 2002)
  - resolution 470 m
  - height 1500m



# Chapter 3

## Deep moist convection and severe thunderstorm parameters

### 3.1 Deep moist convection

Convection is one of the major modes of heat and mass transfer in the atmosphere. Moist convection manifests as clouds, which can embrace all kind of shapes. The range of concomitant phenomena varies from light rain or snowfall to devastating thunderstorms with hail, damaging straightline wind gusts, flash flood-producing rain or tornadoes. Despite the fact that even some of the basic processes of moist convection remain still amorphous, a lot of mysteries of moist convection start to crumble under the increasing power of numerical simulations and remote sensing data. The focus not only in this chapter but in the complete thesis is set to deep, moist convection. In the following sections, an overview is offered about what is already known in forecasting thunderstorms and what causes all those different types of thunderstorms.

In section 3.1, a general overview about deep, moist convection is given. The different types of organized thunderstorms are presented in section 3.2 before the tools for thunderstorm forecasts are discussed (section 3.3). Finally, an overview about severe thunderstorms in Europe is given in section 3.4.

#### 3.1.1 Definition of deep moist convection and the thunderstorm spectrum

In the atmosphere, heat can be transported in three different ways:

- conduction
- radiation

- convection

Convection is responsible for thermally driven turbulent mixing of the atmosphere. The driving force for convection is buoyancy, which is defined as density variations in a fluid:

$$B = -g\left(\frac{T_p - \bar{T}}{\bar{T}}\right) \quad (3.1)$$

where  $T_p$  is the parcel temperature,  $\bar{T}$  the temperature of the environment and  $g$  the acceleration due to gravity. During the ascent of a parcel, phase changes can occur, e.g. from water vapor into liquid. Latent heat of condensation releases  $2.5 \cdot 10^6 J kg^{-1}$  into the surrounding atmosphere. A thunderstorm is able to release energy, comparable to dozens of kiloton bombs, or on average  $3.6 \cdot 10^{13} J$  per thunderstorm (Encyclopedia Britannica). This energy next to sensible heat is the driving mechanism for the intense, deep convection. Sensible heat is a thermal energy and refers to the heat that is added or removed from the air without water vapor content change. Heat, that results in a temperature change is called 'sensible'.

Deep moist convection (DMC) is another well known abbreviation for thunderstorms and exists whenever some form of instability can be observed. The term 'deep' is used, when thermally driven turbulent mixing causes vertical motions from the lower levels up to at least 500 hPa (Michel Davison<sup>1</sup>). DMC arises in many different ways, depending on the environmental shear and thermodynamic quantity. To handle the behavior of thunderstorms in respect to organization, longevity and dilation, a thunderstorm spectrum was created (Fig. 3.1).

### 3.1.1.1 Single cell

The thunderstorm spectrum is the result of different shear conditions throughout the troposphere. In Fig. 3.1, the spectrum starts with the *single cells* or *air mass cells*. In 1946/47 Byers and Braham Jr. (1948) participated in the so called *Thunderstorm project*, which was a cooperative undertaking on the part of four U.S. government agencies: the U.S. Weather Bureau, the U.S. Army Air Force, the Navy, and the National Advisory Committee for Aeronautics. Three stages during the lifetime of a thunderstorm were discovered:

- The **cumulus stage**, where just an updraft from the base to the top of the cloud is present.

---

<sup>1</sup><http://www.hpc.ncep.noaa.gov/international/training/deep/index.htm>

<i>The Thunderstorm Spectrum</i>			
Single Cell	Multicell Cluster	Multicell Line	Supercell
Weak updraft (non-severe)	Weak updraft (non-severe)	Weak updraft (non-severe)	Intense updraft
or	or	or	Almost always severe
Strong updraft (maybe severe)	Strong updraft (severe)	Strong updraft (severe)	Mesocyclone present
Slight threat	Moderate threat	Moderate threat	High threat

**Figure 3.1:** A thunderstorm spectrum, created by the National Weather Service, <http://www.nws.noaa.gov/>.

- The **mature stage**, where raindrops start to fall back to the earth, inducing the local downdraft next to the updraft.
- The **anvil stage**, without upward motion but downward motion in its lower part.

Another important point was the discovery of the influence of entrainment, resulting in either dissipation of a weak updraft chimney or the support of downward momentum due to evaporative cooling. These types of cells are also called the **Byers and Braham cells**. It is hard to observe a true Byers and Braham cell as mostly new convection gets triggered by the storm's outflow along the edges, resulting in multicell development. In typical air mass thunderstorm situations (some instability, weakly capped and focused along weak convergence zones) true single cells are possible.

### 3.1.1.2 Multicell storms

The vertical wind constantly plays a more serious role, as low-level shear and gustfront interaction cause multicell storms to reach a greater longevity compared to single cells. Chisholm and Renick (1972) were the first who coined the term 'multicell' in their study about Alberta hailstorms. Multicell storms can appear in form of a cluster or in a line with new cell growth along the leading edge of outward propagating cold pools generated by the downdraft. If ambient low-level shear supports the growth of new cells, repeated thunderstorm development along the flanking line is the result.

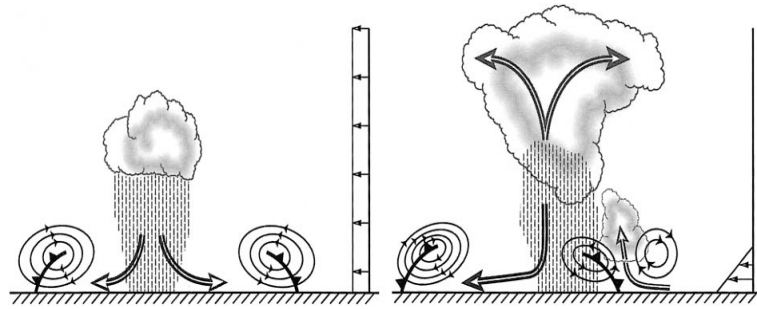


**Figure 3.2:** The left sketch describes the interaction between the gust front and negligible vertical shear and enhancement due to existing low level shear in the right sketch. (Weisman and Rotunno 2003).

The preferred side for new cell development is found where strongest cross-frontal inflow shear is present, increasing low-level convergence and hence increasing probabilities to lift the parcel above the LFC (ref. to subsubsection 3.3.2.1). This scenario is sketched in Fig. 3.2. The title *multicell* comprises many possibilities how convection evolves, including a mesoscale convective system (MCS), a mesoscale convective complex (MCC) and sometimes a mesoscale convective vortex (MCV). The reader is asked to switch to chapter 3.2 to get an overview about those systems.

### 3.1.1.3 Supercell

If shear increases even more in an adequately unstable environment, the most dangerous thunderstorms are able to evolve, called supercells. The term 'supercell' was coined in the early sixties, when a severe thunderstorm struck Wokingham in the UK (Browning and Donaldson 1963). Supercells have a defined and deep-tropospheric updraft coincident with a mid-altitude vorticity maximum (mesocyclone). In most cases, they are easy to detect on radar due to the unique signature, like a hook echo on the PPI or a WER/BWER on the RHI. Supercells have a separated up-/downdraft configuration, which results in long lifetimes, sometimes for several hours. Compared to the complete thunderstorm spectrum, supercells occur very infrequent (in the US less than 1% of all thunderstorms are supercells), but they are responsible for the most serious damage in property and life. A more detailed explanation can be found in the following section (sec.3.2).

## 3.2 Different types of organized, deep moist convection

### 3.2.1 The supercell

Supercells are the most dangerous but also awe-inspiring thunderstorms in the atmosphere. They display an efficient mechanism, which allows those storms to live for hours, producing large hail, severe straightline wind gusts, excessive rainfall amounts and tornadoes. They appear either skeletal with not much precipitation production or shrouded in rain and hail like an 'impervious wall' as described by many eye-witness reports. Supercells can adopt many different shapes and sizes, all studied in detail mainly in North America, but also in Switzerland, where some research was conducted e.g. (Houze et al. 1993). It is not the notion to give a detailed physical explanation of supercells and all its subspecies but a bunched overview about the environment, the different modes and the task of those cells.

#### 3.2.1.1 Definition and the classification

The term *supercell* was coined by Browning (1964), where he named single, large cells 'supercells' which revealed characteristic structures. This denotation endured the following decades with various definitions, when to use the term '*supercell*'. Nowadays, the definition of Doswell III. and Burgess (1993) is basically used in the literature, which states: *A supercell is composed of a deep, persistent, rotating updraft* (called a mesocyclone) and Doswell substantiates that later in a position paper for a penal discussion<sup>2</sup>, where he states that *deep* means that the updraft extends at least through a significant part of the complete updraft chimney. *Persistent* is thought to be the convective time scale a parcel needs to rise from the base of the updraft to its top. That is on the order of 10-20 min. Finally, for the definition of a *mesocyclone*, a value of the vorticity unit (around  $10^{-2} \text{ s}^{-1}$ ) is used. However those are just standard values as supercells have a smooth transition from low-topped to colossal huge supercells with accordingly different values. There are different kinds of supercells, which were classified mainly after the structure on radars but also depending on the amount of precipitation they produce.

---

<sup>2</sup>[http://www.cimms.ou.edu/~doswell/Conference\\_papers/SELS96/Supercell.html](http://www.cimms.ou.edu/~doswell/Conference_papers/SELS96/Supercell.html)

### 3.2.1.2 Internal structure

Supercells are a highly structured phenomenon, which needs certain ingredients to develop:

- instability
- directional and speed wind shear with increasing height

Supercells start like each thunderstorm, with the development of a strong updraft. However, this updraft ingests air in its inflow layer, which is helical (subsection 3.3.3.5) and is affected by strong horizontal vorticity, fostered by strong speed shear in the lowest 1-3 km above the planetary boundary layer. Horizontal vorticity is then looped up into the updraft and in the following tilted into the vertical. It depends on the component of helicity (subsection 3.3.3.5), if it is cross-wise or streamwise. The helicity is streamwise, when a positive correlation between vertical vorticity and velocity exists and crosswise, when a dipole-like structure of cyclonic/anticyclonic vorticity evolves along the fringes of the supercell. In the latter case, downdraft development results in a splitting supercell with a right and left moving storm. If storm relative winds are strong and veer with height, the cyclonic member becomes the dominant one due to upward directed non hydrostatic vertical pressure gradients whereas the anticyclonic member weakens due to subsident motions/negative vertical pressure gradient (Klemp 1987). If the environment supports a strong downdraft, the splitting supercell eventually transforms into a bow echo, which produces concentrated swaths of damaging wind gusts (Moller et al. 1990). In the former case however, a deep and persistent mesocyclone forms as vertical vorticity gets stretched and advected vertically by the upward motion. A more detailed explanation can be found in subsection 3.3.3.5. The higher the horizontal vorticity content in the inflow layer, the stronger the rotation not only at mid-levels but also at lower levels. For a given horizontal gradient of vertical velocity, the height at which significant vertical vorticity is acquired decreases as the horizontal vorticity increases (Markowski and Richardson 2009). Boundaries serve as source for horizontal vorticity, and their value can exceed the one of the environmental vorticity production significantly (Markowski et al. 1998). So it does not surprise at all that supercells can suddenly gain organization and strength, when moving along a boundary (e.g. convergence zone or front).

The strong updraft transports precipitation downstream to the anvil region, so updraft and downdraft remain well separated. After some time, the downdraft downstream of the updraft is established, called the *forward flank downdraft*, *FFD*. Model simulations showed that along the leading edge of the forward flank



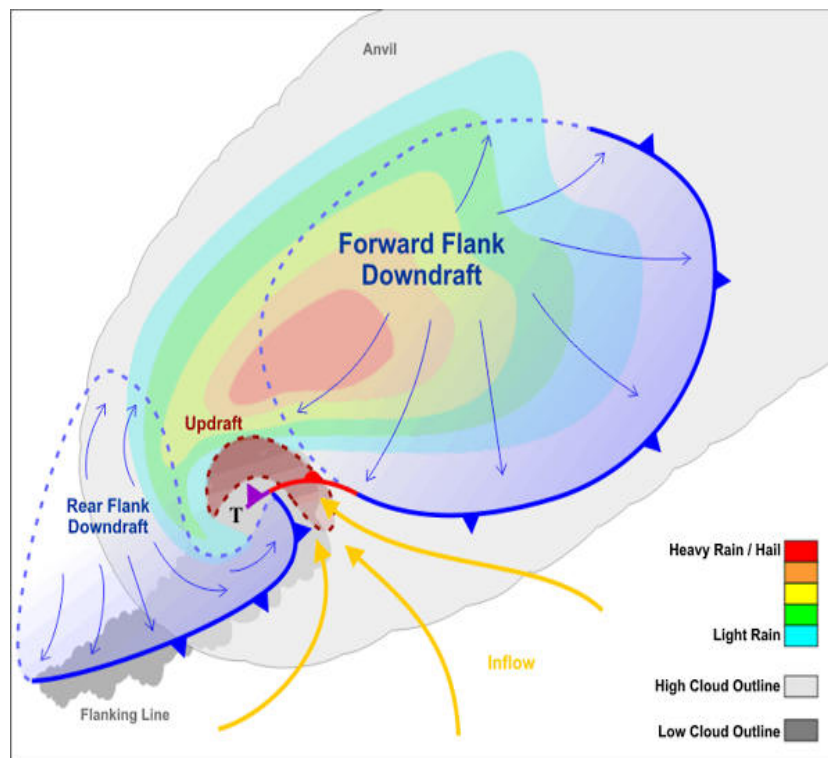


**Figure 3.3:** This sketch is a plan view of a supercell with the rear flank and forward flank downdraft (blue cold front symbols), the mesocyclone/updraft region in red, the flanking line (grey) and broad inflow (yellow arrows). Movement is from left to right. Adapted from <http://weather-warehouse.com>, which in turn was adapted from Lemon and Doswell III. (1979).

downdraft, horizontal vorticity is generated by strengthening horizontal buoyancy gradients, which enter the updraft in a favorable alignment (normal to the storm relative wind in the inflow layer and therefore in a streamwise manner). The downdraft enhances the horizontal vorticity production and hence rotation of the mesocyclone. Upward motion advects this vorticity into the vertical, so strongest vorticity first starts in the mid-levels, mainly at 5-8 km above ground. A planview of a supercell, including the FFD is shown in Fig. 3.3. The main question is, how the low-level mesocyclone develops if vorticity is advected upward into the updraft. The current understanding is that the so called *rear flank downdraft*, (*RFD*) plays a major role by advecting vertical vorticity towards the surface where it can be tilted and then stretched. The RFD was first documented by Van Tassel (1955). The RFD develops along the upshear side of the updraft although the exact level of origin is not yet known or fluctuates from case to case. Lemon et al. (1977) proposed a height of 7-10 km, but this height varied in other studies (4-10 km, e.g. in Brandes (1981) or Klemp and Ray (1981)). The same uncertainties exist for the trigger, where and how an RFD initiates. There are two options, one being the evaporative cooling, hail melting or precipitation loading with another option the vertical pressure gradients, which plays a role due to gradients of vertical vorticity, variations in the horizontal velocity and pressure perturbations due to vertical buoyancy variations (Markowski 2001). The majority of results attributed the initiation of the RFD to the effect of evaporative cooling (Browning and Ludlam (1962), Browning and Donaldson (1963) and Brandes (1981)). The RFD then spreads down to the surface, where different cases of RFDs were noticed: a cold and a warm one as discussed in Markowski and Rasmussen (2003). First results indicate that warm RFDs are more conducive for tornadogenesis as they remain more unstable during the descent which alleviates the tilting beneath the updraft compared to cold and more stable stratified RFDs. Also, LCLs remain lower in the warm RFD cases, which is in line with the observation that tornadogenesis is favored in low LCL environments. However, in studies like Grzych et al. (2006), it was found that not every case with cold and warm RFD configurations supports the aforementioned statement. Averaged over all cases, RFDs associated with non tornadic events were indeed colder than the warmer counterparts. In the field, RFDs can be seen as *clear slots*, which wrap at least partially around the mesocyclone. Despite the 'clear' appearance, large raindrops or even hailstones can be found in this region. Due to the fact that radar reflectivity depends more on the size than on the amount of droplets, this clear slot may not be visible on radar displays. Nevertheless, the presence of a clear slot next to a well structured mesocyclone points to the augmented tornado possibility. When the RFD reaches the surface, a circulation at low levels is formed, which separates the RFD from

the updraft. The descending mesocyclonic rotation starts simultaneously with the descending RFD. The RFD then rapidly occludes and forms the *occluded downdraft*, (Markowski 2001) and tornadoes may form during this stage. The RFD may wrap completely around the updraft which causes temporarily weakening, before a new mesocyclone evolves further downstream along the RFD. Here new tornadogenesis is possible, resulting in cyclic tornadic supercells. Another reason for the cyclic tornado formation could be the result of different horizontal motions between the tornado and the horizontal motion of the main storm-scale updraft and downdraft, discussed in Dowell and Bluestein (2002a) and Dowell and Bluestein (2002b). More detailed information about tornadogenesis can be found in Markowski and Richardson (2009) and Davies-Jones (2004).

Forecasters see several signatures on radars and they use weather parameters, which assist them in the issuance of tornado warnings. In general there are two parameters, which are conducive for tornadic thunderstorm development:

- a high water vapor concentration in the boundary layer
- strong vertical wind shear in the lower levels

Any developing storm has the chance to rotate and potentially produce tornadoes in such an environment. On the radar, the tornado vortex signature indicates strong mid-level rotation, which could finally result in tornado development. Supercells can be detected from persistent hook echoes (Fig. 2.3).

### 3.2.1.3 V-notch, cold-U and the close in warm area

Another signature, which has been analyzed since the late seventies is the *enhanced V-shape or V-notch*, the *cold U-* or *V-shape or the cold-ring shape* and the opposite signatures, the *close in warm area* and the *distant warm area*. All those features have a similar history of development as they all need an intense updraft with an overshooting top<sup>3</sup>, which forms an obstacle for the upper-level flow. The updraft then diverts the flow around it and a warm spot forms along the downshear side (i.e. in the wake) of the overshooting top. There are numerous hypotheses about

---

<sup>3</sup>An overshooting top represents that part of the updraft, which is able to penetrate through the stable stratified tropopause into the lower stratosphere. The longer the overshooting top persists, the higher is the possibility that this thunderstorm could produce severe weather due to a very strong and persistent updrafts. In some cases, gravity wave development was observed and could even influence the initiation of surrounding thunderstorms, e.g. Brunner et al. (2008)

how those warm spots develop, like cirrus anvil clouds, which were blown off the overshooting top with higher emissivity compared to the compact updraft clouds and hence warmer blackbody temperatures (Brunner et al. 2007). Another explanation is subsidence in the lee of the overshooting top, which would lower cloud tops and cause the descending air mass to warm at an adiabatic rate (Heymsfield and Blackmer Jr. 1988). Mixing and entrainment of warmer stratospheric air could also cause the warming trend, as that part of the updraft collapses, which penetrates all the way into the lower stratosphere (Wang 2007). The characteristics of the anvil clouds in enhanced infrared images is an interesting forecast tool as intense updrafts are needed for that kind of brightness temperature anomaly, which quite often produces some kind of severe weather. A more detailed insight into those phenomena can be found e.g. in McCann (1983) or Brunner et al. (2007). Since the three Meteosat Second Generation (MSG) satellites were launched with rapid scanning multi-spectral (15min) and high resolution (up to 1km) imagery, the research of those phenomena in Europe is in rapid progress, with numerous case studies done by the satellite department of the Czech Hydrometeorological Institute, e.g. Setvák et al. (2008) and Setvák and Št'ástka (2008) amongst others.

#### **3.2.1.4 Classic supercell**

This type of supercell was already classified by Byers and Braham Jr. (1949) but is a somewhat spongy phrase as in the real world it is hard to find the 'classic' supercell as the supercell spectrum has a smooth transition. The classic-type supercell is in-between the other categories and therefore exhibits a moderate amount of precipitation efficiency, as strong shear bears most of the precipitation away from the tilted updraft. In general a classic supercell resembles all the typical features, which are expected for a supercell, like hook echo development on radar with strong TVS signatures. Chasers and spotters are up against well defined downdraft regions, wall clouds<sup>4</sup> and clear slots. They indicate a good balance for persistent updraft and downdraft separation and strong updraft rotation and they can produce a swath of large hail and tornadoes in a cyclic fashion. One can summarize them as text-book like supercells.

---

<sup>4</sup>A wall cloud can be found beneath the rain-free portion of a thunderstorm. This type of cloud indicates the area, where the strongest updraft is situated. Rapidly rising air reaches the LCL already at a lower height compared to the surrounding environment, so a wall cloud is well seen. Tornadoes can emerge in that region.

### 3.2.1.5 Low precipitation supercell, (LP)

It is unclear when exactly this kind of supercell was discovered but Davies-Jones et al. (1976), who is mentioned in Beatty et al. (2008) was the first one who described an LP thunderstorm. The main issue with LP supercells is that the very limited precipitation efficiency leads to a low radar reflectivity. In the US they mostly evolve along drylines<sup>5</sup> next to very dry air, so the rapidly rotating updraft is well seen with no precipitation curtains around. Hence the main ingredient for LP storms can be the enforced entrainment of dry air into the updraft which already has a low condensation rate. This can be the main reason for those storms to be insufficient to produce enough precipitation (e.g. for a downdraft). The commonly observed precipitation with LP storms is large to giant hail. The tornado risk is quite low, given the absence of downdraft interaction with the updraft region, but in high helicity and strong storm relative wind environments, spectacular tornado-genesis can occur, well visible and high-based (personal experience). In model simulations, the LP supercells were attained, when the precipitation microphysics were turned off and no interference between downdraft and updraft occurred (Weisman and Bluestein (1985)). Updraft velocities were significant with more than  $35 \text{ m s}^{-1}$ , detected by Bluestein and Woodall Rasmussen and Straka (1997) which inhibits potential precipitation to fall next to updrafts. As mentioned above, radar signature is not suspicious due to the lack of precipitation (e.g. no hook echo, weak velocity signals), so it is important to detect environmental conditions, which could favor LP storms. An attribute of LP storms is the isolated manner of LP storms, which stay discrete during their lifetime.

### 3.2.1.6 High precipitation supercell, (HP)

Nelson and Knight (1987) were the first who described the reflectivity pattern and flow structure of a severe hailstorm, which had a supercell appearance on radar with periodic, intense updraft development during the discrete propagation of the storm. The main issue for HP supercells is an intense rear flank downdraft, which advects potentially colder air from the mid-levels to the surface. During a study

---

<sup>5</sup>Drylines play a major role in the development of severe thunderstorms in the US. They need certain ingredients like an arid region for the development of a dry air mass and a moisture source for a warm and moist air mass and can evolve everywhere in the world, where those ingredients are present. A dryline is a sharp moisture gradient, separating dry and hot air to its postfrontal sector from moist and warm air to its prefrontal sector. The dryline often serves as a trigger for convection, so if environmental shear and instability conditions are supportive for organized thunderstorms, supercells can form. The reader is referred to Schaefer (1974) for more information.

of the Lahoma supercell, Oklahoma, Lemon and Parker (1996) found an extraordinary deep and persistent convergence zone, evolving along the updraft/downdraft interface and they termed this convergent region '*Deep convergence zone, (DCZ)*'. In various case studies, it was found that HP supercells mostly initiate as classic ones and then transform into HP supercells, eventually reaching the stage of a bow echo, as the outflow accelerates. HP supercells commonly develop in a warm and humid air mass, where soundings feature a deep and warm cloud depth, supportive for high precipitation generation (Market et al. 2003). They can produce large hail, destructive straightline winds, sometimes rain wrapped tornadoes and copious amounts of rain. In radar data, they commonly appear as strong hook echoes although it can be hard to detect them on PPIs due to the amount of precipitation, that gets wrapped around the updraft. Nevertheless in storm relative velocity display, intense rotation can be seen.

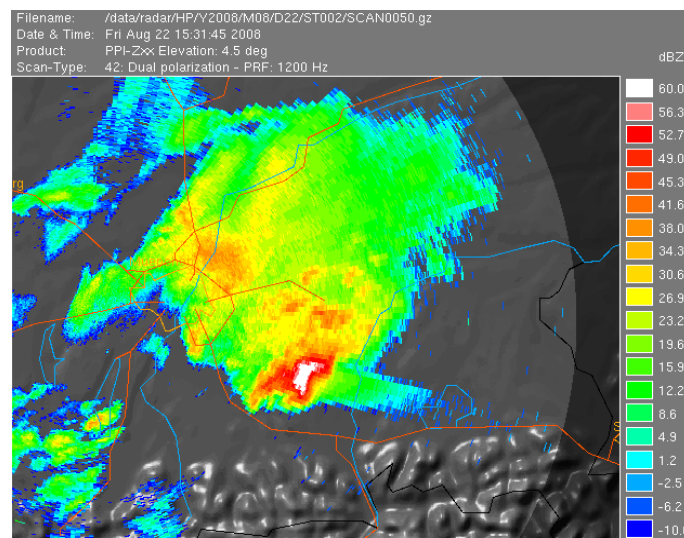
### 3.2.2 Severe hailstorm

Severe hailstorms (in general hail greater 2 cm to 2.5 cm in diameter) are mostly accompanied by supercells, which can produce hail with a size of 5-15 cm in diameter. The main ingredients for large hail are:

- Convective available potential energy, CAPE
- deep layer shear
- lapse rates, which approach the dry adiabatic curve at mid-levels

In the US, the most favorable environment arises when an elevated mixed layer advects eastwards over the moist boundary layer with surface dewpoints of 15-20°C, resulting in extreme instability release of several thousand  $J\ kg^{-1}$  MLCAPE. Low speed and directional shear is already enough for supercells with large hail. However, even in weaker instability environments (e.g. roughly 1000  $J\ kg^{-1}$ ), large hail can be an issue, when speed and/or directional shear values are very strong. To further complicate the forecast scenario, even multicell storms can produce hail, matching the severe criterion as hail cycling in the feeder cells cause a prolonged period of hail growth. The more widespread and serious hail events can be detected when using the ingredient-based forecasting method (Doswell III. and Burgess 1993) with the three parameters mentioned above, but still not every large hail event will be forecast due to the complex nature of thunderstorms. An interesting feature is the so called *three-body-scatter-spike hail spike*, which is seen when a radar beam passes through an hail core. To understand this 'false radar return' one has to follow the path

of the radar beam. First, the radar pulse reaches the hail core, where either wet hail or large hail is present, which scatters the signal in all directions, including downwards. When this downward scattered pulse reaches the surface, the earth, trees and other objects reflect the energy diffusive back to the hail core. Now for a second time, the large and wet hydrometeors scatter the energy with a significant amount now received by the radar. Due to the longer path, the pulses had to travel along, the signal appears to be downwind of the hail core. A good indication for the hail spike is the decrease of reflectivities with distance due to the power loss  $r^3$  ( $r$  is the distance between the radar and the hail core). An example can be seen in Fig. 4.26.



(a) PPI scan at 4.5 °. Reflectivity in dBZ

**Figure 3.4:** An hail spike is clearly visible in southeasterly direction from the radar on a PPI scan, 4.5 ° elevation at 1531 UTC (22 August 2008).

### 3.2.3 The bow echo

Bow shaped convective storms have been well known since the radar was used for meteorological purpose. The term *bow echo* was coined by Fujita (1978), who noted a close connection of damaging surface wind events along the path of those bow echoes. Nolen (1959) mentioned this bowing structure, when he described the *line echo wave pattern, LEWP*<sup>6</sup>. This subject is closely connected to supercell development, but also to mesoscale convective systems (section 3.2.4) and derechoes (subsection 3.2.4.2) as all those mechanisms can play a role for the evolution of

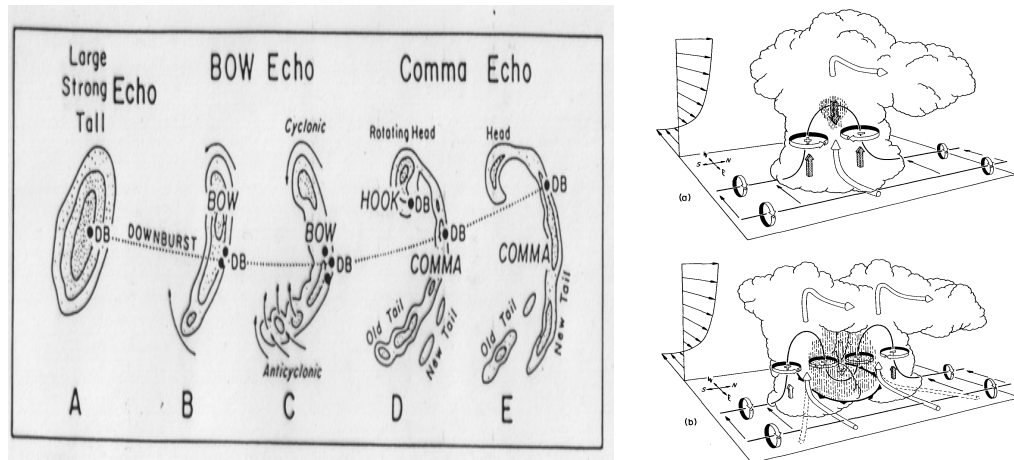
<sup>6</sup>A configuration of radar echoes in which a line of echoes has been subjected to an acceleration along one portion and/or a deceleration along that portion of the line immediately adjacent, with a resulting sinusoidal mesoscale wave pattern in the line (Nolen 1959)

long-lived bow echoes.

In the US, there was no major gain of knowledge of those systems into the eighties. The main problem during that time was the fact that conducted studies, like the *Preliminary Regional Experiment for Stormscale Operational and Research Meteorology, PRE-STORM in 1985* relied on ground-based instrument networks, so the success of those studies depended on the chance that bow echoes crossed the measurement instruments (Cunning 1986). On modeling/numerical basis, a lot of effort was done to understand the dynamics of those storm systems and to prove the observations, which were achieved by then, e.g. (Weisman 1993). Both, modeling and field campaigns like the *Bow Echo and MCV Experiment, BAMEX* but also various case studies like Lee et al. (1992a) and Lee et al. (1992b) made the complex, convective phenomenon more transparent. However in 2003, BAMEX relied on the use of mobile observing systems, including airplanes with the interception of at least 9 bow echoes and the surveillance of up to 40 mesoscale convective vortices, which formed during BAMEX (Davis et al. 2004).

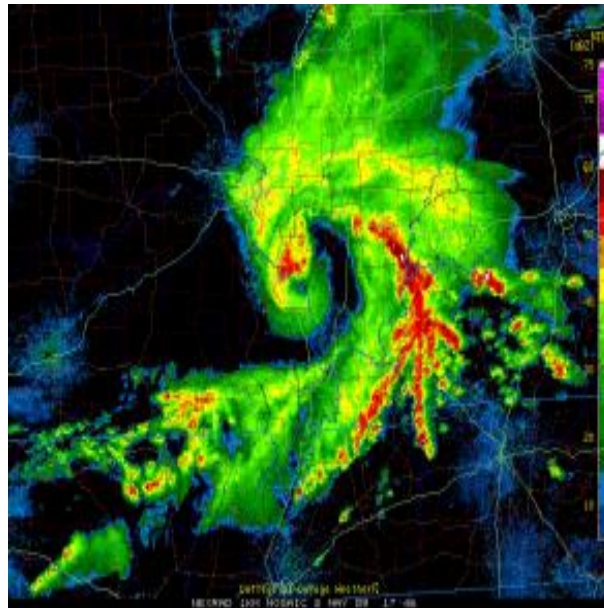
A favorable bow echo environment is a combination of abundant instability release with strong, unidirectional shear in the lowest 2-3 km. In Fig. 3.5 a), the evolution of a bow echo is summarized. The initiation of a long-lived echo starts with the development of a single and persistent cell, which is either more isolated in nature or embedded into an extensive squall line. During that stage, the mechanisms resemble very well the supercell evolution in a crosswise sheared flow (see section 3.3.3.5), where vertical vorticity is generated by the tilting process of the ambient horizontal vorticity beneath the updraft. Due to the unidirectional nature of the shear, vertical velocity and vorticity do not superpose with the result of cyclonic and anticyclonic vortices along the flanks of the updraft, highlighted in (3.5 b). Cell splitting can occur when the downdraft strengthens and stretches vertical vorticity by downdraft acceleration, which was produced by the updraft. Two mirror image supercells can evolve with one being the right mover and the other the left mover. More on cell splitting in unidirectional shear in section (3.3.3.5). Those vortices are called the *bookend vortices* and model simulations suggest that tilting and subsequent stretching of the horizontal vorticity in the ambient vertical background shear is the most prominent contributor the bookend vortices. The vortices remain present as the system then transforms into a quasi-two-dimensional convective line. However, simulations revealed that cell splitting is not the only reason for those vortices to form as bookend vortices also can be found in extensive squall lines at the end of preexisting line segments. It is believed that just the downdraft-updraft configuration is the source of the formation of the vorticity lines (e.g. Weisman (1993)), but more research has to be done on that sector. This





(a) bow echo evolution

(b) Vorticity generation by the wind shear and downdraft process



(c) bookend vortex

**Figure 3.5:** a) Life cycle of a bow echo (Fujita 1978). b) Interaction of strong westerly shear (thin arrows to the left) with a thunderstorm cloud. The direction of the cloud-relative airflow is highlighted by the cylindrical arrows, whereas the heavy solid lines present the vortex lines with the rotation shown by the circular arrows (Weisman 1993). c) An impressive book-end vortex occurred on 8 May 2009 in the central Plains (radar image adapted from NEXLAB (<http://weather.cod.edu/>)).

process was sketched in (Fig. 3.5 b) or (Fig. 3.5c) with a snapshot of an impressive bookend vortex of the deadly central Plains derecho on the 8 May 2009 (Fig. 3.5 c). During the mature stage of a bow echo, the form resembles somewhat a *spearhead*, which is also frequently used in literature (Fujita and Byers 1977). Those vortices play a certain and probably the predominant role for the strength and orientation of the rear inflow jet. One can think of a vortex couplet, where the velocity field in-between those vortices is the net result of the vector sum, so increasing the distance between both vortices results in weaker velocities in between compared to a tight couplet. The rear inflow jet, which is forced by the vortices into the core of the system is the striking feature for bow echoes.

### 3.2.3.1 The rear inflow jet

The development of the rear inflow jet, RIJ, is closely connected to the formation and strength of the cold pool (seen in Fig. 3.6 as the black area beneath the cumulus cloud) and the degree of how buoyant the air mass in the updraft is. In Fig. (3.6) the complete evolution is sketched, starting with Fig. (3.6,a)) with the aforementioned isolated cell which evolves in a vertically sheared environment. In general, the updraft leans downshear due to the horizontal vorticity generation. During the ascent in the updraft, condensation takes place. Dependant on the moisture content of the air mass and the strength of the updraft, enough rain drops can condense, which are too heavy for the updraft and a rain cooled downdraft then forms, which penetrates down towards the surface (3.6,b) and c)). The downdraft describes the region, where downward motion of the cold air mass occurs. The cold air mass spreads out with enhanced vorticity generation along the edges where horizontal buoyancy gradients are the strongest. In case of adequate cold pool strength in respect to the ambient shear (e.g. a balance between both), the updraft tilts more upright with deep convective cells being present along the leading edge. The strong forcing occurs due to the opposite signs of vorticity both the downdraft and the ambient shear exhibit. Later, the cold pool continues to grow in size and strength, eventually overwhelming the magnitude of vorticity of the ambient shear and forces the updraft to gradually tilt upshear, inducing a broad stratiform precipitation region just upstream of the deep convective zone (3.6,c)). This upshear-tilting phase is the hour of birth of the RIJ as horizontal buoyancy gradients along the rear edge of the buoyant plume aloft and the cold pool near the surface induce horizontal vorticity, which enforces the flow from the rear to the front at mid-levels (Weisman 1992). The strength of the jet itself is mainly controlled by CAPE and shear. The CAPE parameter describes how much buoyancy an ascending parcel in an updraft has. That also affects the strength of the front-to-rear flow above the cold pool and

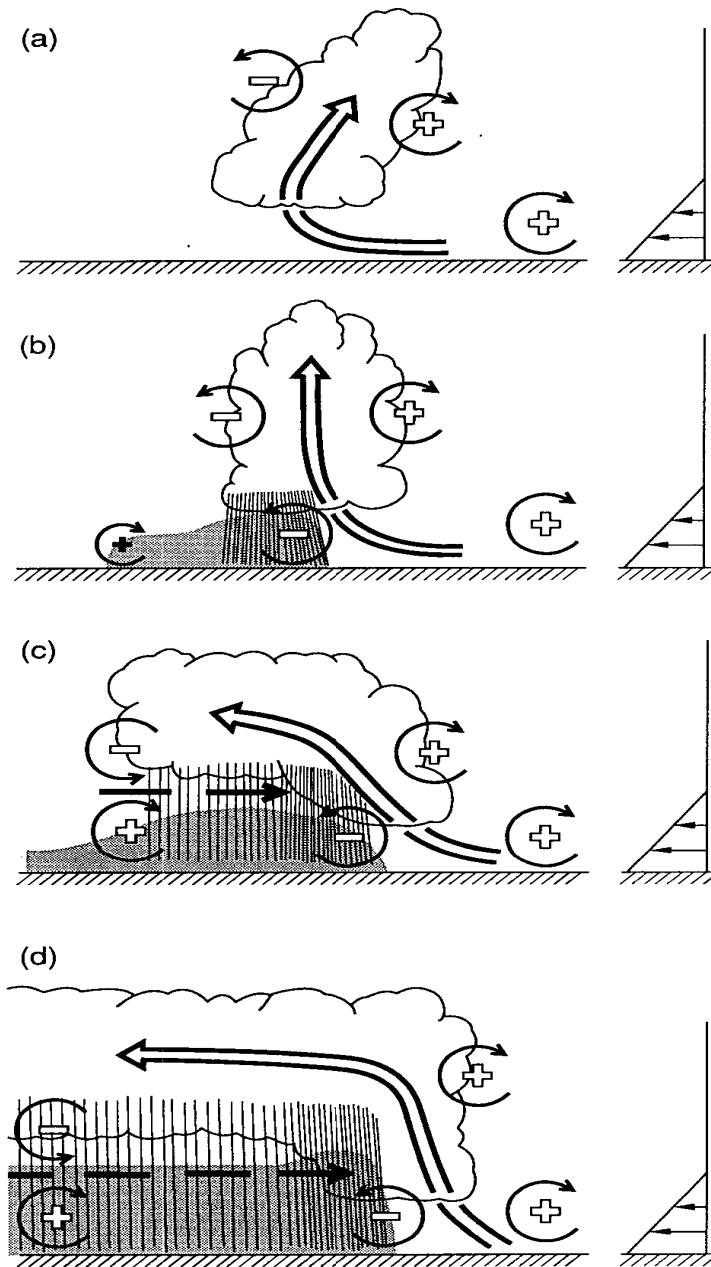


**Figure 3.6:** The chronological evolution of an idealized bow echo. The updraft current is marked by a thick double-lined flow vector with the thick dashed vector features the rear inflow current. The shaded regions represent the developing surface cold pool and the thin, circular arrows depict the most significant source of horizontal vorticity. The thin arrows to the right mark the speed shear. Adapted from Weisman (1993) and Weisman (1992).

the precipitation efficiency, which also determines the strength of the cold pool. A detailed study about how instability influences the RIJ development can be found in Lafore and Moncrieff (1989). However shear, mainly confined to the lowest 2-3 km is another crucial parameter due to the increasing forcing along the gust front, augmenting lift, which increases the net-transport to the rear of the bow. In Fig. 3.6, d) the mature system is shown with the front-to-rear and rear-to-front jet configuration. As an interesting side-note, two different modi of rear inflow jets exist: the *descending jet*, which is present mainly during the decaying stages of an MCS and the *elevated rear inflow jet* is responsible for the regeneration of deep and upright convection along the convergent flow of the outflow. This can cause a weakening system to re-intensify by increasing convective activity. One has to be careful about the general statement that a descending jet is associated with a decaying systems in a weak shear/moderate CAPE environment, as one also speaks of descending RIJs in cases with damaging surface winds, accompanying mature bow echoes. The difference is that in the latter case, which is mostly happening during elevated RIJ events, the jet is able to penetrate down to the surface along the leading edge of the cold pool, where the updraft/downdraft interface is found. The first case with weaker shear just describes the overall weaker cold pool development and hence the higher probability of the RIJ to descend all the way to the surface, still being able to produce strong to severe wind gusts at the surface but not as severe as in the elevated RIJ case.

Another feature in this context is the '*Rear Inflow Notch, (RIN)* or *Weak Echo Channel, (WEC)*', which becomes noticeable in PPI scans, when reflectivity decreases rapidly behind the line. This resembles a 'notch' which thrusts its way through the line from the upstream side. RINs ingest dry mid-troposphere air, which gets advected by the RIJ down to lower levels. Without velocity data, RINs are a distinct feature for imminent or probably already ongoing severe wind events at the surface. When radar velocity data is available, the *Mid Altitude Radial Convergence signature, (MARC)* can be used to forecast the onset of severe wind events in combination with a well structured RIJ, which may be imminent. More about that signature is discussed in (sec.2.3.6.4). During the decaying stage, the bow echo often evolves into a comma-shaped echo with the strongest winds confined to the southern fringe of the cyclonic/north book-end vortex. The reason for that is the Coriolis force, which constantly supports the northern vortex after a few hours so at the end, the whole system is nearly axisymmetric (see Fig. 3.5 a) and Weisman and Davis (1998)). While bow shaped convective systems are observed to occur over a wide range of temporal and spatial scales, the most organized and damaging bow echoes range in size from 20-120 km with a life time of numerous hours.

### 3.2.4 Mesoscale convective systems

The term *Mesoscale convective system*, *MCS* contains a wide variety of mesoscale phenomena. In respect of the definition, a MCS is a weather feature, which exhibits moist convective overturning contiguous with or embedded within a mesoscale circulation that is at least partially driven by the convective processes (Zipser 1982). A cross section and a plan view can be seen in Fig. 3.7. Those systems can appear in all kind of shapes, round or linear, and include many different weather phenomena, including tropical cyclone development or squall lines among others. In the part of the meteorology, which is engaged with the understanding and forecasting of thunderstorms, mesoscale convective systems are mainly referred as thunderstorm clusters and lines. They can live for hours and they can have a dimension of hundreds of kilometers. Therefore, the influence of the Coriolis force is important. The sketch of a typical squall line is shown in Fig. 3.8 with the most important currents, which result in the organization of the convective system and the longevity of up to 20 h in the most extreme cases. In Fig. 3.9, the different stages of an MCS are sketched and the reader is asked to use (sec.3.2.3) for a more detailed explanation about the development of the circulation. They occur worldwide and for many regions like the Great Plains in the US, they produce most of the warm season's precipitation. Different kinds of mesoscale convective systems are well known and studied.

- **Squall line:** A squall line is any line of convection, not necessarily electrified. The broad field of mesoscale convective systems is divided into many different subcategories. The main purpose is to provide a more comprehensive satellite and radar survey of MCSs in terms of number and type of systems and geographical area. The main focus was turned to the development stages to better characterize common patterns by which convection becomes organized and matures into a large and potentially damaging mesoscale convective system. A summary can be found in Jirak et al. (2003). Another approach was to focus on the position of the area with the stratiform precipitation, which can be trailing, leading or parallel to the convective line (Parker and Johnson 2000). One major feature, which is crucial for the persistent influx of warm and moist air is the *low-level jet*, *LLJ*, which is a wind speed maximum at lowest 1-2 km. A good concurrence between the LLJ and the convective system also raises the probability for intense rain amounts <sup>7</sup>, which will not be discussed in this thesis. An MCS configuration, which is closely connected to mature bow echoes is the *quasi-linear convective system*, *QLCS*, which is composed

---

<sup>7</sup>[http://www.hpc.ncep.noaa.gov/research/mcs\\_web\\_test\\_test.htm](http://www.hpc.ncep.noaa.gov/research/mcs_web_test_test.htm)

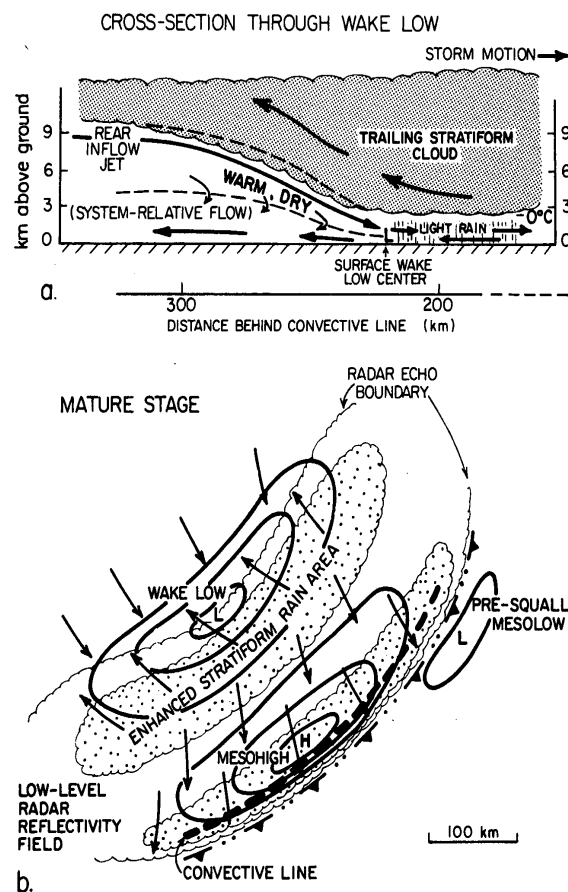


**Figure 3.7:** The conceptual cross section through a mesoscale convective system (vertical outline in a) and a plan view in b)). The arrows indicate the flow through the MCS. Adapted from Johnson and Hamilton (1988).

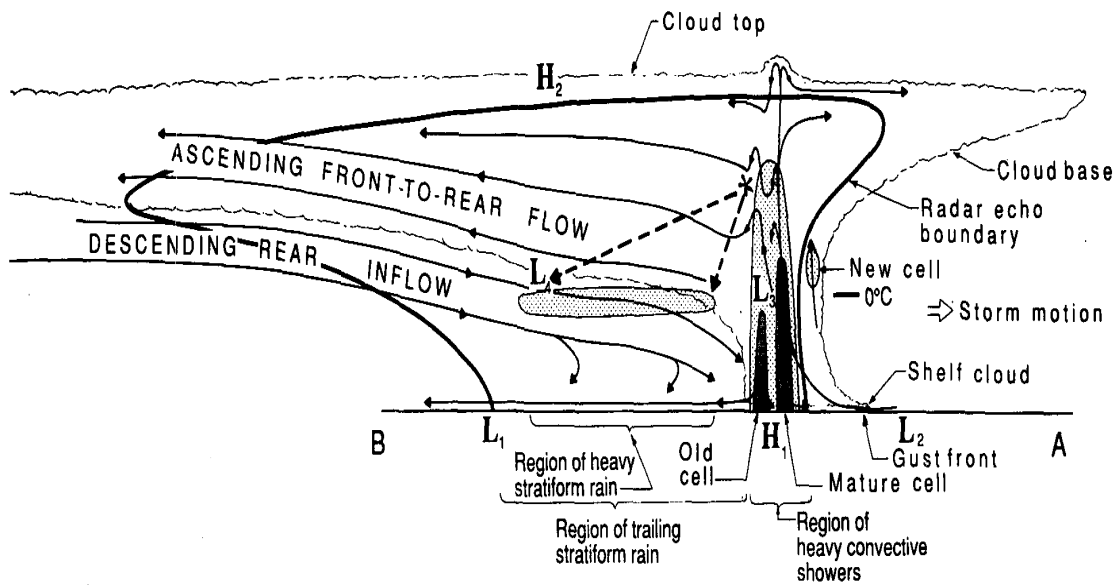
of one or more mesovortices, which locally enhanced the severe wind gust risk along a bow echo (Atkins et al. 2005). Those mesovortices can be seen in radar data and often reveal a MARC structure. The *line echo wave pattern, LEWP* (Nolen 1959) takes on an 'S-shape' with a pseudo warm and cold front. While the pseudo cold front often shelters a rapidly forward penetrating rear inflow jet with damaging winds, an augmented tornado risk exists next to the pseudo low (conjunction of pseudo warm and cold front).

#### 3.2.4.1 The wake depression

Another hint of an imminent or already ongoing severe wind event in conjunction with strong mesoscale convective systems or even bow echoes is a distinct surface pressure anomaly along and behind such a convective line. In general, three different small-scale features were analyzed in the past. The *pre-squall mesolow* is caused by convectively induced subsidence warming in the mid-to-upper troposphere just ahead of the squall line. Followed by the passage of the strongly forced convective line, a *mesohigh* draws near just to the rear of the heaviest precipitation, where the cold pool depth is the strongest. Finally, the wake low<sup>8</sup> placed behind the region with stratiform rain is the final pressure anomaly although it is not yet sure what exactly causes that low. The most prominent hypotheses include *wake low* development by gravity waves or by subsidence warming. The latter one is proposed to start during the stage, when the rear inflow jet evolves with descending motion at the rear edge of the stratiform rainshield. Model results like Gallus Jr. (1996) indicate that rapidly diminishing precipitation rates result in less microphysical cooling, so adiabatic warming prevails, causing the descending air mass to warm with falling pressure at the surface. Those pressure oscillations can become significant with tight pressure gradients, which indicate the augmented chance for damaging surface wind gusts. A pressure drop of 10.8 hPa in one hour was noted e.g. in northeast Louisiana and southeast Arkansas, USA on 18 April 2009. These wake lows also develop during the decaying stage of a mesoscale convective system as precipitation rates start to weaken, so next to a decrease in organization of the mesoscale convective feature, intense wind gusts can still occur in combination with the passage of the wake low

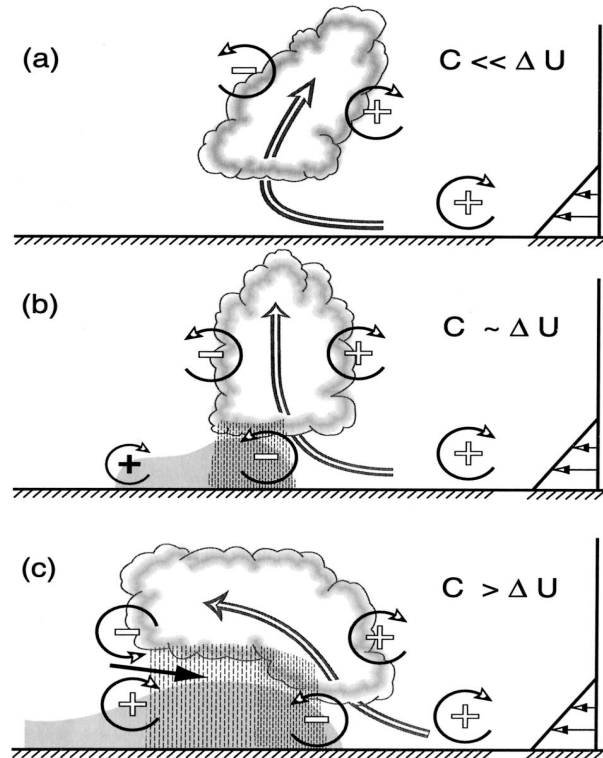
---

<sup>8</sup>In the literature, various names were used for wake low (wake depression, wake mesolow) and mesohigh (pressure dome and bubble high)



(a) Structure of a mesoscale convective system

**Figure 3.8:** Conceptual model of a squall line with the leading convective and the trailing stratiform part. The view is normal to the movement of the squall line, which moves from left to right (Houze Jr. et al. 1989).



(a) Evolution of a mesoscale convective system

**Figure 3.9:** The evolution of a mesoscale convective system during the initiation a), mature b) and decaying c) stage. The black area beneath the cloud is the cold pool, the positive and negative signs are the horizontal vorticity, the arrows to the right represent the speed shear and the remaining arrows indicating the flow through the thunderstorm. (Weisman (1993)).



### 3.2.4.2 The derecho

A derecho is a widespread and long-lived windstorm that is associated with a band of rapidly moving showers or thunderstorms. This term was coined by Dr. Gustavus Hinrichs, a physic professor at the University of Iowa in 1888<sup>9</sup>. Those line of storms have to produce sustained winds of  $25 \text{ m s}^{-1}$  during the passage of the thunderstorms and they need an expansion of at least 400 km. The reports of severe wind gusts have to occur chronologically either within a single or numerous series of swaths. In addition, within the broad-scale damaging wind swath, there have to be at least three reports with wind gusts of  $33 \text{ m s}^{-1}$  or more, separated by 64 km or more and with no more than 3 h interception between those reports. There are several types of derechos (Fig. 3.10) which occur in different environments:

- **Serial derecho:** This type of derecho is in general associated with an extensive squall line and a deep and migrating low pressure region. Various bow echoes can be embedded in that squall line, resulting in concentrated swaths of damaging straight-line winds.
- **Progressive derecho:** This kinds of squall line is restricted in length and it can just involve a single bow echo. Progressive derechos often travel along stationary boundaries and occur without any significant synoptic-scale forcing like low pressure regions. In the US, progressive derechos are often seen during the summer season, when extreme instability has established within a moderate shear environment. Those events are still very hard to predict due to the inability of operational forecast models to resolve them.
- **Hybrid derecho:** This is a mixture of both types of derechos, which develop in the vicinity of a deep low pressure area but with a restricted length.

The main risk of derechos is the severe/damaging wind gust threat, which can affect a broad swath.

Derechoes can occur all over the world, with Gatzen (2003) showing a deadly example from 2002 in northeast Germany.

---

<sup>9</sup><http://www.spc.noaa.gov/misc/AbtDerechos/earlyderechopaper.htm>

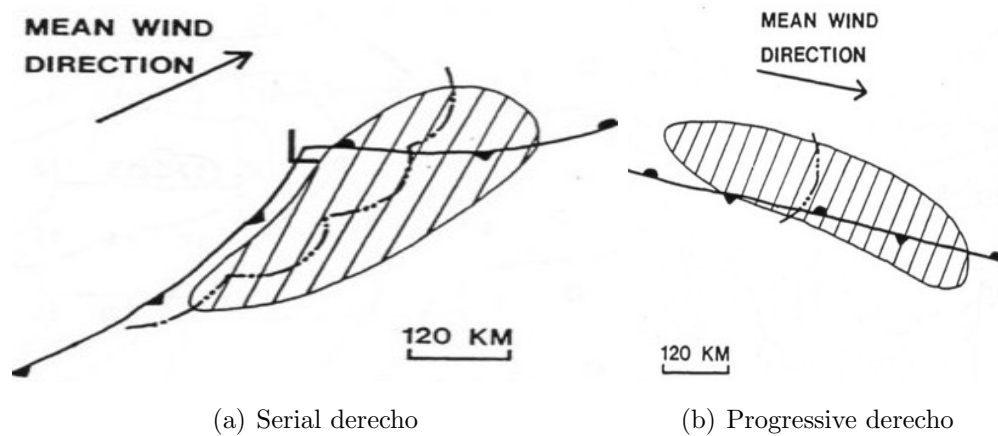


**Figure 3.10:** The appearance of a serial derecho, a) and a progressive one in b). Adapted from (Johns and Hirt (1987)).

#### 3.2.4.3 Mesoscale convective complex, MCC

Despite the connection to the mesoscale convective systems, an MCC has its own characteristics and evolves under different synoptic conditions. In 1976 Maddox (1980) investigated IR satellite images from the US carefully and recognized this specific convective system. The following criterium was established to be able to distinguish between an MCC and an MCS:

**Size:** A cloud shield with continuously low IR temperature  $\leq -32\text{ }^{\circ}\text{C}$  must have an area  $\geq 100,000\text{ km}^2$

B-Interior cold cloud region with temperature  $\leq -52\text{ }^{\circ}\text{C}$  must have an area  $\geq 50,000\text{ km}^2$

**Initiation:** Size definitions A and B are first satisfied

**Duration:** Size definitions A and B must be met for a period of  $\geq 6$  h

**Maximum extent:** Contiguous cold cloud shield (IR temperature  $\leq -32\text{ }^{\circ}\text{C}$ ) reaches a maximum size

**Shape:** Eccentricity (minor axis/major axis)  $\geq 0.7$  at time of maximum extent

**Termination:** Size definitions A and B no longer satisfied

MCCs are of special interest as they can seriously impact the accuracy of operational model forecasts and they are accompanied by flash flood producing rains and all kind of severe weather hazard. In the US however, MCCs also produce most of the warm season rainfall and hence it is not astonishing that the atmosphere has to be moist and potentially unstable at least throughout the lowest 3km for the development of an MCC. Another ingredient is a strong and persistent low-level jet in the lowest 1-2 km, which persistently advects the warm and humid air mass towards the MCC. During the growing stage of an MCC, the center of greatest instability shifts towards the southern part of the MCC (at least in the Northern Hemisphere) due to the persistent influx of the unstable air mass as a result of the LLJ. It was shown that a mature MCC has a strong link between mid-level convergence and upper divergence. At upper levels, a region of strong anticyclonic outflow evolves and remains present during the rest of its lifetime. In this period, intense rainfall with flash flooding depicts a serious threat. The system finally reaches its maturity with an extensive anvil, playing a significant role for longwave radiation cooling but also precipitation initiation (e.g. seeder-feeder effect<sup>10</sup>) and in that stage, an MCC often reveals its maximum extent with a large area of stratiform rain. The anticyclonic outflow at upper levels (roughly 200 hPa) strengthens and is well seen on satellite data, mainly along its northern and eastern fringes. An MCC has a lifetime of many hours. The decaying stage starts, when the supply of moisture weakens or gets cut off (e.g. when the boundary layer stabilizes and the inflow gets elevated betimes) or the low-level convergence at the surface decreases. During that time, the stratiform area of the MCC even increases although the convective part is on a constant decline. The strong anticyclonic outflow remains established until the system has practically disintegrated. To forecast the path of those MCCs is quite complex due to the dependence of various parameters, like the strength and position of the low-level jet, the orientation of the mean wind flow but also internal processes like the development of a cold pool. Corfidi et al. (1996) came up with a method, which provides for the two important components of a propagating mesoscale convective system: *advection and propagation*. For the forecaster it is important to assess the motion of the thunderstorm complex due to its high efficiency to produce intense rainfall. As a short side-note; MCCs are a very important mechanism for the genesis of tropical cyclones, mentioned e.g. in Cheung (2004). Emanuel (1993)

---

<sup>10</sup>This effect occurs when ice crystals from mid- or high-level clouds fall down to the surface and enter another cloud shield below. Those ice crystals support precipitation efficiency of the lower clouds and could cause an increase in precipitation at the surface.

and Zehr (1992) proposed the following initiation of the vortex of a tropical cyclone. An MCC often produces a stable, warm core vortex with a horizontal scale of up to 200km in diameter. They are strongest at mid-levels with no appreciable signature at the surface.

#### 3.2.4.4 Mesoscale convective vortex, (MCV)

During the study of radar and satellite data, features like spiral rainbands and a well established cyclonic and anticyclonic flow perturbations in different heights indicate the presence of a cyclonic circulation in an MCC, an inertially stable warm core vortex, generated by mesoscale convection. This vortex is called *mesoscale convective vortex*. Despite a diameter of more than 200 km an MCV can reach, it is hard to detect on synoptic charts (too small) but also with Doppler radar (too large). It is still no yet understood under which circumstances those vortices evolve. MCVs can live for days (e.g. during the BAMEX field campaign an MCV survived for nearly 4 days) and serve as foci for new thunderstorm initiation. The reader is referred to Davis and Galarneau Jr. (2009) for more information. A transformation from a mature MCC into a MCV can be seen in Fig. 3.11, where the cold cirrus canopy decays after the nocturnal convection peak and a well structured vortex appears. It is worth noting that this MCV was tracked into the Atlantic Ocean three days later.

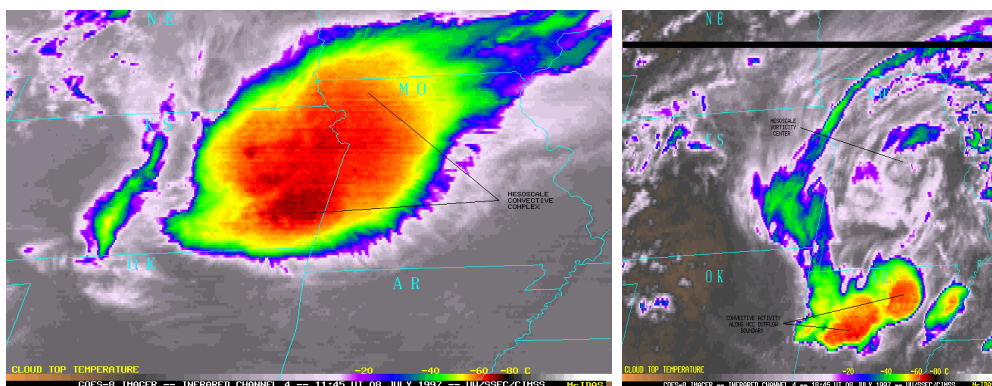


**Figure 3.11:** The evolution of a mesoscale convective complex (MCC) into a mesoscale convective vortex (MCV) on 07 July 1997 over Nebraska. Adapted from CIMSS.

### 3.3 Severe thunderstorm parameters and their (dis)advantages

Forecasters on duty have many different tasks to fulfill. These include writing and issuing forecast discussions, analyzing new model and surface data, talking to emergency services before and during dangerous weather situations and issuing warnings in the nowcast; correct ones at best. It is no surprise that time is precious for forecasters during severe weather situations like flooding, severe thunderstorms or hurricane-force winds during the passage of an intense extratropical storm. In the following, we will concentrate on the forecast of organized convection as many different parameters were established for that. Most of them have their origin in the United States, where severe thunderstorm research was practiced already in the past. However during several talks at different places (including TV stations but also National Weather Services) the author of this thesis had the impression that those parameters were too heavily weighted during the preparation of the daily forecasts. In fact, some of them based their severe thunderstorm forecast solely on those parameters, e.g. in case the significant tornado parameter had a maximum over parts of the forecast area, that there had to be a tornado for sure. The main part of a forecasting process, the diagnosis of the current atmospheric state by analyzing various weather processes and the integration of their understanding of these processes into a coherent picture of the weather vanishes gradually. Doswell III. (1986) provides a summary of the problem.

Severe thunderstorm forecast indices are made up of different parameters, like speed wind shear, directional wind shear, instability, moisture at various levels, lapse rates and temperatures amongst others. They can be listed in the following categories:

- basic surface
- thermodynamic fields
- kinematic fields
- composite indices

Severe thunderstorm forecast parameters have their use, but as is the case with all parameters in synoptic meteorology, one has to:

- understand the parameters, what they describe and which weaknesses and strengths they have

- combine those parameters with the current knowledge of the synoptic and mesoscale weather pattern.

Another reason why severe thunderstorm parameters ought to be used carefully is the difference how forecasters prepare their forecasts and how the algorithms of a weather model were constructed. Whereas forecasters use their knowledge of atmospheric processes to develop a feedback between the ongoing diagnosis and forecast steps, numerical models just develop a trend by their methodology of variable input and output, so the major distinction between numerical models and the forecasters is the lack of feedback with the former (Doswell III. 1986). Parameters are the result of those numerical model calculations and therefore feature the same weakness. In addition, some severe thunderstorm parameters are composed of various others, so the strength and weakness of each is combined in one parameter. This hampers the forecaster to get an overview about the utility of that final composite parameter.

Another potential weakness of a pure parameter-based forecast preparation, which was noticed during the thesis, is the limited potential instability buildup in Europe compared to the US. In the worst-case scenario (e.g. winter-like slim instability but strong shear), many parameters failed to indicate the existing potential for organized convection (see Hautmont case in the chapter 4). This has to be proven in later elaborations when mapping a more extensive data set. However, this problem has also become evident during the preparations of the outlooks for the European Storm Forecast Experiment, as organized thunderstorm events occurred with just weak or non-existing signals in the forecasting parameter fields.

Those severe thunderstorm parameters will be evaluated in the following sections, which were used in the case studies. In addition to the short description, some (dis)advantages of those parameters will be discussed.

### **3.3.1 Basic surface**

”Basic surface” is a coarse item for numerous measured data, which are used during the preparation of a thunderstorm forecast. Strictly speaking, those values are neither parameters nor diagnostic variables but just basic observed variables. The following are the most frequently used ones, including:

- surface pressure
- temperature and dewpoint measurements
- wind speed, gusts and wind direction

The World Meteorological Organization (WMO) specifies how those variables are measured correctly <sup>11</sup>. Dependent on the region, the measurements are carried out in different time intervals ranging from 5 min to 60 min in Europe. Those variables are irreplaceable during the nowcast, when thunderstorm initiation is imminent or already ongoing. Model outputs are available every 1 to 6 hours and sounding data just at 00 UTC and 12 UTC with a few stations also reporting at 03 UTC, 06 UTC and 18 UTC, so surface data can be used for a better overview, how the models handle the situation. Soundings can be modified, which is essential for example for the forecast how fast the cap erodes or if surface based convection is possible.<sup>12</sup> It is also possible to detect features on the mesoscale, like weak convergence zones, which can trigger new thunderstorms but are not resolved in mesoscale and global models, so for nowcast purpose, those basic observed variables are useful.

### 3.3.2 Thermodynamic fields

The reason for the development and growth of a small cumulus humilis but also the explosive development of large cumulonimbi has the same driving force: *buoyancy*. There are several types of instability in the earth's atmosphere, that influence the weather in some way. There is baroclinic instability, responsible for the development of large extratropical cyclones, but also barotropic instability, playing a major role in the tropics (e.g. for the intensification of tropical cyclones). In the context of severe thunderstorm forecasting, we are mainly interested in the instabilities, that can be explained with the *Parcel theory*<sup>13</sup>. For that the main question is how variables like T, p and V (volume) change when being displaced vertically. A short theoretical review will explain that. One starts with the *First Law of Thermodynamics*, which states:

$$du = dq + dw \quad (3.2)$$

---

<sup>11</sup>[http://www.wmo.int/pages/prog/www/IMOP/publications/CIMOGuide/CIMO\\_Guide-7th\\_Edition2008.html](http://www.wmo.int/pages/prog/www/IMOP/publications/CIMOGuide/CIMO_Guide-7th_Edition2008.html)

<sup>12</sup>Thunderstorms can appear either elevated in nature or surface based although it is hard to make a sharp disjunction between both. Moore et al. (1998), Colman (1990) and Horgan et al. (2006) published definitions for elevated thunderstorms: The term *elevated convection* is used to describe convection where the constituent air parcels originate from a layer above the planetary boundary layer (Corfidi et al. 2008). Elevated supercells are notorious hail producers whereas the tornado risk increases, when thunderstorms become surface based. It is not uncommon for long lived storms to undergo both stages, e.g. starting as surface based thunderstorms south of a warm front and then cross the front with an increasingly more stable boundary layer and therefore transform into an elevated thunderstorm.

<sup>13</sup>[http://www.mpch-mainz.mpg.de/~lawrence/vorlesung\\_WS2004-5/thermo.pdf](http://www.mpch-mainz.mpg.de/~lawrence/vorlesung_WS2004-5/thermo.pdf)

expressed in terms of the specific energy per unit parcel mass  $M$ .

$du$  is the change in internal energy,  $dq$  the heating of a parcel and  $dw$  the work done on a parcel. Internal energy is composed of kinetic energy and potential energy. The thermal velocity of molecules is determined by

$$kt = \frac{2}{3} < \frac{1}{2} M_m v^2 > \quad (3.3)$$

where  $k$  is the Boltzmann constant ( $k = 1.38 \times 10^{-23} \text{ JK}^{-1} \text{ molecule}^{-1}$ ),  $M_m$  the weight of a single molecule in the gas and  $v$  the velocity in  $\text{ms}^{-1}$ . The translational kinetic energy is a part of the internal energy, so the change in internal energy can be expressed as:

$$du = cdT$$

where  $c = \text{const.}$  Therefore, the change in internal energy is a function of change in temperature. Heating is either due to molecular collision or absorption of radiation. Work also results in changes in a parcel's kinetic energy and can be expressed by:

$$dw = P d\alpha$$

where  $P$  is the pressure and  $\alpha$  the inverse of the density

$$\left( \alpha = \frac{1}{\rho} \right) \quad (3.4)$$

or the specific volume. Using equation 3.2 one obtains:

$$cdT = dq - Pd\alpha \quad (3.5)$$

with the sign convention indicating that heating and working are done by the atmosphere. From this formula, one gets the relation that compressing a parcel ( $dV < 0$ ) adiabatically ( $dq = 0$ ), the temperature should increase and so does the internal energy. That is exactly what is used in the parcel theory. A parcel, ascending through the atmosphere, expands and therefore increases its volume whereas the temperature starts to decrease. A sketch can be seen in Fig. 3.12 where an ascending parcel is traced.

### 3.3.2.1 Convective available potential energy

The parcel theory describes the vertical displacement and the changes of state of a well-defined parcel of air in the atmosphere. To achieve a lifted parcel, one needs either buoyant or mechanical forces, which act on the parcel. so it is able to cool off as the pressure decreases, which in fact forces the parcel to expand. Further cooling eventually means condensation and droplet formation, which in turn causes the



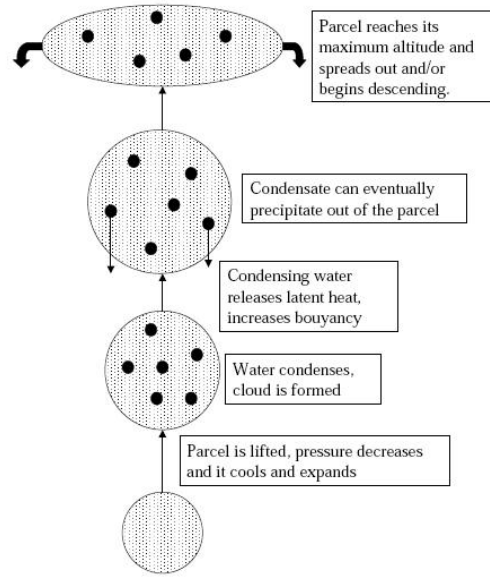


**Figure 3.12:** Conceptual sketch of how the parcel theory works. Adapted from <http://www.mpch-mainz.mpg.de/~lawrence/>

release of latent heat and a warming trend of the parcel. When this parcel becomes neutral or negative buoyant or the parcel adjoins the stable tropopause it starts to descent back towards the earth. The most prominent example for the parcel theory is the calculation of the *convective available potential energy*, (*CAPE*) which represents the vertically integrated positive buoyancy of a parcel. The term buoyancy phrases the net acceleration of a parcel of different densities from the surrounding air in a gravitational field, so the upward velocity in an updraft can also be evaluated.

$$CAPE = g \cdot \int_{z_{LFC}}^{z_{EL}} \left( \frac{T_{v_p} - T_{v_e}}{T_{v_e}} \right) \cdot dz \quad (3.6)$$

$$w_{max} = \sqrt{2 \cdot CAPE} \quad (3.7)$$

One has to keep in mind that CAPE is not a measure of instability but rather an integrated measure of the parcel buoyant energy with the units  $J \, kg^{-1}$  (Blanchard 1998) and (Moncrieff and Miller 1976).

In Eq. 3.6, LFC means the level of free convection, EL the equilibrium level,  $T_v$  the virtual corrected temperature and  $g$  is the strength of the gravitational field, which is  $9.8 \, m^2 \, s^{-2}$ , varying with latitude. All those parameters are an important tool for forecasters to evaluate the possibility for thunderstorm initiation or if atmospheric conditions become better or worse for deep convection. It is also possible to verify if global or mesoscale models are on track with the current synoptic situation. For

this purpose, thermodynamic diagrams are used, which have a somewhat different presentation but all diagrams contain the same set of lines. The colors of those lines only apply to soundings of the 'University of Wyoming':

- isobars (lines connecting points with equal pressure (horizontal, blue lines))
- isotherms (connecting points with equal temperature (blue lines with a slantwise ascent to the upper right))
- dry adiabats (represent a line with constant potential temperature (green curves))
- moist adiabats and pseudo-adiabats (containing latent heat release; blue lines with a slantwise ascent to the upper left)
- mixing ratios (lines representing the dewpoint of a rising parcel; purple lines with a slantwise ascent to the upper right)

Those diagrams are in use since the early 19<sup>th</sup> century and the calculations, which are carried out are based on the well known relationships between temperature, pressure and humidity and the basic laws of thermodynamics. The most common diagrams are the *Emagram*, the *Tephigram*, the *Skew-T/Log-P diagram*, and the *Stüve diagram*, which all differ mainly in the orientation of the lines. It has to be stressed that the Stüve diagram is not a thermodynamic diagram since it does not display the energy-area equivalence correctly. More detailed information about those diagrams can be found in all theoretical meteorology books. I want to focus on the Skew-T diagram, which will be used in this thesis, as instability release is easy to detect on that one. The Skew-T diagram is a modification of the Emagram, which was proposed by N. Herlofson in 1947. The main reason for that was the ambition to get a large angle between the isotherms and the dry adiabats, which provides an easier way to assess the degree of instability, that is available. An example of a Skew-T diagram is shown in Fig. 3.13.

The lifted condensation level (LCL) is the level, where saturation takes place when the parcel is cooled by dry adiabatic lifting. On the diagram, one has to start at the surface temperature, following the dry adiabatic lapse rate line while following the saturation mixing line upward for the surface dewpoint. When both lines intersect, condensation starts to take place. That is where the LCL can be found. There are several publications like Bolton (1980) and Inman (1968), describing a numerical approach for the LCL calculation. A few of them were tested in this thesis for the CAPE calculation, with similar results. It is important to

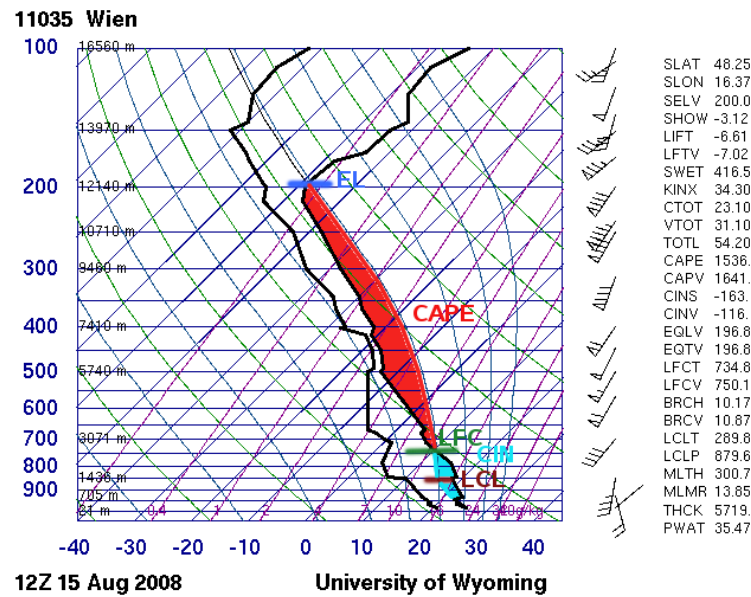


**Figure 3.13:** A skew-T plot with CAPE/CIN and the most used abbreviations (source of the sounding: WYOMING).

know that there are different approaches to calculate the LCL for different CAPE. One can work with the surface temperature and dewpoint and therefore calculate the so-called **surface based CAPE, SBCAPE**. Another way is to mix the lowest levels, whereas the magnitude of that level in general varies between the lowest 50-100 mb. This CAPE is called **mixed or mean layer CAPE, MLCAPE** and results in more realistic values than the SBCAPE when comparing those values with real-time measurements. In reality, the inflow layer into a thunderstorm is buoyant and sheared, so it is unlikely that the measured temperature and dewpoint from the immediate surface indeed represent the profile for the inflow. It is crucial to choose the right dewpoint as minor variations could have a large impact on the final degree of instability release. Another way to define the degree of instability is the **most unstable CAPE, MUCAPE**. The most unstable parcel found within the lowest 300 hPa of the atmosphere is used for that calculation and is useful in situations, when a more stable boundary layer has established or thunderstorms are elevated in nature, which is sometimes the case during strong warm air advection events mainly along warm fronts. In those situations, both SBCAPE and MLCAPE give unrepresentative values and cannot be used for the forecasts of thunderstorms. Fig.3.14 is an example how serious the difference can be and how carefully a forecaster has to choose the right CAPE.

The LCL, computed on a map, is a great tool to get an overview about the quality of the boundary layer. A moist boundary layer is characterized by low LCLs due to a low temperature-dewpoint (T-Td) depression.

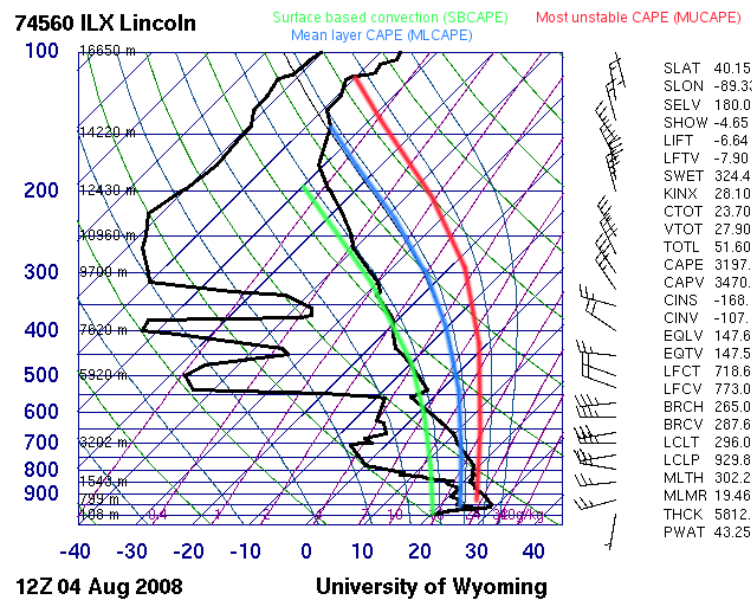


**Figure 3.14:** This sounding samples the potential discrepancies between MUCAPE, SBCAPE and MLCAPE. A derecho event occurred on that day over Chicago (source of the sounding: WYOMING).

Amongst others, Rasmussen and Blanchard (1998) and Davies (2005) published that lower LCLs are conducive for the tornado development, with an LCL median for tornadic thunderstorms of 780 m and roughly 100 m higher for ordinary cells in the US. This reduces low-level evaporative cooling as no deep and dry subcloud layer exists as rain, which enters the dry air mass beneath the updraft causes evaporative cooling and a strengthening downdraft. Hence, limited downdraft production does not interrupt the updraft.

In Europe, Groenemeijer (2005) found a 50 mean layer LCL median height of 600-800 m for tornadic thunderstorms with just slightly different values for ordinary cells<sup>14</sup>. Brooks (2008) found a 90% or higher risk for significant tornadoes in Europe, when the mean layer LCL drops to well below 1000 m in conjunction with 5-10 m s<sup>-1</sup> 0-1 km low level shear. What comes to the fore is the limited use of this parameter when not analyzing the ambient environment as the interquartile ranges of the box-whisper plots of the ordinary and tornadic cells in Groenemeijer (2005) have a strong overlap. High LCLs on the other hand are an indicator of a well mixed subcloud layer with low-level lapse rates, approaching the dry adiabats. Strong downbursts are possible, called *microbursts* (duration up to 15 min and an extent of 400 m to 4000 m), *macrobursts* (duration up to 60 min and an extent of more than 4000 m) or *heatbursts*. The latter one is a not yet well understood

<sup>14</sup><http://www.estofex.org/files/scriptie.pdf>

phenomenon but a careful validation of a few heat burst cases indicated a similar mechanism. Evaporative cooling often initiates the downward moving air mass, which accelerates due to a dry adiabatic subcloud layer, warms adiabatically and eventually overshoots the equilibrium level, where the warmer air would become positive buoyant. Heat bursts are not related to severe organized thunderstorms and therefore no further examination is done. More information about the complete facet of downbursts can be found in Johnson (1983), Fujita (1985b) and 'Microbursts - The Handbook for visual identification'<sup>15</sup>.

Beside the LCL height, the forecaster is also interested in the *level of free convection*, *LFC*. Below that level, a parcel is cooler than the environment with a net downward motion. Any source of low-level lift however, which is able to bring the parcel to the LFC and therefore becomes warmer than the environment is able to continue to rise upward. On a thermodynamic diagram, the LFC is the level, where the parcel from the LCL follows a moist adiabatic ascent and crosses the measured temperature profile. A useful method how to work with both parameters, the LCL and the LFC, is shown on Oscar van der Velde's web page<sup>16</sup>. The difference between both levels is a good indicator about the strength of the cap and therefore the required force to lift a parcel far enough for free rise. A small difference indicates just little forcing and lift is needed and forecasters can expect quite widespread and simultaneous initiation when background forcing is strong enough. On the other hand, a broad layer, confined by LCL and LFC, points to a strong cap, where either no storms can evolve or strong forcing or orographically support is needed. E.g. for discrete supercells the atmosphere still has to be capped to a certain degree so only the most intense updraft can break the cap whereas weaker updrafts cannot penetrate through the warm layer. Hence only a few thunderstorms develop, which can ingest the warm and moist air mass surrounding them. The area with convective inhibition (CIN or more colloquial called 'cap') was highlighted in blue colors in Fig. 3.13.

The *equilibrium level*, *EL* is the level, where the ascending parcel again crosses the ambient temperature profile, which is only possible in the case of some CAPE (Fig. 3.15).

EL displays the expected vertical extent, that thunderstorm clouds can reach. In Europe, EL temperatures of -40°C to -60°C are common during the summer, which is the tropopause level or roughly 10-12 km. Radar data and satellite estimations however sometimes measure heights of well above 15 km in Europe during very severe thunderstorms and overshooting tops can even penetrate further

<sup>15</sup><http://www.cimms.ou.edu/~doswell/microbursts/Handbook.html>

<sup>16</sup>[www.lightningwizard.com](http://www.lightningwizard.com)

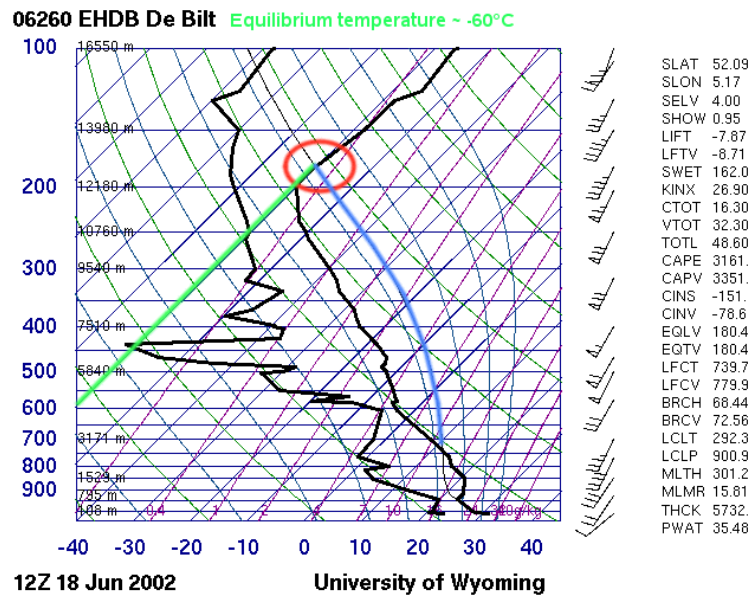


**Figure 3.15:** Calculation of the equilibrium level (source: WYOMING).

into the lower stratosphere. More about overshooting tops and their ability to detect supercells in section 3.2.1.2. For forecast purposes, equilibrium temperatures are of most interest during the winter, when deep convection is questionable but shear is strong enough for storm organization, assumed that thunderstorms manage to evolve. The so called *mini-supercell* is a phenomenon, that was analyzed mainly in the US during the landfall of hurricanes, where ambient lapse rates are close to moist adiabats and therefore limited instability stands by (McCaul Jr. and Weisman 1996). In Europe however, EL temperatures are crucial for low topped supercell detection during the winter time, where cool EL temperatures indicate, if deep and even electrified convection is possible. As mentioned above, the main research was done in the US with the following ambient thermodynamic and kinematic results for mini (shallow) supercells (Knight and Knight 1993)<sup>17</sup>. In Europe, a few case studies have been conducted with the main focus on the environment of shallow supercell activity. Hamid and Delobbe (2007) and Teittinen and Hohti (2007) had similar results compared to those from the US:

- very low EL temperatures (quite often in conjunction with a low tropopause) with heights between 4-7 km (**below 8 km**)
- limited instability release present with average values well below  $1000 \text{ J kg}^{-1}$  (**up to  $1000 \text{ J kg}^{-1}$** )

<sup>17</sup>[http://www.crh.noaa.gov/lmk/soo/docu/mini\\_supercell.php](http://www.crh.noaa.gov/lmk/soo/docu/mini_supercell.php)

- strong vertical wind shear (roughly  $20 \text{ m s}^{-1}$ ) and storm-relative helicity values ( $200\text{-}500 \text{ m}^2\text{s}^{-2}$ ) (**variable values with 0-6km bulk shear between 20-60  $\text{m s}^{-1}$  and SRH3 up to 400  $\text{m}^2\text{s}^{-2}$** )

Those supercells revealed the typical signs in reflectivity and velocity radar data like a BWER or mesocyclones. When forecasting those low topped supercells, it is crucial to review the forecast EL temperatures, if convective updrafts are deep enough for organization.

Another parameter, which is focused on the distribution of the CAPE in the vertical is the so called **normalized CAPE, (NCAPE)**.

$$NCAPE = \frac{g \cdot \int_{Z_{LFC}}^{Z_{EL}} \left( \frac{T_{vp} - T_{ve}}{T_{ve}} \right) \cdot dz}{Z_{EL} - Z_{LFC}} \quad (3.8)$$

It is not only of interest where the CAPE is maximized, but also if the CAPE field is 'tall and thin' or 'short and wide'. Studies like the one of Knight and Knight (1993) led to the assumption that CAPE at lower levels plays a more significant role due to the incorporation of strong low-level shear. McCaul Jr. and Weisman (1996) did some modeling work where they got the result in zero-wind simulations that buoyancy maximized at 2.75 km had upward velocities almost double the value for the case where buoyancy was maximized at 5.82 km. NCAPE therefore scales CAPE by its depth and it expresses the acceleration for the layer between the EL and the LFC. In the United States, values less than 0.1 point to 'tall and skinny' CAPE profiles whereas values closer to 0.4 indicate a 'fat' profile, which either enhances the large hail risk, when being present at mid-levels or the tornado risk, when confined to the lowest 3 km. It has to be added that again one should not exclude the effect of kinematics, as both the 'shorter and fatter' but also the 'taller and more skinny' soundings can highlight an environment conducive to extremely large hail, as was the case in Oregon, Missouri (USA) on the 7 June 2009 (13 cm in diameter) and in NE Hungary (Europe) on the 7 June 2009 (10-12 cm) respectively. In the latter case, deep layer shear reached a magnitude of  $30 \text{ m s}^{-1}$  with some veering present of the vertical wind field.

Another CAPE parameter has its focus on the potential strength of the downdraft, which is called the **downdraft CAPE, (DCAPE)**. It reflects the maximum energy, which is available for a descending parcel and it is enclosed by the descending parcel curve and the environmental temperature profile. The choice of the level, where to start from is crucial and forces the resulting DCAPE to significant variations. It can be used as a rough estimate. Strong downdrafts are possible (especially when the forecaster assesses the possibility for microbursts) but it should not be used alone for wind gust forecasts. Not much attention was paid to this parameter in this

thesis. There are more CAPE parameters, like TCAPE (Ninić et al. 2006), but those were not evaluated in the following case studies.

Showalter (1953) with the *Showalter Index*, Galway (1956) with the *Lifted Index* and Miller (1967)<sup>18</sup> came up with the first indices, which assist forecasters in the decision if thunderstorms are within the realms of possibility but also if storms are capable to gain organization.

The *Showalter index* ( $SI = T_{500} - T_p500$ , where  $T$  is the environmental temperature and  $T_p$  the temperature of the parcel) is calculated as follows: computing the LCL from 850 hPa, then following the moist adiabat up to 500 hPa and differentiate the parcel's temperature from the environmental temperature. Therefore the lower the values, the higher the chance for convection and thunderstorms. This index is often used in mountainous regions, where boundary layer conditions are often decoupled from the free atmosphere (e.g. gap flows, mountain-valley wind etc.). Starting at 850 hPa or even 700 hPa, which is done for example in Switzerland by Huntrieser et al. (1997) solves that problem. It has to be noted that the LCL of the parcel is calculated in a layer where sharp inversions and therefore moisture and temperature gradients are present, which can all affect the SI-index significantly. On some SI-tables, the SI number and the expected risk of thunderstorms is listed but it is not really straightforward to say that a SI of -3 to -6 culminates in severe thunderstorms or that values below -6 point to a tornado risk. Various ingredients like the kinematics are speculated, so next to the knowledge that deep convection is possible with strong updrafts and the assessment of instability release, no further information can be revealed as mentioned on the NWS page<sup>19</sup>. This index is also a useful tool for the forecast of elevated thunderstorm activity e.g. along warm fronts or nocturnal stable boundary conditions, which is discussed in Trier and Parsons (1992).

The *Lifted Index* ( $LI = T_{500} - T_p500$ ) is a similar index where the calculation of the LCL starts at the boundary layer. In this case, the layer below the inversion is included but one has to keep in mind that superadiabatic conditions at the surface could yield unrealistic low LI values as mixing is excluded. Nevertheless, the LI can be used when the forecaster evaluates the chances for deep moist convection. The lower the LI, the stronger the potential instability release and therefore the updraft speed.

The term *lapse rates* is used for the vertical temperature gradient. It can be expressed as:

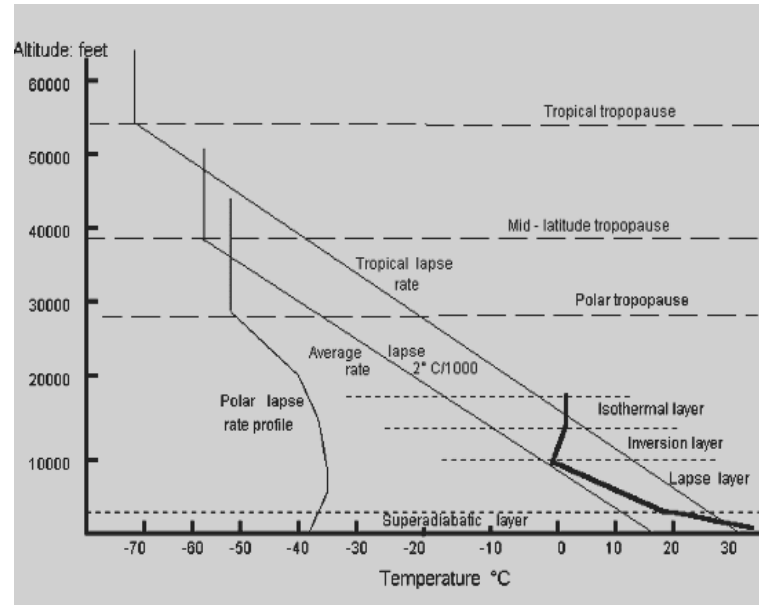
---

<sup>18</sup>It ought to be honored that Major E. J. Fawbush and Captain R. C. Miller from the Tinker Airforce Base Weather Detachment, Oklahoma issued the first tornado warning for the US on the 25 March 1948, which even verified. More on that can be found in Maddox and Crisp (1998).

<sup>19</sup>National Weather Service: <http://www.srh.noaa.gov/elp/wxcalc/showalter.shtml>



$$\Gamma = -\frac{\partial T}{\partial z} \quad (3.9)$$



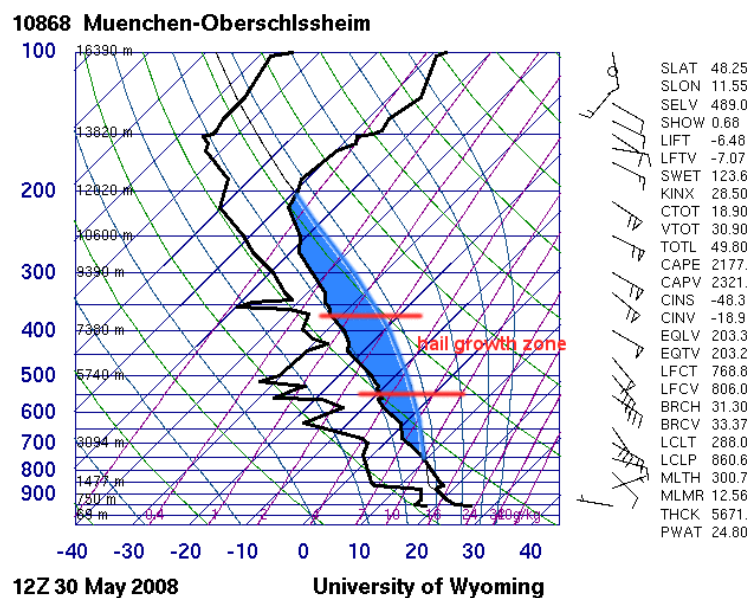
**Figure 3.16:** An overview about the different lapse rates (source of the sounding: <http://www.auf.asn.au/>).

Fig. 3.16 gives a short overview about the most important lapse rates, where super adiabatic lapse rates mainly occur just above the surface. Diabatic heating and different properties of air and the surface in respect of heat conducting cause lapse rates to exceed the dry adiabats. When forecasting thunderstorms, the main attention is restricted to the area between the dry and moist adiabats. For instability release and therefore robust updraft strength, lapse rates, approaching the dry adiabats through most of the layer, are needed. There are two regions of interest, one is the mid-level region (2 - 4 km is often used) in respect of hailstorm forecast and the other one the low-levels, where steeper lapse rates in the lowest hundreds of meters reflect a good chance for some low-level CAPE, if surface moisture assists in that.

Before leaving the summary about CAPE we still have to oppose low-level and mid-level CAPE as both can play a different role when forecasting the type of severe thunderstorms. Next to the quality of the rear flank downdraft, a favorable dispersal of CAPE throughout the lowest 3 km of the troposphere and therefore surface based CAPE, increases the chances for tornado development by vortex stretching. McCaul Jr. and Weisman (1996) first explored the positive effect on tornado genesis with augmented low-level CAPE.

Davies (2005) and especially Markowski and Rasmussen (2002) discovered the importance of the favorable, buoyant low-levels for tornado development with surface based instability being a necessity with Davies (2005) detecting an average 0-3 km 100 mb - MLCAPE of  $100 \text{ J kg}^{-1}$  for weak and strong tornado cases. Except for the stretching effect, another reason for better tornado genesis is the interaction between low-level shear and low-level instability, peaking in an augmented ascent and stretching, which was published in Rotunno and Klemp (1982).

'Fat' CAPE profiles or maximized instability release in the mid-levels are supportive for large hail, if the kinematic environment is favorable, too. Strong upward motions in the hail growth zone keep the hail in the updraft for a long period, so the hailstones can grow. A CAPE distribution like Fig. 3.17 is the result of steep mid-level lapse rates, approaching the dry adiabats.



**Figure 3.17:** A sounding, where large hail is expected (source: <http://weather.uwyo.edu/upperair/sounding.html>).

### 3.3.3 Wind shear

Just releasing instability into the atmosphere is not enough for rotating storms. Another ingredient is the shear, which causes thunderstorms to separate their updrafts and downdrafts over a long period of time, which augments the life time of a thunderstorm. Forecasting severe thunderstorms also requires that the forecaster monitor the shear in different layers closely as this can be crucial for forecasting which thunderstorm mode will dominate. First of all, it ought to be discussed, what kind of shear one has to deal with. Then the discussion shifts to the different layers

in the atmosphere, as shear can affect thunderstorms and its evolution drastically. Wind shear, which can be summarized as the difference in wind speed and direction over a short distance in the atmosphere, is not only useful to look at during the thunderstorm forecast but also when preparing aviation weather forecasts. It is a microscale phenomenon and is observed for various reasons, like in the vicinity of the low level jet, next to inversions (Kelvin-Helmholtz waves) and man-made buildings. Severe thunderstorms, which arise from the presence of strong shear can produce dangerous situations, when e.g. strong downbursts affect the airport. There exists more shear and turbulence phenomena for the aviation<sup>20</sup>, like the clear air turbulence (CAT), but the focus is centered on the shear, where sustained and organized thunderstorms arise from.

It has to be emphasized that in this thesis, shear is expressed as the bulk shear of two different layers ( $m\ s^{-1}$ ). Another option to express shear is  $|\frac{\partial \vec{v}}{\partial z}|$ , which has the units  $s^{-1}$ .

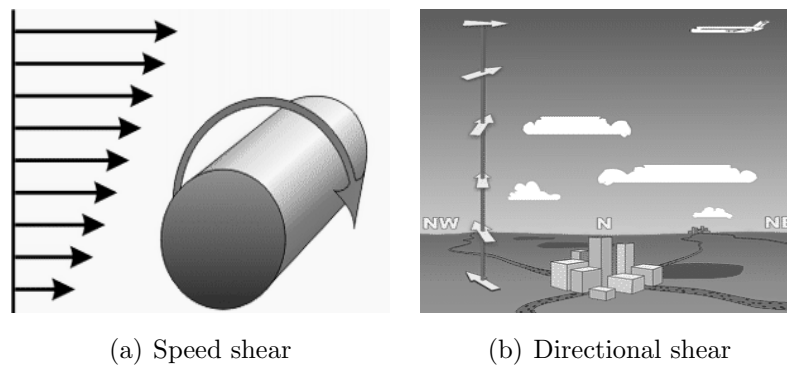


**Figure 3.18:** Overview about the different contingencies of shear. Source: JetStream - Online School for Weather, NOAA (<http://www.noaa.gov/>)

The speed shear is the result of different velocities throughout a layer, increasing its strength with height (Fig. 3.18). In general, the stronger the shear throughout the troposphere, the better the constant separation of updraft and downdraft. This constellation keeps thunderstorms long-lived without the downdraft interfering the updraft and therefore burking the warm and moist inflow. Speed shear is considered in various layers, which all have different effects on the storm's longevity.

### 3.3.3.1 Anvil-layer storm relative wind (9-11km)

The anvil storm relative windshear layer<sup>21</sup> is used to discriminate between the different types of supercells. The reader is referred to section 3.2.1 for more insight about the whole supercell spectrum. In Rasmussen and Straka (1997) it

<sup>20</sup><http://www.weather.gov.hk/aviat/articles/WSturbbookletwebver.PDF>

<sup>21</sup>Storm-relative velocity is the velocity of the background wind field minus the storm motion

was shown that for LP storms, storm relative anvil flow was the strongest with weaker values for the HP type supercell. The strength of that wind field helps to assess if hydrometeors are involved again into the updraft of a supercell or if they spread out downstream of the updraft. Rasmussen and Straka (1997) figured out that the most significant difference in the hodographs is constricted to the upper troposphere at roughly 7 km AGL. In this study, LP storms revealed a shear magnitude between the boundary layer and 9 km of  $33 \text{ m s}^{-1}$  whereas HP storms had slightly lower values of  $26 \text{ m s}^{-1}$  and similar differences for the 4-10 km shear. The more hydrometeors remain in the updraft of a supercell, the higher the precipitation efficiency will be, increasing the risk of HP supercells. For that the supercell has to stay more discrete as otherwise hydrometeors from other storms or cirrus canopy could also find their way to the updraft. More about discrete supercells either in subsection 3.2.1 or in the paper of Bunkers et al. (2006).

### **3.3.3.2 Mid layer storm relative wind (4-6 km)**

Mid-level shear is crucial for the discrimination between tornadic and non-tornadic supercells. Brooks et al. (1994) a) and Brooks et al. (1994) b) highlighted the significance of the mid-level storm relative wind field, which yields a smooth balance between mid-level and low-level rotation. The mid-level winds have two different effects, like changes in the precipitation distribution and changes in the storm motion. In Davies-Jones and Brooks (1993), the evolution of a low-level mesocyclone and attendant tornadogenesis is discussed in more detail. A significant factor is the development of vertical vorticity due to baroclinic generation of horizontal vorticity as the rear flank downdraft with attendant evaporative cooled air wraps around the updraft. Tilting during the descend and then again beneath the updraft finally creates a low-level mesocyclone, so the strength of the downdraft and therefore the amount of precipitation is a crucial factor for tornado forecasting. Brooks et al. (1994) concluded that mid-level winds, which are too strong, act to blow most of the precipitation far away so less precipitation is available. This reduces the strength of downdrafts and therefore suppresses low-level mesocyclone formation (Brooks et al. 1994). On the other hand, when the wind field in this layer features weak velocities, then more precipitation can enter or fall in the vicinity of the updraft, which fosters a rapid development of a low-level mesocyclone. However, if the downdraft is too strong, it can also undercut the mesocyclone what limits the potential for tornadogenesis. Therefore a fine balance is needed between the downdraft and the strength of the mid-level flow, especially for long-tracked, tornadic supercells.

### 3.3.3.3 Low-level shear (boundary layer-1km)

Low-level shear is an important ingredient when forecasting tornadoes. Markowski and Straka (2000) for example mentioned two conditions, which are necessary ingredients for significant tornadic thunderstorms:

- strong low-level wind shear
- moderate to high values of low-level absolute moisture and relative humidity

Numerical simulations but also observations in the field suggest that the lowest 1000 m above ground play a crucial role for tornadogenesis. When talking about low-level shear, including speed and directional shear, one has to include the term: *storm relative helicity* as all those parameters are closely connected to each other. A more detailed explanation can be found in section 3.3.3.5. The risk for tornado development is augmented, when both speed and directional shear are enhanced and this becomes more visual, when using the hodographs<sup>22</sup>. In the US, amongst others, Miller (2006) did a research about the shape of hodographs at low levels during the outbreak of significant tornadoes. Next to a rapid increase of speed throughout the lowest hundreds of meters, the directional shear was substantial, resulting in a typical 'kink' in the otherwise more smoothly shaped hodograph. This feature is represented in Fig. 3.19 and it is also visible during major tornado events in central Europe, as it was the case in Poland, on the 15 August 2008.

### 3.3.3.4 Storm relative vorticity

Two officers, Fawbush and Miller, recognized an interrelation between the veering of the environmental wind field and its increase with height for a growing intensity of thunderstorms already in the early fifties. Among others, it was Maddox (1976), who eventually verified scientifically the relationship between wind shear and the degree of thunderstorm organization. He constructed a mean tornado proximity hodograph, where it became obvious that storms, which moved with the mean wind, experienced less veering and overall weak winds whereas a storm, which moved off the hodograph (a **deviant motion** to the right of the mean storm motion) caused a strengthening of the wind field at all levels but also a veering profile. Numerical

---

<sup>22</sup>In general, hodographs are plots in polar representation form. They use wind speed, marked as circles and the height above ground to show the velocity and meteorological wind direction. When the wind blows from the south with a certain velocity, the forecaster will mark the velocity north of the center of the hodograph. Repeating that for the remaining layers and then connecting those points finally features the wind profile throughout the troposphere on an hodograph. The reader is referred to Doswell III. (1991) for a more detailed discussion.

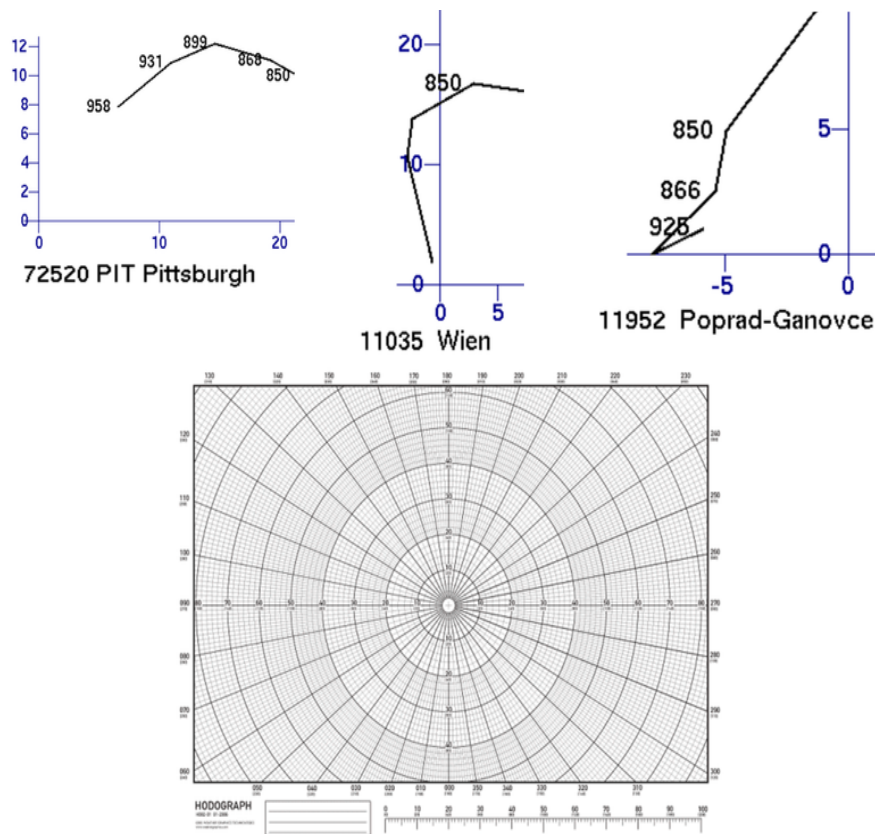


**Figure 3.19:** An outline of a few hodographs, which represent the environment of significant tornado events. Pittsburgh (US), 00 UTC, 1 June 1985, and Vienna and Poprad Ganovce, both in Europe at 12UTC, 15 August 2008. The blank hodograph is available at [weathergraphics](http://weathergraphics.com)<sup>23</sup>.

computer simulations, accomplished e.g. by Wilhelmson and Klemp (1978) revealed the presence of two different wind conditions through the troposphere: *unidirectional* and *clockwise turned* hodographs. The simulation with the unidirectional shear produced a storm split with a right and left mover, which rotated in cyclonic and anticyclonic fashion, respectively. Despite some better organization of the right mover, when including the Coriolis force, the right mover became the dominant storm, as the hodograph shape turned more clockwise whereas the left mover got suppressed.

Rotunno and Klemp (1982) made an attempt to explain why storms move to the right and left of the mean shear vector and they came up with the solution that high pressure is located on the upshear side of an updraft with low pressure on the downshear side (Fig. 3.20). This is the case during unidirectional shear conditions. In case the wind field veers with height, the pressure induced high and low pressure areas are displaced clockwise around the updraft and an upward directed pressure gradient force is situated on the right side of the updraft with the

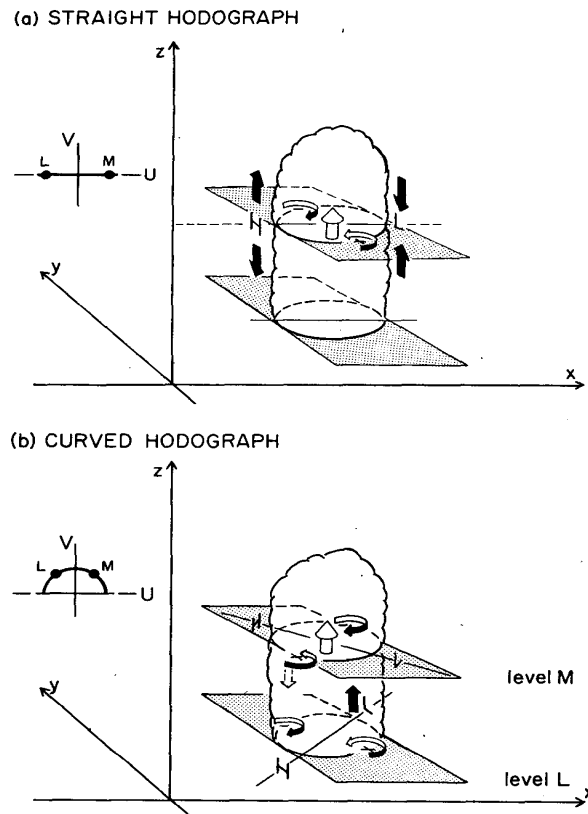


**Figure 3.20:** *a)* A case where the wind shear vector does not change with height, whereas in *b)* strong veering is present. The  $+/-$  sign marks the positive/negative vorticity. The black arrows indicate the vertical pressure gradient forces between the low and mid-levels. The appropriate hodographs are inserted on the left side. The sketch is adapted from Rotunno and Klemp (1982).

counterpart on the left side. This is the explanation, why in general the updraft continues to grow along its right side, inducing a movement to the right of the mean flow. This updraft continues to draw up initially horizontal vortex tubes and it generates cyclonic (anticyclonic) vorticity on its right and left side, respectively. This is called a *positive correlation of vertical vorticity and vertical velocity*. We now deal with the terms like *storm relative helicity*, *crosswise* and *streamwise helicity* as they have a major impact on storm motion and thunderstorm organization. The reader is referred to Dahl (2006) and Davies-Jones (1984) for a detailed theoretical explanation.

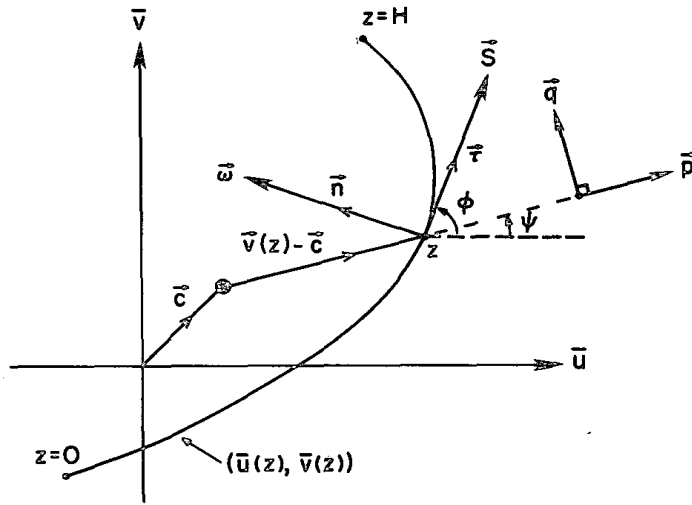


**Figure 3.21:** This is a part of a hodograph  $(u(z), v(z))$  with  $c$  representing the storm motion vector,  $v(z)-c$  the relative wind vector,  $\vec{S}$  the shear vector and  $\vec{\omega}(z)$  the environmental vorticity vector, which is in fact normal to  $\vec{S}$ . The unit vectors  $\vec{\tau}$ ,  $\vec{n}$ ,  $\vec{p}$ ,  $\vec{q}$  are in the direction of  $\vec{S}$ ,  $\vec{\omega}$ ,  $\vec{v}-\vec{c}$  and normal to  $\vec{v}-\vec{c}$ .  $\Psi$  and  $\Phi$  represent the directions of the relative wind and shear vector, respectively, measured counterclockwise from the x-direction. The sketch is adapted from (Davies-Jones 1984).

The environmental shear vector  $\vec{S} = \frac{\partial \vec{v}_h}{\partial z} = (\frac{\partial u}{\partial z}, \frac{\partial v}{\partial z})$  and the environmental vorticity vector  $\vec{\omega}_h = (-\frac{\partial v}{\partial z}, \frac{\partial u}{\partial z})$ <sup>24</sup> are the most interesting ones and are also sketched in Fig. 3.22.  $\vec{\omega}$  is placed 90° to the left of the shear vector with both

<sup>24</sup>The reason why one is just concerned about the horizontal vorticity is the fact that the vertical vorticity in the back-ground is significant lower compared to the horizontal one, so  $\omega \equiv \nabla \times \mathbf{v} = [-(\frac{\partial v}{\partial z}), (\frac{\partial u}{\partial z}), 0] = \mathbf{k} \times \vec{S}$ , assumed that  $O[-\frac{\partial w}{\partial x}]$  and  $O[\frac{\partial w}{\partial y}] \ll O[-\frac{\partial v}{\partial z}]$  and  $O[\frac{\partial u}{\partial z}]$ , where  $\mathbf{k}$  is the vertical unit vector and  $\mathbf{v}=(u,v,w)$  the velocity vector. Doswell III. (2000) compared both magnitudes with the result that for synoptic scale flow vertical velocities were in general in the order of  $10^{(-5)} s^{(-1)}$ , with horizontal vorticity magnitudes running roughly 100 times larger, namely  $10^{(-3)} s^{(-1)}$ . One can summarize that in general, wind variations with height are usually much larger than the variation of wind along a level surface.



vectors having the same magnitude. Another important issue is the fact that one has to use a reference frame, which moves with the thunderstorm, which was done in Fig. 3.21 by shifting the origin to the tip of the storm motion vector  $\vec{c}$ . The environmental horizontal vorticity vector can be split up into a *streamwise* component, which is aligned parallel to the mean wind and a *crosswise* component, which is normal or to the left of the mean flow. Dahl (2006) solved this by chopping the horizontal vorticity vector  $\omega_h$  up into a streamwise and crosswise vorticity. He achieved the following formula for the streamwise component,  $\omega_{sw}$ :

$$\omega_{sw} = -V \frac{\partial \alpha}{\partial z} s \quad (3.10)$$

and for the crosswise component,  $\omega_{cw}$ :

$$\omega_{cw} = \frac{\partial V}{\partial z} n \quad (3.11)$$

where  $s$  and  $n$  are the unit vectors tangential and normal to the streamline (in 3.21  $s$  is called  $\vec{\tau}$ ),  $V$  is the magnitude of the velocity vector and  $\alpha$  the angle between the velocity vector and the x-axis of some Cartesian grid. From eq. 3.10 and eq. 3.11 the meaning of streamwise and crosswise vorticity can be resolved as streamwise vorticity  $\omega_{sw}$  is equal to the storm relative wind speed ( $\vec{v}(z) - \vec{c}$ ) times the rate at which the storm-relative winds veer with height (directional shear), whereas crosswise vorticity  $\omega_{cw}$  is equal to the rate of increase of storm relative wind speed with height (speed shear). Just for the sake of completeness, a veering (clockwise turned) wind profile is defined, having *positive streamwise vorticity* and a backing (anticlockwise turned) wind profile features *negative streamwise vorticity*.

### 3.3.3.5 Storm relative helicity

In the following it will be shown, why storm relative vorticity and helicity are closely linked. The term *helicity* can be traced back to Kelvin (1869), who already recognized that vortex lines behave like material lines or as stated today, they are 'frozen in the fluid'. This in turn means that the flux of vorticity through any open surface bounded by a curve moving with the fluid is conserved (Moffat and Tsinober 1992). In the meteorology it was Kraichnan (1973) amongst others, who documented long-lived features in the fluid mechanics and suggested that helicity may suppress the downscale of energy in homogenous and isotropic areas. They came up with analysis of the Beltrami flow, where the cascade of energy from large to small scales is blocked as stretching and tilting terms are balanced by the

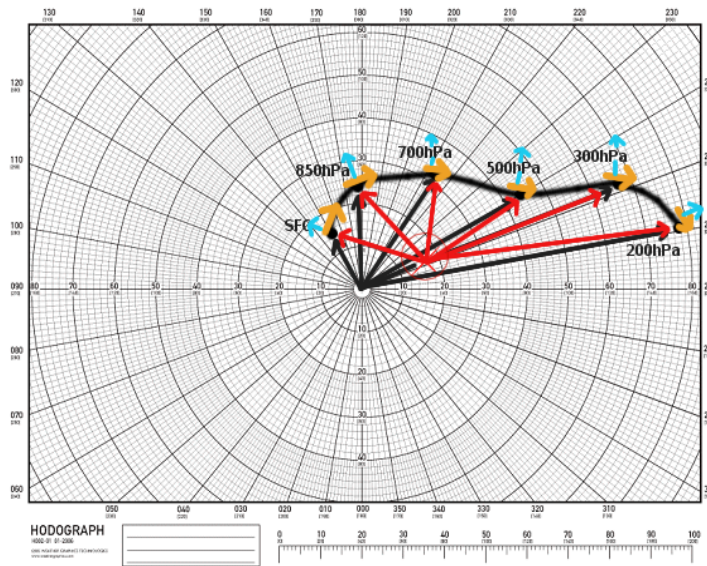


**Figure 3.22:** A virtual clockwise curved hodograph was created. The circled red cross gives the storm motion with the red vectors indicating the storm relative flow. The blue arrows stand for the horizontal vorticity vector, whereas the heavy, orange arrows show the shear vector. The numbers represent the height in the atmosphere (hPa), with the  $u$  and  $v$  components in  $\text{m s}^{-1}$ . The blank hodograph was provided by weathergraphics.

advection terms. From that point of view they drew a comparison to supercells. Those storms feature velocity and vorticity vectors, which are aligned not perfectly and buoyancy forces are present, too, but the cascade of energy loss ought to be at least inhibited. Lilly (1983) eventually came up with the hypothesis that helicity could be the reason for supercells to be longer lived and less frail to dissipation. In the following years, some doubts arose to which degree helicity is the dominant parameter for long-lived thunderstorms, but Woodall (1990) amongst others, proposed that helicity could be an important parameter, when used for the inflow layer of the thunderstorm, e.g. the lowest 3 km. The step from storm relative vorticity to storm relative helicity were the following (a more funded discussion is visible in Droegemeier et al. (1992)):

$$\text{Helicity density} = \mathbf{V} \cdot \boldsymbol{\omega}_{sw} = -V^2 \cdot \frac{\partial \alpha}{\partial z} \quad (3.12)$$

$$\text{Helicity} = \int_{\Omega} H d\Omega = \int_{\Omega} \vec{V} \cdot \vec{\omega} d\Omega \quad (3.13)$$

where  $H$  is the helicity density,  $\Omega$  the volume of integration,  $\mathbf{V}$  the velocity vector and  $\boldsymbol{\omega}$  the vorticity vector. The storm relative helicity then is defined as:

$$\text{Storm relative helicity} = \int_{0km}^h [(\vec{v}_h - \vec{c}) \cdot \vec{\omega}_h] dz \quad (3.14)$$

$$\text{Storm relative helicity} = -\vec{k} \cdot \int_{0km}^h (\vec{v}_h - \vec{c}) \times \frac{\partial \vec{v}_h}{\partial z} dz \quad (3.15)$$

where  $\vec{c}$  is the storm motion vector,  $\vec{\omega}_h = \vec{k} \times \frac{\partial \vec{v}_h}{\partial z}$  the horizontal vorticity vector and 'h' is the height of the inflow layer, which has to be chosen. In general there are two layer depths, with 3 km the one for supercell forecast although one has to be careful in situations, when thunderstorms do not root into the boundary layer as the inflow layer may be elevated in nature and hence the 3 km may be unrepresentative. The magnitude of the storm relative helicity is discernible on hodographs, too (Fig. 3.23).

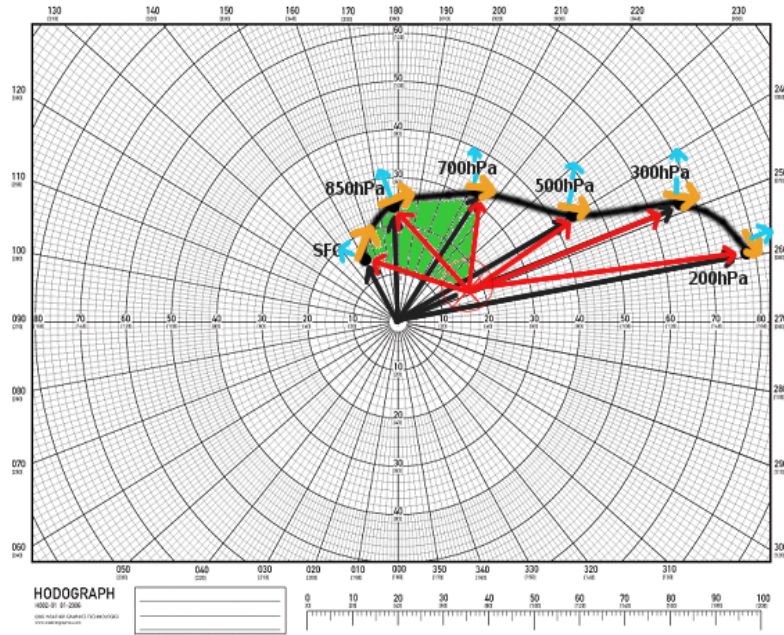


**Figure 3.23:** A virtual clockwise curved hodograph was created. The circled red cross gives the storm motion with the red vectors indicating the storm relative flow. The blue arrows stand for the horizontal vorticity vector, whereas the heavy, orange arrows indicate the shear vector. The numbers represent the height in the atmosphere (hPa), with the u and v components in  $\text{m s}^{-1}$ . Additionally, the green area represents the storm relative helicity for the lowest 0-3 km. The blank hodograph was provided by weathergraphics.

It was already mentioned that Lilly (1983) reduced the longevity of supercells to the helical environment. One can reinforce that thesis when we consider the

vorticity equation. First, a short introduction is given how to achieve the vorticity equation. A more detailed derivation can be found in Houze, sections 7-8 and Bluestein, section 3.4.:

Using the Boussinesq approximated equations, neglecting the Coriolis force and friction:

$$\begin{aligned}\frac{du}{dt} &= -\frac{1}{\rho_0} \frac{\partial p'}{\partial x} \\ \frac{dv}{dt} &= -\frac{1}{\rho_0} \frac{\partial p'}{\partial y} \\ \frac{dw}{dt} &= -\frac{1}{\rho_0} \frac{\partial p'}{\partial z} + B\end{aligned}\tag{3.16}$$

$B$  is used as the abbreviation for buoyancy. One has to reform the formula into the vector form:

$$\frac{\partial \vec{V}}{\partial t} = -\vec{V} \cdot \nabla \vec{V} - \frac{1}{\rho_0} \nabla p' + Bk\tag{3.17}$$

The term  $-\vec{V} \cdot \nabla \vec{V}$  can be modified when using the following algorithm for  $\nabla$  operators:

$$\begin{aligned}\nabla(A \cdot B) &= (A \cdot \nabla)B + (B \cdot \nabla)A + A \times (\nabla \times B) + B \times (\nabla \times A) \\ &\quad \text{When } A = B = V : \\ \nabla(\vec{V} \cdot \vec{V}) &= (\vec{V} \cdot \nabla)\vec{V} + (\vec{V} \cdot \nabla)\vec{V} + \vec{V} \times (\nabla \times \vec{V}) + \vec{V} \times (\nabla \times \vec{V}) \\ \nabla(\vec{V} \cdot \vec{V}) &= 2 \cdot (\vec{V} \cdot \nabla)\vec{V} + 2 \cdot \vec{V} \times (\nabla \times \vec{V}) \\ (\vec{V} \cdot \nabla)\vec{V} &= \nabla\left(\frac{\vec{V} \cdot \vec{V}}{2}\right) - \vec{V} \times (\nabla \times \vec{V})\end{aligned}\tag{3.18}$$

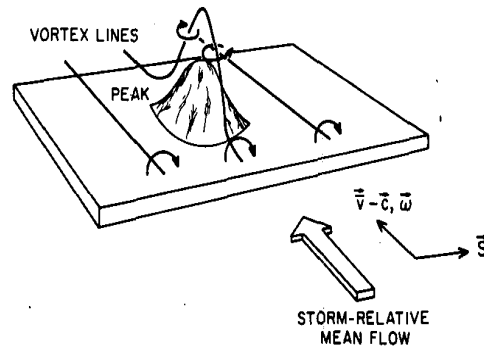
So using the information of eq. 3.18, eq. 3.17 modifies to:

$$\frac{\partial \vec{V}}{\partial t} = -\nabla\left(\frac{\vec{V} \cdot \vec{V}}{2} + \frac{p'}{\rho_0}\right) + \vec{V} \times \vec{\omega} + Bk\tag{3.19}$$

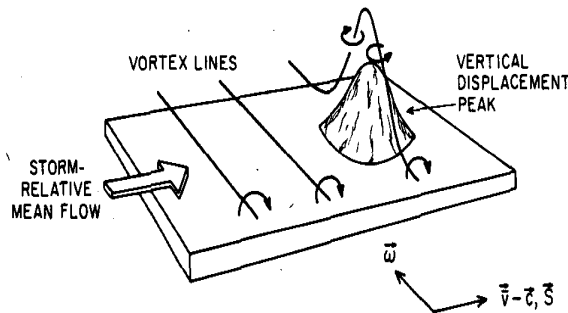
One finally gets the vorticity equation, by calculating the curl of eq. 3.19, so the final solution for the vorticity equation is:

$$\frac{\partial \vec{\omega}}{\partial t} = \nabla \times (\vec{V} \times \vec{\omega}) + \nabla \times (Bk)\tag{3.20}$$

What we know about storm relative helicity is the parallel alignment of the storm-relative velocity vector  $\vec{V}$  and the vorticity vector  $\vec{\omega}$ , so  $\vec{V} \times \vec{\omega} = 0$ . This forces the first term on the right hand side (eq. 3.20) to become zero, with the consequence that the tilting, stretching and advection terms also vanish as they evolve out of that term. Hence the horizontal gradient of buoyancy provides the only source of horizontal vorticity, whereas the vertical component of vorticity is conserved, which in fact causes the storm to keep its rotation. So right-movers or large clockwise curved hodographs favor storm rotation, as the storm relative wind component is large. In equation 3.15, the storm motion vector  $\vec{c}$  is very important as one has to keep in mind that the calculation depends heavily on the coordinate system which follows the storm, so an estimation of  $\vec{c}$  is crucial, before one is able to calculate the helicity. More on that in subsection 3.3.3.6. In different studies, it was found that there is a certain threshold for supercell development, although no fixed value can be mentioned, where supercells evolve for sure as other environmental parameters like the deep layer shear also play a substantial role in supercell formation. In respect to the 0-3 km storm relative helicity, values greater than  $250 \text{ m}^2\text{s}^{-2}$  and for the 0-1 km layer values greater than  $100 \text{ m}^2\text{s}^{-2}$  suggest an increase for tornadic supercells, if those occur in both layers simultaneously. The higher the SRH values, the higher the chance for supercells (potential tornadic). For SRH, larger values are generally better, but there are no clear "boundaries" between non-tornadic and significant tornadic supercells. So from what was said above, a forecaster would most likely expect organized and long-lived storms, when the hodograph presents strong vertical wind shear, which veers with height. It is important to point out that helicity does not determine whether storms evolve or not but instead it indicates how conducive the environment is for thunderstorms to become organized or not. When looking at the pure streamwise case in Fig. 3.24 a), nice correlation between vertical velocity and vorticity exists. In Fig. 3.24 b), a case with pure crosswise vorticity is shown, where no correlation between  $\omega$  and  $(v - c)$  exists as vorticity, which tilts upward beneath the updraft forms two counterrotating vortices along the edges of the thunderstorm, so no net-upward force becomes realized. Furthermore veering wind profiles distribute the linear pressure perturbation maxima and minima in such a manner that an upward directed vertical pressure gradient force evolves along the right side of the storm with subsidence along the left side (Fig. 3.25 b)). However thunderstorms can ingest abundant of helical flow, when storms move off the straight hodograph, which is denoted in the virtual hodograph of Fig. 3.25 a).  $R$  and  $L$  label the rough position of a right and left moving storm. In addition, this environment features no unidirectional flow (otherwise the hodograph would cross the zero point) and any observer, who travels with such storms would see storm-relative streamwise vorticity. This is a hodograph for a typical splitting storm situation.



(a) streamwise vorticity



(b) crosswise vorticity

**Figure 3.24:** In a) the vorticity is streamwise with  $(\vec{\omega} \parallel (\vec{v} - \vec{c}))$  a positive correlation between vertical vorticity and velocity. b) The effects of an growing updraft on vortex lines become visible in an environment with purely crosswise vorticity  $(\vec{\omega} \perp (\vec{v} - \vec{c}))$ . Cyclonic vorticity evolves along the right edge of the updraft with anticyclonic one along its left fringe. There is no correlation between vertical velocity and vertical vorticity with the strongest updraft displaced upstream of the peak. Both sketches are adapted from Davies-Jones (1984).

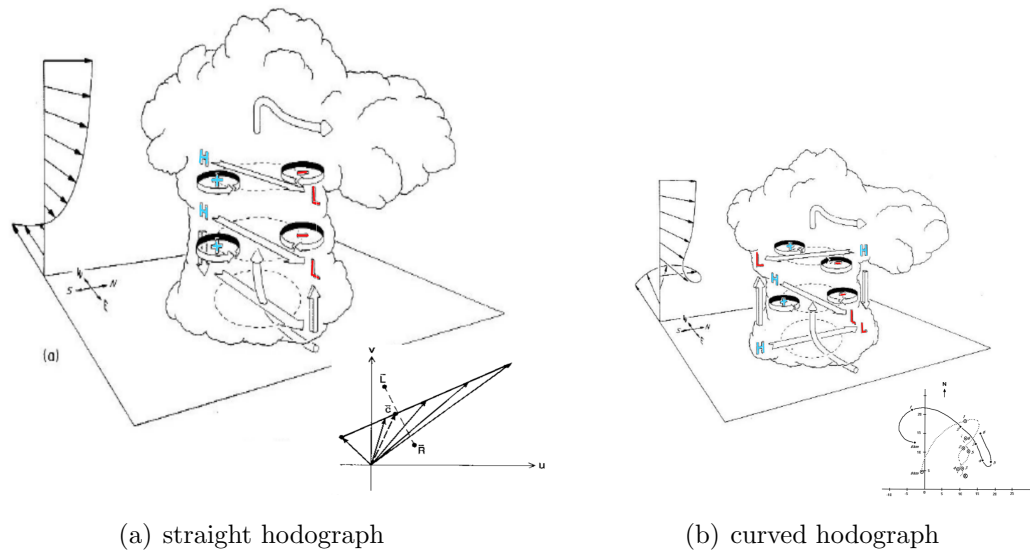


**Figure 3.25:** The interaction of an updraft with the environmental shear in an unidirectional flow (a) and where directional shear is present (b). The images are adapted from Rotunno and Klemp (1982). The fictitious straightline hodograph (flow not unidirectional) and the curved hodograph were adapted from Doswell III. (1991). Note that the curved hodograph represents the immediate environment where a violent tornado occurred near Binger, OK on 22 May 1981.

SRH is also used as a tool for tornado forecast as studies revealed augmented low-level storm relative helicity in the lowest 1000 m for tornado days but it is a more useful tool for mid-level rotation and hence supercell probability forecast. Vorticity loops, which are ingested into the updraft are still advected away from the surface, so without any other mechanism like downdraft evolution, no persistent low-level rotation could be materialized. Nevertheless one has to be careful when weather forecast models hint on an area with augmented SRH between 0-1 km (SRH1) and 0-3 km (SRH3), combined with abundant instability release for persistent updrafts, as tornadic supercells are possible.

### 3.3.3.6 Storm motion

Thunderstorms in general are hard to predict, as most models still cannot resolve the scale, which would be necessary for thunderstorm forecast (although mesoscale models like COSMO-DE and the Weather Research Forecast model (WRF) already succeed first success). Another point is that the internal dynamics and external factors like boundaries or topography all have an effect on the storm motion. A reliable forecast of storm motion can increase the lead time for severe thunderstorm warnings. Many studies, which address that topic, were carried out and a short

summary on that topic will be given.

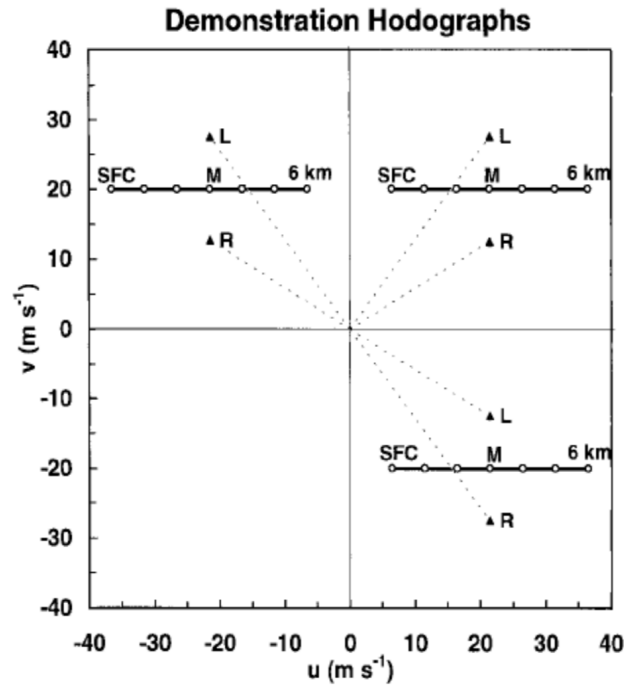


**Figure 3.26:** Galilean invariance relationship between supercell motion and the vertical wind shear for unidirectional wind shear profilers in an idealized 0-6 km hodograph. The 0-6 km mean wind is marked by an M whereas L and R represent the left-moving/anticyclonic and right-moving/cyclonic supercell motion. The sketch was adapted from Bunkers et al. (1999).

There exists a process, the so called Galilean invariance<sup>25</sup>, which exists between supercell motion and the vertical wind shear. This is shown in Fig. 3.26, where three different vertical wind shear profiles are positioned in three different quadrants of the hodograph, however the storm motion is the same relative to the vertical wind shear in all those cases. Internal dynamics in organized thunderstorms can cause right and left-moving supercells, which are included in the sketch as R and L, respectively. It can be seen that e.g. in the upper-right case the right mover would move slower and to the right of the mean wind whereas in the upper-left one, it

<sup>25</sup>The Galilean invariance was described by Galileo Galilei (*The dialogue concerning the two chief world systems*) in 1632 and states that the fundamental laws of physics are the same in all inertial frames.



would move to the left of the mean wind; however in all cases, the right mover exists to the right of the vertical wind shear. In the past, considerable research was done to handle the storm motion in an acceptable way and the fact that most vertical wind shear profiles for severe thunderstorm environments can be found in the upper-right quadrant alleviates that. Nevertheless, there are sometimes organized thunderstorm events in unusual environments where the hodograph resides in different quadrants of the hodograph, which provoked problems, especially for storm motion algorithms, which are not Galilean invariant. The following algorithms were created in the past, featuring at least some success for storm forecasting:

- Maddox (1976) conducted a proximity tornado sounding study and found out that the predominant storm motion was  $30^\circ$  to the right of the mean wind direction, while thunderstorms moved with roughly 75 % of the mean wind speed. In the literature, this is abbreviated with 30R75. This observation, linked closely to prior observations works well in most of the severe thunderstorm cases for the United States, but there are two weak points with that: No objective basis for the choice of 30R75 was presented and this method is not Galilean invariant.
- The method presented by Colquhoun (1980) is not used as acute as the aforementioned method as it is computational intensive and non Galilean invariant. The main assessment for the storm motion is the balance of the mass flux between the updraft and downdraft.
- Davies and Brooks (1993) came up with a slight modification of Maddox (1976), using the 30R75 method for wind  $\leq 15 \text{ m s}^{-1}$  and for the rest they used the modified method, called 20R85. It is calculated for a shallower layer and reduces the deviant motion for stronger mean wind environments, but otherwise no major changes were done compared to Maddox (1976).
- Davies (1998) had his focus on supercell environments, when the background flow was weaker compared to the more common cases and he noticed a greater deviant storm motion in those cases. He therefore calculated the storm motion for three different mean wind domains, one for  $0\text{-}10 \text{ m s}^{-1}$ , then for  $11\text{-}15 \text{ m s}^{-1}$  and finally for  $15 \text{ m s}^{-1}$ .
- Rasmussen and Blanchard (1998) presented a method, which is sketched in Fig. 3.27. The supercell motion is computed as an  $8.6 \text{ m s}^{-1}$  deviation from the  $0.5$  to  $4 \text{ km}$  wind shear vector, which is aligned orthogonal to the shear vector with the beginning at 60% of the shear magnitude. This method is Galilean invariant and used frequently in the past.

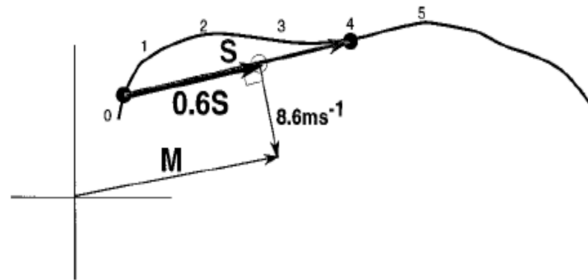


**Figure 3.27:** Storm motion calculation for RB98 where  $M$  is the predicted storm motion vector,  $S$  the boundary layer-4 km shear vector and the dots the 500m and 4000m levels. The sketch was adapted from Rasmussen and Blanchard (1998)

### 3.3.3.7 ID method

The main issue with the presented storm motions, beside their failure in non typical environmental conditions for organized thunderstorms is the too subjective approach, so a more physically based method was needed. In numerical studies it was shown that two factors determine the motion of organized thunderstorms, one is the **advection** of the thunderstorm by the mean wind and the other one the **interaction** of a convective updraft within a sheared environment. Parallel to the observational studies and proximity sounding analysis, modeling studies were carried out which proposed e.g. that the deviant motion is mainly due to a favorable dynamic vertical pressure gradient distribution, supporting rising motion along the right fringe of the storm. The so called **internal dynamics** method of supercells (ID-method) resembles the aforementioned results and methods (Fig. 3.28):

Bunkers et al. (1999) describes in more detail how they came up with the ID method and what the verification results are. The main issue of that method is to incorporate the advective but also the propagation component of a storm and to account for the internal dynamics of a supercell. They used the following equations for right and left movers respectively:

$$\vec{V}_{RM} = \vec{V}_{mean} + D \left| \frac{\vec{V}_{shear} \times \vec{k}}{|\vec{V}_{shear}|} \right| \quad (3.21)$$

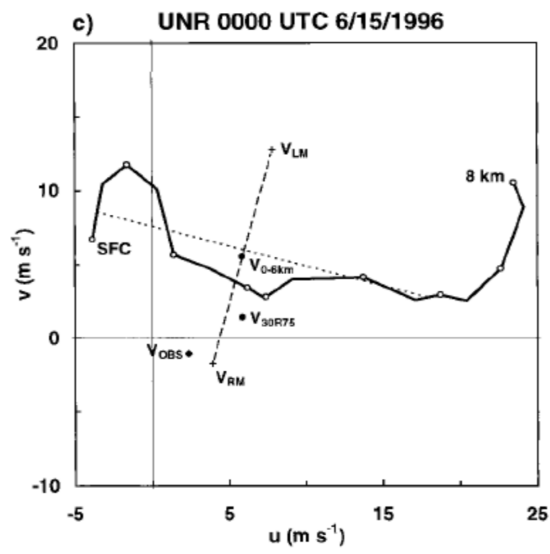


**Figure 3.28:** Non pressure weighted 0-6 km mean wind is marked as  $V_{0-6km}$  (a black dot),  $V_{Obs}$  describes the observed motion of the supercell and  $V_{RM}$  and  $V_{LM}$  stand for right and left mover, respectively.  $V_{30R75}$  means the storm motion assessment of Davies and Brooks (1993), whereas the short dashed line represent the 0-6 km vertical wind shear. The sketch was adapted from Bunkers et al. (1999).

$$\vec{V}_{LM} = \vec{V}_{mean} - D \left| \frac{V_{shear} \times \vec{k}}{|V_{shear}|} \right| \quad (3.22)$$

where  $V_{mean}$  is the mean wind vector,  $V_{shear}$  the vertical wind shear vector and  $D$  is the magnitude of the deviation of supercell motions from the mean wind (Bunkers et al. 1999). The way how to construct the storm motion is similar to the RB98 method.

Edwards et al. (2002) made some research on how good those different storm motion algorithms perform and each method had its (dis-) advantage as e.g. 30R75 had major problems in the forecast speed of those supercells as this method significantly underestimated the real thunderstorm propagation. Research for that topic was also done in Europe although not yet in-depth (e.g. Supercell storm motion prediction @ Milovan Radmanovac).

### 3.3.4 Composite indices

The above mentioned parameters represent the basics for preparing the thunderstorm forecast. However, those parameters cover a huge part of the severe thunderstorm spectrum, appearing in supercell, bow echo, hailstorm forecasts. There is a possibility to trim those parameters to certain smaller spectra like focusing on tornado forecasting or the evolution of bow echoes. Composite parameters join numerous different parameters, which all have their own advantages and disadvantages. On the one hand it is nice to have those parameters available, as they often help forecasters to focus on a certain area, which is helpful during stressful situations but on the other hand, the confusion of so many indices makes it hard to keep an overview about potential frailties of the particular parameters and therefore of the composite parameter. There are more failures with those parameters like the limited number of cases, which were assessed before creating a new parameter. A fruitful discussion about that problem can be found in Doswell III. and Schultz (2006). Nevertheless, a couple of composite parameters, used carefully and in combination with deep background knowledge of the synoptic and mesoscale weather situation, prove successful in the US and those were also included into this thesis.

#### 3.3.4.1 Energy helicity index

The EHI was developed in 1991 by John Hart and Josh Korotky (Hart and Korotky 1991). It is a parameter, which combines instability and helicity into one number. The aim is to assess these factors in an environment, which favors

supercell development. Like all the other parameters, it is just one piece of truth but it is a useful tool when e.g. discriminating between tornadic and non tornadic supercells; see e.g. (Rasmussen 2003), although they use a modified EHI in contrast to Hart and Korotky (1991). The basic premise is that thunderstorms in an high CAPE and SRH environment tend to gain rotation rapidly, so maximized values of both and therefore of the EHI ought to indicate the area with the highest supercell and tornado risk. The EHI is computed as follows:

$$EHI = (CAPE \cdot H) - 160.000 \quad (3.23)$$

For CAPE, it is common to use the mean layer CAPE, where the parcel is mixed out over the lowest 50 or 100 hPa to account for turbulent mixing in the planetary boundary layer during the day. Helicity is calculated either over the lowest 1000 m or 3000 m. Values higher than 1-2 were associated with significant tornado events in the US.

#### 3.3.4.2 Vorticity generation parameter, VGP

The VGP was invented by Rasmussen and Wilhelmson (1983) and it estimates the rate of tilting and stretching of horizontal vorticity by a thunderstorm updraft. Valuated in the US, values greater than 0.2 point to an enhanced tornado risk.

$$VGP = \left( \frac{\delta \zeta}{\delta t} \right) = \eta \cdot \nabla w \quad or \quad VGP = shear \cdot (CAPE)^{\frac{1}{2}} \quad (3.24)$$

$\zeta$  represents the vertical component of the vorticity, with  $\eta$  displaying the horizontal vorticity vector,  $w$  the vertical velocity component and shear featuring the mean shear throughout the troposphere. The main advantage with this index is the visible variation of the VGP between ordinary cells, supercells and tornadic supercells. The VGP gives the forecaster a hint on the region, where the models calculates the most promising conditions for organized thunderstorms like the EHI does. The box-and-whiskers diagram in Rasmussen and Blanchard (1998) (Fig.14) gives a nice overview about the use of the VGP for severe thunderstorm forecasting.

#### 3.3.4.3 Significant tornado parameter, STP and the Supercell composite parameter, SCP

In 2003, Thompson et al. (2003) came up with two new parameters which are used frequently. It is a multi-parameter index, which combines instability, shear and

other useful indices, which are all used for tornado forecasting. The main problem with those parameters is that it is a composition of numerous indices, which all can discriminate between supercells and tornadic supercells to a certain degree. Still a huge overlap on the box-and-whiskers diagrams is present. So using this composed parameter does not necessarily amend the accuracy in assessing the final degree of a certain weather phenomenon but it can save the forecaster some time, when he is guided to the potential threat area. The STP and SCP are defined as follows:

$$STP = \left( \frac{MLCAPE}{1500 \text{ J kg}^{-1}} \right) \cdot \left( \frac{2000 - MLLCL}{1500 \text{ m}} \right) \cdot \left( \frac{ESRH}{150 \text{ m}^2 \text{ s}^{-2}} \right) \cdot \left( \frac{ESHEAR}{20 \text{ m s}^{-1}} \right) \quad (3.25)$$

Both CAPE and the LCL are calculated for a mixed layer, whereas the effective layer<sup>26</sup> is used for the storm relative helicity and shear. In the US, a majority of the significant tornadoes occurred with STP values greater than 1 with lower values for non tornadic supercells. Just for completion. There are numerous thresholds for the calculations as MLLCL lower than 1000 m AGL, the complete MLLCL term is set to zero. More on that in the accordant paper of (Thompson et al<sup>27</sup>.)

$$SCP = \left( \frac{MUCAPE}{1000 \text{ J kg}^{-1}} \right) \cdot \left( \frac{ESRH}{50 \text{ m}^2 \text{ s}^{-2}} \right) \cdot \left( \frac{ESHEAR}{20 \text{ m s}^{-1}} \right) \quad (3.26)$$

In this multi-parameter index, the ingredients are normalized to the typical supercell 'threshold' values. If the SCP reveals high values, a good overlap exists, pointing to an augmented chance for supercells. Dependent on the use of positive or negative values the SCP forecasts right or left moving supercell potential. Regions with high STP and or SCP do not necessarily have to result in a supercell and or tornado outbreak if initiation is suppressed, which is not considered in those formula.

### 3.3.4.4 Bulk Richardson number

Weisman and Klemp (1982) already came up with the conjunction of vertical wind shear and CAPE in the early eighties and invited a nondimensional ratio, known as the bulk Richardson number (BRN):

---

<sup>26</sup>The effective layer is used to be more flexible in respect of the strong variations of the thunderstorms in respect to their height. Despite fixed layers like a 4-6 km layer supportive for supercell formation, one defines the vertical shear in respect to a measure of the depth of the particular storm. Elevated storms are a nice example, where the MUCAPE parcel height and the attendant EL layer are calculated, which define the lowest/upper most top of the effective layer. This method allows for a better assessment for different storm profiles. See Thompson et al. (2006) for results.

<sup>27</sup>[http://w1.spc.woc.noaa.gov/publications/thompson/stp\\_scp.pdf](http://w1.spc.woc.noaa.gov/publications/thompson/stp_scp.pdf)

$$BRN = \frac{CAPE}{\frac{1}{2} \cdot U^2} \quad (3.27)$$

U represents the difference between the density weighted mean winds in the 0-6 km and 0-500 m layers and CAPE the energy, which can be released into the atmosphere. The parameter can discriminate between supercells and non supercells, (seen in Fig.15 of (Thompson et al. 2003)) with a BRN number between 10-50 for supercell development. Lower BRN values suggest that the vertical shear is too strong in respect to the available buoyancy whereas larger BRN values hint on the predominant multicell cluster storm mode. Another way to differentiate between supercells and non supercells is the BRN shear, which is the denominator in the BRN calculation. It is similar to the general bulk wind difference calculation, however it uses a difference between the low-level wind and a density-weighted mean wind through the mid-levels. First results hint on  $35-40m^2s^{-2}$  for supercell occurrence.

#### 3.3.4.5 K-index

The following indices, including this one, are not made for supercell or non supercell distinction but more to assess the risk of air mass thunderstorms. They describe the thermal structure throughout parts of the troposphere, assessing the temperature difference in certain heights, which is similar to lapse rates calculation (Fig. 3.29 a)).

$$K - index = T_{850} - T_{500} + Td_{850} - (T_{700} - Td_{700}) \quad (3.28)$$

A K-index with values between  $31^\circ\text{C}$  -  $35^\circ\text{C}$  is an indicator for vivid thunderstorm activity and numerous storms are possible with K-index values greater than  $36^\circ\text{C}$  (George 1960).

Another and quite similar parameter is the **Total totals**, composed of the **Vertical totals**,  $VT = T_{850} - T_{500}$  and the **Cross totals**,  $CT = Td_{850} - T_{500}$ :

$$Total\ totals, TT = VT + CT \quad (3.29)$$

It is a simple derived index to see how steep the lapse rates between 850 hPa and 500 hPa are and how good the moisture content at 850 hPa is (all three indices were created by Miller (1967)). If the TT index reaches  $50^\circ\text{C}$ -  $55^\circ\text{C}$ , scattered to numerous thunderstorms are possible.

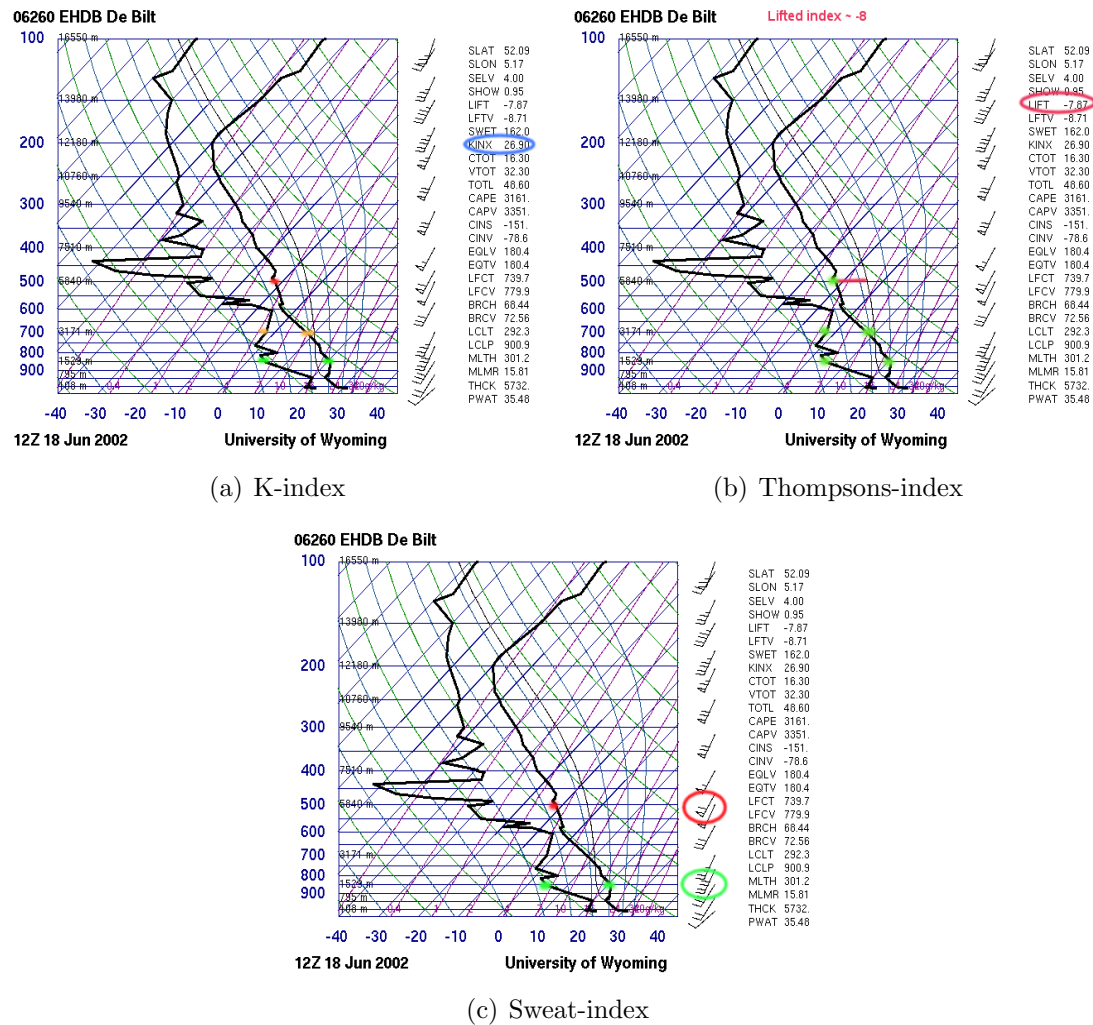


**Figure 3.29:** An outline of those levels, where the diagnostic variables are calculated.  
Source of soundings: Wyoming



### 3.3.4.6 Thompson index

This index is the difference between the aforementioned K-index and the LI at 500 hPa. The Thompson index is widely used, especially in the US and Europe as it serves as a good tool for potential thunderstorm chances. It also performs worse mainly in areas with a deep, well mixed/dry boundary layer like in Spain or Turkey during the summer months (Fig. 3.29 b)).

### 3.3.4.7 Severe weather threat index, SWEAT

At the very last the severe weather threat index is introduced, also computed by Miller (1967). This index now combines more indices, which are useful for thunderstorm forecasts, like the low level moisture content and the wind speed and direction at different levels (Fig. 3.29 c)).

$$SWEAT = 12 \cdot Td_{850} + 20 \cdot (T_{850} + Td_{850}) - 2 \cdot T_{500} - 49) + 2 \cdot F_{850} + F_{500} + 125 \cdot \sin(D_{500} - D_{850} + 0.2) \quad (3.30)$$

$F$  is the abbreviation for wind speed and  $D$  the abbreviation for the wind direction. This is one of the first parameters, which combined instability and shear for supercell and tornado forecasts. If all those indices are augmented the final value for SWEAT tops out high, with values of 300 and higher pointing to a severe thunderstorm risk and values greater than 400 indicating a chance for tornadoes. One has to keep in mind that these indices, including the SI, LI, K-index, TT, SWEAT and Thompson index are empirical only and not governed by any physical law. A good forecaster needs to keep the environment in mind in which the index is measured, as thunderstorms need lift, moisture and instability, which are not all included in those indices.

## 3.4 Severe thunderstorms in Europe

### 3.4.1 Short review about European severe thunderstorm research

Despite the fact that thunderstorm research in the US was carried out with more vim compared to Europe and most of the nowadays significant discoveries concerning severe thunderstorms were done in North America, Europe also had its own group of researchers, who carried out research on that topic. Dotzek (2001) gives an

overview about the chronological evolution of tornado research and what influence the history had. After first publications in the early twentieth century, Wegener (1917) made a detailed study about how many tornadoes occur in Europe per year and his number of about 100 cases per year was used as reference for decades. Alfred Wegener did a lot of research during that time (e.g. (Dotzek 2003) and (Dahl 2006)). Another European researcher was Johannes P. Letzmann, who continued with the tornado and waterspout research during the upcoming years and during that time, he was leading worldwide on this subject area. Dotzek et al. (2000) gave an outline about his work. During the war time and also in the fifties and sixties, not much effort was made on that topic although numerous strong tornado events in the sixties and seventies finally paved the way again for a more fruitful research on tornadoes, at least in Germany. In 1997, TORDACH<sup>28</sup> was founded for establishing a reliable climatology data set for Switzerland, Austria and Germany. Finally in 2002 the European Severe Storms Laboratory, ESSL<sup>29</sup> was created. A summary about the ESSL and also about the European Severe Weather Database (ESWD), is discussed in Dotzek et al. (2009). Each European country has its own beginnings with tornado research, e.g. the United Kingdom founded the *Tornado and Storm Research organization (TORRO)* in 1974 in order to determine realistic spatial, temporal and intensity distributions of tornado events in the UK and eventually throughout Europe (Elsom et al. 2001). The first ever documented tornado in Europe was in Rosdalla, Ireland on 30 April 1054 listed in the *Tornado project*. This is ahead of the first potential tornado report in the US, which was received in Massachusetts, July 1643, as Govenor John Winthrop described a sort of wind gust that could have been one of the first recorded tornadoes in history (source: <http://www.tornadochaser.net/history.html>). Despite the tornado research, which gradually evolves into an European project, severe thunderstorm research is still carried out with different effort in the individual European countries. It would go beyond the scope of this thesis to describe the research effort in all European countries, so only a few works from southern Germany and Switzerland are mentioned. In Switzerland, the focus was centered on the research of mesoscale convective systems, mainly by Schiesser and Houze Jr. (1991), Schiesser et al. (1992), Schiesser et al. (1995) and Schiesser et al. (1996) but also on damaging hailstorms, analyzed by Schmid et al. (1990) and Houze et al. (1993). However, there was also research done on thunderstorm indices for Switzerland and a new parameter was developed, called SWISS, which stands for combined stability and wind shear index for thunderstorms in Switzerland (Huntrieser et al. 1997) and is used whether a thunderstorm day is used or not. In south Germany, numerous studies were done about mesoscale

---

<sup>28</sup><http://www.tordach.org/>

<sup>29</sup><http://www.essl.org/>

convective systems and organized thunderstorms. In conjunction with POLDIRAD, a detailed analysis was done for a few cases, like Höller and Reinhardt (1986) and Höller (1994) but also Hagen et al. (1999), Hagen et al. (2000) and Hagen and Heimann (1994). The main interest was the distinction between different types of thunderstorms like stationary, moving thunderstorms and thunderstorm lines but also to get a better understanding of the structure of numerous squall lines, which affected southern Germany.

### 3.4.2 Ingredients for severe thunderstorm outbreaks in Europe

Different source regions are needed for any geographic region in the world to receive organized thunderstorms. There has to be a source of warm and humid air over the specific area to establish a moist boundary layer. Another ingredient is a well mixed layer at mid-levels, emanating from an arid region or an high plateau. Finally, the geographic region ought to be in the influence of some synoptic mechanism, which causes strong winds, like the westerlies in the midlatitudes but also lift to assist in the development of thunderstorms, although for initiation, mesoscale forcing is of greater concern. Van Delden (2001) published an overview, using a 4-year climatology. The author of this thesis also includes some experience he gained through the preparation of weekly European synoptic discussions in the **European Storm Forecast Experiment, ESTOFEX** ([www.estofex.org](http://www.estofex.org)).

In Europe the topography plays a restrictive role with the east-west aligned Alps, protecting most parts of Europe from a direct and more intense influx of moist air from the Mediterranean. Nevertheless, mainly during the summer months, far southward digging upper troughs are able to advect a subtropical air mass far to the north over central Europe. In eastern Europe, the Black Sea is the source region for very humid air, which affects most parts of eastern Europe during the summer months. Moist air also arrives from the Atlantic Ocean, however, the moisture content in this cooler air mass is not comparable to the air mass from the Mediterranean. In summer, mainly during weak pressure gradient situations, moisture pooling along convergence zones can locally increase the quality of the boundary layer significantly and plays a major role for thunderstorm initiation forecasts. However this is a more local phenomenon. The best buildup of moisture can be found just south of the Alps, where missing frontal intrusions from the north allow the air mass to modify, resulting in a very moist boundary layer with dewpoints sometimes soaring into the lower twenties. Another region can be found over southeast and east France, where strong pressure gradients evolve during the approach of a front from the west, resulting in strong low-level jet winds, which draw the moisture rapidly towards the

north.

### 3.4.2.1 Elevated mixed layer, EML

The *elevated mix layer*, *EML* was discussed in the mid to late 1960s and many studies were carried out about that phenomenon, Carlson et al. (1983). The EML has many properties, which assist in the development of intense thunderstorms. The most important are listed:

- Thunderstorms remain more discrete, when developing in an environment with a pronounced EML due to the stronger cap. Higher CIN suppress most thunderstorms despite those, which are backed up by stronger convergence or regional higher moisture content in the boundary layer
- The EML results in stronger capping, which increases the moisture quality beneath that cap. Convection awaits until either a forcing mechanism causes thunderstorm initiation or intense diabatic heating overtakes the cap. In general this happens late in the day, during the afternoon and evening hours, and intense updrafts take profit of the warm and moist reservoir at lower levels, which accumulated during the day.

An EML mainly evolves in arid regions, where intense diabatic causes a well mixed air mass with lapse rates approaching the dry adiabats throughout a deep layer, e.g. up to 500 hPa is the Iberian Peninsula. In summer, when a trough over the eastern Atlantic digs far to the south, very hot and dry air gets advected northwards from Morocco and Algeria or gradually evolves over the Iberian Peninsula, when a long period of high pressure allows the air mass over Spain to modify. In case the trough from the E-Atlantic further approaches Europe, this very hot and dry air mass starts to move towards the northeast, covering most parts of central Europe, dependent on how intense and persistent the advection is. This plume of well mixed air is called *Spanish plume* and is discussed e.g. by Morris (1986). While crossing the Mediterranean, some modifications of the lower levels occurs, however the mid-levels remain well mixed with almost dry adiabatic lapse rates. That is the stratification for robust potential instability release, which causes some of the highest CAPE over central Europe during the summer months. Due to the close connection of the Spanish plume with an approaching trough, dynamics, shear and abundant instability overlap and cause organized thunderstorms.

Bissolli et al. (2007) did a study about certain synoptic weather patterns, which result in augmented tornado chances for Germany. The southwest flow advects the

warm and moist air mass well to the north beneath the elevated mixed layer. Especially during the summer months highly amplified troughs which tap into the hot and warm air mass from the Mediterranean often produce more or less confined thunderstorm outbreaks, especially over the Po valley region. Dependent on the quality of the boundary layer regarding the moisture content, each more dynamic feature can produce organized thunderstorms over central and eastern Europe although sharp and progressive troughs quite often cause the most serious severe thunderstorm outbreaks, e.g. 15 August 2008. In respect of tornado outbreaks, a strong low pressure area over United Kingdom and Scotland results in an overlap of strong shear and some instability over northern France, Belgium, Luxembourg, the Netherlands and west and northwest Germany, e.g. 27 March 2006, where at least 8 tornadoes occurred. During the winter time however, strong cold fronts in an environment with at least some low-level CAPE or cold fronts, which move beneath a dry slot<sup>30</sup> are also known to produce all kind of severe weather, including damaging wind gusts and tornadoes. This is the case mainly for the northern parts of Europe, e.g. north of the Alps, where intense autumn-/winter-like depressions sometimes come ashore. Nevertheless, the maximized severe thunderstorm risk during the winter time is concentrated along regions, where deep moisture is present, e.g. the Mediterranean and the Black Sea region.

It becomes necessary to look into the climatology of the past years to refine the quite oversimplified statements, which were briefly treated in this section. Instead severe thunderstorm reports of the *European Severe Weather Database*, *ESWD*<sup>31</sup> can be used. Each region in Europe has its own synoptic constellation for severe thunderstorms, which can occur over a huge scope of possibilities for instability and shear combinations and forecasters not only have to deal with the more typical 'US-like' thunderstorm situations, featuring abundant instability and shear. They also have to work with severe thunderstorm environments, where either one or both of those parameters reveal very slim magnitudes, still capable of producing organized thunderstorms.

However, it is still not yet possible to define all synoptic weather patterns, which

---

<sup>30</sup>Adapted from the glossary of the National Weather Service: 'A zone of dry (and relatively cloud-free) air which wraps east- or northeastward into the southern and eastern parts of a synoptic scale or mesoscale low pressure system. A dry slot generally is seen best on satellite photographs.' For forecasters, dry slots are an important phenomenon during the complete year. In summer time, dry slots cause a decrease in cloud cover and in a row more diabatic heating. Sometimes, global forecast models have a hard time to resolve that feature and hence, thermodynamic conditions could change beneath the dry slot which could be enough for thunderstorm initiation. During the winter time, dry slots are of interest when they overrun a surface cold front, potential instability may be released due to the lift and drier mid-/upper levels, which can cause thunderstorm development in a highly sheared environment.

<sup>31</sup><http://www.essl.org/ESWD/>

favor some kind of severe weather over particular regions in Europe. Local weather offices indeed have experience when organized thunderstorms can be expected, but this knowledge is still anchored in the respective weather offices.

# Chapter 4

## Case studies

### 4.1 Calculation of a few selected parameters

In the course of this diploma thesis, 118 parameters were visualized and programmed. For that, the data was not calculated on pressure but on model levels. The  $\mu$ -coordinate was used which is a modified version of the Gal-Chen-coordinate. Those levels follow the terrain before becoming parallel to each other in the free atmosphere. The model levels were chosen due to the small vertical spacing and the high option of choice at which height one wants to calculate the special parameter. For the calculation of convective available potential energy the virtual temperature ( $T_v$ ) was used. This was done to account for the moisture in the atmosphere. Although the magnitude of CAPE does not vary a lot, it still becomes noticeable for low CAPE environments, where the exact amount of CAPE is crucial for the final severe thunderstorm risk. Using  $T_v$  always has a positive effect on the final amount of CAPE as added water vapor makes the parcel less dense which is comparable to a warming of the parcel. See Doswell III. and Rasmussen (1994) for more detailed information. The mean-layer CAPE was mixed throughout the lowest 500 m. A smoothing factor was used for those parameters, which are highly variable in high resolution models like the upward vertical velocity or the relative and absolute vorticity maps. Instead, the Gauss-Kernel was used. For the storm relative helicity calculation, the storm Bunkers ID method was chosen with  $7.5 \text{ m s}^{-1}$  to the left and right of the mean storm motion vector.

### 4.2 Choice of events and verification

Most parts of this thesis were performed with a subjective verification. First of all the POLDIRAD archive over southern Germany was used for detecting organized thunderstorms. A search was made for radar signatures typical of organized thun-

derstorms e.g. hail spikes, bounded weak echo regions, sharp reflectivity gradients, rotation or strong hail cores. 15 years of radar data on thunderstorm days were perused. The search was refined by matchings with the particular environmental conditions, for example by means of sounding or observational data. The same was done for the past 5 years for the larger region Europe to detect the major severe thunderstorm events, which occurred over France, Germany or Poland. For the severe thunderstorm events, the reports of the *European Severe Weather Database*, (<http://www.essl.org/ESWD/>) were used for verification if the thunderstorms were organized enough in producing severe hail, wind gusts or tornadoes. The fact that for the severe thunderstorm events over France and Poland, no POLDIRAD could be used, other remote sensing data had to be collected to prove, that thunderstorms were organized to a certain degree. One example was the presentation in modified satellite images, where the anvil temperature was shown. Signatures like the U-shape were included in the evaluation of the thunderstorm strength. In addition, regional radar data was used, too, with the aforementioned radar signatures. Finally, COSMO-DE data were compared for example with sounding reports or surface data to evaluate how well the model handled the environment.

The section 'case studies' starts with an bow echo event (subsection 4.3.1), which is the only non-supercell event in this section. The second (subsection 4.3.2) and third (subsection 4.3.3) case studies face two different environments for tornado development in respect of environmental support and handling of the mesoscale model. The fourth (subsection 4.3.4) event was chosen due to the excellent characteristics of an hail storm in the range of a polarimetric radar and the same for a well structured supercell with an attendant mesocyclone in the fifth (subsection 4.3.5) case study.

## 4.3 Case studies

### 4.3.1 26 May 2009: Bow echo, Southern Germany

#### 4.3.1.1 Overview

A severe thunderstorm outbreak occurred over parts of Switzerland and S/SE-Germany as a long tracked bow echo raced northeastwards on 26 May 2009. Thunderstorms developed over Switzerland between 11 and 12 UTC and a continuous line evolved, running from the Black Forest area all the way down to Ticino. The most organized part of the MCS was situated over N-Switzerland with a rapid motion towards the northeast. During the passage of the Lake of Constance, radar scans revealed further organization into a well structured bow echo with a sharp reflectivity gradient along the leading edge and a pronounced rear inflow jet. During the passage of Landsberg, Doppler velocity radar data measured 35-40  $\text{ms}^{-1}$  winds in the

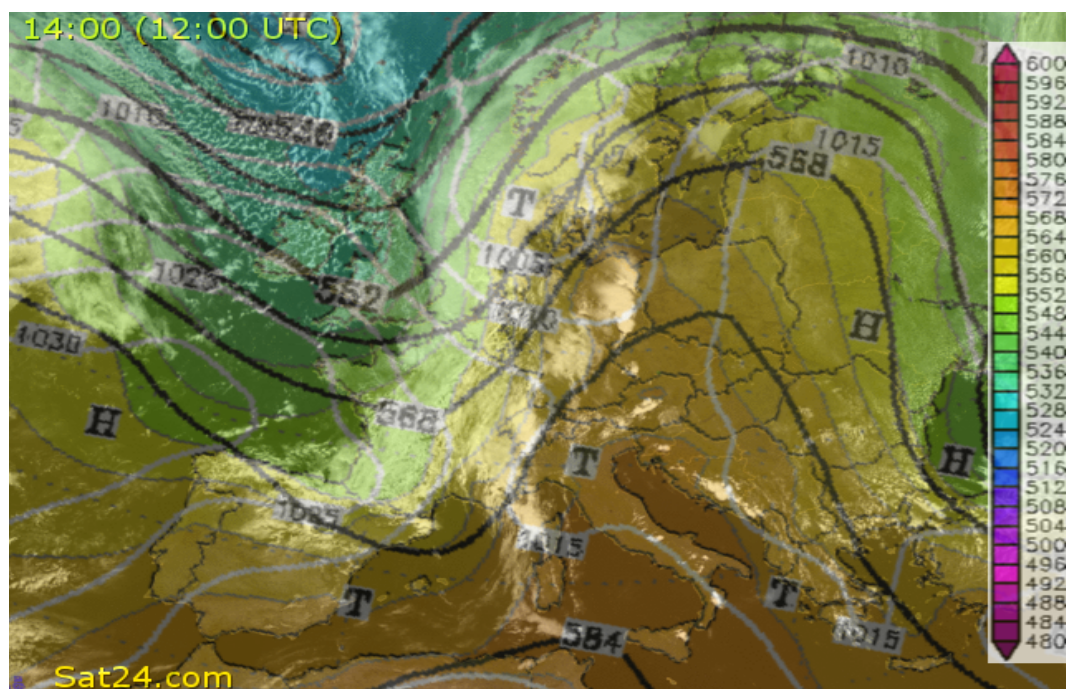


lowest 500-2000 m in agreement with a  $39 \text{ ms}^{-1}$  wind gust from Landsberg. Intense rain amounts with flash flooding and 3-4 cm hail were observed in this line, which produced a swath of severe wind gusts and hail from NE-Switzerland to SE-Bavaria with wind gusts in excess of  $25 \text{ ms}^{-1}$ . The bow echo finally decayed over SE-Bavaria during the evening hours with new initiation next to Salzburg.

#### 4.3.1.2 Synoptic-scale overview and mesoscale discussion

The time period between the 25 to 26 May 2009 was marked by numerous significant severe thunderstorm events, which affected France, Belgium, the Netherlands, Luxembourg, Germany and Switzerland. The general pattern, seen on Fig. 4.1 a) is marked by an amplified upper-level trough over the far eastern Atlantic and western Europe and large-scale ridging downstream over central and eastern Europe. This is also apparent on the visible channel (hereafter VIS), which features mainly cloud-free conditions beneath the strong ridge and the cellular, shallow convection beneath the upper trough axis. An active frontal zone runs from northern Spain all the way to Norway and Sweden and separates a cool and more stably stratified air mass to its west from the hot and humid air mass to its east. The latter air mass is characterized by already developing thunderstorms over Switzerland, Germany and the western Mediterranean. Zooming into the area of interest, Germany and surrounding regions, the southwesterly flow becomes again visible in Fig. 4.1 b) when using the 300hPa geopotential height and wind field analysis of COSMO-DE. In addition, the mid-level lapse rates, marked with the background colors, are shown, which back the aforementioned different air mass quality with near dry adiabatic lapse rates over those parts, where thunderstorms evolve. This is the far northward advancing elevated mixed layer or Spanish Plume (chapter 3, subsec.3.4.2.1), which spread out far to the north ahead of the approaching trough. The upper trough gradually moved eastwards during the following 12 h with the trough axis finally leaving Germany on 27 May 2009 around 12 UTC. In respect of mid-level forcing, the situation became complex due to the simultaneous approach of the upper trough axis and a northeastward ejecting short-wave, which crossed Switzerland and south Germany until 18 UTC (not shown).

The most striking features at the surface were the passage of two cold fronts, shown in Fig. 4.2 with the stronger one approaching southwest Germany around 09 UTC from the west. Just 2 hours later, the cold front was situated over extreme west/northwest Switzerland and southwest Germany and the southern part of the cold front slowed down due to the blocking effects of the western Alps. Driven by the northeastward advancing disturbance, a solid line of thunderstorms evolved, which extended all the way to the Black Forest region. In Fig.4.3 the track of the bow echo was sketched. For that, four PPI radar images were selected with



*2-4km lapse rates, wind and geopotential heights (300hPa)*

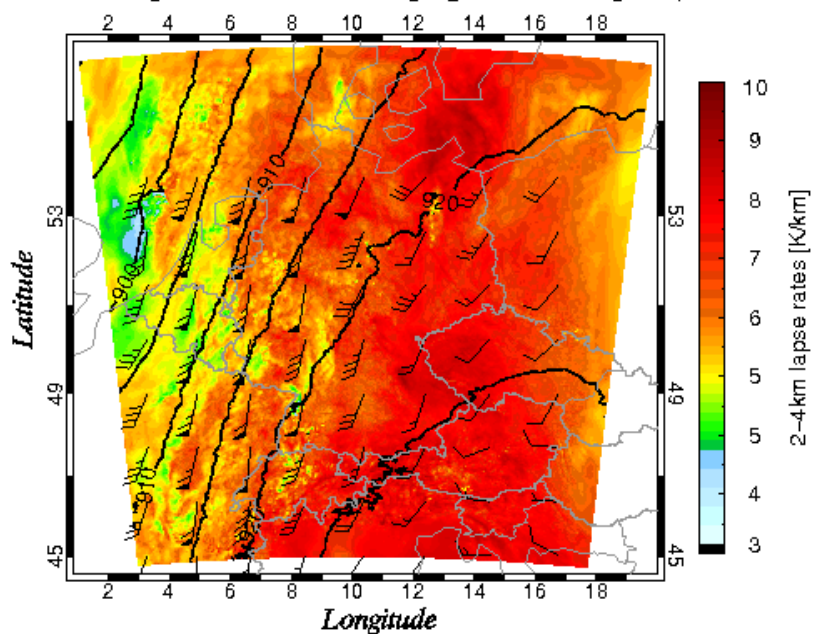


**Figure 4.1:** A composite image is prepared in a), where the 12 UTC visible channel is combined with 500hPa (gpdm, black line), relative topography (gpdm, colored) and surface pressure (hPa, white line) (12 UTC). The source for the satellite data is *Sat24.com* and for the meteorological parameters *wetter3.de*. In b), the 300hPa geopotential heights (gpdm) with black lines, the wind at that level (black wind barbs) and the 2-4 km mid-level lapse rates of COSMO-DE are shown.

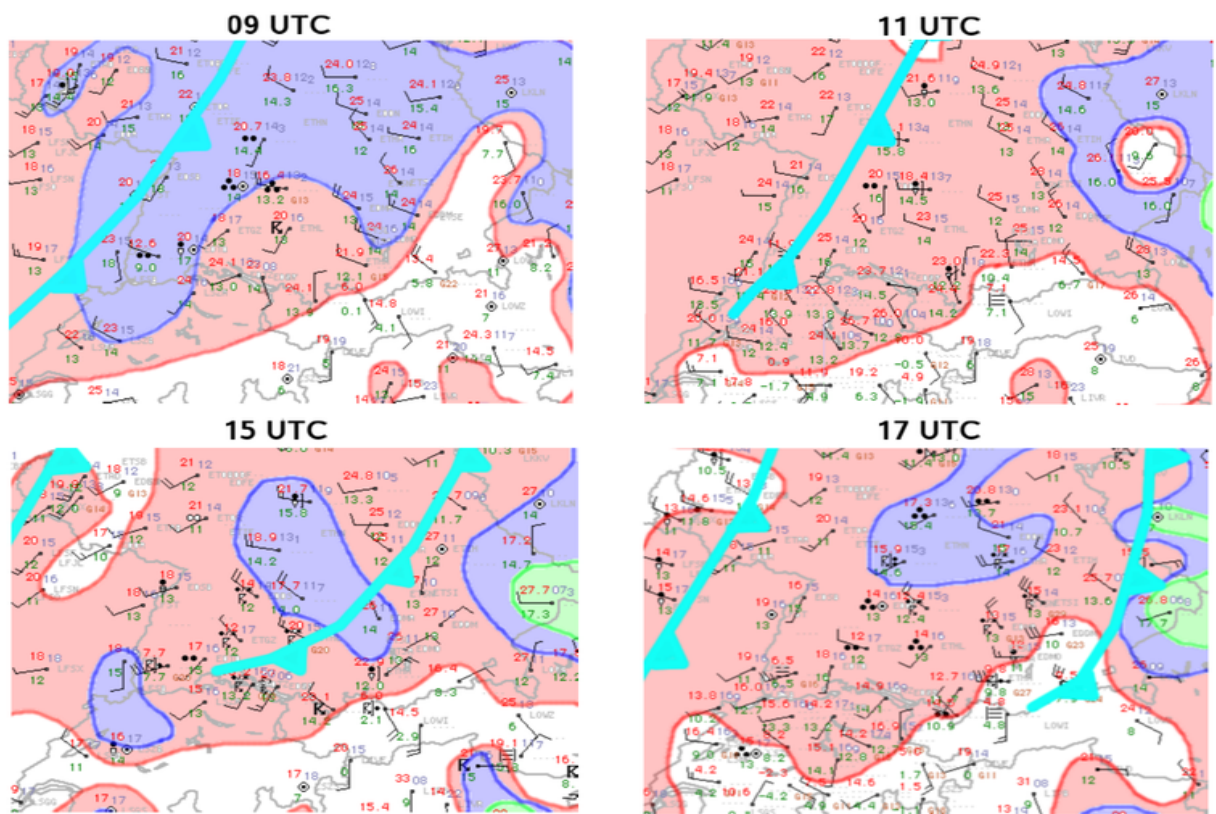


**Figure 4.2:** The surface dewpoint maps at 4 different time steps. The modified synoptic maps are adapted from Pieter Groenemeijer ([www.estofex.org](http://www.estofex.org)). The following color code was used: 11-14°C in red, 14-17°C in blue, 17-20°C in green and 20-23°C in yellow.

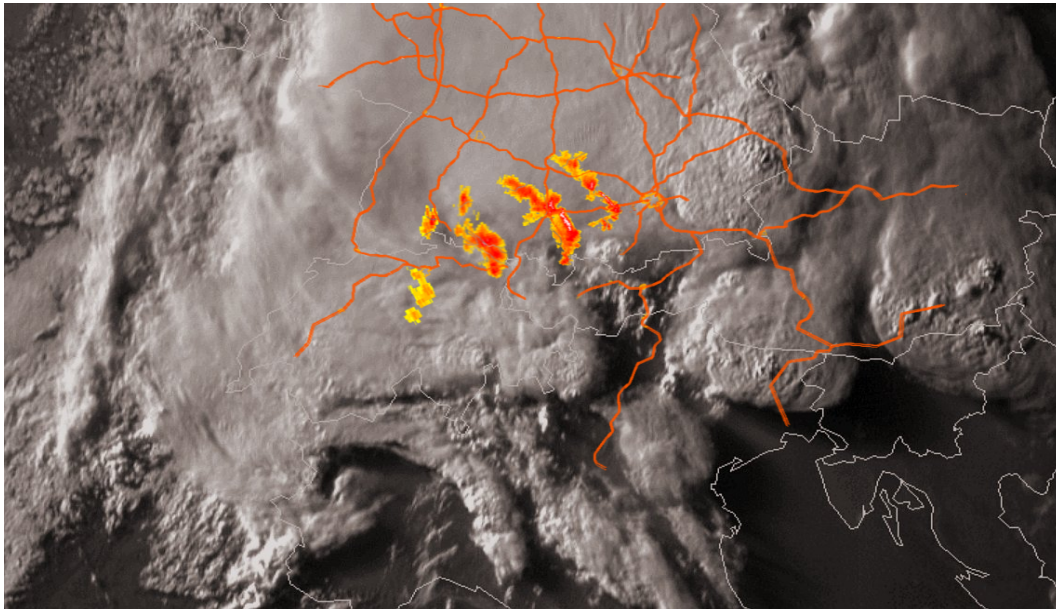


**Figure 4.3:** A radar composite with radar echoes greater 30 dBZ for four different time steps. Radar data is provided by POLDIRAD, orange lines are the major highways and the satellite image is copyright 1810 UTC, 26 May 2009 of EUMETSAT. 4 time steps are drawn, the first one over north-central Switzerland at 1310 UTC, the second one over the Lake of Constance at 1410 UTC, the third one at 1510 UTC and the last one just west of Munich at 1551 UTC.

reflectivity contours for values greater than 30 dBZ. It has to be noted that all the radar data is from the DLR in Oberpfaffenhofen, just west of Munich, with an beam elevation of  $1^\circ$ . Therefore the reflectivity pattern over Switzerland and probably far southwest Germany is weaker than it was in reality. The beam already bent up through the troposphere, only slicing parts of the thunderstorm clouds at an altitude of 8-9 km. Nevertheless, the most active cells were tracked at 1310 UTC over north central Switzerland. Rapid strengthening of the thunderstorms took place until 1410 UTC, the second image in the composite. The cluster of thunderstorms already had the typical bow-like appearance with cloud tops exceeding 12 km. A DWD weather station measured a maximum gust of  $32 \text{ m s}^{-1}$  at the eastern part of the Lake of Constance with numerous gusts at or above  $27 \text{ m s}^{-1}$ . One hour later, a major bow echo with a tight reflectivity gradient is seen. The tight reflectivity gradient is the indication of a sharp convergence flow between the downdraft and the warm and moist inflow from the east, which had velocities of  $5 \text{ m s}^{-1}$ . The RHI of POLDIRAD (Fig. 4.4,c) supports that with reflectivity values at or above 50 dBZ up to 9 km above ground. Due to the intense nature of the updraft, a BWER is seen, which was present in the following scans, too. With the help of Fig. 4.4 a) and Fig. 4.4 b) in the PPI and RHI modi (the latter one is not shown),



the type of precipitation can be evaluated. LDR values around -15 dB, marginal positive ZDR values along the leading edge and reflectivity values exceeding 60 dBZ all point to a mixture of intense rain amounts and hail, probably melting due to the extensive nature of LDR values around -15 dB. This matches observations from storm chasers, which experienced flash flooding and large amounts of hail, 2-4 cm in diameter. On reflectivity PPI images (not shown), numerous RINs were seen, which are an indicator of a forward propagating RIJ atop of an existing cold pool and hence a precursor for a potential severe wind threat. Indeed, DWD surface data revealed a sharp 10-15 °C temperature drop behind the reflectivity gradient with a pressure rise of 4-6 hPa (DLR, private weather station, see Fig. 4.6) as the cold pool approached. The pressure increase may have been even higher north of the DLR, where the bow echo passed by. The thesis of the descending RIJ is supported by velocity data of the POLDIRAD, which had inbound velocities of 35 m s<sup>-1</sup> barely above ground and surface wind gusts reports in excess of 27 m s<sup>-1</sup> (for example 39 m s<sup>-1</sup> at Landsberg, west of Munich). The final radar image in Fig.4.3 is from 1551 UTC. It can be seen that the bow echo is just west of Munich. The weaker appearance is mainly due to the proximity to the radar station. On radar scans of the DWD (not shown), the bow echo passed by Munich just to its north before finally weakening around 17 UTC northeast of Munich.

This text-book like example also reveals the structures, seen in mature bow echo events, which indicate the strength of the system. Sketched in Fig. 4.4 d) the tight reflectivity gradient along the leading edge can be seen (highlighted by a white arrow), indicating a zone of deep convergence. In addition, numerous WECs or RINs were present, highlighted by black arrows. Development and definition of those features can be found in section 3.2.3.1. The complete system can be classified as a symmetric, progressive bow echo event. *Symmetric* due to the extensive area with stratiform rain behind the leading convection line and *progressive* due to the limited length of the bow echo and the orientation perpendicular to the mean environmental wind. The 'noise' in the RHI ahead of the approaching bow echo is probably caused by dust, which can be confirmed by visual observation. However there are also numerous rays with high reflectivity, also visible in the PPI in westsouthwesterly and southeasterly direction. This noise has no meteorological background but is a Wireless Local Area Network (WLAN), which emits signals permanently and therefore is received by the radar permanently. Hence the reflectivity keeps its high values also behind the hail and rain core, where normally attenuation would cause some weakening.

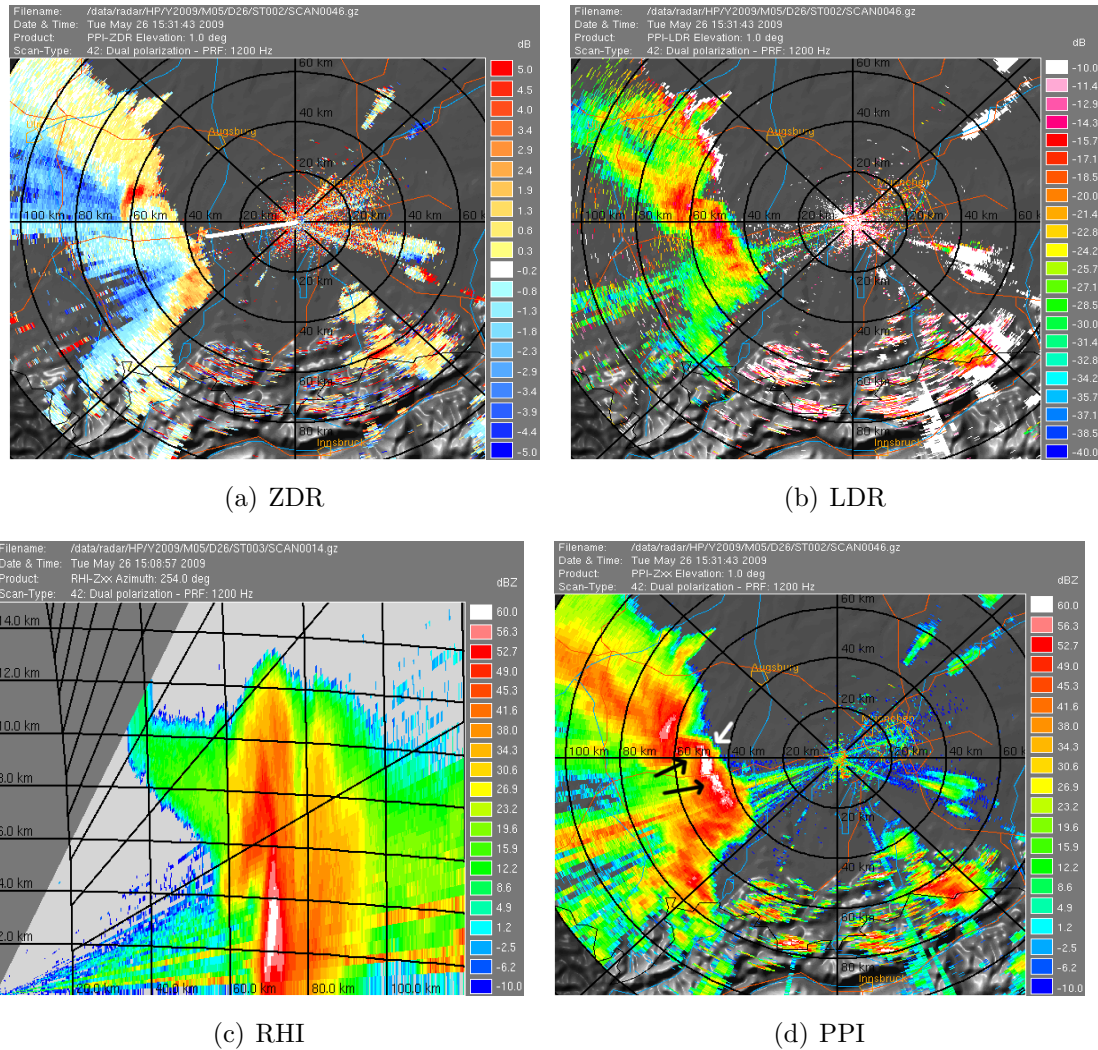


**Figure 4.4:** a) is the differential reflectivity (ZDR, dB), b) the linear depolarisation ratio (LDR, dB) at 1511 UTC, c) the range height indicator (RHI, dBZ) at 1509 UTC and d) the plan position indicator (PPI, dBZ) at 1531 UCT all showing the mature bow echo, which moves towards the northeast. The white line in a) is the direction of the RHI scan in c). The white arrow in d) highlights the tight reflectivity gradient, whereas the black arrows indicate the positions of the rear inflow notches.

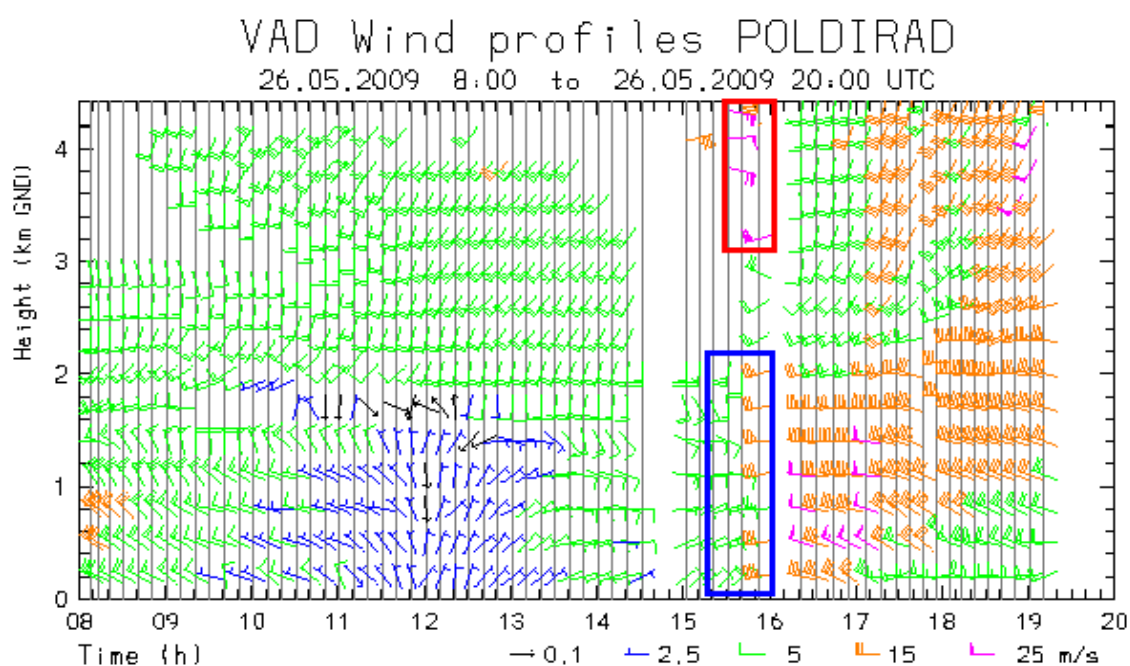


**Figure 4.5:** VAD wind profile from POLDIRAD measurements on the 26 May 2009. The antenna of POLDIRAD resides at 602,5 m AGL. The red rectangle marks the folding, whereas the blue one highlights the time, when the bow echo affected POLDIRAD.

In Fig. 4.5, the strength and direction of the wind in the lowest 6 km is shown on the velocity azimuth display, VAD. The color code reflects the strength of the wind field. Velocity aliasing effects can be seen between 15 UTC and 16 UTC at 3 km and above, where both speed and direction cannot be used (red rectangle). For this part of the study, the lowest 2-3 km are of main interest. Weak wind speeds were measured during the morning hours with rising pressure, seen in Fig. 4.6 and the pressure curve revealed a similar pattern to undisturbed summer days. Around noon, a constant decrease of the surface pressure began as surface winds backed to the east with  $2-7 \text{ m s}^{-1}$ , which was already seen in velocity data from POLDIRAD. This inflow layer became almost 2 km deep, which increased the convergence at the leading edge of the bow echo. Around 16 UTC, the bow echo passed by the radar, where no measurements were performed due to intense straightline wind gusts of  $25 \text{ m s}^{-1}$ . The DLR itself was just along the edge of the bow with the main core of the RIJ passing to the north but still wind speeds of  $25 \text{ m s}^{-1}$  or more were measured in the lowest 2 km. In both figures, the cold pool becomes visible with a sharp drop of the surface temperatures and a constant increase in surface pressure with more than 5 hPa in 2 hours.



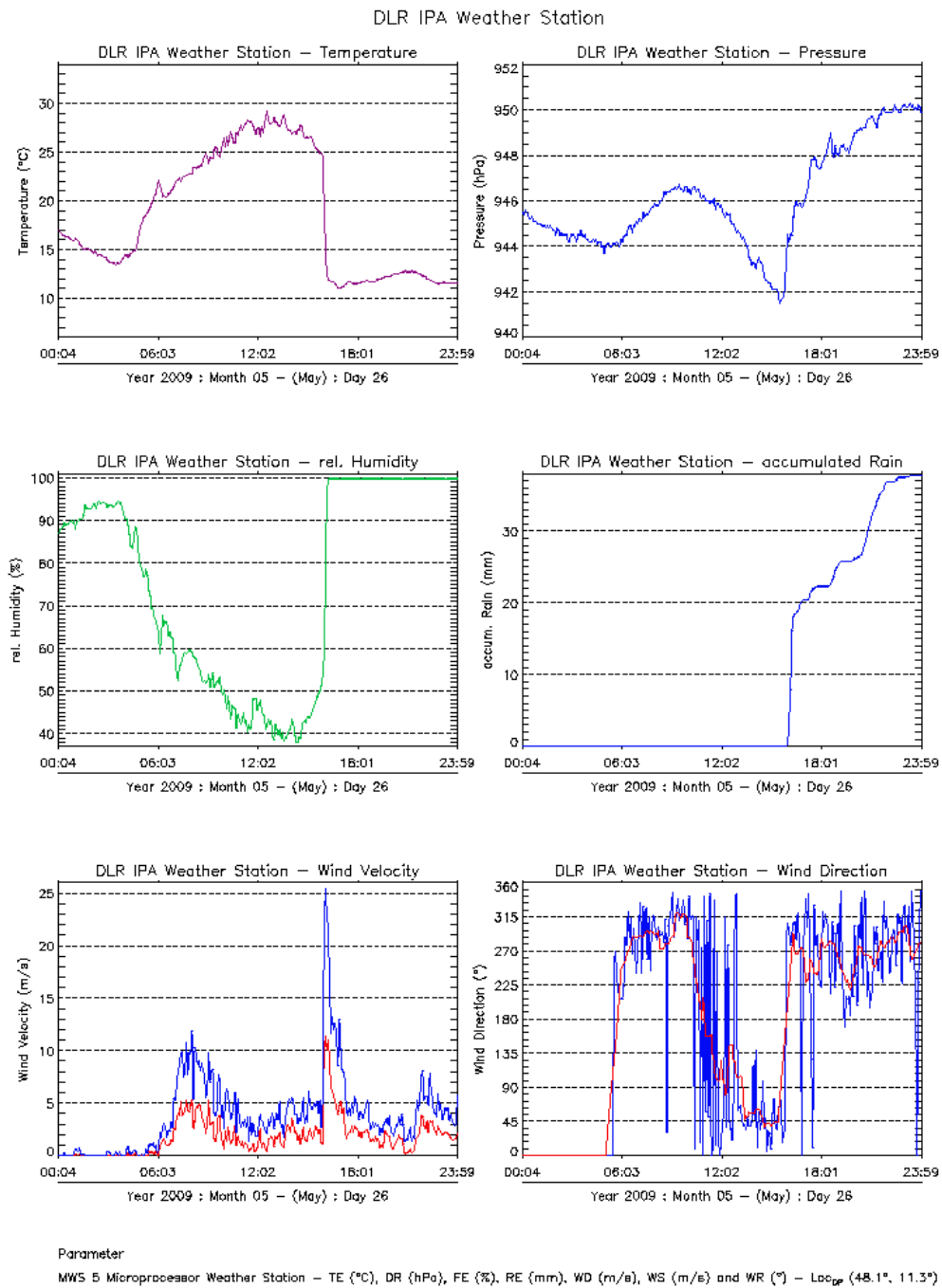


**Figure 4.6:** The weather station at the DLR (provided by Patrick Tracksdorf). The time of day is in UTC.

### 4.3.1.3 COSMO-DE performance

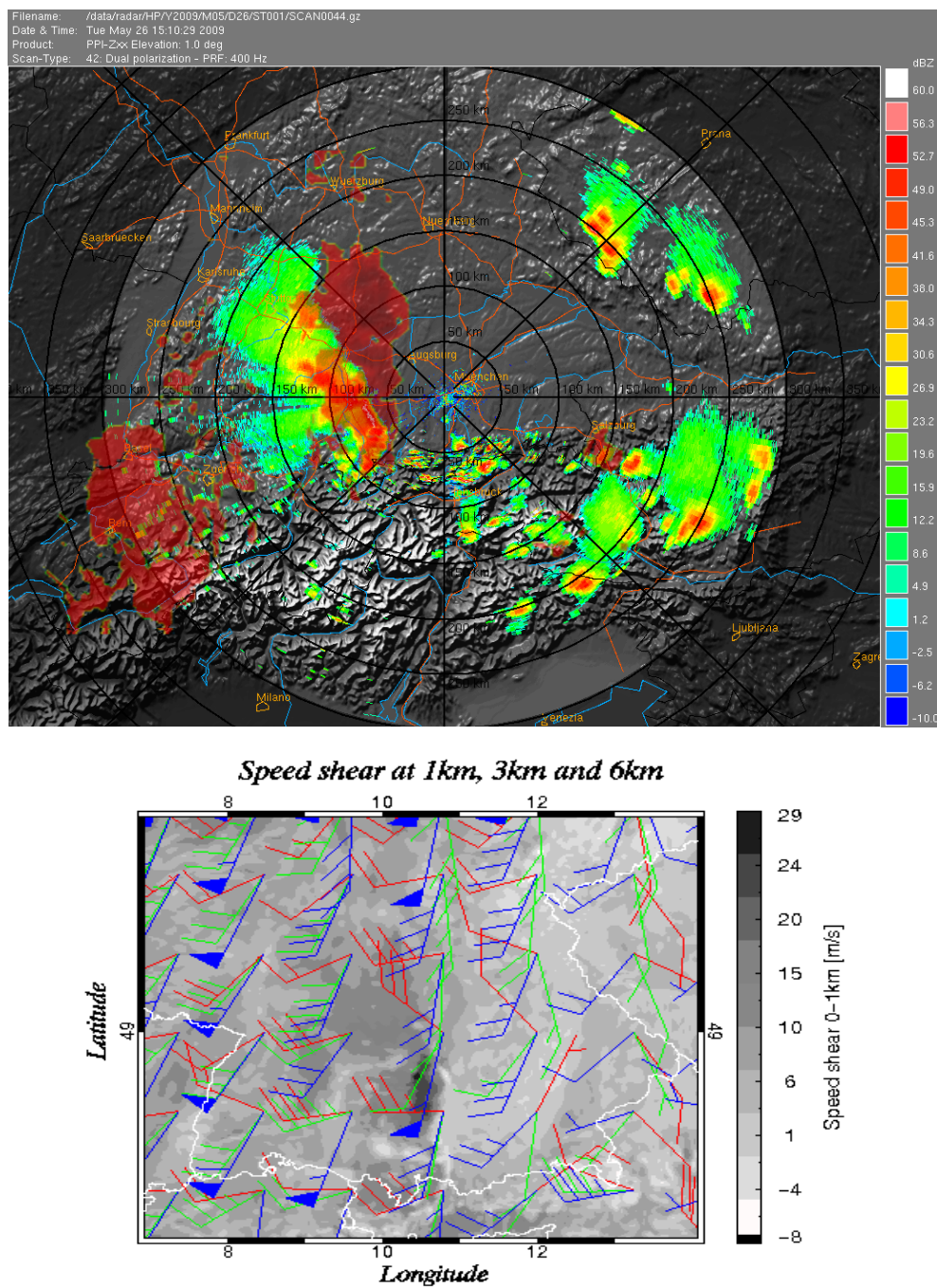


**Figure 4.7:** Comparison between COSMO-DE and POLDIRAD. a) The PPI (colorbar) and COSMO-DE output are from 1510 UTC. In COSMO-DE, reflectivity values greater 40 dBZ were cut off. The speed shear composite (COSMO-DE) in b) was evaluated for 1500 UTC. The background color is the 0-1 km speed shear, and the red, green and blue wind barbs feature the speed shear throughout the 0-1 km, 0-3 km and 0-6 km layer, respectively.

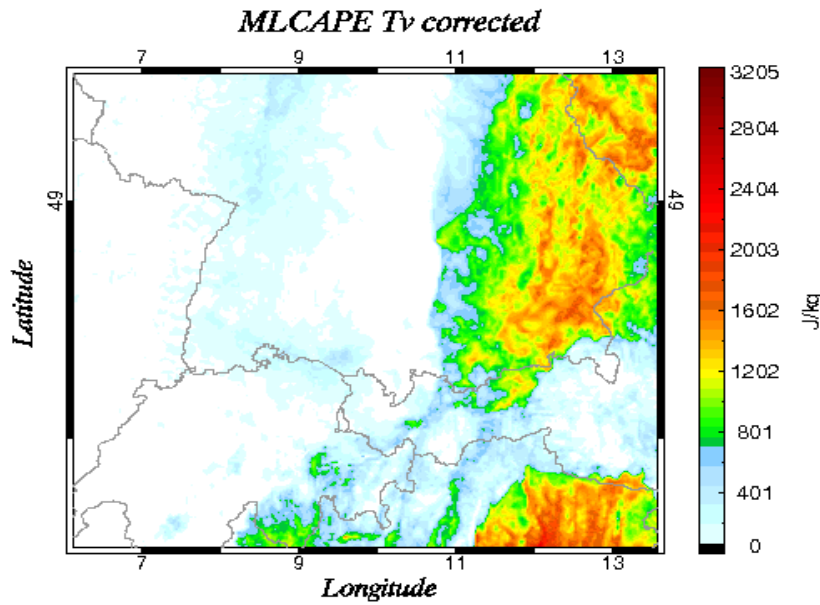


**Figure 4.8:** MLCAPE at 1500 UTC.

The high resolution model did a good job in respect of forecasting the strength and track of the bow echo. In Fig. 4.7 a), a composite image of the POLDIRAD and the COSMO-DE forecast at 15 UTC was presented as an example. The background features the 1510 UTC PPI image with the COSMO-DE radar output overlaid. The values for the COSMO-DE output were cut-off at 40 dBZ. We now refer to the bow echo in COSMO-DE as *COSMO-bow*. The model performed well in the development of an intense convective line ahead of a more stratiform precipitation region. Especially the southern part of the COSMO-bow was captured with model and real time data showing reflectivity peaks in excess of 60 dBZ and a good overlap in both data. Also the dimensions of this bow were quite similar with COSMO exaggerating somewhat. Further north, COSMO-DE was too fast with the forward propagating bow echo and produced too high reflectivity values over an too broad area. One has to keep in mind that there is a 10 min delay between both sources, which increases overlap between the model and the radar data. Next to placement and timing, it looks like COSMO also recognized the physical nature of this bow as the COSMO-bow resembled a bow-shaped feature for a few images (not shown). COSMO-DE produced another area of strong reflectivities behind the bow echo over far western Switzerland, which was the result of the approaching cold front. Despite some exaggeration in reflectivity peaks, a mixture of showers, thunderstorms and stratiform rain indeed occurred over that area. However, the model had problems in resolving the thunderstorm activity south and east of the bow echo (e.g. the Alps), where isolated thunderstorms evolved. The reason for that was probably the missing forcing, like the cold front further west, so the crucial ingredients for thunderstorm

initiation were not resolved in COSMO-DE, like the complex topography and local wind systems.

How well the bow echo was resolved in COSMO-DE can be recognized by the impressive low-level shear, seen in Fig. 4.7 b). The background color shows the strength of the 0-1 km speed shear with wind barbs, featuring the speed shear throughout the 1 km, 3 km and 6 km layers with red, green and blue colors respectively at 15 UTC. COSMO-DE produced a swath of intense speed shear, up to  $30 \text{ m s}^{-1}$  in the lowest 1000 m AGL. 0-3 km shear even increased to  $35 \text{ m s}^{-1}$  at 700 hPa (not shown), so a combination of extreme shear and a strong cold pool ought to have resulted in this rapidly eastward moving bow echo. As mentioned above, surface wind gusts exceeded  $30\text{-}35 \text{ m s}^{-1}$  during that time. This is in line with real time measurements of the POLDIRAD with roughly  $30 \text{ m s}^{-1}$  throughout the lowest 2 km. In Fig. 4.8, the degree of instability of the air mass ahead of the bow is sketched. As it was the case in the surface maps (Fig. 4.2), the degree of instability was not unusual with MLCAPE values of  $500 - 1000 \text{ J kg}^{-1}$ . In addition, the persistent inflow from the east ahead of this bow echo with values of roughly  $5 \text{ m s}^{-1}$  also did not reveal a large amount of instability and helicity with non existent 0-3 km CAPE and SRH-1 values. This is in line with the cold season (high shear, low CAPE) case, which was classified in the United States. There, cold season cases have CAPE on the order of  $500 - 2000 \text{ J kg}^{-1}$  and strong shear, for example up to  $30 \text{ m s}^{-1}$  at 850 hPa. This fits perfectly with this case. Another striking feature in those cold season bow echo events in the United States was a dry and potentially colder air mass at roughly 3-7 km. Implicated in the downward sinking mid-level RIJ, evaporative cooling causes the downward momentum to increase and hence strengthens the RIJ. COSMO-DE indeed had a layer of dry air with RH values of 30 - 40 % between 4-6 km (not shown) with a decrease of potential temperatures bounded by 70 - 100% RH. In Fig. 4.4 c) and in following scans, the stratiform precipitation area behind the bow echo had a vertical extent of 3-7 km, descending next to the leading line of deep moist convection. Velocity data in the RHIs revealed that the RIJ originated probably around 5 km above ground, although some uncertainty exists due to rapid deterioration of the quality of the radar beam during the passage of the rain and hail core. So next to the extensive stratiform precipitation area with strong cold pool development, also mid-layer dryness seemed to assist in the development of an intense RIJ.

### 4.3.2 3 August 2008: F4 tornado in Hautmont, France

#### 4.3.2.1 Overview

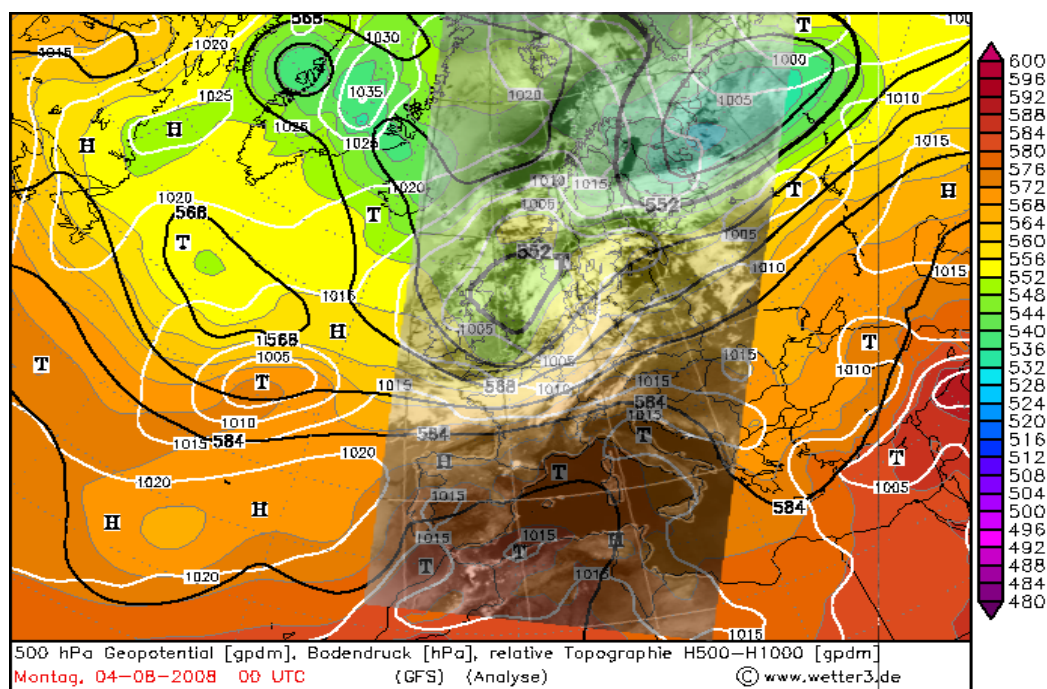
A rapid alternation of eastward moving troughs and ridges, affected west and north-west Europe during that period. On 3 August 2008, another trough approached from the Atlantic late that day and crossed N-France during the night hours. Around 2030 UTC that day, a violent tornado developed along the eastward moving cold front and struck the community of Hautmont and Mauberge. This tornado was rated as an F4 tornado on the hexamorous tornado list with wind speeds probably exceeding  $90 \text{ m s}^{-1}$ . The tornado itself caused 3 fatalities and 18 casualties with more than 700 homes left damaged. No further severe thunderstorm report was received on ESWD over northeast France during that night.

#### 4.3.2.2 Synoptic-scale overview and mesoscale discussion

The weather pattern was characterized by a far southward expanding polar vortex, which can be seen in Fig. 4.9 a). An eastward rotating upper trough reached the western English Channel at around 18 UTC and northeastern France just around midnight. The shortwave quickly moved eastward. So there was not much time left for a more robust warm air advection to get established over France and hence at least no pronounced moisture advection was possible during the previous hours. This can be also seen in Fig. 4.9 b) as mid-level lapse rates over east and northeast France were marginal ahead of the front, which was positioned just to the north of the lapse rate minimum. No EML was able to get advected ahead of the trough and remained over far southern France and Spain (not shown). This was an important point during that event due to limited potential instability release as a result of the weak lapse rates.

The passage of the trough was accompanied by an active cold front, which was situated over northern France shortly after the tornado occurred (2035 UTC), which can be seen in Fig. 4.10. Comparing the alignment of the front with the background flow, for example in Fig. 4.9 b), one is aware of the nearly parallel alignment which causes the front to slow down due to a weaker advective component of the postfrontal (a cold one in this case) air mass. Despite slow forward propagation, intense shear at all levels caused the active convective line to take over a 'broken' structure, similar to an LEWP (sec. 3.2.3). The air mass ahead of this cold front featured surface dewpoints in the mid to upper tens ( $^{\circ}\text{C}$ ) but the troposphere was warm and moist with weak lapse rates at all levels. This caused instability release to be on the weaker side. The 00 UTC soundings from Trappes and Idar-Oberstein (position marked by white arrows) in the prefrontal air mass caught this nicely. It is important to note that deep convection cannot be ruled out as either forcing or a regional more moist





### 2-4km lapse rates, wind and geopotential heights (300hPa)

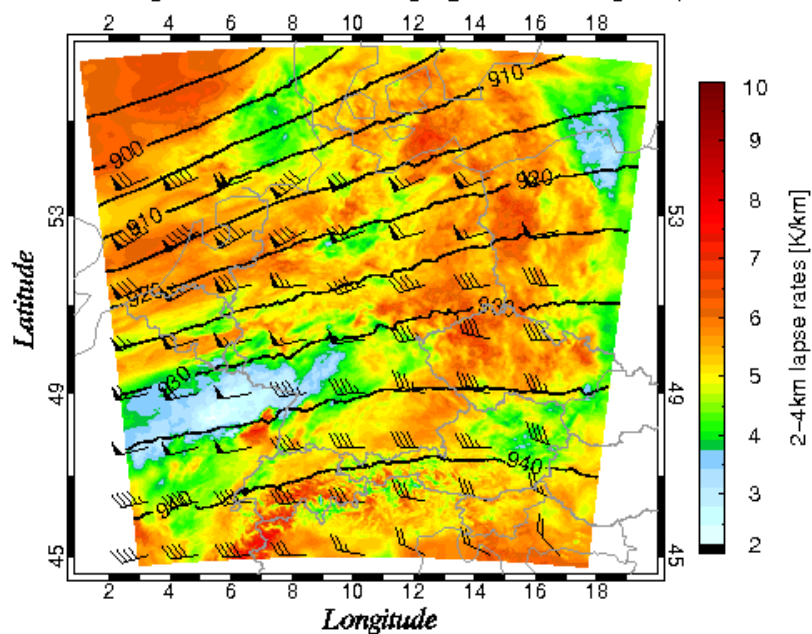


**Figure 4.9:** A composite image is prepared in a), where the 0152 UTC, 04 August 2008 thermal infra-red channel is combined with the GFS analysis of 500hPa (gpdm, black line), relative topography (gpdm, colored) and surface pressure (hPa, white line) (00 UTC, 04 August 2008). The source for the satellite data is *Dundee* and for the meteorological parameters *wetter3.de*. In b), the 300hPa geopotential height (gpdm), the wind at 300 hPa (black barbs) and the 2-4 km lapse rates (background color) are shown (COSMO-DE).

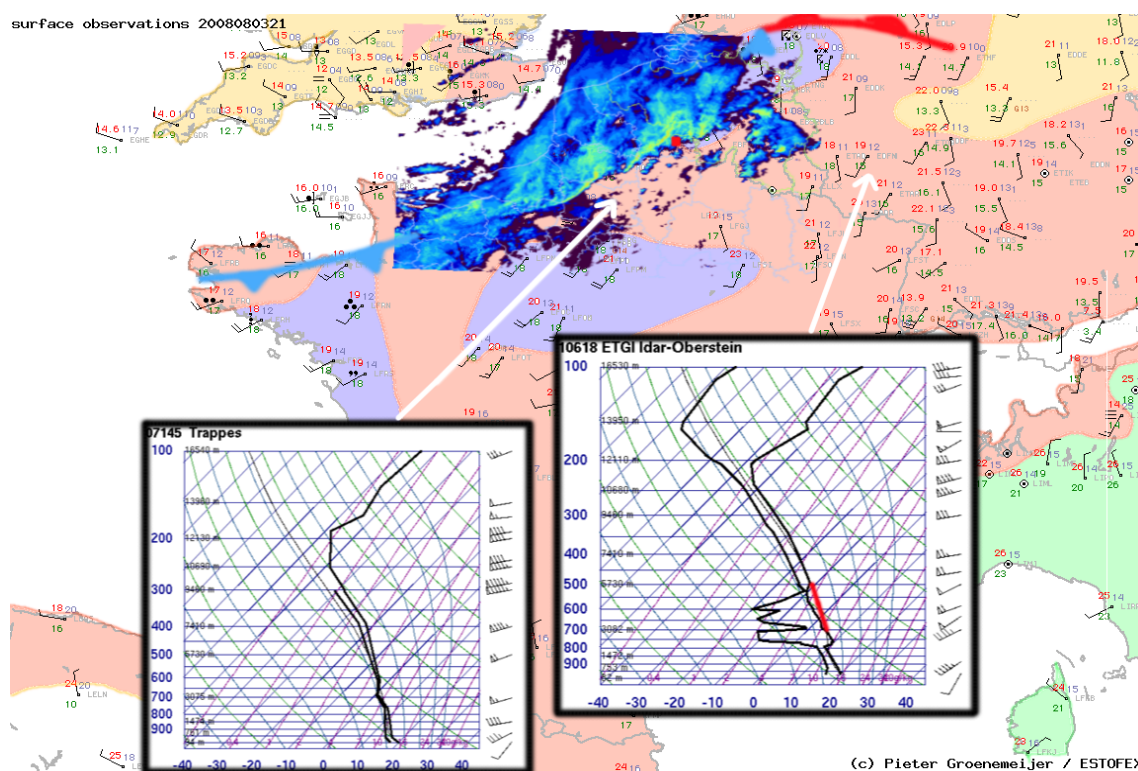
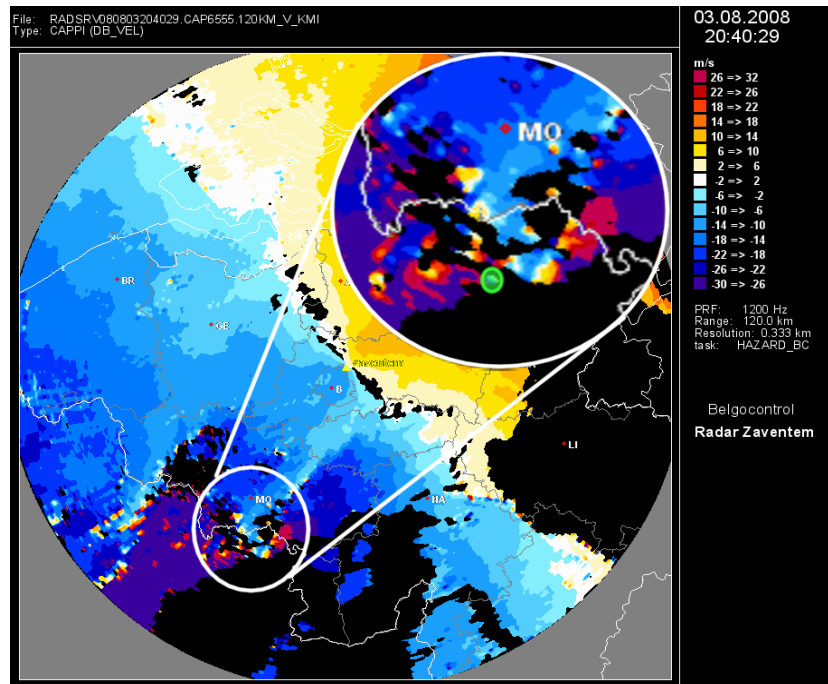


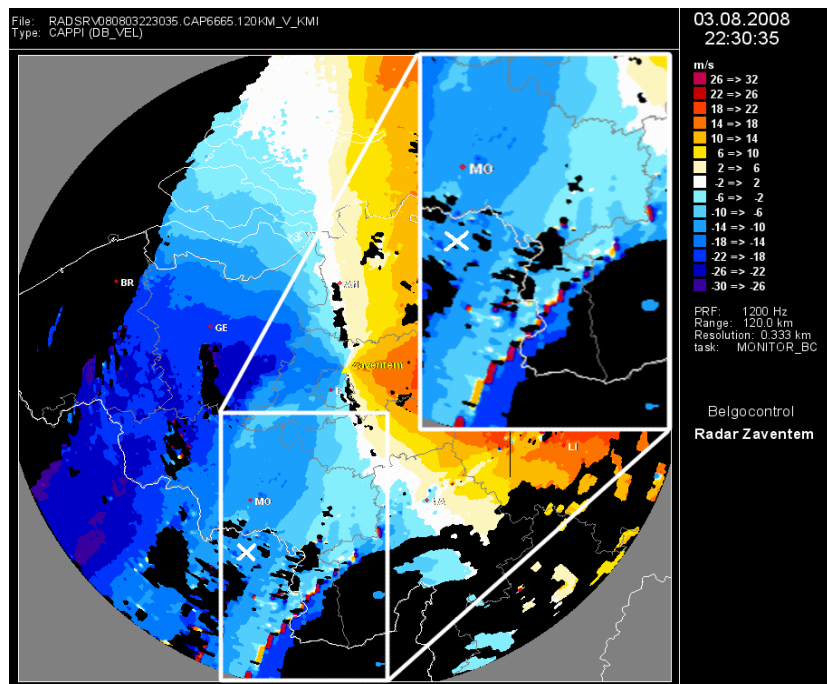
**Figure 4.10:** The colored background of this composite image features the surface dew-point distribution (11-14°C yellow, 14-17°C red, 17-20°C purple and 20-23°C green; reference: Pieter Groenemeijer ([www.estofex.org](http://www.estofex.org))), the 00 UTC sounding data from Wyoming and a 21 UTC radar image from Météo France in courtesy of KERAUNOS. The red 'dot' marks the position of Hautmont.

and warmer air mass could cause parcels to penetrate far into the troposphere, probably as high as 10-12 km. Speed and directional shear were strong, so any updraft, which would be able to manage to withstand the shear and entrainment of environmental air had a good chance to produce all facets of severe thunderstorm reports, including tornadoes and severe wind gusts.



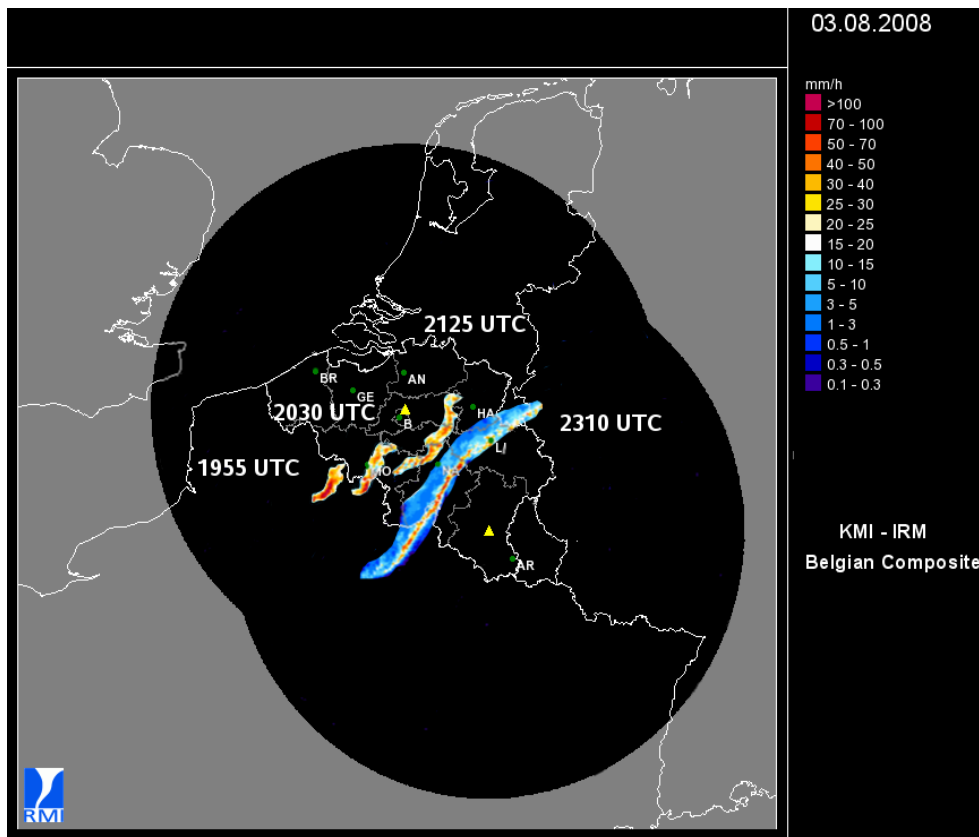


(a) Radial velocity data at 2040 UTC



(b) Radial velocity data at 2230 UTC

**Figure 4.11:** CAPPI radial velocity images at 1.5 km for a) 2040 UTC and b) 2230 UTC respectively ((c)Belgocontrol/RMI). The maximum range of the radar is 120 km. Hautmont is marked with a green circle in a) (south of Mons (MO)) and with a white cross in b).



(a) CAPPI at 1.5 km

**Figure 4.12:** A composite of radar reflectivity data is shown at 1955 UTC, 2030 UTC, 2125 UTC and 2310 UTC with the focus on the thunderstorm, which produced the Hautmont tornado ((c)Belgocontrol/RMI).

In Fig. 4.11 a), the velocity product of the radar 'Zaventem' is shown only minutes after the violent tornado struck the town. The location of Hautmont is marked by a green circle in the zoomed region and the radar is placed to the northeast. The data is a bit noisy due to velocity aliasing but the rotation can be seen better in Fig. 4.13 a), Fig. 4.13 b), Fig. 4.13 c) and Fig. 4.13 d), where the data were filtered. A strong in- and outbound couplet appears, which persists for 15 minutes before starting to weaken gradually east of Hautmont. The track of this thunderstorm cell was composed in Fig. 4.12. The tornadic thunderstorm developed along the southern fringe of the line as it moved further to the east. Between 2230 UTC and 2330 UTC, an elongated line of enhanced convection was evident on radar images, which is also shown in Fig. 4.11 b).

To prove that the conditions were favorable for updrafts to rapidly organize, the most important parameters of that day will be presented. All images are zoomed into the area of interest over northeast France. The surface front has just crossed Hautmont and hence can be tracked just to the southeast of Hautmont (red cross).

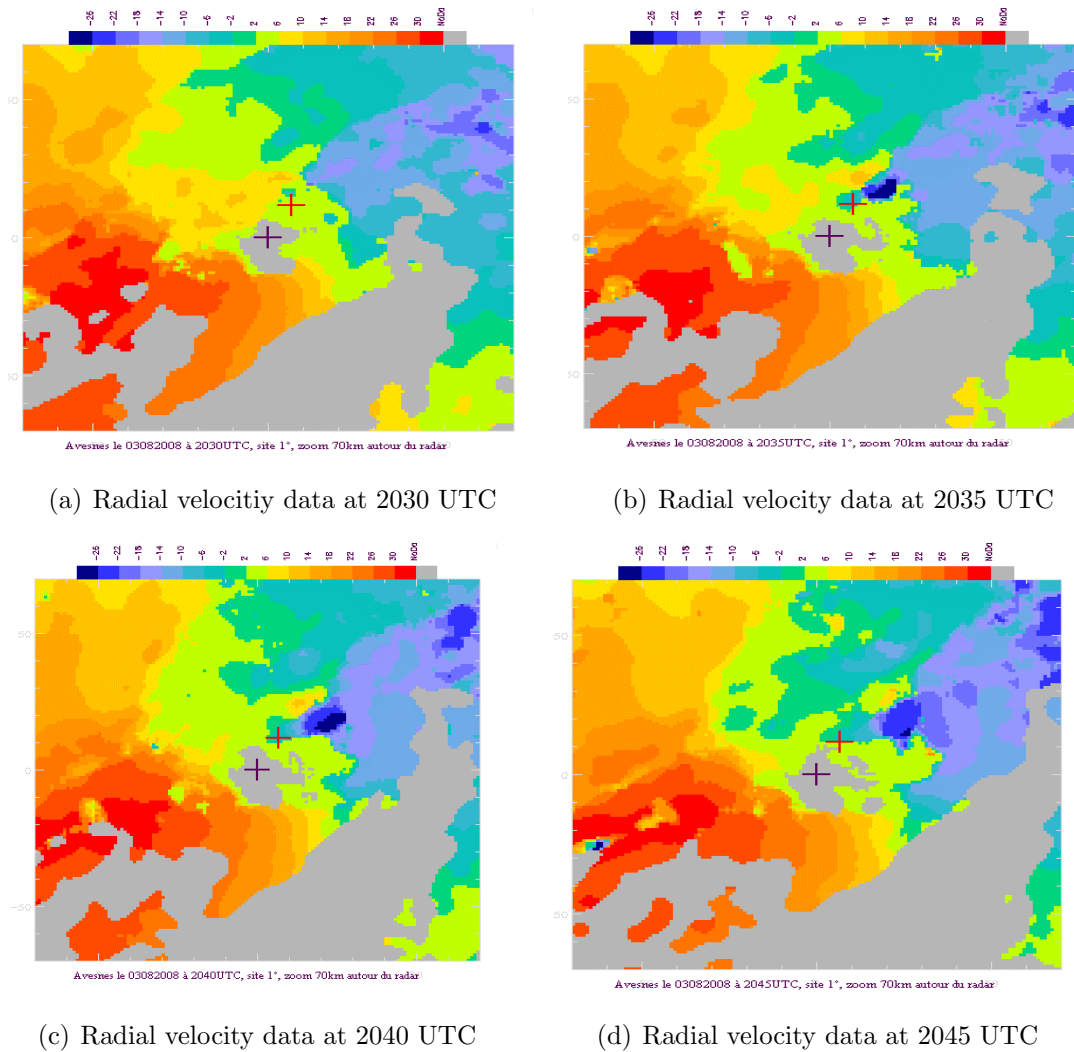


**Figure 4.13:** Radial velocity data from the radar at Avesnes (black cross) with the location Hautmont sketched with a red cross. The distance between the radar and Hautmont is roughly 16 km. Adopted from Lorandel and Dupuy (2008)

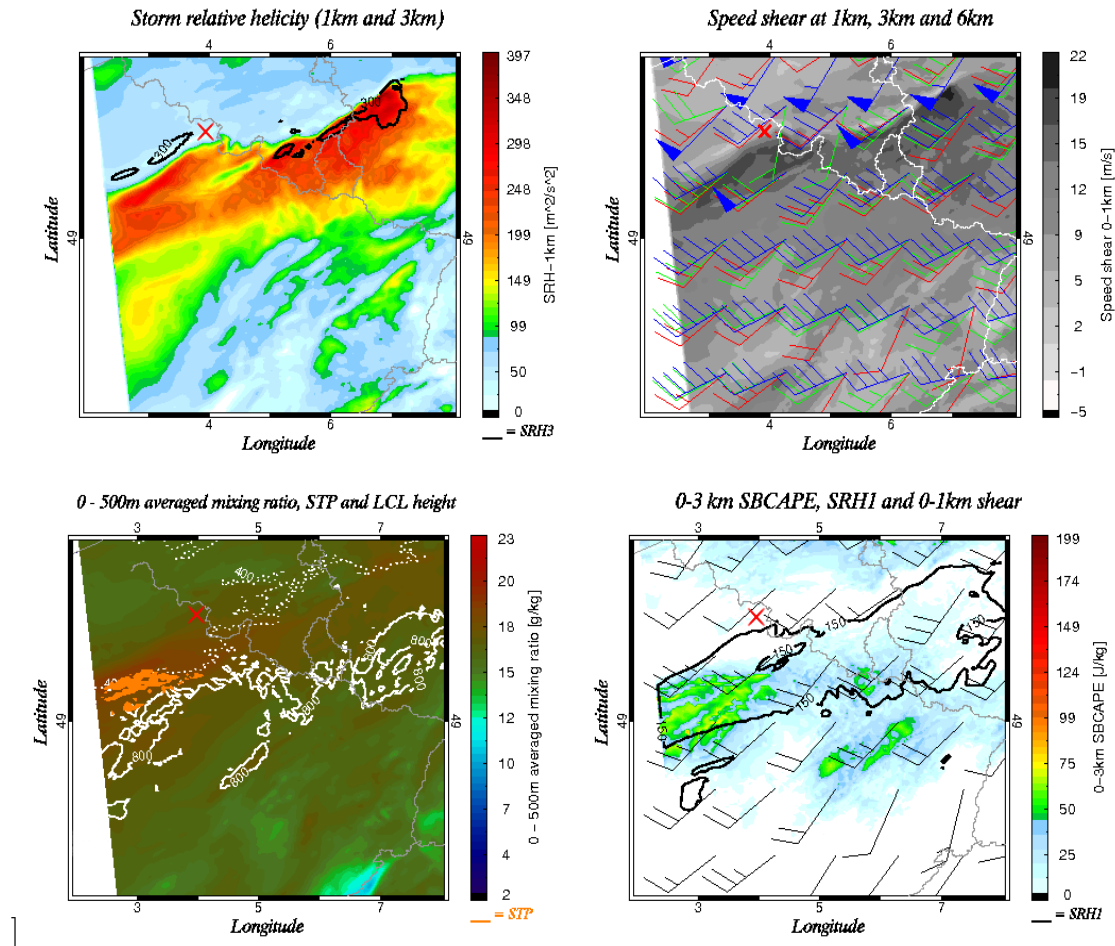


**Figure 4.14:** a) presents the directional shear between 0-1 km (color) and 0-3 km (black line), whereas in b) the speed shear components at three different levels are composed (0-1 km as background color, 0-1 km wind barb in red, 0-3 km wind barb in green and 0-6 km wind barb in blue). The main ingredients for tornado forecasting are sketched in c) and d). In addition, white lines (dotted and continuous) represent the LCL height at 400 m and 800 m respectively (c)) and the black line in d) is the storm relative helicity between 0-1 km ( $150 \text{ m}^2 \text{ s}^{-2}$ ). The town 'Hautmont' is marked by a red cross. The COSMO-DE run at 21 UTC was used, with the tornado event only 30 min prior.

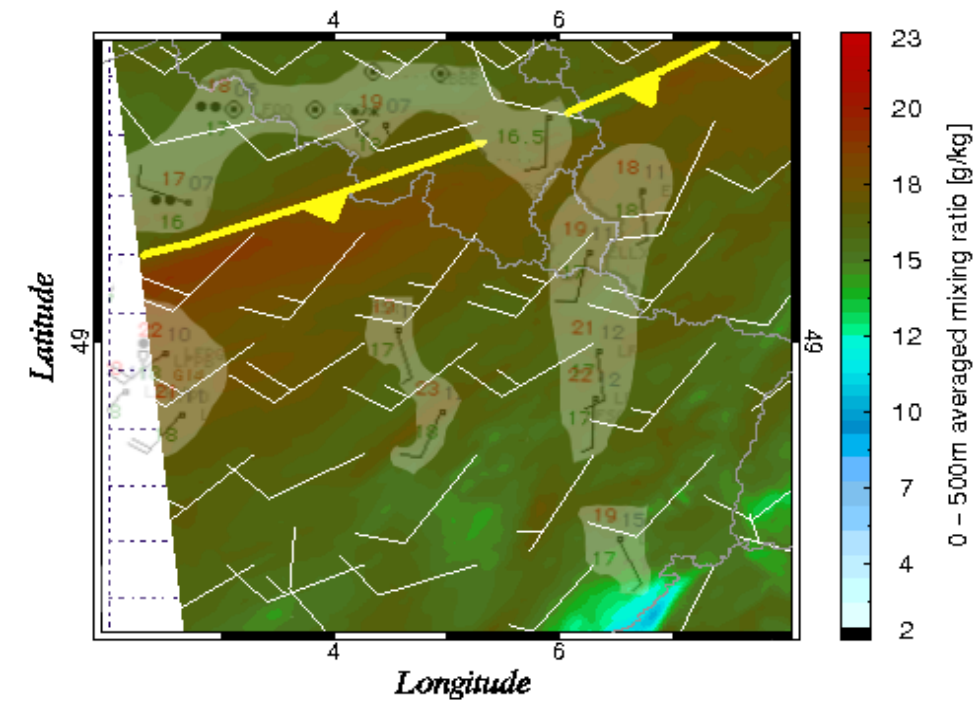
Fig. 4.14 a) depicts the directional shear in two different levels. The SRH1 parameter has a magnitude of more than  $300 \text{ m}^2 \text{ s}^{-2}$ , which is enough for strong tornadoes (in the United States,  $100 \text{ m}^2 \text{ s}^{-2}$  is considered as a threshold for an augmented tornado risk), so any thunderstorm, which would be able to develop would have experienced a huge amount of helical inflow, supportive for low-level mesocyclone generation (Thompson et al. (2006) and the Storm Prediction Center, <http://www.spc.noaa.gov/>). The SRH3 was overlaid as a black line where only magnitudes greater  $300 \text{ m}^2 \text{ s}^{-2}$  were displayed. This threshold was used due to publications from the United States, where  $250\text{-}300 \text{ m}^2 \text{ s}^{-2}$  are the magnitude, where probabilities for mid-level rotation and hence supercell development are high (Thompson et al. (2003) and the Storm Prediction Center, <http://www.spc.noaa.gov/>). A perfect overlap co-exists over N-Luxembourg and south Belgium, with another maximum further west over northeastern France. It is interesting to see those maxima in helicity, which overlap with the line segments of the LEWP-type cold front (Fig. 4.10), so each of those line segments was accompanied by a local maximum of directional shear; at least in COSMO-DE. Comparing the dBZ output of COSMO-DE and excluding dBZ values less than 40 dBZ, the high resolution model indeed develops a wavy line of deep convection with directional shear maxima along the outward bulging parts of that convective line (not shown). The same for the speed shear in Fig. 4.14 b) with  $20 \text{ m s}^{-1}$  0-1 km speed shear in the immediate prefrontal environment. Again,  $10 \text{ m s}^{-1}$  speed shear in the lowest 1000 m is a threshold values in the United States for supercell tornado development (Miller (2006) and the Storm Prediction Center, <http://www.spc.noaa.gov/>). In Fig. 4.14 c) and Fig. 4.14 d) the main ingredients for tornado forecasting are outlined. The STP (refer to sec. 3.3.4.3) is highlighted in orange with the 400 m and 800 m LCL height contours in dotted and thick, white lines, respectively. Convergence along fronts causes an effect, called *moisture pooling*, where dewpoints and the depth of the moist boundary layer locally increase. This can be seen by a noticeable increase of the 500 m mixed mixing ratios along this cold front. When we keep in mind that 00 UTC soundings in this air mass either need some surface heating or low-level moisture increase for the potential initiation of deep moist convection it sounds reasonable why any developing convection would be confined to the cold front itself. The LCL gradient, typical for cold fronts, was aligned parallel to the front, with 800 m LCL heights in the prefrontal environment and 400 m along the favorable tongue of higher mixing ratios. LCLs even further decreased over Hautmont. In Fig. 4.14 d) the effect of the moisture pooling along the front can be seen. The 0-3 km surface based CAPE was used since the air mass was well mixed with no low-level inversion present below 750 hPa. The 0-3 km level is crucial for tornadogenesis in low-CAPE environments due to rapid stretching of high helical inflow beneath developing updrafts. As seen

in Trappes 00Z and Fig. 4.14 d), the local increase of the BL moisture was already sufficient for some low-level CAPE in the order of  $50 - 100 \text{ J kg}^{-1}$ . This is adequate for an augmented tornado risk. This zone of better low-level instability overlapped nicely with intense shear (SRH1 well above  $150 \text{ m}^2 \text{ s}^{-2}$  and strong low-level speed shear). Finally, one parameter was calculated, which is composed of all those values like LCL, CAPE and shear: It is the STP (section 3.3.4.3), highlighted in orange colors in Fig. 4.14 c). This proves that COSMO-DE indeed created an environment, favorable for tornadoes along the cold front due to intense shear, low LCLs and regionally enhanced low-level CAPE.

#### 4.3.2.3 COSMO-DE performance

COSMO-DE again did a great performance in forecasting the regional supportive environment for tornadoes. Whereas for example global forecast models like the GFS (convection parameterized) developed a brought area with  $50\text{-}100 \text{ J kg}^{-1}$  all over the place, COSMO-DE indeed captured the small-scale effects ahead of the cold front, which assisted in the development of the LL-CAPE tongue. Otherwise, this mesoscale-model produced only traces of SBCAPE ahead and behind the cold front. As mentioned above, the dBZ output of this model also developed a line of enhanced convection along the cold front with dBZ values greater 40 dBZ (not shown). Even the wavy and broken structure of this line was detected, which in general is the case in very strong shear environments with high helicity values. Each of those 'bulges' in the line was accompanied by a local shear maximum as LL wind field backed during their passage. COSMO-DE however is not yet able to resolve those broken lines correctly regarding their position, probably due to the subgrid-scale effects and overall short length of those features. This also had effects on the accurate position of the front, as COSMO-DE locally placed the cold front too far to the southeast compared to real time data. This is visualized in Fig. 4.15 a), where the position of the cold front was sketched with the yellow line. It has to be noted that the position was mainly drawn along the maximized zone of LL moisture and the convergent flow in the 950 hPa wind field. Overlaid on this data, surface synoptic data from 21 UTC was included, which indicates that COSMO-DE was a bit too fast with the forward propagating cold front over Belgium, but it placed the front well further west over northeast France. It is important to know how well the mesoscale model handles the boundary layer due to the importance for instability release. Hence in Fig. 4.15 b), the LCL height was compared between COSMO-DE (background color) and the LCL calculated from synoptic reports at 21 UTC. The white line sketches the position of the cold front. The sharp drop of the LCL heights from 300-600 m ahead of the cold front to 100 - 200 m in the postfrontal air mass was handled well by the mesoscale model with LCL heights below 200 m also in the strongly sheared

*500m mixing ratio, SBCAPE Tv corrected and 950hPa wind*



*Height of the LCL*

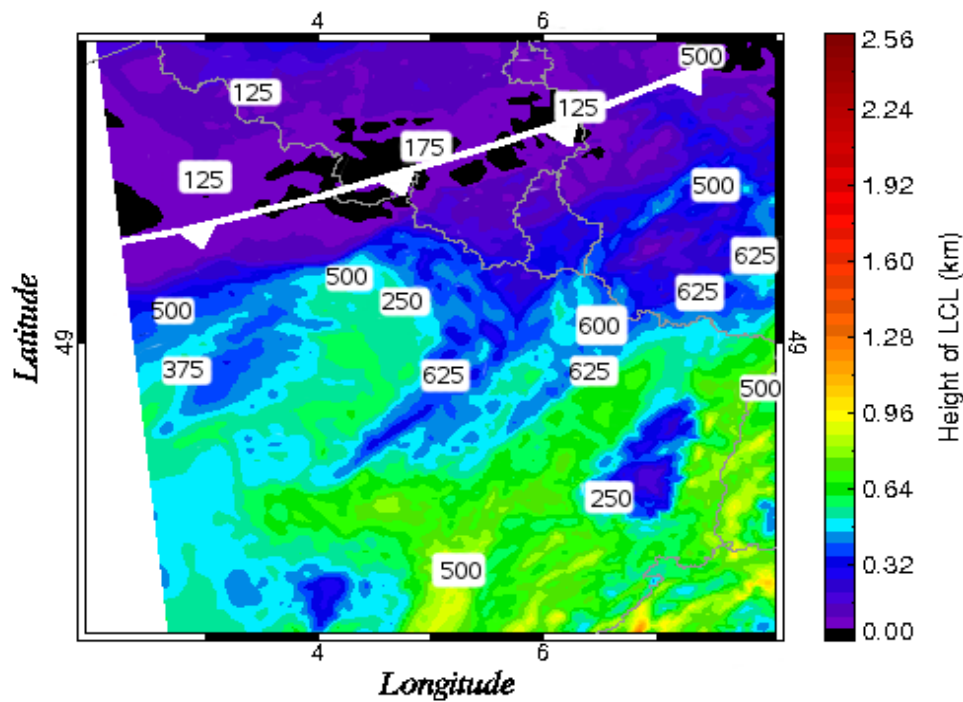


**Figure 4.15:** a) COSMO-DE 500 m mixed mixing ratios (color) and wind field at 950 hPa (COSMO-DE) and combined with observations at the surface (at 21 UTC) ([www.estofex.org](http://www.estofex.org)). The yellow line marks the cold front. b) The background color is the LCL (km AGL) of COSMO-DE. The big numbers are the LCL (m AGL) computed from surface temperature and dewpoint measurements. The white line is the cold front position. All data at 21 UTC.

and unstable part of the cold front.

It can be summarized that COSMO-DE was able to resolve the components, which finally caused the development of this violent tornado.

### **4.3.3 15 August 2008: Regional tornado outbreak, Poland**

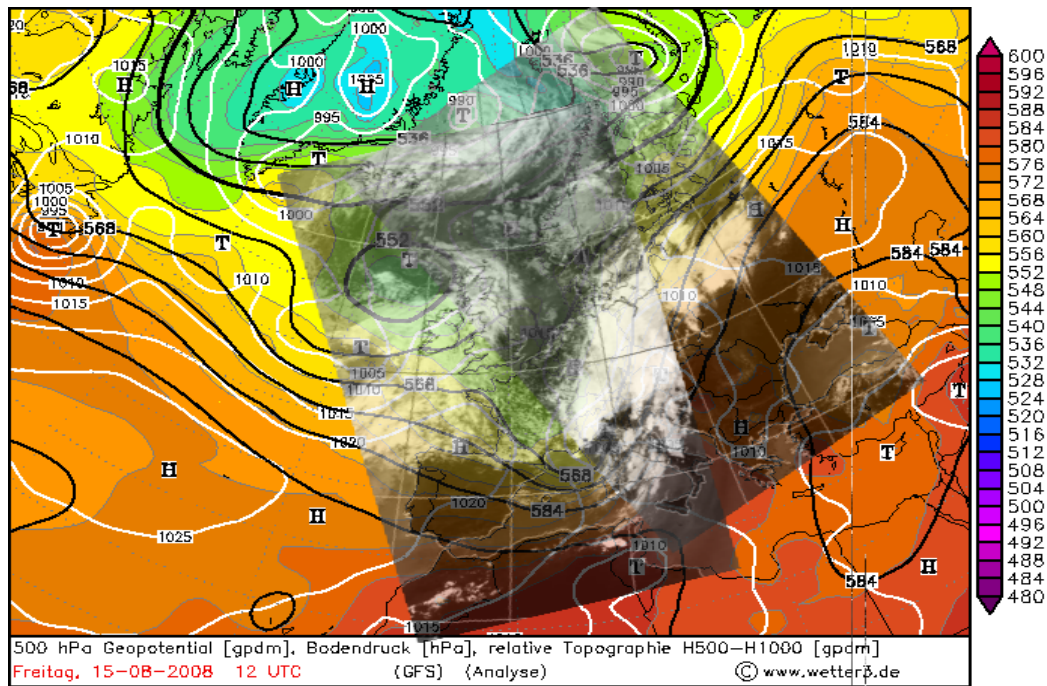
#### **4.3.3.1 Overview**

Unlike the Hautmont case, where conditions for tornadogenesis were not clear even a few hours ahead of the event, the environment was very conducive for an outbreak of organized thunderstorms over a broad swath, running from north Italy all the way to Poland. In the course of that, 8 people lost their lives, 3 in Poland, 2 in Slovakia, 2 in Italy and 1 person in Austria. This event was remarkable due to the intensity, the huge extent and numerous waves in which organized thunderstorms evolved. Extremely large hail was reported already in the early morning hours over extreme south Poland, where hail of 5-9 cm in diameter produced damage with unconfirmed reports of hail near 15 cm in diameter. In the early afternoon hours, another and more serious round of supercells developed over southern Poland and moved northeastwards. Numerous tornadoes occurred with at least one strong tornado. Large hail up to 5 cm in diameter and severe wind gusts afflicted south, central and northeast Poland well into the night. Other parts of Europe also experienced severe weather as for example a line of high precipitation supercells over Slovenia organized into a powerful bow echo during the evening and night hours. This bow caused severe non-tornadic wind damage across Slovenia, west Hungary, east Austria and southwest Slovakia. Large hail and flash flooding also caused damage over those areas. Below the focus is shifted to the tornado outbreak in south Poland as environmental parameters were supportive in containing the region of highest tornado probabilities.

#### **4.3.3.2 Synoptic-scale overview and mesoscale discussion**

As it was the case in the Hautmont case, the weather pattern featured a far southward extended polar front jet with numerous embedded disturbances. A branch of the polar vortex covered the North Atlantic with a constant development of upper-level troughs along its fringes. The set-up of this day was a characteristic one as one of those troughs evolved over extreme northwestern Europe on 14 August 2008. This dynamic and sharp upper-level trough swung rapidly eastwards and crossed France, Germany and the Alps during a 24 h period. In Fig. 4.16 a) two thermal infrared satellite images are merged. The satellite image to the east was prepared roughly 2 hours earlier than the one to the west. The broad upper-level trough, already situated over eastern France at 12 UTC, can be recognized by its expan-





### 2-4km lapse rates, wind and geopotential heights (300hPa)

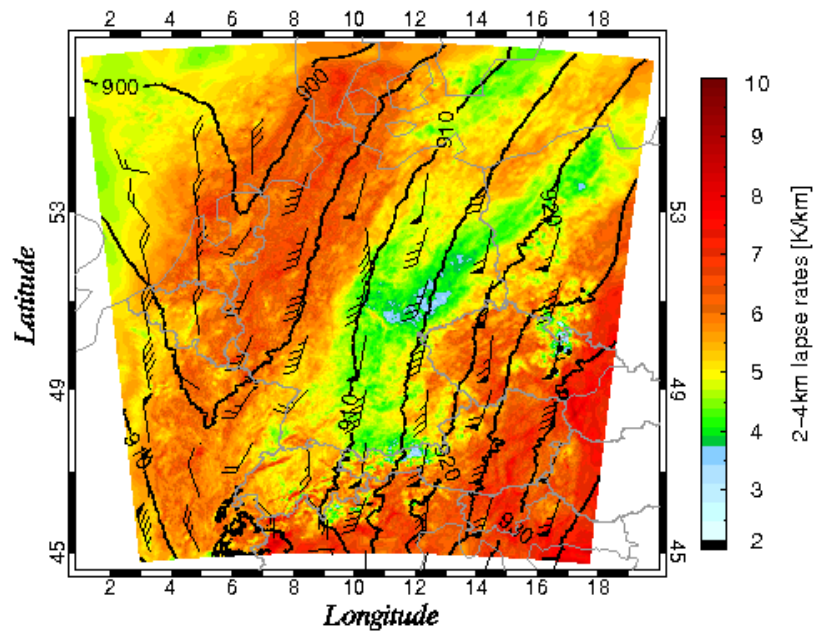


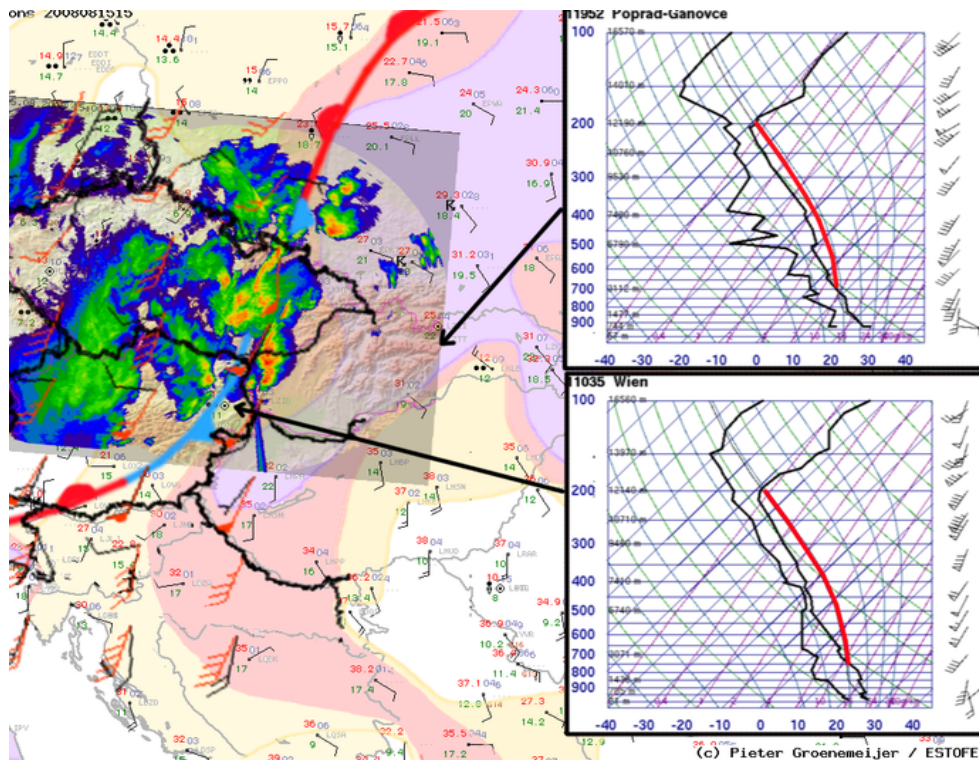
**Figure 4.16:** The synoptic overview in a) is sketched with the 500 geopotential height (gpm) as black lines, the white lines the surface pressure (hPa) and the relative geography of 500-1000 hPa as background color (source: wetter3, 12 UTC). Two thermal infrared images are overlaid at 1132 UTC and 1313 UTC respectively. In b) the 300 hPa geopotential heights [black lines], the wind field at 300 hPa (black wind barbs) and the 2-4 km lapse rates (background color) are composed (COSMO-DE, 15 UTC).

sive warm conveyor belt<sup>1</sup> over the Alps, Germany, Poland and the Czech Republic and the broken and diurnal driven convection in the infiltrating cold air mass over France. The area of most concern is situated at the eastern fringe of the upper trough, where warm, moist air and strong shear at all levels overlap. In Fig. 4.16 b), parts of central Europe are zoomed out with the geopotential heights and wind field at 300 hPa and the mid-level lapse rates overlaid. At 15 UTC, the center of the trough was still over eastern France with numerous short-waves ejecting out of the base of the trough with a strong one entering southwest Poland from the southwest. For this time of year, the wind field is fairly strong with a 35-45 m s<sup>-1</sup> wind speed maximum rounding the base of the trough with higher winds along its tip (not shown). The different types of air mass can be seen from mid-level lapse rates. Over eastern Austria, Slovenia, Hungary, Slovakia and southern Poland, steep 2-4 km lapse rates represent the far northward protruding EML. To the west of the frontal zone (Fig. 4.17), affecting northwest Poland and east, southeast Germany, a cool and stable air mass is present with lapse rates approaching a moist adiabatic ascent due to the more stratiform nature of the precipitation. Further west, the trough axis draws near and lapse rate again become steeper as mid-levels cool down. It is quite common that the magnitude of those lapse rates is less than those measured in the EML.

In Fig. 4.17 the quality of the boundary layer but also the position of the surface front is sketched. The prefrontal air mass is very moist with surface dewpoints in the upper tens and lower twenties all the way up to Poland. Moisture had been advected from the warm Mediterranean for several days. The trough on 15 August finally caused a strong advection of that air mass well to the north. It is visible that the highest moisture content covers those areas, where tornadic thunderstorm are imminent or already occurring, namely southwest Poland. As mentioned above (Fig. 4.16 b)) differences between the air masses can be seen on the radar of the CHMI, too, where more stratiform and moderate radar echoes occur along the cold side of the surface front, with intense convection already present along its warm side. Both 12 UTC soundings sample the very unstable and strongly sheared air mass. Speed and directional wind shear in the low- and mid-levels of the troposphere favor organized thunderstorms with strong mid-/ and low-level rotation. MLCAPE is not excessively high, but in the range of 1000 J kg<sup>-1</sup>, which is adequate for strong updrafts, resisting the intense shear. The backed (easterly) wind field at the surface over southern Poland indicates that the intense directional shear at low-levels is still

---

<sup>1</sup>The warm conveyor belt feeds the extratropical cyclone with warm, moist air. This belt of warm air originates in the warm sector of the depression and flows poleward. The belt ascends as the air mass approaches the warm front before eventually turning anticyclonically into the upper-level jet.



(a) Surface map

**Figure 4.17:** A composite was prepared, showing the surface data from 1515 UTC (11-14°C yellow, 14-17°C red and 17-20°C purple; data in courtesy of Pieter Groenemeijer, ESTOFEX), the radar reflectivity data from radars Brdy and Skalky (CHMI) and the 12 UTC soundings from Wyoming. The red curve is the path of the ascending parcel. The enclosed area between the red curve and the temperature profile is the CAPE area. A short review about the diagram can be found at subsec. 3.3.2.1. Wind data from COSMO-DE are overlaid with black wind barbs representing the wind at 850 hPa and orange wind barbs at 500 hPa.

present 3 hours after the release of both soundings (Fig. 4.17). Using the COSMO-DE 500 hPa wind field and the 12 UTC soundings, both show wind speed maxima of  $25 \text{ m s}^{-1}$ , so hence no real change in the environmental wind field, which is in line with the global and high resolution models, which bring the wind speed maximum out of the base of the trough quite late (roughly 18 UTC).

As mentioned in the outline of that event, the first focus is the tornado outbreak over extreme southwest Poland between 1500 UTC - 1930 UTC with the most serious tornado occurring at roughly 15 UTC at (50.47 N, 18.37 E) (see ESWD entry). Hence, 15 UTC is used to calculate the severe thunderstorm parameters in COSMO-DE. It has to be noted that parts of that activity occur next to the border of the COSMO-DE domain so the the outer 15 to 20 grid points along the border of the domain have to be questioned or at least evaluated carefully (personal communication with Dr. Keil, DLR, 15 August 2009). However the main outbreak occurred far enough away from the boundary of COSMO-DE. In Fig. 4.18 a), the tornado, hail and funnel reports are included in diffuse red, green and white respectively. They do not give the exact position of each report (please refer to ESWD (<http://www.essl.org/ESWD/>) for that) but they rather indicate, in which region the severe events occurred. SRH1 is sketched with the background color and the  $300 \text{ m}^2 \text{ s}^{-2}$  SRH3 contour. The first thunderstorms developed between 1300 UTC and 1330 UTC over the eastern Czech Republic and organized rapidly with echo tops greater 10 km before 1400 UTC. However, the most dominant thunderstorm emerged out to the flat area of southwestern Poland from 1500 UTC onwards. COSMO-DE has SRH1 values in excess of  $300 \text{ m}^2 \text{ s}^{-2}$  with SRH3 values of  $500 - 1000 \text{ m}^2 \text{ s}^{-2}$ , which is in the range of 'extreme directional shear'. This environment remained in place also in the 16 UTC output of COSMO-DE (not shown). When keeping in mind that the tornado producing thunderstorm deviated from the 0-6 km bulk shear vector, SRH values may have peaked out higher than what was calculated by COSMO-DE. Nevertheless, those values are enough for mesocyclone development at mid-levels and later-on also at low-levels. The question, why the SRH1 drops off so quickly over Poland can be answered with the following approach:

- One should not concentrate on the magnitude of the SRH at local spots but keep the overall magnitude of the SRH over a certain region in mind. The parameter SRH is highly variable in nature as discussed in Markowski and Straka (1998)
- COSMO-DE had back-building thunderstorms along the cold front over east Czech Republic producing a sharp temperature and humidity gradient with a  $\theta_e$  difference of 20 K or more. This looks like to have also an influence in the

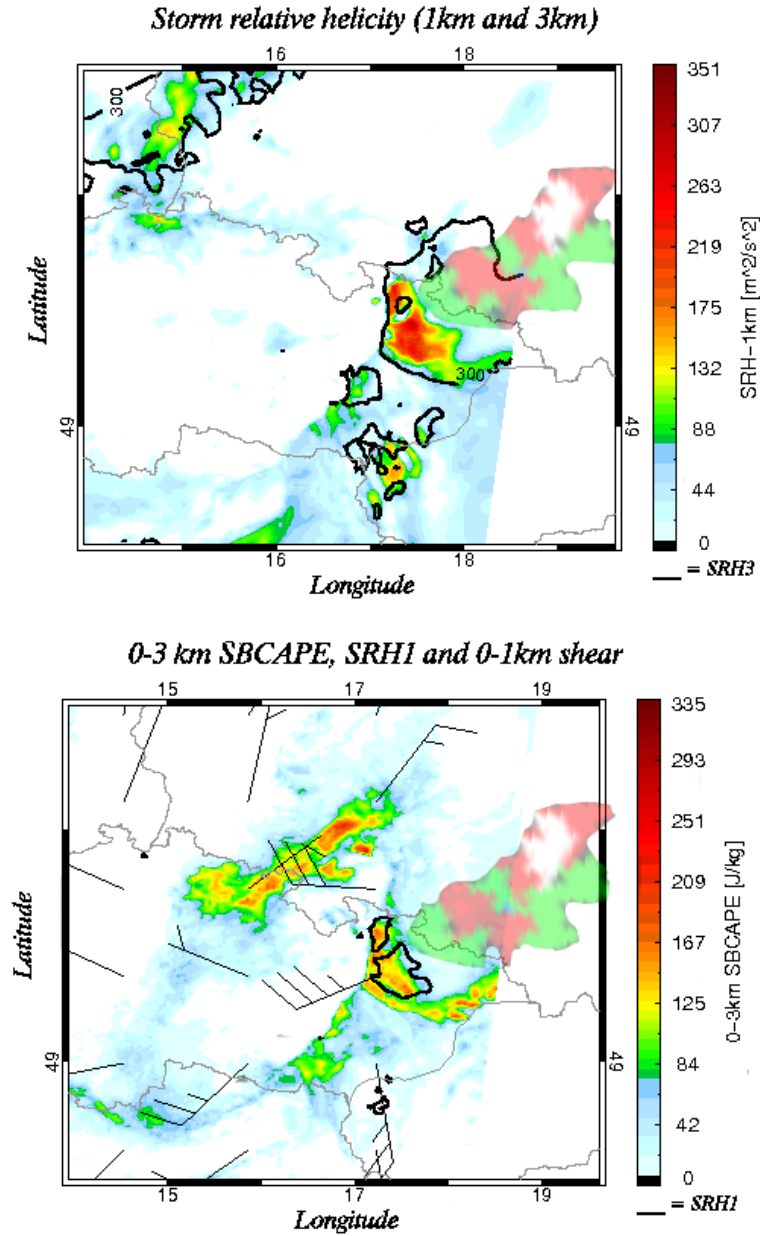


**Figure 4.18:** a) represents the storm relative helicity between 0-1 km (background color) and 0-3 km (black line equals  $300 m^2 s^{-2}$ ). The diffuse green, red and white region over Poland features the ESWD tornado (red), hail(green) and funnel(white) reports. In b), the background color depicts the 0-3 km SBCAPE, the wind barbs the 0-1 km shear and the black line storm relative helicity between 0-1 km (equals  $150 m^2 s^{-2}$ ). Diffuse colors again represent the ESWD data reports.



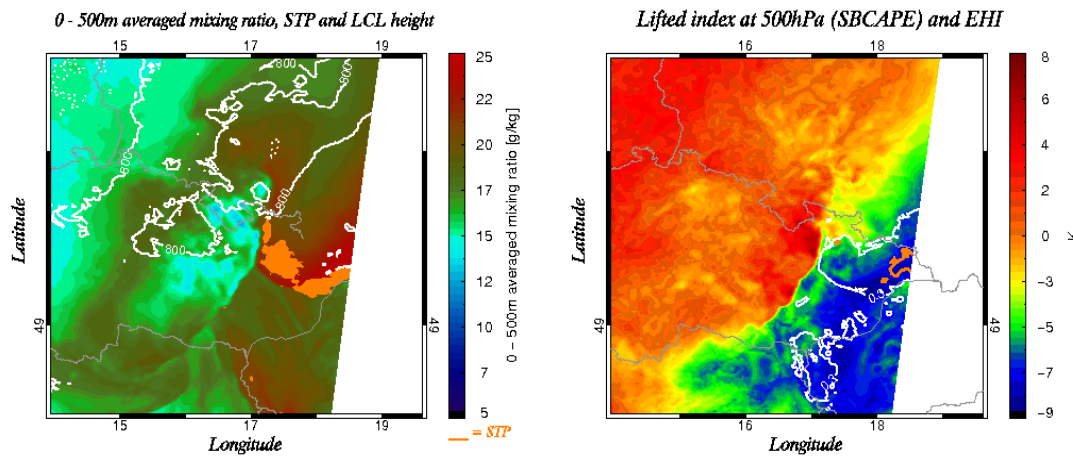


**Figure 4.19:** The boundary layer moisture is displayed with background colors in a), whereas the dotted and continuous white lines show the LCL at 400 m and 800 m respectively. The orange contour is the STP. Finally in b), the LI at 500 hPa is outlined with the white and orange lines showing the EHI with the magnitude of 0.3 and 0.6 respectively. All data from COSMO-DE at 15 UTC.

wind field with COSMO-DE increasing wind speeds at 950 hPa to more than  $30 \text{ m s}^{-1}$  with no real forward propagation of the front

Fig. 4.18 b) shows the surface based CAPE of the lowest 3 km, which is sketched in background colors with a magnitude of  $100 - 300 \text{ J kg}^{-1}$ . In addition, 0-1 km speed shear reaches  $15\text{-}25 \text{ m s}^{-1}$ , visualized by the wind barb. SRH1 was again used to indicate the very favorable low-level conditions for low-level rotation and tornadogenesis. Later-on, enhanced low-level CAPE spread out to the east and northeast, which further increased the favorable environment for tornadoes over south Poland. The quality of the boundary layer moisture is captured in Fig. 4.19 a), where the mixing ratio is shown as the background color. The very moist prefrontal air mass can be seen and also the sharp drop to lower values over the east-central Czech Republic as COSMO-DE constantly developed new thunderstorms along this boundary. This is supported by the 12 UTC soundings, where LCL heights were roughly 1000 m above ground and 800 m in COSMO-DE. The mesoscale model decreased LCL height over southwest Poland to 400 m, where tornadoes later evolved. Overlaid with orange contours, the STP is included, also supporting the idea of an augmented tornado chance with any thunderstorm in that area. In fact, STP regions of that extent and magnitude (peak values of 2 to 3) are not very often seen in Europe and therefore serve at least as an indication that an outbreak of tornadic thunderstorms is possible. Nevertheless, when using those combined parameters, one can already focus on the area with the highest possibilities for tornadoes due to the favorable shear and instability overlap. Other parameters, like the lifted index are useful in pinpointing

the general thunderstorm risk. In Fig. 4.19 b), the LI at 500 hPa, calculated from a sounding with SBCAPE, is plotted. The air mass, supportive for thunderstorms, can be seen with LI values of -7 to -9 over far eastern Czech Republic and in general east of the surface front. The EHI was overlaid to indicate the possibility how to confine such a broad area with the right parameters. The white line represents the EHI with 0.3 and the orange line with 0.6. The right use of the different parameters can therefore assist the forecaster in detecting the area of most concern in a shorter time.

Many hail reports were entered into the ESWD, so a short look on the hail pa-

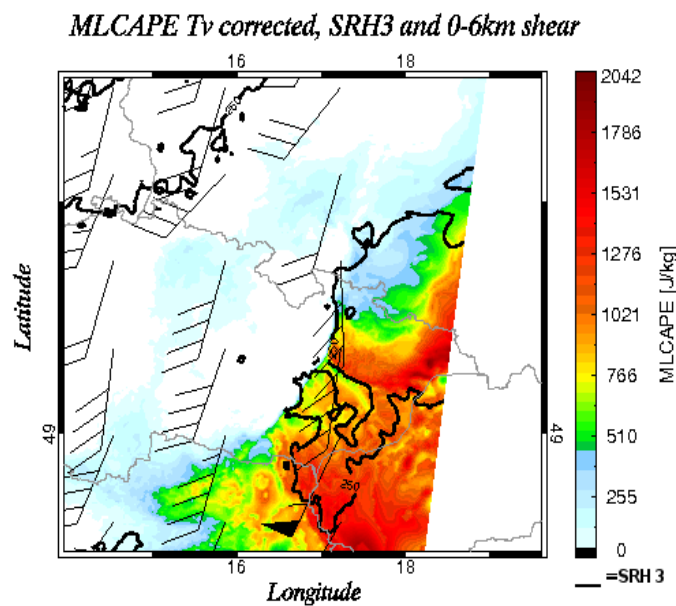
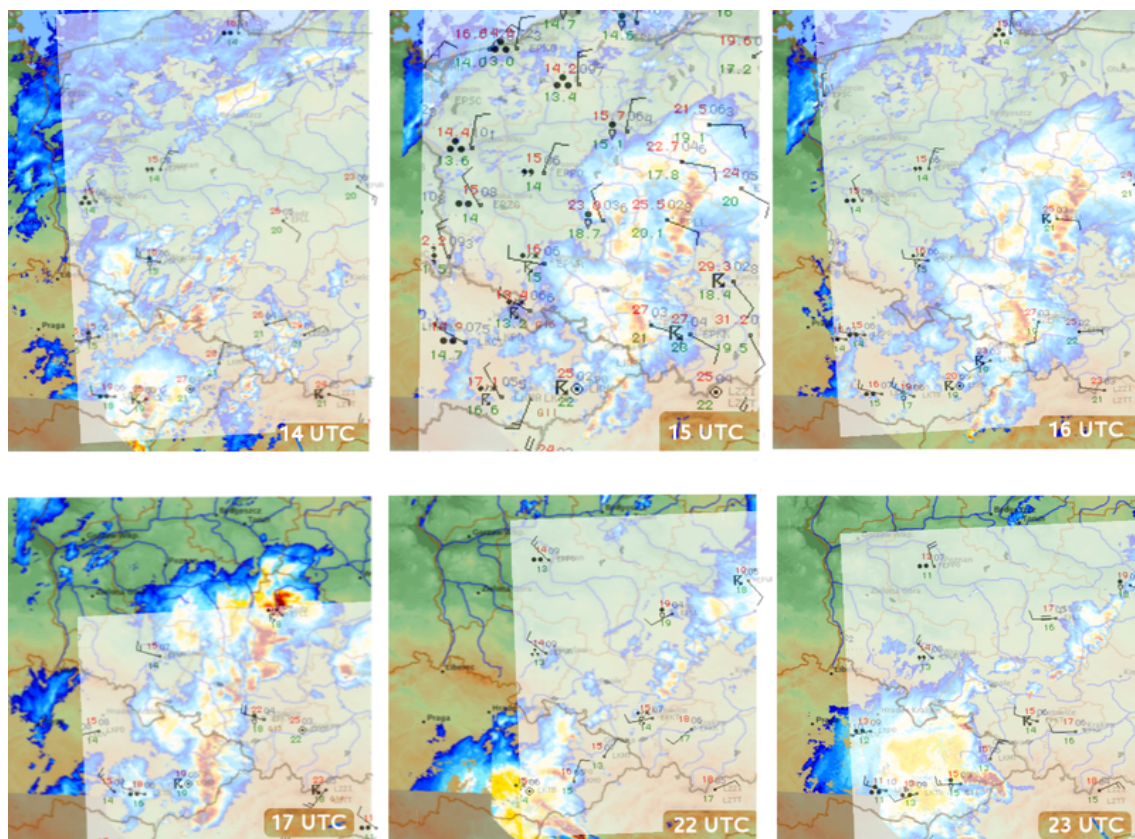


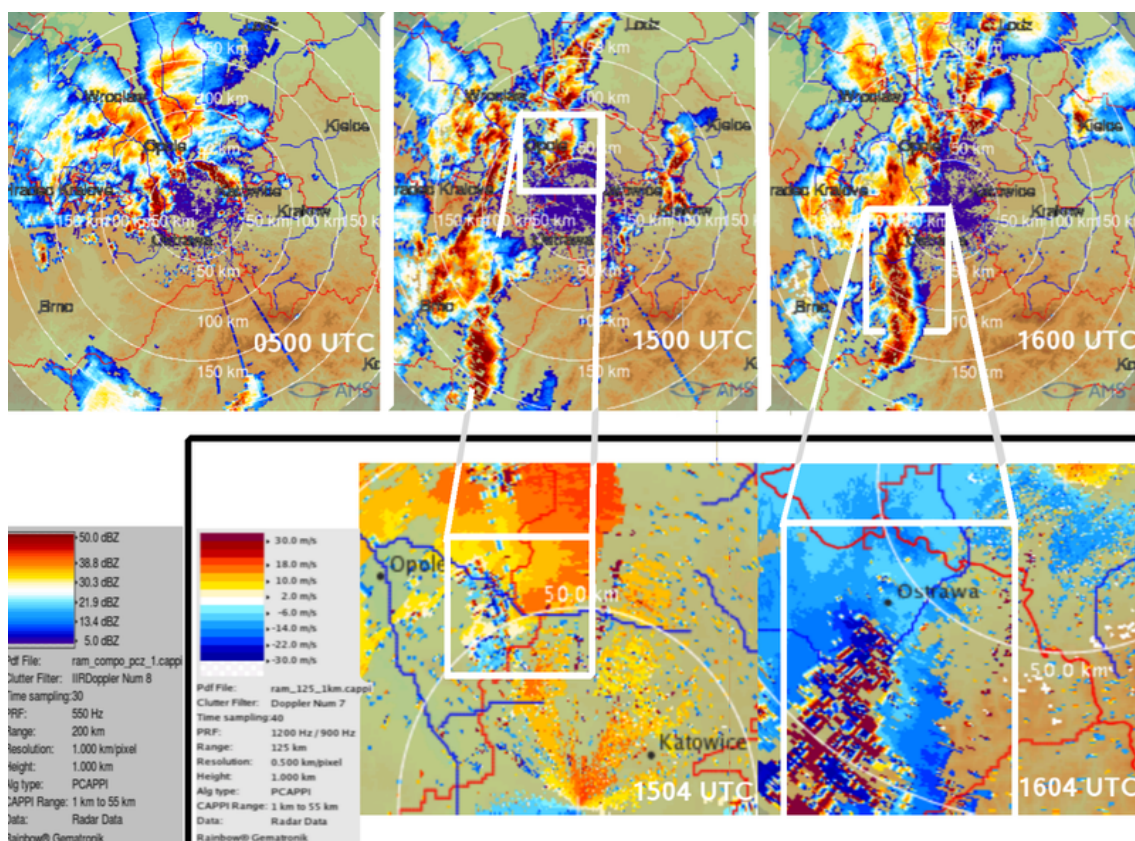
**Figure 4.20:** MLCAPE (color) with the black line showing the SRH3 ( $250\text{m}^2\text{s}^{-2}$ ) and the wind barbs the 0-6 km bulk shear. COSMO-DE at 15 UTC.

rameters is added to that discussion. In Fig. 4.20, the air mass east of the surface front is very unstable with MLCAPE values of  $1500 - 2000 \text{ J kg}^{-1}$  and even higher SBCAPE values. This is also visible in both 12 UTC soundings, which feature abundant CAPE in the favored hail growth zone of  $-10^\circ\text{C}$  to  $-30^\circ\text{C}$ . The mesoscale model calculated too much CAPE over Austria, the eastern Czech Republic and south Poland as 12 UTC soundings had  $500 - 1500 \text{ J kg}^{-1}$  and it had less CAPE to the south over northeast Italy with  $2000 \text{ J kg}^{-1}$  where Udine had  $3000 \text{ J kg}^{-1}$  MCALPE. High SRH3 values, supportive for supercell development and up to  $25 \text{ m s}^{-1}$  0-6 km speed shear overlapped, so the COSMO-DE also indicated a high risk for large hail with more discrete thunderstorms.

In Fig. 4.21 a), the composite reflectivity data from Poland is shown from 14 UTC until 17 UTC and then again at 22 UTC and 23 UTC. During the mature phase of the tornadic thunderstorms, easterly surface winds ahead of the front with



(a) Radar data and surface observations



(b) Reflectivity and radial velocity radar data

**Figure 4.21:** a) CAPPI 0.7 km at 14 UTC, 15 UTC, 16 UTC, 17 UTC, 22 UTC and 23 UTC with surface data. b) CAPPI 1km for velocity (15 UTC and 16 UTC) and reflectivity (5 UTC, 15 UTC and 16 UTC). Data provided from the IMGW, Poland.



surface dewpoints of roughly 20°C are present and indicate strong low-level shear with low LCLs as a consequence of the slim spread between surface temperatures and dewpoints. During the preliminary stage of those storms, the storm mode was more discrete with a gradual clustering trend during the late afternoon and early evening hours. Between 22 UTC and 23 UTC, the low-level and mid-level wind field increased further (not shown) with a classic pattern for bow echoes, given intense unidirectional shear with high magnitude especially below 3 km. Numerous bow echoes affected parts of Slovenia, eastern Austria and the eastern Czech Republic during the night hours with the most dominant one affecting eastern Czech Republic at 23 UTC. In Fig. 4.21 b), reflectivity data at 05 UTC, 15 UTC and 16 UTC is shown with the attendant velocity data for the 15 UTC and 16 UTC time frame. Severe hailstorms already caused damage during the early morning hours of the 15 August 2008 with numerous hail reports of 5cm and more. Despite the development of a nocturnal stable boundary layer, which can be seen in 00 UTC sounding data (e.g. Poprad-Ganovce, not shown), steep mid-level lapse rates and strong shear caused long-lived supercells during the early morning hours, which were elevated in nature. Abundant CAPE in the hailgrowth zone and the shear caused the augmented hail risk with those thunderstorms. As diabatic heating caused an erosion of the stable boundary layer, the risk for tornadoes increased as thunderstorms now ingested an unstable and strongly sheared low-level air mass, supportive for mesocyclone development. Numerous individual thunderstorms and small lines of thunderstorms are visible at 15 UTC and 16 UTC. Despite the fact that the velocity data is very noisy and has to be used with caution, rotation still can be seen at 15 UTC and folding with the thunderstorm line southwest of the radar at 16 UTC. This also visualizes how the severe thunderstorm risk can change from large hail to a tornado risk to a severe wind gust risk in a course of hours.

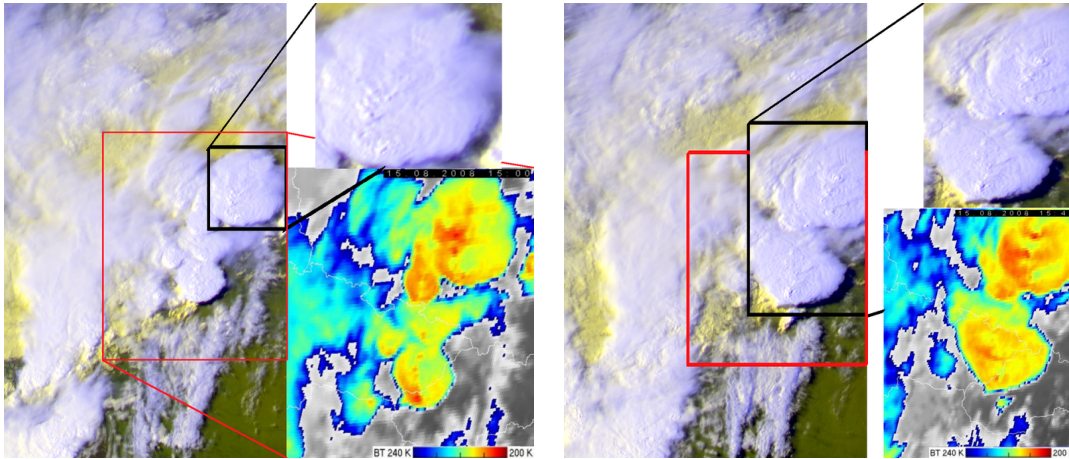


**Figure 4.22:** a) and b) show high resolution VIS images from the DLR (false color composite (0.6  $\mu\text{m}$ , 0.8  $\mu\text{m}$  (VIS), 10.8  $\mu\text{m}$  (thermal) and HRV channels; MSG2)) and brightness temperature from the Czech Republic (MSG2 every 15min) at 1500 UTC and 1545 UTC respectively. The range of the brightness temperature involves 200-240 K.

The updrafts of those thunderstorm were intense and caused the typical signatures in satellite images, seen in Fig. 4.22. The 'cold-U' shape, enclosing a warmer spot, is a signature, where strong updrafts penetrate into the tropopause or even into the lower stratosphere (cf. subsection 3.2.1.3).

This day featured abundant instability release and therefore a glance on the expected updraft velocities in COSMO-DE was taken. The model expected vertical velocities of 50-80  $\text{m s}^{-1}$  from Poland to Italy. Although those values are not impossible, they need an environment with extreme instability release, 4 to 5 times larger than what was measured on that day in Poland. A rough estimation from radar data was done and the strongest updrafts reached 30-40  $\text{m s}^{-1}$  so the calculation (see equation 3.7) is too coarse as no water loading or entrainment or vertical dynamic pressure gradient force is included. One has to be careful, when using this kind of updraft strength assessment and probably the safest way is the use of the instability maps.

#### 4.3.3.3 COSMO-DE performance

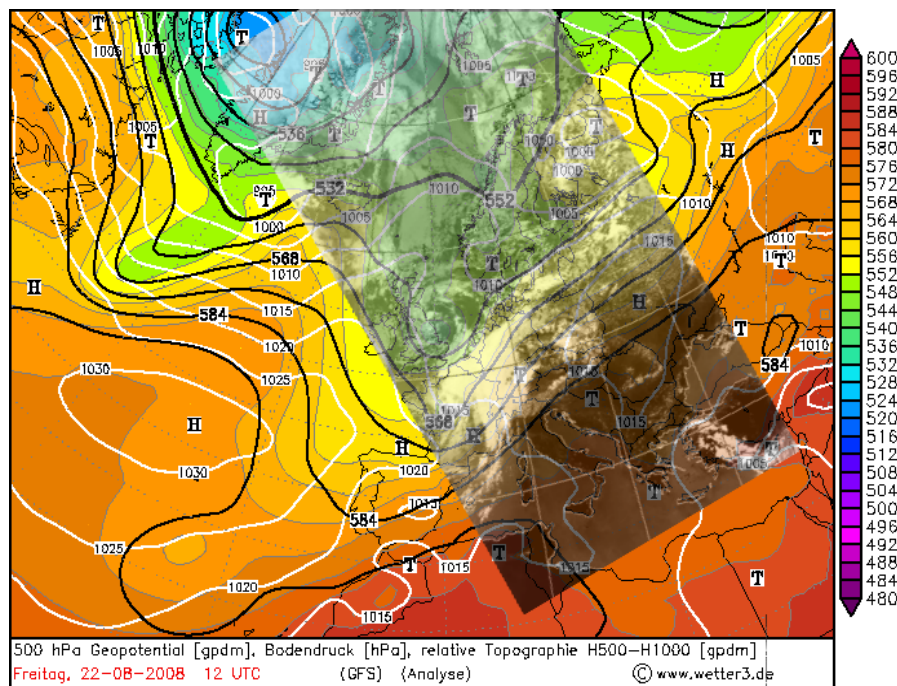
The high resolution model performed well in respect of detecting the thermodynamic and kinematic environment over the eastern Czech Republic and south Poland. In addition it evolved deep convection where tornadic thunderstorms evolved at 15 UTC although it had problems in resolving the more discrete storm mode as the thunderstorms in COSMO-DE clustered rapidly. Magnitude of shear and instability however were captured well despite some deviance.

#### **4.3.4 22 August 2008: Severe hailstorm, south Germany**

##### **4.3.4.1 Overview**

An isolated and long-lived thunderstorm developed southwest of the 'Ammersee' in Bavaria, south Germany and crossed south Bavaria from west to east. The thunderstorm acquired characteristics of a supercell with rotation and an intense hail core. A swath of damaging hail and severe wind gusts accompanied this supercell, before it left Bavaria to the southeast at 18 UTC.

##### **4.3.4.2 Synoptic-scale overview and mesoscale discussion**



#### 2-4km lapse rates, wind and geopotential heights (300hPa)

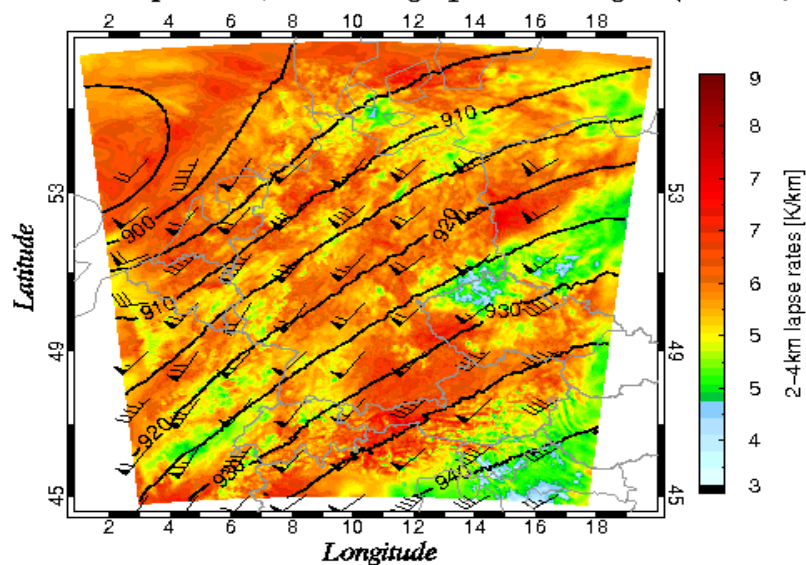


**Figure 4.23:** The synoptic overview is outlined in a). The background map shows the 500 gpdm geopotential height, the background color the relative topography between 1000 and 500 gpdm and the white lines the surface pressure, at 12 UTC. Overlaid the thermal infrared image also at 12 UTC (from Dundee). b) 14 UTC data of COSMO-DE were used for the 300 hPa geopotential height (black line), the 300 hPa wind field (black wind barbs) and the 2-4 km lapse rates (background color).

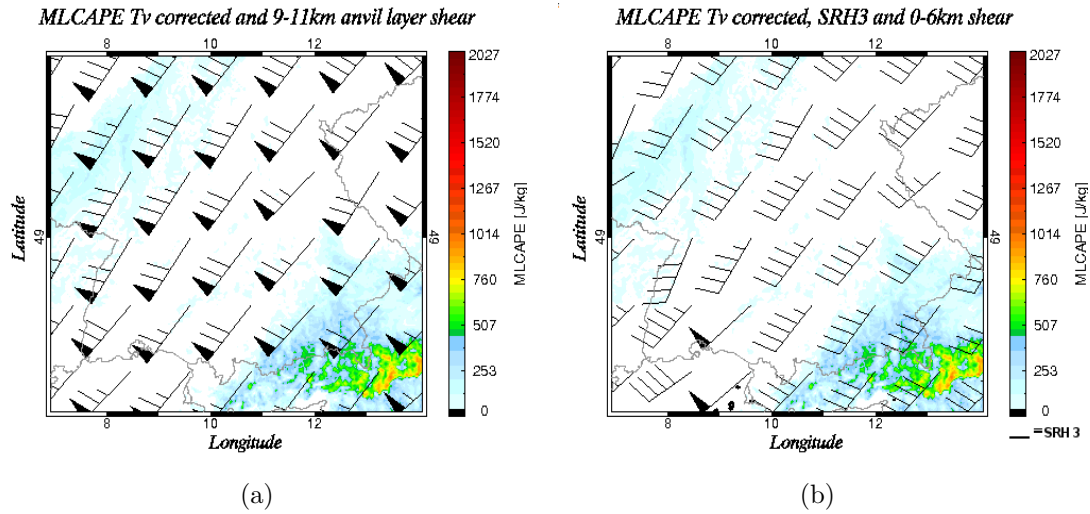


**Figure 4.24:** The 9-11 km anvil layer shear is shown in a) (black wind barbs) with the MLCAPE as background color. The composite image in b) features the 0-6 km speed shear (black wind barbs), the storm relative helicity in the lowest 3 km (black color with 250 m<sup>2</sup>s<sup>-2</sup> SRH3 and greater) and the 1000 J kg<sup>-1</sup> contour as background color.

The general upper-level pattern features an amplified upper-level trough over western Europe with a broad southwesterly jet affecting Europe on that day. Persistent warm air advection further downstream assisted in the development of a strong ridge over the Mediterranean and eastern Europe, where hot conditions were present. Due to a far southward moving cold front the week before (see the 15 August 2008 event), the air mass over the Mediterranean was not as moist as a few days ago but moisture advection was still adequate for the build-up of at least moderate instability east of the frontal zone, which ran from northern Spain to the Alps and Belarus. In Fig. 4.23 a), the warm conveyor belt can be seen, which affects France. Further east, capped conditions preclude thunderstorms to evolve, at least until 12 UTC (not shown). Cold air advection is seen west of the frontal zone with mainly shallow convection due to an enhanced temperature gradient between cold mid-levels atop of the warm sea. The strong southwesterly jet is also seen in Fig. 4.23 b) with up to 40 m s<sup>-1</sup> in the core of the jet. The center of the approaching upper-level low is centered just west of Belgium and the Netherlands at 14 UTC. It is interesting to see that the air mass east of the frontal zone has no EML-type lapse rate pattern with weak values south and east of the Alps. The reason for that is the continuous passage of the far southward traveling troughs. Attendant cold fronts moved far to the south and they therefore did not allow an EML to develop. 2-4 km lapse rates indicate more common values in the well mixed postfrontal air mass what would be expected in general in a maritime air mass from the Atlantic with patches of stronger and weaker lapse rates.

The overall set-up on this day was characterized by very limited instability release due to the surface moisture (surface dewpoints in general between 10-13 °C and up to 16 °C over southern Bavaria; not shown) and weak lapse rates but strong shear. During the afternoon hours, a speed maximum at 500hPa approached from Switzerland with wind speeds of 25-30 m s<sup>-1</sup> in its core. This also caused 0-6km speed shear to reach roughly 25 m s<sup>-1</sup> with 15 m s<sup>-1</sup> in the lowest 3 km. These speed shear values are more than adequate for mid-level updraft rotation, if any thunderstorm can manage to form with SBCAPE and MLCAPE values of 300 - 600 J kg<sup>-1</sup> (not shown). In Fig. 4.24 a) the anvil layer shear was included. In the United States, shear magnitudes of 30 m s<sup>-1</sup> and greater are referred to an augmented chance for low precipitation (LP) supercells in combination with a dry environment (see sec. 3.3.3.1). In this case, shear values were of the magnitude of 30 - 40 m s<sup>-1</sup> with moist environmental conditions along the frontal zone, so supercells could be expected but not necessarily LP ones. Entries in the ESWD indicate a swath of damaging hail with hail diameter of 4-5 cm but also severe wind gusts with this supercell. COSMO-DE however had no real hint on the development of a damaging hailstorm, when comparing the typical hail forecasting parameters, (Fig. 4.24 b). The only promising parameter was the 0-6 km speed shear, highlighted with wind barbs, which was in the range of 20 - 25 m s<sup>-1</sup>. Storm relative helicity at the lowest 3 km was at least slightly augmented over extreme southeast Bavaria, where higher surface moisture content and somewhat higher instability was forecast. It has to be noted that MLCAPE only greater 1000 J kg<sup>-1</sup> was overlaid with black lines. So a pure ingredient-based forecast highlights southeast Bavaria with the highest risk of large hail, which was also mentioned in the ESTOFEX outlook of that day:

... SE-GERMANY AND THE CZECH REPUBLIC ...

IN CONTRAST TO THAT, THE HAIL RISK WILL BE ENHANCED WITH MORE DISCRETE STORMS OVER S/SE BAVARIA AND DISCRETE STORMS AHEAD OF THE POTENTIAL MCS AND IF INSTABILITY RELEASE MATCHES MODEL OUTPUT EVEN A SIGNIFICANT HAIL EVENT CANNOT BE RULED OUT,[...] (ESTOFEX <sup>2</sup>)

The environment was supportive for convection, which could even develop up to the tropopause at roughly 12 km (12 UTC sounding of Munich-Oberschleissheim, not shown) and the main concern was the potential development of discrete thunderstorms ahead of the eastward moving cold front, which was forecast to cross south Germany during the daytime hours from the west. At 14 UTC, a more discrete thunderstorm ahead of the front indeed evolved east of the Lake of Constance, seen

---

<sup>2</sup>[http://estofex.org/cgi-bin/polygon/showforecast.cgi?text=yes&fcstfile=2008082306\\_200808211919\\_2\\_stormforecast.xml](http://estofex.org/cgi-bin/polygon/showforecast.cgi?text=yes&fcstfile=2008082306_200808211919_2_stormforecast.xml)



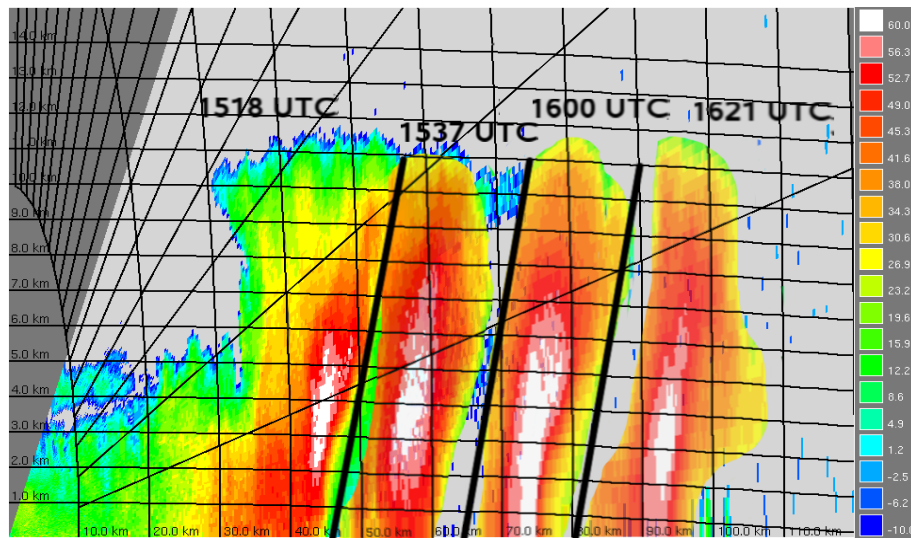
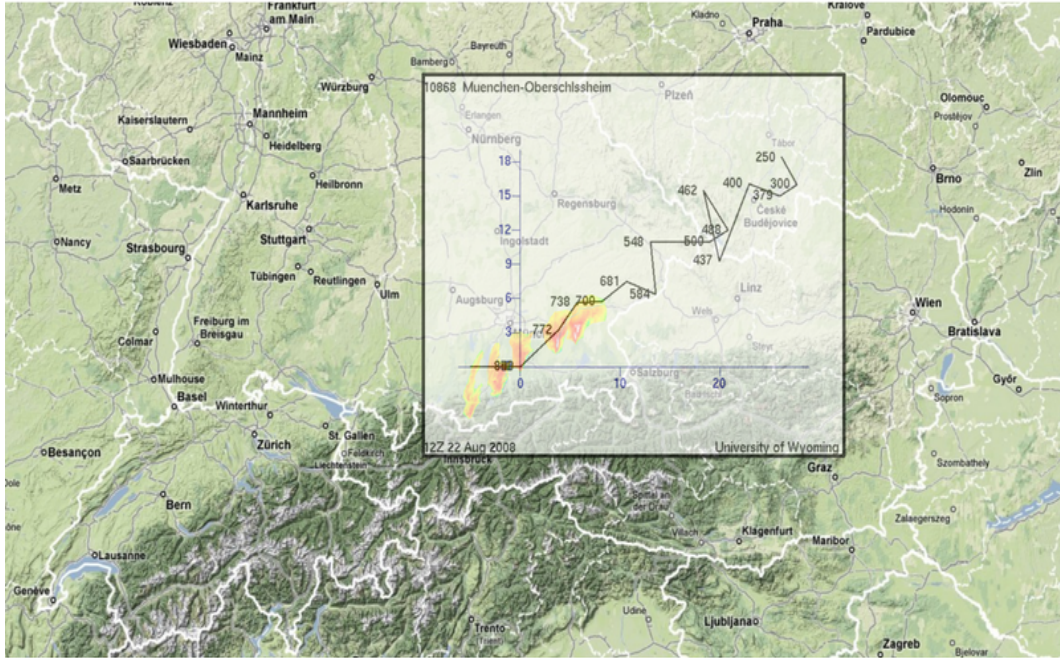


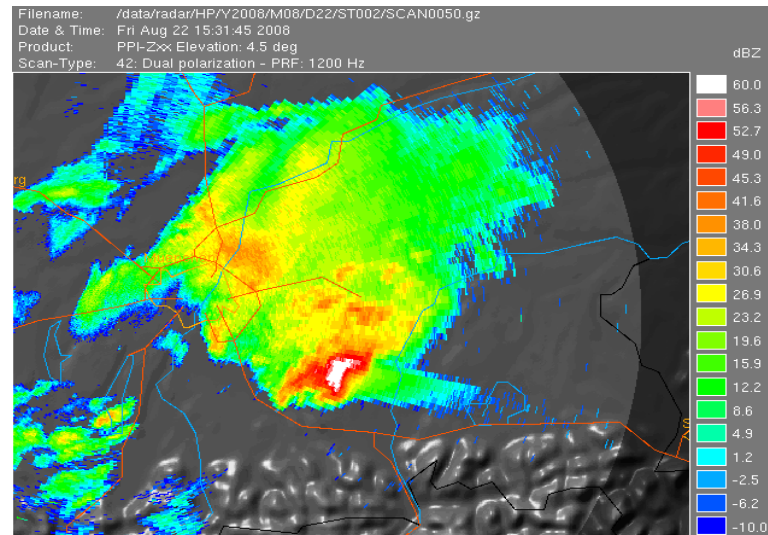
**Figure 4.25:** a) A composite image with the POLDIRAD data at 1405 UTC, 1448 UTC, 1511 UTC, 1551 UTC and 1613 UTC in PPI mode (30 dBZ and greater). Only the discrete cell ahead of an eastward moving cold front is shown atop of the the Munich-Oberschleissheim 12 UTC hodograph from Wyoming (pressure in hPa and wind speed in  $m s^{-1}$  ( $1 m s^{-1} = 3.6 km h^{-1}$ )). Background map source of Google maps. A composite of RHI images from POLDIRAD through the supercell is shown in b). Recording time is from left to the right with 1518 UTC, 1537 UTC, 1600 UTC and 1621 UTC respectively with an azimuth of  $102^\circ$ .

in Fig. 4.25 a). The thunderstorm remained discrete during its lifetime and gained strength and organization as it moved toward the northeast. A very strong hail core evolved about one hour later at 15 UTC and persisted until it left the range of POLDIRAD. The cell resembled a supercell due to the compact structure with an intense updraft along its southern fringe and a northeastward displaced area with stratiform rain. A striking but not mandatory signal for a supercell was the deviant motion compared to the 0-6 km bulk shear vector that the thunderstorm acquired. To highlight that, the hodograph of Munich-Oberschleissheim at 12 UTC was overlaid in Fig. 4.25 a). It had the classic shape of unidirectional shear with a high potential for any persisting thunderstorm to split. However it can be seen that the supercell moved off the hodograph, especially south of Munich, where the storm motion increased from  $18 \text{ m s}^{-1}$  to more than  $20 \text{ m s}^{-1}$ , which is in line with the strength of the steering flow, featuring  $25 \text{ m s}^{-1}$ . This also is at least one more explanation for the thunderstorm to become such a dominant supercell. Due to the deviant storm motion, helicity in the lowest 1 km and 3 km increased considerably compared to what was forecast by COSMO-DE. Later the day, when the supercell left the range of POLDIRAD, the supercell even made another right-turn, which again increased the SRH.

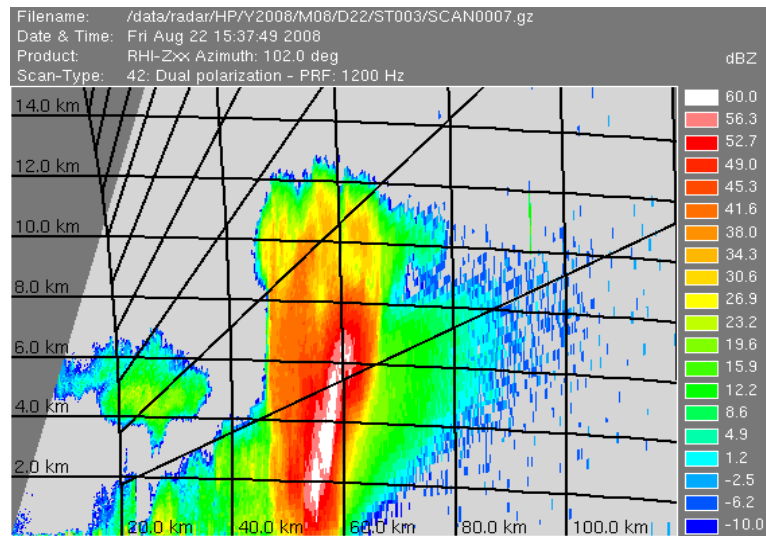
In Fig. 4.25 b) POLDIRAD now is used for a more detailed view of that supercell. In general the overall track was not the best as the radar beam had to cross the rain and hail core before measuring the updraft itself. However, those frames were used, where the quality of the radar beam seemed reasonable enough for further investigation. In Fig. 4.25 b), the hail core of the supercell was tracked, preceding in time from the left, starting at 1518 UTC. The increase in forward speed of this supercell can be seen as RHI scans were done every 20 minutes with a significant increase in forward speed at 1537 UTC onwards. However the main issue of this composite is the developing hail core at 3 - 5 km above ground just upstream of the main updraft, characterized by a sharp reflectivity gradient and a bounded weak echo region. This area is known as the *stagnation point* in an hailstorm, where the upper-level flow has to divert around the strong updraft with weak winds just upstream of the updraft. This causes a prolonged period of time for hail growth and hence is well seen in reflectivity maps with values in excess of 56 dBZ. Only 20 minutes later, the hail core grew in the vertical, now extending from 3 to 7 km but no descent of the hail core was yet seen. Nevertheless, reflectivity values in excess of 56 dBZ at 1 - 2 km above the ground already indicated the risk for hail just above the surface. Between 1530 UTC and 1600 UTC, numerous hail reports were entered into the ESWD, which is plausible, when using the RHI scan at 1600 UTC. An intense hail core descended to the surface with reflectivity values of 60 dBZ and more all the way up to 6 km. Both, large hail of up to 5 cm but also a huge amount



of smaller hail with severe straightline wind gusts was reported during that time. About 20 minutes later, already near the maximum radar range, a new hail core developed, which was placed at 3-4 km above ground. To summarize, a cycling hail core was present in this supercell, which was well captured with POLDIRAD. With such an impressive hail core, another radar signature can be seen, the *three body scatter spike or hailspike*, see sec. 3.2.2.

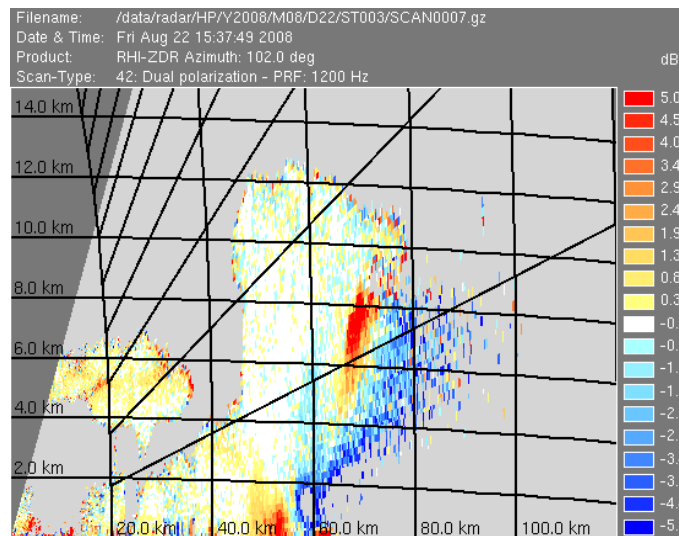


(a) PPI scan at 4.5 °. Reflectivity in dBZ

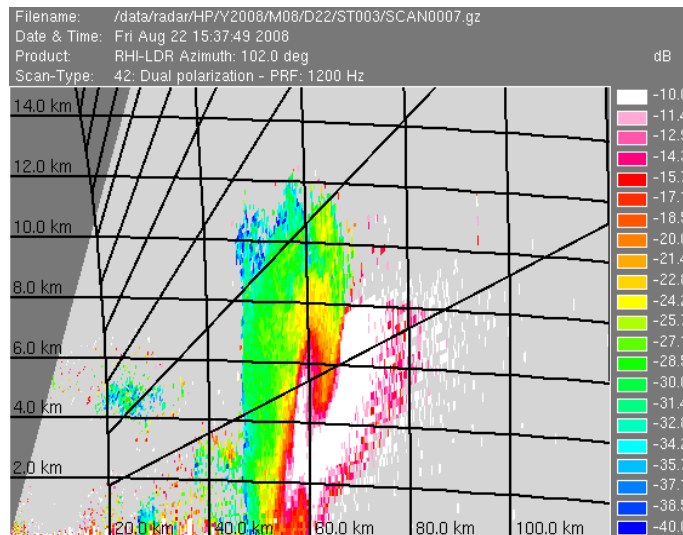


(b) RHI scan at 102 °, reflectivity in dBZ

**Figure 4.26:** a) PPI scan of reflectivity (dBZ), 4.5 ° elevation at 1531 UTC and roughly 50-60 km apart from POLDIRAD. b) RHI scan, 102 ° azimuth at 1537 UTC from POLDIRAD



(a) RHI scan at 102 °, ZDR in dB



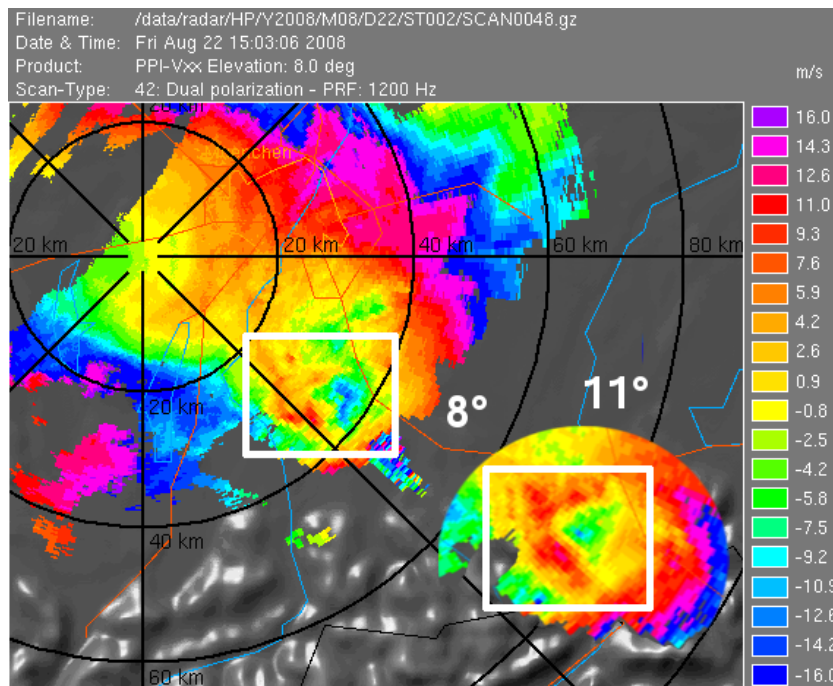
(b) RHI scan at 102 °, LDR in dB

**Figure 4.27:** RHI scan from POLDIRAD, 102 ° elevation at 1537 UTC a) ZDR b) LDR.

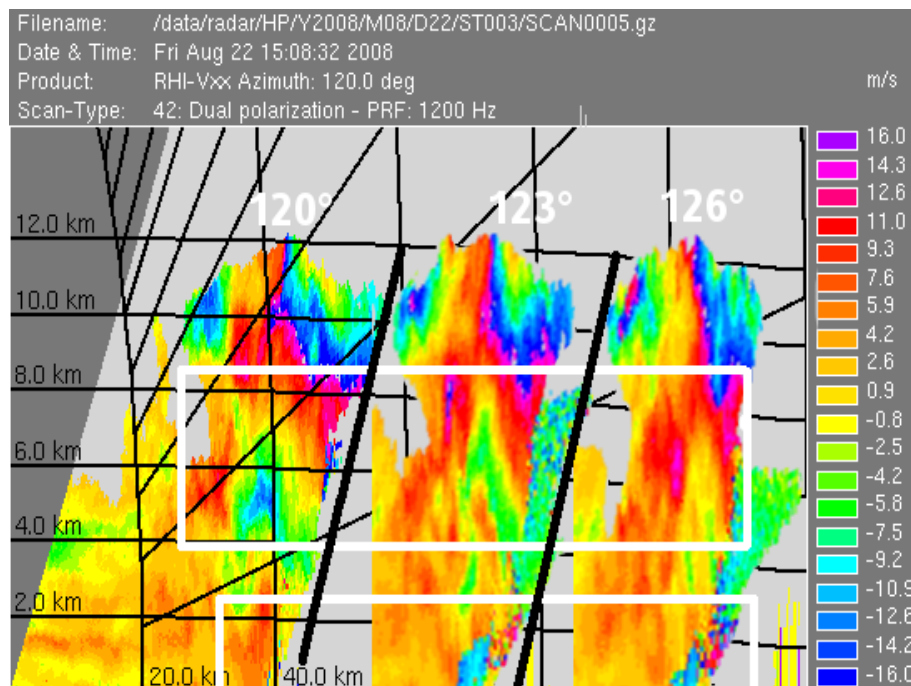
In Fig. 4.26 a), the hail spike is seen with the 4.5 ° elevation scan southeast of the intense hail core. It can be seen that the intensity of the reflectivity indeed drops further downstream of the hailcore. In addition, the shape of the hail core but also the influence of the surface caused the hail spike to attain an asymmetric structure with locally stronger or weaker reflectivities. In Fig. 4.26 b) the same hail spike is seen on the RHI with an azimuth of 102 °. The 'false echo' is seen downstream of the hail core. The use of the polarimetric data of POLDIRAD now allows to back that assumption up. Additional radar data from stations south, east or west of the supercell are needed to ascertain that no rain is present due to the significantly disturbed radar beam. In Fig. 4.27 a) and Fig. 4.27 b), the ZDR and LDR is shown respectively. During the passage of the polarimetric radar beam through the

thunderstorm, a significant disruption of the characteristics of the beam occurs due to the more asymmetric and complex structure of the hydrometeors, which can be seen by an abrupt drop of the ZDR values behind the hail core and the opposite for the LDR, where higher values are shown downstream of the hail. This feature persisted also during the following RHI scans although with decreasing intensity probably due to the increasing distance from the radar and the aforementioned development of another hail core.

This thunderstorm had a persistent mesocyclone at least at mid-levels and therefore the thunderstorm could be classified as a supercell. In Fig. 4.28 a), two PPIs at different elevations, one at  $8^\circ$ , the other one at  $11^\circ$  were created. In the  $8^\circ$  scan the area of rotation is roughly 36 km apart and can be found at 5 km whereas in the  $11^\circ$  scan the distance is 35 km with a height of almost 7 km. Both scans reveal strong rotation with blue showing inbound velocities and red outbound velocities, see sec. 2.3.6.1. The diameter of this mesocyclone at 5 km above ground was roughly 6 km with a shear magnitude of  $26 \text{ m s}^{-1}$  between the inbound and outbound peak velocity, which were roughly 3 km apart. Translated to the magnitude of vorticity, one achieves a value of roughly  $0.016 \text{ s}^{-1}$ , which corresponds well with observations from the United States (Desrochers and Harris (1996)). Both PPI scans were overlaid and the maxima of rotation match well. The mesocyclone persisted also in the following scans and even revealed a range gate-to-gate shear of  $17 \text{ m s}^{-1}$  10 min later. From 1600 UTC onwards, the mesocyclone lost its structure and also its intensity but one has to be careful with the interpretation due to the increasing distance to the radar. In Fig. 4.28 b) the rotation is also visible in the RHI scans at 1508 UTC, where three scans with different azimuth were plotted, one at  $120^\circ$ , the centered one with  $123^\circ$  and the right one with  $126^\circ$ . The mid-level mesocyclone was placed in a white box at 5 - 7 km above ground and was the strongest in that layer with decreasing intensity downwards. Another signal of rotation can be seen just above the ground, also marked by a white box. However, the low elevation of the radar beam and the penetration through the rain and hail make an interpretation more uncertain. In addition, this feature just appeared for 2 scans before changing more to an intense convergence zone along the downstream side of the thunderstorm as rain cooled downdraft starts to spread out with near hurricane-force wind gusts were measured along the path.



(a) PPI with 8 ° and 11 ° elevation



(b) RHI with different azimuths

**Figure 4.28:** a) The PPI (radial velocity from POLDIRAD) is captured with an elevation of 8 ° and 11 ° at 1503 UTC. b) The rotation is also visible on the RHI with azimuth of 120°, 123° and 126 ° at 1508 UTC.

### 4.3.5 23 June 2008: Supercell thunderstorm over southern Germany

#### 4.3.5.1 Overview

On 22 June 2008, a cold front crossed north France, Belgium, the Netherlands and Luxembourg and slowed down significantly over north-central France and central Germany during the following 24 hours. This cold front was marked by a sharp temperature and moisture gradient and served as focus for initiation on the 23 June. Placed along the anticyclonic shear side of the polar front jet, shear was sufficient for organized thunderstorms and even supercells were possible. During the late morning hours, initiation was underway along the cold front with numerous, discrete supercells moving eastsoutheastwards.

#### 4.3.5.2 Synoptic-scale overview and mesoscale discussion

A strong southwesterly jet covered most parts of France and Germany during the period between a 995 hPa depression over Norway and Sweden and a 1020 hPa high pressure area over Italy. In Fig. 4.29, the 300 hPa wind field and geopotential height are shown, where numerous speed maxima can be seen, one over north Germany and the south North Sea and the other one over eastern France and south Germany. No major short wave was seen in COSMO-DE but weak disturbances were still embedded in this flow, seen on upper vertical velocity maps (not shown). In color, the mid-level lapse rates were mapped to highlight the differences between of the prefrontal and postfrontal air mass. The surface cold front, also seen in Fig. 4.30 is situated over south central Germany during the late morning hours. Almost dry adiabatic lapse rates ahead of the front were forecast by COSMO-DE with up to 9.5 K/km over extreme eastern France. In the immediate postfrontal region, lapse rates decreased gradually and indicate the well mixed maritime air mass, which covered Luxembourg, Belgium, the Netherlands and north and central Germany during that period. Even lower values were present over north Germany beneath an eastward moving occlusion. In Fig. 4.30, the cold front is placed over eastern France, south Germany and the northern Czech Republic. In fact, the cold front became stationary during the following hours. There is a gap between the satellite image (0715 UTC) and the surface data (1215 UTC). No major shift of the front was noticed during those 5 h but the satellite image became quite messy with developing thunderstorms at 12 UTC, so the decision was made to include the early morning satellite data with the surface data representing the immediate boundary layer conditions during the initiation of the thunderstorms, five hours later. Dewpoints ahead of the stationary front were in the upper tens or lower twenties with dewpoints of 4 - 10°C north of the front. Strong diabatic heating took place north and south of the front, so the

front itself weakened during that period as the temperature gradient diminished, but the front was still the focus for initiation as the convective temperature was reached. This eventually was the case at 11 UTC over southwest Germany.

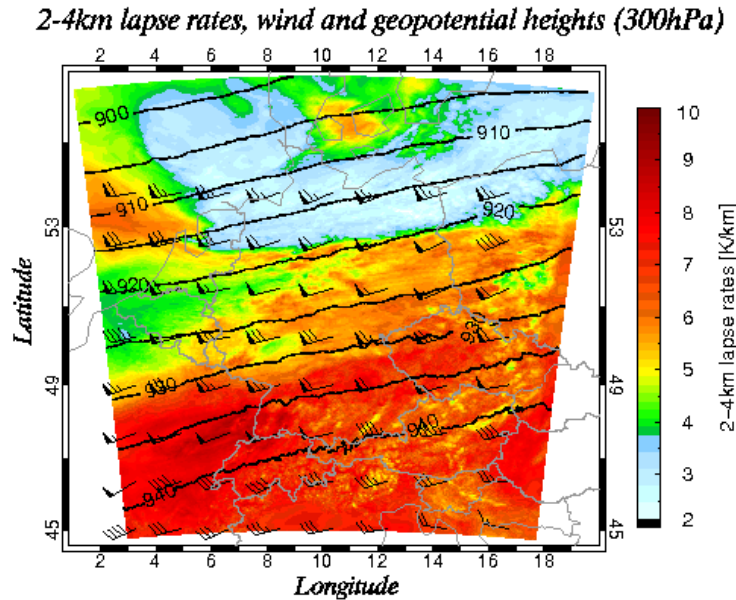


**Figure 4.29:** 300 hPa geopotential height in gpdm, wind field (wind barbs) and 2-4 km mid-level lapse-rates (background color). COSMO-DE on 23 June 2008.

As already mentioned, the environment ahead of the front was supportive for strong instability release with a moist boundary layer and steep mid-level lapse rates in a strongly sheared environment. COSMO-DE sampled the environment nicely, which can be seen in the following maps. In Fig. 4.31 a) the speed shear at three different layers is shown with rapidly strengthening shear profiles to the north. Some directional shear was present in the lowest 1000 m, but otherwise, straightline hodographs could be expected with strong southwesterly winds. The position of the front can be evaluated in Fig. 4.31 b), where directional shear throughout the lowest 1000 m and 3000 m is sketched. COSMO-DE has somewhat enhanced directional shear values just along the boundary with regional peaks of  $100 - 200 \text{ m}^2 \text{ s}^{-2}$  SRH1. South of the front, directional shear decreased rapidly. Fig. 4.31 c) comprises the probability for tornadoes. CAPE in the lowest 3000 m is very supportive on that day with  $100 - 200 \text{ J kg}^{-1}$ , which is a lot. This indicates that at 12 UTC, a warm, moist and well mixed boundary layer is already in place. 12UTC sounding data (not shown) supports that. However, the speed and directional shear in the lowest 1000 m is weak and an inhibiting factor for a more serious tornado threat. No SRH1 contour can be seen, which means that SRH1 was not higher than  $150 \text{ m}^2 \text{ s}^{-2}$ . COSMO-DE forecast the possibility for organized thunderstorms, seen in the SCP map (not shown) and STP map (see Fig. 4.31 d)). The areas, highlighted in orange, show



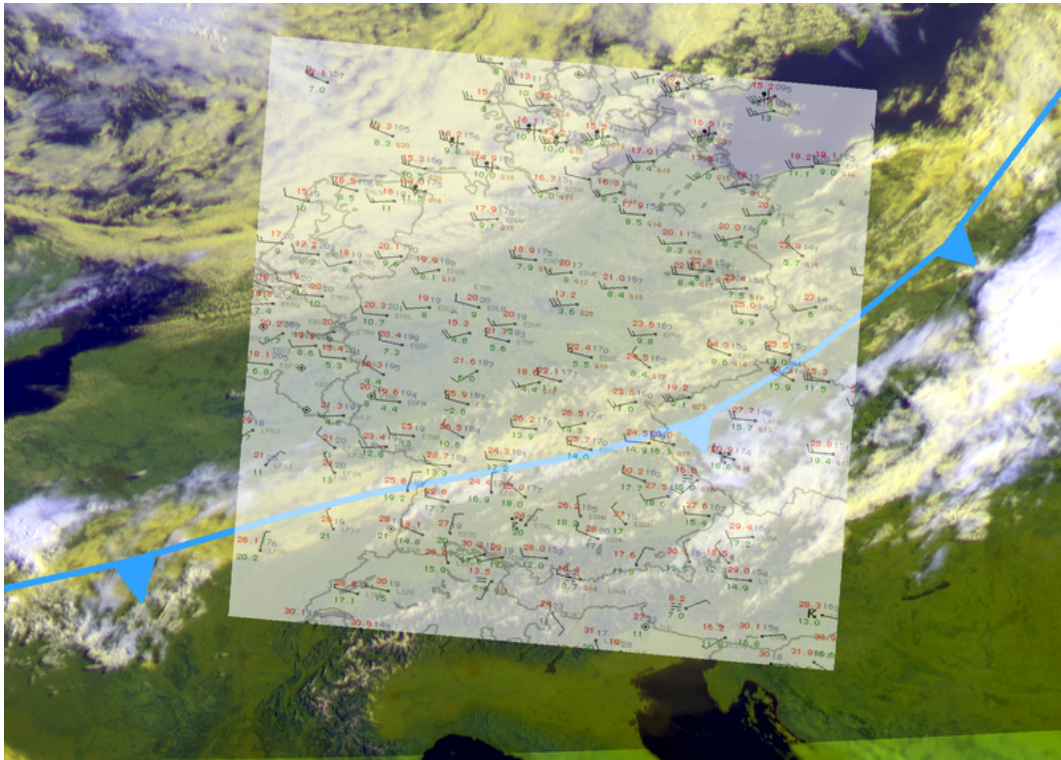


**Figure 4.30:** MSG-2 HRV satellite image at 0715 UTC and the surface map at 1215 UTC on 23 June 2008.

augmented STP values. The magnitude of the STP was low but there was at least the chance for supercell tornadoes along this boundary. COSMO-DE captured the prefrontal air mass nicely but underestimated MLCAPE somewhat with expected values of  $500 - 900 \text{ J kg}^{-1}$  at 12 UTC whereas Stuttgart and Munich had  $1000 - 1500 \text{ J kg}^{-1}$ .

The VAD wind profile from POLDIRAD, DLR west of Munich (Fig. 4.32) is representative for the wind field in the prefrontal air mass with overall weak wind speeds below 2 km. One interesting aspect is the backing of the surface wind during the noon and afternoon hours with northerly or northeasterly winds over south Germany. When modifying the 12 UTC hodograph of Munich, Fig. 4.33 the northerly surface wind field increases the curvature of the hodograph, but overall weak magnitude of wind speed keeps the hodograph more or less straight throughout the troposphere.

Regarding the classic supercell environment with strong speed and directional shear, mainly the speed shear was present.  $0-6 \text{ km}$  bulk shear of  $20 \text{ m s}^{-1}$  is enough for organized thunderstorms but a forecaster expects to see higher helical values especially throughout the lowest 3 km for thunderstorms with deviant storm motion. With such a straightline hodograph, storm splitting would have been expected. On

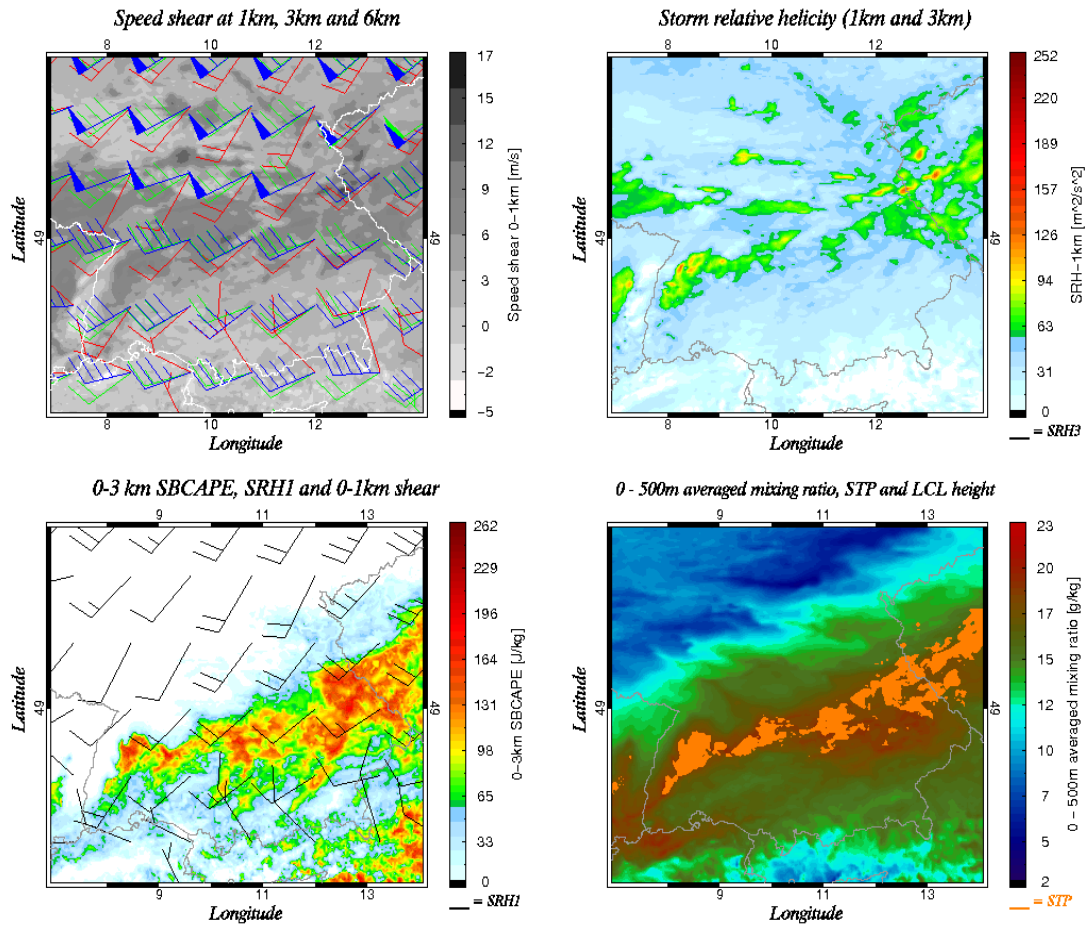


**Figure 4.31:** a) Background color represents 0-1 km speed shear, the red barb is 0-1 km speed shear, the green barb 0-3 km and the blue one is the 0-6 km speed shear. In b), the SRH1 is sketched as the background color and SRH3 greater  $250 m^2s^{-2}$  as a black line (not reached at 12 UTC). 0-3 km CAPE is shown as background color in c) with 0-1 km speed shear (wind barbs) and SRH1 greater  $150 m^2s^{-2}$ . The low-level mixing ratio is the background color in d) with the STP in orange filled contours (all magnitudes were allowed with a peak magnitude of 0.8) and LCL greater 1km as white lines (not reached at 12 UTC). All data from COSMO-DE at 12 UTC with the display detail showing southern Germany.



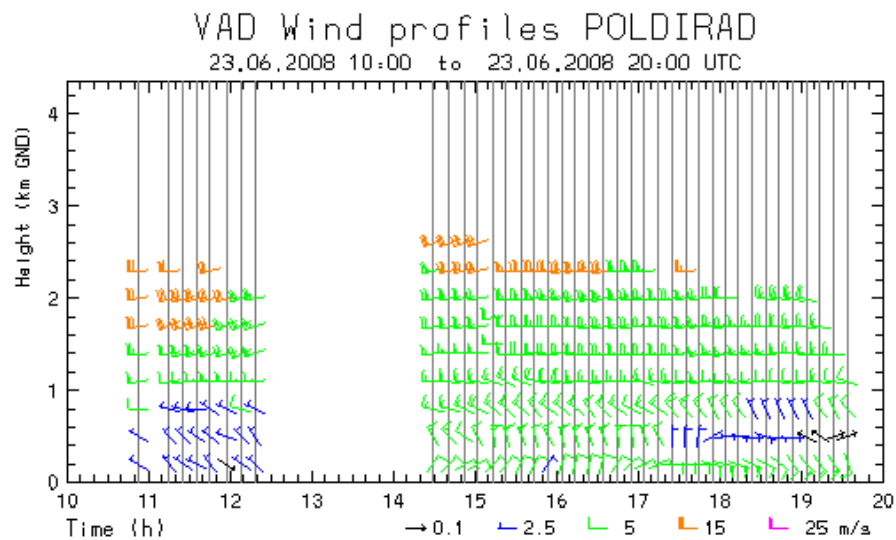
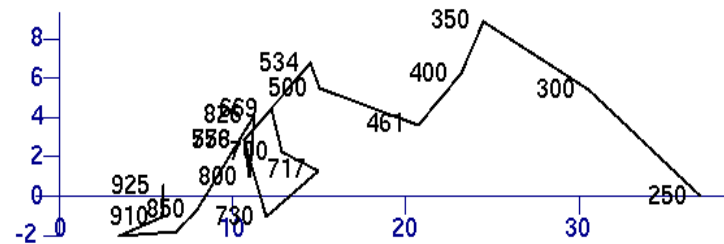


**Figure 4.32:** VAD profile of POLDIRAD, 10-20 UTC, 23 June 2008.

10868 Muenchen-Oberschlsheim



12Z 23 Jun 2008

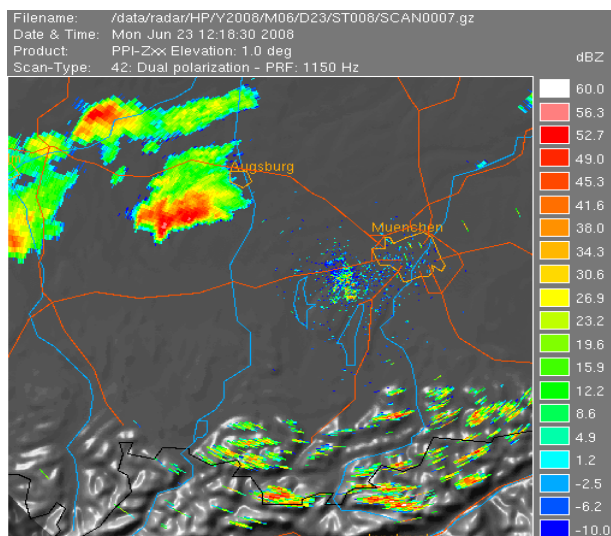
University of Wyoming

**Figure 4.33:** Hodograph from Munich at 23 June 2008, 12 UTC. Source: Wyoming. Wind speed in  $m s^{-1}$  ( $1 m s^{-1} = 3.6 km h^{-1}$ ), pressure in hPa.

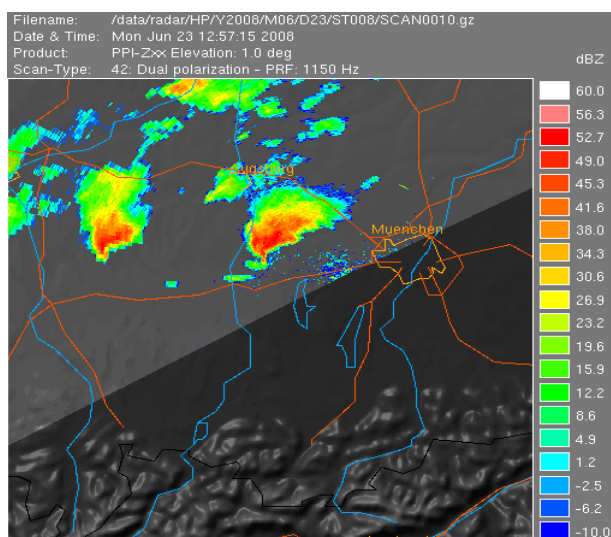
23 June however, supercells developed at roughly 11 UTC along the boundary over southwest Germany, moving rapidly towards the eastsoutheast without splitting.

This movement can be seen in Fig. 4.34 a), b) and c). A PPI scan at  $1^\circ$  elevation was used with 30 min difference between a) and b) and 60 min difference between b) and c). Keeping the hodograph in mind, the steering flow was from the west-southwest with  $20 \text{ m s}^{-1}$  speed shear, so the expected storm motion should have been to the eastnortheast. However, the PPI sequence shows a strong deviant storm motion of both supercells to the east and later eastsoutheast. Plotting this kind of storm motion into the hodograph, the magnitude of the storm relative helicity especially at mid-levels was significantly higher. So deviant storm motion has an effect on the final magnitude of helicity, which has to be included into the forecasting strategy. Especially in environments, when deep layer shear is strong, even slight deviant storm motion could cause an increase of the SRH and therefore an augmented chance for supercells. The thunderstorms in all three PPI scans indicate a typical structure for supercells with a pronounced and long lived hook echo and a tight reflectivity gradient next to the updraft (a bounded weak echo region was present in RHI scans, not shown). POLDIRAD was well placed in respect to the supercells as no hail or rain core was present between the radar and the updraft, which could have caused attenuation or artifacts.

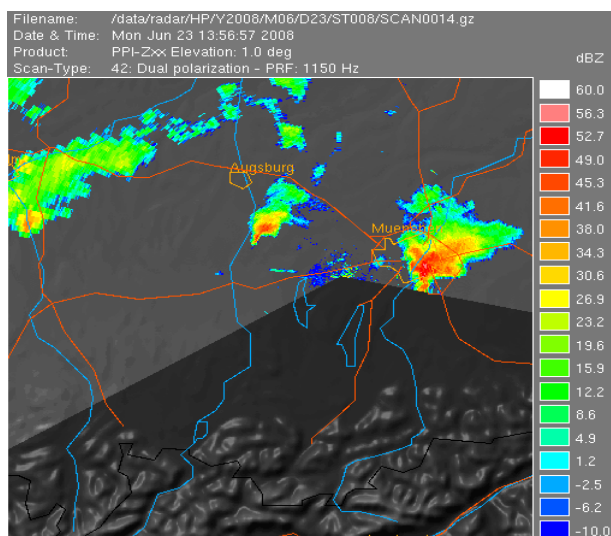
The first supercell at 1237 UTC is shown in Fig. 4.35. In a), the PPI at  $1^\circ$  elevation reveals a textbook like supercell with a pronounced hook echo, a bounded weak echo region (also seen at RHI scans) and a forward-flank rain and hail core. The beam has an altitude of roughly 700 m above ground (38.5 km to the northwest of POLDIRAD), so the lower part of the supercell is seen. Strong rotation can be seen from the radial velocity in c) and d). The elevation is  $1^\circ$ ,  $4^\circ$  and  $5^\circ$ , which corresponds to a radar beam height at the mesocyclone of 700 m, 2600 m and 3200 m respectively. Especially the inbound velocities revealed folding, which corresponds to a strong rear flank downdraft with wind speed of  $20 - 25 \text{ m s}^{-1}$  just above the surface. A severe wind gust report at 14 UTC west of Munich and observations from storm chasers support the existence of such speeds (see ESWD report). The mesocyclone lived for roughly 2 hours and was present up to 7 km above ground. Only a few minutes after the radar scans, a photo was taken by the storm chaser Tobias Hämmer northwest of the Ammersee (Fig. 4.36). A pronounced wall cloud is present with dry air approaching from the left of the picture (view to the north), which probably is the descending drier air within the rear flank downdraft. Rotation was noticed by the storm chaser but no tornado evolved out of this supercell. Large hail and severe wind gusts were reported.



(a)



(b)



(c)

**Figure 4.34:** Three PPI reflectivity scans from POLDIRAD with an elevation of  $1^\circ$ . a) at 1218 UTC, b) at 1257 UTC and c) at 1357 UTC.

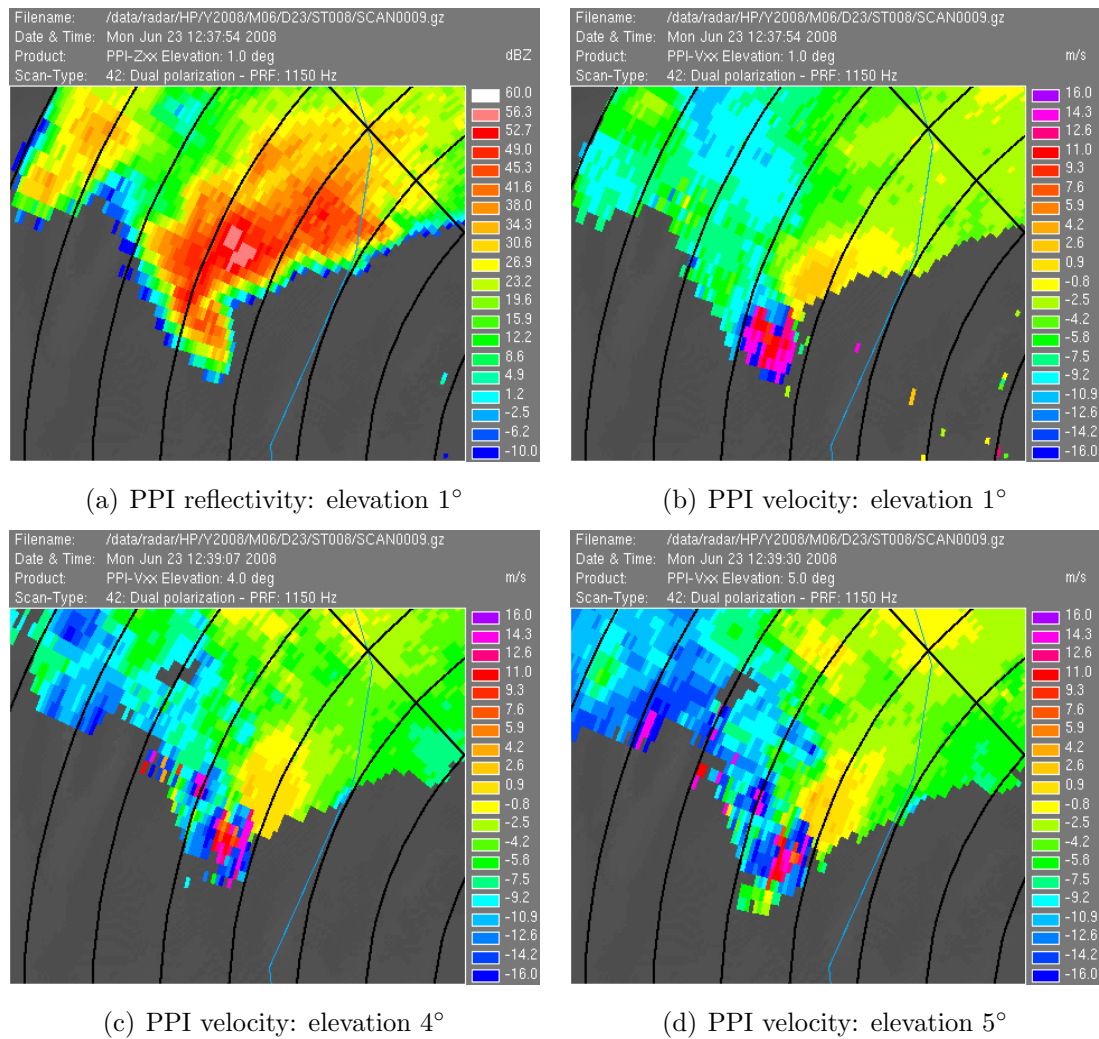


**Figure 4.35:** a) POLDIRAD PPI reflectivity at an elevation of 1° at 1237 UTC. The PPI radial velocity was added in b), c) and d) at 1°, 4° and 5° and 1237 UTC, 1239 UTC and 1239 UTC respectively.



**Figure 4.36:** This photos captures the supercell northwest of the Ammersee, Bavaria during the time of Fig.4.35 (roughly 1240 UTC). The photo was provided by the storm chaser Tobias Hämmer ([www.wetteraction.de](http://www.wetteraction.de)). Viewing direction is to the northwest.



## Chapter 5

# Conclusions and outlook

The goal of this thesis was the study of how useful severe thunderstorm parameters were in five thunderstorm events in Europe and how COSMO-DE performed in forecasting those particular events. The forecast parameters were useful in situations, where ample shear and instability were present. In those cases, the knowledge of the strength and weakness of those parameters allowed the efficient concentration on the area of most concern on 15 August 2008 over southwest Poland. That day featured typical conditions for all facets of severe weather as the LCL was low, directional and speed shear at all levels was very strong with instability values in excess of  $1000 \text{ J kg}^{-1}$ . On days like the Hautmont tornado event over NE-France on 3 August 2008, most of the forecast parameters failed to forecast this event due to the very limited instability release. However the use of a mesoscale forecast model like COSMO-DE and the knowledge of certain configurations supportive for severe thunderstorm events, like augmented release of convective available potential energy in the lowest 2-3 km with intense directional and speed shear in the lowest 1000 m, pointed to the enhanced possibility of severe wind gusts and tornadoes. This result is an important rule for severe thunderstorm forecasts during the winter time in Europe, as most of the times, instability release is low despite a favorably sheared environment.

In this case, the potential influence of a front or a convergence zone on the organization stage of a thunderstorm was studied, as enhanced moisture in the low-levels and augmented low-level shear exhibited all required ingredients for thunderstorms to develop and organize. The concentration of strong speed shear to the lowest 3 km was also supportive for concentrated swaths of severe wind events, like it was shown for the bow echo case on 26 May 2009 over southern Germany. Strong shear in a buoyantly stratified hail growth zone are one hint on large hail occurrence despite the still overall marginal knowledge of hail forecasting.

The forecast situation was handled very well by the parameters in situations, when conditions resembled those of the Great Plains in the USA in respect of abundant

instability release and shear. The prime example was the tornado outbreak in Poland (15 August 2008), when all parameters for organized severe thunderstorms (STP, SCP, shear and instability) indicated an augmented risk for all kind of severe weather over Poland. There, the composite parameters helped a lot in confining the area, where the highest severe thunderstorm risk was expected, whereas parameters like LI or KI only highlighted the region, where thunderstorms were possible, independent on the degree of thunderstorm organization. A basically different picture arose in the Hautmont tornado event (3 August 2008), where no appreciable CAPE was available. The STP parameter was present, but well displaced to the south with values just shy above 0. The basic parameters like the LI however pointed to at least some chances for deep convection with slightly negative values along the cold front over northeastern France. This case highlighted the major problems in low CAPE environments, when the composite indices remain too low due to the weighting of CAPE in those composite parameters. Those cases often occur during the winter time, when not much modification is needed for the initiation of deep convection. Then, it is more useful to balance if deep, moist convection is possible instead of looking for augmented composite indices. Both cases demonstrated that the best use of the forecast parameters is a combination between the 'composite indices (e.g. STP or SCP)' and the 'basic (e.g. LI)' ones. The basic parameters assist in the question, if thunderstorms develop and the composite indices determine the degree of thunderstorm organization.

Due to the same 'physics' how thunderstorms evolve and organize, those parameters are valid all over the world - whether they evolve in the USA or in Europe. However, the geographical differences necessitate to question those parameters, especially the composite ones. Those parameters in the USA are often tuned to regional conditions and the warm and moist Gulf of Mexico in combination with the north-south aligned mountain ranges support higher instability release compared to Europe. Especially during the winter time and over northern Europe, the focus ought to shift to the lowest few kilometers AGL, for example for instability release or the moisture dispersal. Another example is the organized convection beneath the dry slot of an extratropical cyclone, which sometimes occurs mainly during the winter time. Compared to the USA, intense extratropical depressions are able to penetrate well inland over Europe, which is not the case in North America due to the Rocky Mountains.

Despite the fact that only five case studies were carried out, they cover a broad field of atmospheric conditions, which can be expected in Europe. Especially the 15 August and 3 August 2008 case studies face environments, which are found both in winter and summer and which can occur during the entire year. The



events over southern Germany (23 June 2008, 22 August 2008 and 26 May 2009) all feature environmental conditions, which can occur in most places of Europe, with the same degree of thunderstorm organization and potential for damaging wind or hail. The information in those case studies can be used for thunderstorm forecasts in Europe, but one must not forget that for example the topography and internal dynamics of a thunderstorm also play a major role in the final degree of organization and therefore caution is needed when preparing convective outlooks. It was shown that the calculation of the updraft velocity is too coarse, not including effects like water loading, pressure perturbation effects or entrainment and therefore displaying updraft velocities, which were too high. Values of COSMO-DE were partially twice as much as what was assessed in local radar data. The correction with a factor 0.5, which was added in the USA, also reveals more reasonable values in the European cases.

More analysis has to be done for tornado and hail forecasting, where for example the 'Po-valley' in N-Italy would be suitable for further research. Another major topic is the *flash flood* potential with convective activity, which is another topic of interest for example for the Mediterranean area in the autumn and winter time. Only a good understanding of how and why those events occur could lead to an increase in warning time and hence to the protection of people, goods and chattels.



# References

- Atkins, N., C. Bouchard, R. Przybylinski, R. Trapp, and G. Schmocker, 2005: Damaging surface wind mechanisms within the 10 June 2003 Saint Louis bow echo during BAMEX. *Mon. Wea. Rev.*, **133**, 2275–2296.
- Aydin, K., T. Seliga, and V. Balaji, 1986: Remote sensing of hail with a dual linear polarization radar. *J. Appl. Meteor.*, **25**, 1475–1484.
- Beatty, K., E. Rasmussen, and J. Straka, 2008: The supercell spectrum. Part I: A review of research related to supercell precipitation morphology. *Electronic J. Severe Storms Meteor.*, **3**, 1–21.
- Bissolli, P., J. Grieser, N. Dotzek, and M. Welsch, 2007: Tornadoes in Germany 1950–2003 and their relation to particular weather conditions. *Global and Planetary Change*, **57**, 124–138.
- Blanchard, D., 1998: Assessing the vertical distribution of convective available potential energy. *Wea. Forecasting*, **13**, 870–877.
- Bolton, 1980: The computation of equivalent potential temperature. *Mon. Wea. Rev.*, **108**, 1046–1053.
- Brandes, A., 1978: Mesocyclone evolution and tornadogenesis: Some observations. *Mon. Wea. Rev.*, **106**, 995–1011.
- Brandes, A., 1981: Fine structure of the Del City-Edmond tornadic mesocirculation. *Mon. Wea. Rev.*, **109**, 635–647.
- Brandes, A., 1984: Vertical vorticity generation and mesocyclone sustenance in tornadic thunderstorms: The observational evidence. *Mon. Wea. Rev.*, **112**, 2253–2269.
- Bringi, V., T. Seliga, and K. Aydin, 1984: Hail detection with a differential reflectivity radar. *Science*, **225**, 1145–1157.
- Brooks, H., 2008: Proximity soundings for severe convection for Europe and the United States from reanalysis data. *Atmospheric Research*, 546–553.
- Brooks, H., C. Doswell III, and J. Cooper, 1994: On the environments of tornadic and nontornadic mesocyclones. *Wea. Forecasting*, **9**, 606–618.

- Brooks, H., C. Doswell III, and R. Wilhelmson, 1994: On the role of midtropospheric winds in the evolution and maintenance of low-level mesocyclones. *Mon. Wea. Rev.*, **122**, 126–136.
- Browning, A., 1964: Airflow and precipitation trajectories within severe local storms which travel to the right of the wind. *J. Atmos. Sci.*, **21**, 634–639.
- Browning, A., and R. Donaldson, 1963: Airflow and structure of a tornadic storm. *J. Atmos. Sci.*, **20**, 533–545.
- Browning, A., and F. Ludlam, 1962: Airflow in convective storms. *Q. J. R. Meteorol. Soc.*, **88**, 117–135.
- Browning, A.K. and Wexler, R., 1968: The determination of kinematic properties of a wind field using doppler radar. *J. Applied Meteorology*, **7**, 105–113.
- Brunner, J., S. Ackerman, A. Bachmeier, and R. Rabin, 2007: A quantitative analysis of the enhanced-V feature in relation to severe weather. *Wea. Forecasting*, **22**, 853–872.
- Brunner, J., S. Ackerman, A. Bachmeier, and R. Rabin, 2008: Some influences of background flow conditions on the generation of turbulence due to gravity wave breaking above deep convection. *Journal of Applied Meteorology and Climatology*, **47**, 2777–2796.
- Brunner, J., F. W.F., S. Ackerman, J. Moses, and R. Rabin, 2007: Toward an objective enhanced -V algorithm. pp. 8.
- Bunkers, M., M. Hjelmfelt, and P. Smith, 2006: An observational examination of long-lived supercells. Part I: Characteristics, evolution, and demise. *Wea. Forecasting*, **21**, 673–688.
- Bunkers, M., B. Klimowski, J. Zeitler, R. Thompson, and M. Weisman, 1999: Predicting supercell motion using a new hodograph technique. *Wea. Forecasting*, **15**, 61–79.
- Byers, H., and R. Braham Jr., 1948: Thunderstorm structure and circulation. *J. Atmos. Sci.*, **5**, 71–86.
- Byers, H., and R. Braham Jr., 1949: *The thunderstorm project*. 287 pp.
- Carlson, T., S. Benjamin, G. Forbes, and Y.F. Li, 1983: Elevated mixed layers in the regional severe storm environment: conceptual model and case studies. *Mon. Wea. Rev.*, **111**, 1453–1473.
- Cheung, K., 2004: Large-scale environmental parameters associated with tropical cyclone formations in the western North Pacific. *Journal of Climate*, **17**, 466–484.

- Chisholm, A., 1973: Alberta hailstorms. Part I: Radar case studies and airflow models. *Amer. Meteor. Soc.*, 1–36.
- Chisholm, A., and J. Renick, 1972: The kinematics of multicell and supercell alberta hailstorms. *Alberta hail studies*, 24–31.
- Colman, B., 1990: Thunderstorms above frontal surfaces in environments without positive CAPE. Part II: Organization and instability mechanisms. *Mon. Wea. Rev.*, **118**, 1123–1144.
- Colquhoun, J., 1980: A method of estimating the velocity of a severe thunderstorm using the vertical wind profile in the storm's environment. *Weather Forecasting and Analysis*, 316–323.
- Cook, B., 1958: Hail determination by radar analysis. *Mon. Wea. Rev.*, **86**, 435–438.
- Corfidi, S., S. Corfidi, and D. Schultz, 2008: Elevated convection and castellanus: ambiguities, significance, and questions. *Wea. Forecasting*, **23**, 1280–1303.
- Corfidi, S., J. Merritt, and F. Fritsch, 1996: Predicting the movement of mesoscale convective complexes. *Wea. Forecasting*, **11**, 41–46.
- Cunning, J., 1986: The Oklahoma-Kansas preliminary regional experiment for storm-central. *Society Bull. Amer. Meteor. Soc.*, **67**, 1478–1486.
- Dahl, J.M.L., 2006: Supercells - their dynamics and prediction. pp. 122.
- Davies, J., 1998: On supercell motion in weaker wind environments. *Preprints, 19th Conf. on Severe Local Storms, Minneapolis, MN, Amer. Meteor. Soc.*, 685–688.
- Davies, J., 2005: Tornadoes associated with small SRH or high LCL environments. *Annual Southeast Severe Storms Symposium*, 16.
- Davies, J., and H. Brooks, 1993: *Mesocyclogenesis from a theoretical perspective. The tornado; Its structure, dynamics, prediction and hazards* (C. Church, Ed. ed.). Number 79. Amer. Geophys. Union, 637 pp.
- Davies-Jones, R., 1984: Streamwise vorticity: The origin of updraft rotation in supercell storms. *J. Atmos. Sci.*, **41**, 2991–3006.
- Davies-Jones, R., 2004: Tornadogenesis in supercell storms - what we know and what we don't know. *Symposium on the Challenges of Severe Convective Storms 2006, American Meteorological Society*, 15.
- Davies-Jones, R., and H. Brooks, 1993: Mesocyclogenesis from a theoretical perspective. *The Tornado Its Structure, Dynamics, Prediction, and Hazards, Geophys. Monogr, Amer. Geophys. Union* (79), 105–114.

- Davies-Jones, R., D. Burgess, and L. Lemon, 1976: An atypical tornado-producing cumulonimbus. *Weather*, **31**, 336–347.
- Davis, C., N. Atkins, D. Bartels, L. Bosart, M. Coniglio, G. Bryan, W. Cotton, D. Dowell, B. Jewett, R. Johns, D. Jorgensen, J. Knievel, K. Knupp, W.C. Lee, G. McFarquhar, J. Moore, R. Przybylinski, R. Rauber, B. Smull, R. Trapp, S. Trier, R. Wakimoto, M. Weisman, and C. Ziegler, 2004: The bow echo and MCV experiment. *Society Bull. Amer. Meteor. Soc.*, **85**, 1075–1093.
- Davis, C., and T. Galarneau Jr., 2009: The vertical structure of mesoscale convective vortices. *J. Atmos. Sci.*, 686–704.
- Desrochers, P., and F. Harris, 1996: Interpretation of mesocyclone vorticity and divergence structure from single - doppler radar. *J. Appl. Meteor.*, **35**, 2191–2209.
- Doms, G., and U. Schättler, 2002: A description of the non-hydrostatic regional model lm.
- Doswell III., C., 1986: The human element in weather forecasting. *Natl. Wea. Dig.*, **11**, 6–18.
- Doswell III., C., 1991: A review for forecasters on the application of hodographs to forecasting severe thunderstorms. *National Weather Digest*, **16**, 2–16.
- Doswell III., C., 2000: A primer on vorticity for application in supercells and tornadoes. pp. 19.
- Doswell III., C., and D. Burgess, 1993: Tornadoes and tornadic storms: A review of conceptual models. *Geophysical Monograph 79, Amer. Geophys. Union*, 161–172, 161–172.
- Doswell III., C., and E. Rasmussen, 1994: The effect of neglecting the virtual temperature correction on CAPE calculation. *Wea. Forecasting*, 625–629.
- Doswell III., C., and D. Schultz, 2006: On the use of indices and parameters in forecasting. *EJSSM*, **1**, 1–22.
- Dotzek, N., 2001: Tornadoes in Germany. *Atmos. Res.*, **56**, 233–251.
- Dotzek, N., 2003: An updated estimate of tornado occurrence in Europe. *Atmos. Res.*, **67–68**, 153–161.
- Dotzek, N., G. Berz, E. Rauch, and R. Peterson, 2000: Die Bedeutung von Johannes P. Letzmanns "Richtlinien zur Erforschung von Tromben, Tornadoes, Wasserhosen und Kleintromben" für die heutige Tornadoforschung. *Meteor. Z.*, **9**, 165–174.

- Dotzek, N., P. Groenemeijer, B. Feuerstein, and A. Holzer, 2009: Overview of ESSL's severe convective storm research using the European Severe Weather Database ESWD. *Atmos. Res.*, **93**, 575–586.
- Doviak, R., and D. Zrnic, 1984: *Doppler radar and weather observations*. Academic Press, 458 pp.
- Dowell, D., and H. Bluestein, 2002a: The 8 June 1995 McLean, Texas storm, PartI: Observations of cyclic tornadogenesis. *Mon. Wea. Rev.*, **130**, 2626–2648.
- Dowell, D., and H. Bluestein, 2002b: The 8 June 1995 McLean, Texas, storm. PartII: Cyclic tornado formation, maintenance, and dissipation. *Mon. Wea. Rev.*, **130**, 2649–2670.
- Droegemeier, K., S. Lazarus, and R. Davies-Jones, 1992: The influence of helicity on numerically simulated convective storms. *Mon. Wea. Rev.*, **121**, 2005–2029.
- Edwards, R., R. Thompson, and J. Hart, 2002: Verification of supercell motion forecasting techniques. *Preprints, 21st Conf. Severe Local Storms, San Antonio*, 4.
- Elsom, D., G. Meaden, D. Reynolds, M. Row, and J. Webb, 2001: Advances in tornado and storm research in the United Kingdom and Europe: the role of the Tornado and Storm Research Organisation. , **56**, 4.
- Emanuel, K., 1993: The physics of tropical cyclogenesis over the Eastern Pacific. *Peking University Press*, 136–142.
- Forbes, S., 1975: Relationship between tornadoes and hook echoes on April 3, 1974. *Amer. Meteor. Soc.*, 280–285.
- Fujita, T., 1958: Mesoanalysis of the Illinois tornadoes of 9 April 1953. *J. Meteor.*, **15**, 288–296.
- Fujita, T., 1973: Proposed mechanism of tornado formation from rotating thunderstorms. *Amer. Meteor. Soc.*, 191–196.
- Fujita, T., 1978: Manual of downburst identification for project NIMROD. *SMRP Research Paper 156*, 104.
- Fujita, T., 1984: *Sci. Amer.*
- Fujita, T., 1985a: The downburst. *Meteorol Monogr.*, 122.
- Fujita, T., 1985b: *The Downburst: Microburst and Macrobust*. University of Chicago, 122 pp.
- Fujita, T., and H. Byers, 1977: Spearhead echo and downburst in the crash of an airliner. *Mon. Wea. Rev.*, **105**, 129–146.

- Fujita, T., and R. Wakimoto, 1982: Anticyclonic tornadoes in 1980 and 1981. *Americ. Meteor. Soc.*, 213–216.
- Funk, W., E. Darmofal, J. Kirkpatrick, T. Shields, W. Przybylinski, Y.J. Lin, G. Schmocker, and T. Shea, 1996: Storm reflectivity and mesocyclone evolution associated with the 15 April 1994 derecho, Part II: Storm structure and evolution over Kentucky and southern Indiana. *Amer. Meteor. Soc.*, 516–520.
- Gallus Jr., W., 1996: The influence of microphysics in the formation of intense wake lows: A numerical modeling study. *Mon. Wea. Rev.*, **124**, 2267–2281.
- Galway, J., 1956: The lifted index as a predictor of latent instability. *Bull. Amer. Meteor. Soc.*, **37**, 528–529.
- Garrett, A., and D. Rockney, 1962: Tornadoes in northeastern Kansas, May 19, 1960. *Mon. Wea. Rev.*, **90**, 231–240.
- Gatzen, C., 2003: A derecho in Europe: Berlin, 10 July 2002. *Wea. Forecasting* (2003, 75), 20.
- George, J., 1960: Weather forecasting for aeronautics. *Academic Press*, **90**, 407–415.
- Geotis, S., 1962: Some radar measurements of hailstorms. *Society Bull. Amer. Meteor. Soc.*, **2**, 270–275.
- Groenemeijer, P.H., 2005: Sounding-derived parameters associated with severe convective storms in the Netherlands. pp. 1–87.
- Grzych, M., B. Lee, and C. Finley, 2006: Thermodynamic analysis of supercell rear-flank downdrafts from project ANSWERS. *Mon. Wea. Rev.*, **135**, 240–246.
- Hagen, M., B. Bartenschlager, and U. Finke, 1999: Motion characteristics of thunderstorms in southern Germany. *Meteorol. Appl.*, **6**, 227–239.
- Hagen, M., and D. Heimann, 1994: Detailed analyses of the squall line over southern Germany. *DLR Forschungsbericht*, 67–94.
- Hagen, M., H.H. Schiesser, and M. Dorninger, 2000: Monitoring of mesoscale precipitation systems in the Alps and the northern Alpine foreland by radar and rain gauges. *Meteorol. Atmos. Phys.*, **72**, 87–100.
- Hamid, K., and L. Delobbe, 2007: F3 tornado in Belgium. pp. 2.
- Hart, J.A., and W. Korotky, 1991: The sharp workstation v1.50 users guide. *U.S. Department of Commerce*, 30.
- Heymsfield, G., and R. Blackmer Jr., 1988: Satellite-observed characteristics of midwest severe thunderstorm anvils. *Mon. Wea. Rev.*, **116**, 2200–2224.



- Hitschfeld, F., 1986: *The Invention of Radar Meteorology*. Society Bull.Amer.Meteor.Soc., 5 pp.
- Höller, H., 1994: Mesoscale organization and hailfall characteristics of deep convection in southern Germany. *Beitr. Phys. Atmos.*, **67**, 219–234.
- Höller, H., 1998: Hochreichende Konvektion. *Annalen der Meteorologie*, 38, DWD. *Herbustschule Radarmeteorologie 1998*, 111–121.
- Höller, H., and M. Reinhardt, 1986: Munich hailstorm of 12 July 1984: Convective development and preliminary hailstorm analysis. *Beitr. Phys. Atmos.*, **59**, 1–12.
- Hohenegger, C., and C. Schär, 2007: Atmospheric predictability at synoptic versus cloud-resolving scales. *Bull.Amer.Meteor.Soc.*, **88**, 1783–1793.
- Holleman, I., and H. Beekhuis, 2002: Analysis and correction of dual PRF velocity data. *J. Atmos. Oceanic Technol.*, **20**, 443–453.
- Horgan, K.L., D.M. Schultz, J.E. Hales Jr., S.F. Corfidi, and R. Johns, 2006: A five-year climatology of elevated severe convective storms in the United States east of the Rocky Mountains. *Wea. Forecasting.*, **22**, 1031–1044.
- Houze, R., 1994: *Cloud dynamics* (reprint, illustrated ed.). Academic Press, 573 pp.
- Houze, R., W. Schmid, R. Fovell, and H. Schiesser, H., 1993: Hailstorms in Switzerland: Left movers, right movers, and false hooks. *Mon. Wea. Rev.*, **121**, 3345–3370.
- Houze Jr., R., S. Rutledge, M. Biggerstaff, and B. Smull, 1989: Interpretation of doppler weather radar displays in midlatitude mesoscale convective systems. *Bull.Amer.Meteor.Soc.*, **70**, 608–619.
- Huntrieser, H., H.H. Schiesser, W. Schmid, and A. Waldvogel, 1997: Comparison of traditional and newly developed thunderstorm indices for Switzerland. *Wea.Forecasting*, **12**, 108–125.
- Illingworth, A.J., J.W.F. Goddard, and S.M. Cherry, 1986: Detection of hail by dual-polarization radar. *Nature*, **320**, 431–433.
- Inman, R., 1968: Computation of temperature at the lifted condensation level. *Journal of applied meteorology*, **8**, 155–158.
- Jing, Z., and G. Wiener, 1992: Two-dimensional dealiasing of doppler velocities. *J. Atmos. Oceanic Technol.*, **10**, 798–808.
- Jirak, I., W. Cotton, and R. McAnelly, 2003: Satellite and radar survey of mesoscale convective system development. *Mon. Wea. Rev.*, **131**, 2428–2449.

- Johns, R., and W. Hirt, 1987: Derechos: Widespread convectively induced windstorms. *Wea.Forecasting*, **2**, 32–49.
- Johnson, B., 1983: The heat bursts of 29 May 1976. *Mon. Wea. Rev.*, **111**, 1776–1792.
- Johnson, R., and P. Hamilton, 1988: The relationship of surface pressure features to the precipitation and airflow structure of an intense midlatitude squall line. *Mon. Wea.Rev.*, **116**, 1444–1472.
- Kelvin, L., 1869: On vortex motion. *Trans.Roy.Soc.*, 7–60.
- Klemp, B., 1987: Dynamics of tornadic thunderstorms. *Ann.Rev.Fluid Mech.*, **19**, 33.
- Klemp, B., and P. Ray, 1981: Observed and numerically simulated structure of a mature supercell thunderstorm. *J. Atmos. Sci.*, **38**, 1558–1580.
- Knight, C.A., and N.C. Knight, 1970: The falling behaviour of hailstones. *J. Atmos. Sci.*, **7**, 672–681.
- Knight, C.A., and N.C. Knight, 1993: Single-doppler radar observations of a mini-supercell tornadic thunderstorm. *Mon. Wea. Rev.*, **121**, 1860–1870.
- Kraichnan, R., 1973: Helical turbulence and absolute equilibrium. *J.Fluid Mech.*, **59**, 745–752.
- Lafore, J.P., and M. Moncrieff, 1989: A numerical investigation of the organization and interaction of the convective and stratiform regions of tropical squall lines. *J.Atmos.Sci.*, **46**, 521–544.
- Lee, W.C., R. Wakimoto, and R. Carbone, 1992a: The evolution and structure of a 'bow-echo-microburst' event. Part I: The microburst. *Mon. Wea.Rev.*, **120**, 2188–2210.
- Lee, W.C., R. Wakimoto, and R. Carbone, 1992b: The evolution and structure of a 'bow-echo-microburst' event. Part II: The bow echo. *Mon. Wea.Rev.*, **120**, 2211–2225.
- Lemon, L., J. Donaldson, R.J., D. Burgess, and R. Brown, 1977: Doppler radar application to severe thunderstorm study and potential real-time warning. *Bulletin American Meteorological Society*, 1187–1193.
- Lemon, L., and C. Doswell III., 1979: Severe thunderstorm evolution and mesocyclone structure as related to tornadogenesis. *Mon. Wea.Rev.*, **107**, 1184–1197.
- Lemon, L., and S. Parker, 1996: The Lahoma storm deep convergence zone: Its characteristics and role in storm dynamics and severity. *18th Conference on Severe Local Storms, San Francisco*, 70–75.

- Leuenberger, D., 2005: High-resolution radar rainfall assimilation: Exploratory studies with latent heat nudging. *Diss., Eidgenössische Technische Hochschule ETH Zürich, Nr. 15884, 2005*, 1–119.
- Lilly, D., 1983: Dynamics of rotating thunderstorms. *Mesoscale Meteorology-theories, observations and models*, 531–543.
- Lorandel, R., and P. Dupuy, 2008: Rapport préliminaire sur les données radar disponibles au moment de la tornade du 3 août 2008 autour de la commune Hautmont dans les département du nord. pp. 32.
- Maddox, R., 1976: An evaluation of tornado proximity wind and stability data. *Mon. Wea. Rev.*, **104**, 133–142.
- Maddox, R., 1980: Mesoscale convective complex. *Bull. Amer. Meteor. Soc.*, **61**, 1374–1387.
- Maddox, R., and C. Crisp, 1998: The tinker AFB tornadoes of march 1948. *Wea. Forecasting*, **14**, 492–499.
- Market, P., S. Allen, R. Scofield, R. Kuligowski, and A. Gruber, 2003: Precipitation efficiency of warm-season midwestern mesoscale convective systems. *Wea. Forecasting*, **18**, 1273–1285.
- Markowski, P., 2001: Hook echoes and rear-flank downdrafts: A review. *Monthly Weather Review*, **130**, 852–876.
- Markowski, P., E. Rasmussen, and J. Straka, 1998: The occurrence of tornadoes in supercells interacting with boundaries during VORTEX-95. *Wea. Forecasting*, **13**, 852–859.
- Markowski, P., and Y. Richardson, 2009: Tornadogenesis: Our current understanding, forecasting considerations, and questions to guide future research. *Atmospheric Research*, **93**, 3–10.
- Markowski, P., and J. Straka, 1998: Variability of storm-relative helicity during VORTEX. *Mon. Wea. Rev.*, **126**, 2959–2971.
- Markowski, P., and J. Straka, 2000: Some observations of rotating updrafts in low-buoyancy, highly sheared environments. *Mon. Wea. Rev.*, **128**, 449–461.
- Markowski, P. M., S.J.M., and E.N. Rasmussen, 2002: Direct surface thermodynamic observations within rear-flank downdrafts of nontornadic and tornadic supercells. *Mon. Wea. Rev.*, **130**, 1692–1721.
- Markowski, P. M., S.J.M., and E.N. Rasmussen, 2003: Tornadogenesis resulting from the transport of circulation by a downdraft: Idealized numerical simulations. *J. Atm. Sci.*, **60**, 795–823.

- McCann, D., 1983: The enhanced-V: A satellite observable severe storm signature. *Mon. Wea. Rev.*, **111**, 887–894.
- McCaul Jr., E., and M. Weisman, 1996: Simulations of shallow supercell storms in landfalling hurricane environments. *Mon. Wea. Rev.*, **124**, 408–429.
- Michalakes, J., S. Chen, J. Dudhia, L. Hart, J. Klemp, J. Middlecoff, and W. Skamarock, 2001: Development of a next generation regional weather research and forecast model. *World Scientific*, 269–276.
- Miller, D., 2006: Observations of low level thermodynamic and wind shear profiles on significant tornado days. pp. 6.
- Miller, R., 1967: Notes on analysis and severe storm forecasting procedures of the military weather warning center. *Tech. report 200*.
- Moffat, H., and A. Tsinober, 1992: Helicity in laminar and turbulent flow. *Annu. Rev. Fluid Mech.*, **24**, 281–312.
- Moller, A., C. Doswell III, and R. Przybylinski, 1990: High-precipitation supercells: A conceptual model and documentation. *Amer. Meteor. Soc.*, 52–57.
- Moncrieff, M.W., and M. Miller, 1976: The dynamics and simulation of tropical cumulonimbus and squall lines. *Quart. J. Roy. Meteor. Soc.*, **102**, 373–394.
- Moore, J.T., A. Czarnetzki, and P. Market, 1998: Heavy precipitation associated with elevated thunderstorms formed in a convectively unstable layer aloft. *Meteor. Appl.*, **5**, 373–384.
- Morris, R., 1986: The Spanish plume - testing the forecaster's nerve. *Meteorol. Mag.* **115**, 349–357.
- Nelson, S., and N. Knight, 1987: The hybrid multicellular - supercellular storm- and efficient hail producer. *J. Atmos. Sci.*, **44**, 1042–2059.
- Ninić, N., Z. Jurić, and S. Nižetić, 2006: Thermodynamical aspect of definitions CAPE and TCAPE. *GEOFIZIKA*, **23**, 143–154.
- Nolen, R., 1959: A radar pattern associated with tornadoes. *Bull. Amer. Meteor. Soc.*, **40**, 277–279.
- Parker, M., and R. Johnson, 2000: Organizational modes of midlatitude mesoscale convective systems. *Mon. Wea. Rev.*, **128**, 3413–3436.
- Pruppacher, and Beard, 1970: A wind tunnel investigation of the internal circulation and shape of water drops falling at terminal velocity in air. *Quart. J. Roy. Meteor. Soc.*, **96**, 247–256.
- Przybylinski, W., 1995: The bow echo: Observations, numerical simulations, and severe weather detection methods. *Wea. Forecasting*, 203–218.

- Rahimi, A., A. Holt, and G.J.G. Upton, 2005: Attenuation calibration of an x-band weather radar using a microwave link. *J. Atmos. Oceanic Technol.*, **23**, 395–405.
- Rasmussen, E., 2003: Refined supercell and tornado forecast parameters. *Wea.Forecasting*, **18**, 530–535.
- Rasmussen, E., and D. Blanchard, 1998: A baseline climatology of sounding-derived supercell and tornado forecast parameters. *Wea.Forecasting*, **13**, 1148–1164.
- Rasmussen, E., and J. Straka, 1997: Variations in supercell morphology. Part I: Observations of the role of upper-level storm-relative flow. *Mon.Wea.Rev.*, **126**, 2406–2421.
- Rasmussen, E., and R. Wilhelmson, 1983: Relationship between storm characteristics and 12 GMT hodographs, low-level shear, and stability. *Amer. Meteor. Soc.*, **126**.
- Rinehart, R., 1991: *Radar for meteorologists*. Society Bull.Amer.Meteor.Soc., 334 pp.
- Roesli, H., J. Kerkmann, and D. Rosenfeld, 2006: Harmonising SEVIRI RGB composites for operational forecasting. *EUMETSAT*, 8.
- Rotunno, R., and J. Klemp, 1982: The influence of the shear-induced pressure gradient on thunderstorm motion. *Mon. Wea. Rev.*, **110**, 136–151.
- Sadowski, A., 1969: Size of tornado warning area when issued on basis of radar hook echo. *ESSA Tech.Memo*, 26.
- Schaefer, J., 1974: The life cycle of the dryline. *J. Appl. Meteor.*, **13**, 444–449.
- Schiesser, H.H., and R. Houze Jr., 1991: Mesoscale organization of precipitation systems in Switzerland. *Society Bull.Amer.Meteor.Soc.*, 509–512.
- Schiesser, H.H., R. Houze Jr., and H. Huntrieser, 1995: The mesoscale structure of severe precipitation systems in Switzerland. *Mon. Wea. Rev.*, **123**, 2070–2097.
- Schiesser, H.H., R. Houze Jr., and A. Waldvogel, 1992: Mesoscale organization of precipitation systems causing severe damage by intense or long-lasting rain in Switzerland. *Preprints, Interprevent, Schutz des Lebensraumes vor Hochwasser, Muren und Lawmen*, 71–82.
- Schiesser, H.H., R. Schmid, W. Houze Jr., and B. Bauer, 1996: A tornado-producing mesoscale convective system in northern Switzerland. *Society Bull.Amer.Meteor.Soc.*, 459–461.
- Schmid, W., H.H. Schiesser, R. Houze Jr., and R. Fovell, 1990: Severe left-moving hailstorms in central Switzerland. *Society Bull.Amer.Meteor.Soc.*, 467–472.

- Schmocker, K., R. Przybylinski, and J. Lin, 1996: Forecasting the initial onset of damaging downburst winds associated with a mesoscale convective system (MCS) using the mid-altitude radial convergence (MARC) signature. *Society Bull.Amer.Meteor.Soc.*, 306–311.
- Schraff, C., and R. Hess, 2003: A description of the nonhydrostatic regional model lm. part iii: Data assimilation. *LM F90 3.3*, 1–85.
- Schroth, A., M. Chandra, and P. Meischner, 1988: A C - band coherent polarimetric radar for propagation and cloud physics research. *Society Bull.Amer.Meteor.Soc.*, 803–822.
- Seliga, T., and V. Bringi, 1976: Potential use of radar differential reflectivity measurements at orthogonal polarizations for measuring precipitation. *J. Appl. Meteor.*, **51**, 69–76.
- Setvák, M., D. Lindsey, P. Novák, R. Rabin, P. Wang, J. Kerkmann, M. Radová, and J. Št'ástka, 2008: Cold-ring shaped storms in Europe. pp. 10.
- Setvák, M., and J. Št'ástka, 2008: Cloud top temperature and height product of the nowcasting SAF applied to tropopause-penetrating cold-ring shaped storms. pp. 8.
- Showalter, A., 1953: A stability index for thunderstorm forecasting. *Society Bull.Amer.Meteor.Soc.*, **34**, 250–252.
- Shuman, F., 1978: Numerical weather prediction. *Bull. Amer.Meteor. Soc.*, **59**, 1–13.
- Sokol, Z., 2008: Effects of an assimilation of radar and satellite data on a very-short range forecast of heavy convective rainfalls. *Atmos.Res.*, **93**, 188–206.
- Stephan, K., S. Klink, and C. Schraff, 2008: Assimilation of radar-derived rain rates into the convective-scale model cosmo-de at dwl. *Q. J. R. Meteorol. Soc.*, **134**, 1315–1326.
- Steppeler, J., G. Doms, U. Schättler, H. Bitzer, A. Gassmann, U. Damrath, and G. G., 2003: Meso-gamma-scale forecasts using the nonhydrostatic model lm. *Meteorol. Atmos. Phys.*, **82**, 75–96.
- Stout, E., and A. Huff, 1953: Radar records Illinois tornadogenesis. *Bull. Amer. Meteor. Soc.*, 281–284.
- Teittinen, J., and H. Hohti, 2007: Analysis of a tornadic mini-supercell in Finland by using Doppler radar. pp. 5.
- Thompson, R., R. Edwards, J. Hart, K. Elmore, and P. Markowski, 2003: Close proximity soundings within supercell environments obtained from the Rapid Update Cycle. *Wea.Forecasting*, **18**, 1243–1261.

- Thompson, R., R. Edwards, and C. Mead, 2006: Effective storm-relative helicity and bulk shear in supercell thunderstorm environments. *Wea.Forecasting*, **22**, 102–115.
- Trier, S., and D. Parsons, 1992: Evolution of environmental conditions preceding the development of a nocturnal mesoscale convective complex. *Mon. Wea. Rev.*, **121**, 1078–1098.
- Van Delden, A., 2001: The synoptic setting of thunderstorms in western Europe. *Atmos. Res.*, **56**, 89–110.
- Van Tassel, L., 1955: The North Platte Valley tornado outbreak of June 27, 1955. *Mon. Wea. Rev.*, **117**, 1113–1140.
- Vulpiani, G., P. Tabary, J. Chatelet, O. Bouquet, M.L. Segond, and F. Marzano, 2007: Hail detection using a polarimetric algorithm at C- band: impact on attenuation correction. pp. 5.
- Wang, P., 2007: The thermodynamic structure atop a penetrating convective thunderstorm. *Atmos.Res.*, **83**, 254–262.
- Wegener, A., 1917: Wind - und Wasserhosen in Europa. *Friedr. Vieweg und Sohn (die Wissenschaft)*, 301.
- Weisman, M., 1992: The role of convectively generated rear-inflow jets in the evolution of long-lived mesoconvective systems. *J.Atmos.Sci.*, **49**, 1826–1847.
- Weisman, M., 1993: The genesis of severe, long-lived bow echoes. *J.Atmos.Sci.*, **50**, 645–670.
- Weisman, M., and H. Bluestein, 1985: Dynamics of numerically simulated LP storms. *Amer. Meteor. Soc.*, 167–171.
- Weisman, M., and C. Davis, 1998: Mechanisms for the generation of mesoscale vortices within quasi-linear convective systems. *J.Atmos.Sci.*, **55**, 2603–2622.
- Weisman, M., and J. Klemp, 1982: The dependence of numerically simulated convective storms on wind shear and buoyancy. *Mon. Wea. Rev.*, **110**, 504–520.
- Weisman, M., and R. Rotunno, 2003: "a theory for strong long-lived squallines" revisited. *J.Atmos.Sci.*, **61**, 361–382.
- Wilhelmson, R., and J. Klemp, 1978: A numerical study of storm splitting that leads to long-lived storms. *J.Atmos.Sci.*, **35**, 1974–1986.
- Wood, V., 2008: Improvement of WSR-88D VAD winds: cyclonic wind fields. *Amer. Meteor. Soc.*, 14.
- Woodall, G., 1990: *Qualitative analysis and forecasting of tornadic activity using storm relative environmental helicity*. NOAA, Tech.Memo., 57 pp.

- Zehr, R., 1992: Tropical cyclogenesis in the western North Pacific. *NOAA Technical Report NESDIS 61*, U. S. Department of Commerce, 181.
- Zipser, E., 1982: Use of a conceptual model of the life cycle of mesoscale convective systems to improve very-short-range forecasts. *Academic Press*, 191–204.
- Zrnic, D., and R. Doviak, 2006: *Doppler Radar and Weather Observations* (2 ed.). Academic Press, 592 pp.



# Acknowledgments

I want to thank the following person:

- Prof. Georg Mayr, who enabled me the chance to write my diploma thesis at the DLR. He stood by me when I had problems or questions and he assisted me whenever it became necessary. Thank you very much, Georg!
- Dr. Martin Hagen, who put me up at the DLR. He supported me when I had questions and he was very forthcoming, when I was asking for money for meteorological data from other Meteorological Institutions.

But what is a study without the colleagues! During the four years in Innsbruck, I had the luck to come across a group of young meteorologists, who aid one another and who developed a great interpersonal relation. Thank you all for the gorgeous years and I already miss you all!

A special thanks goes to André Summer, who spend so much time when I had questions about physics or math and who was willing to participate in 'Lerngruppen' all the time (including numerous, onesided tabletop soccer games).

I give my props to Felix Welzenbach for the exciting hillwalks, especially the unforgettable 'Patscherkofel-Föhnsturm-Touren', but also the daily synoptic talks, which made the study so interesting.

A big thanks also goes to the 'Lerngruppe des Internationalen Studentenhauses': Florian 1, Florian 2 and Florian 3 for all those working hours, partially burning the midnight oil, and the awesome teamwork.

Last but certainly not least I express my gratitude to the friend and colleague, with whom I underwent so many adventures not only during the lecture period but most notably outside of the university. Thank you so much for everything, Wolfgang!

There are way more students I could talk about but this would go beyond the scope of that chapter. However I happy about having met you all in Innsbruck.

I also want to thank Kirstin Kober for the great time during the ICAM, but also for numerous amendments and suggestions for improvement but also Patrick Tracksdorf, Johannes Dahl, Jens Reimann, Pieter Groenemeijer and Vera Meyer for the sedulous effort to help me with questions in IDL and who also gave useful ideas for improvement while cross-reading parts of my thesis.

However, I'm most grateful to my parents who always believed in me and who supported me in every conceivable way. Without you, I wouldn't be where I am now!

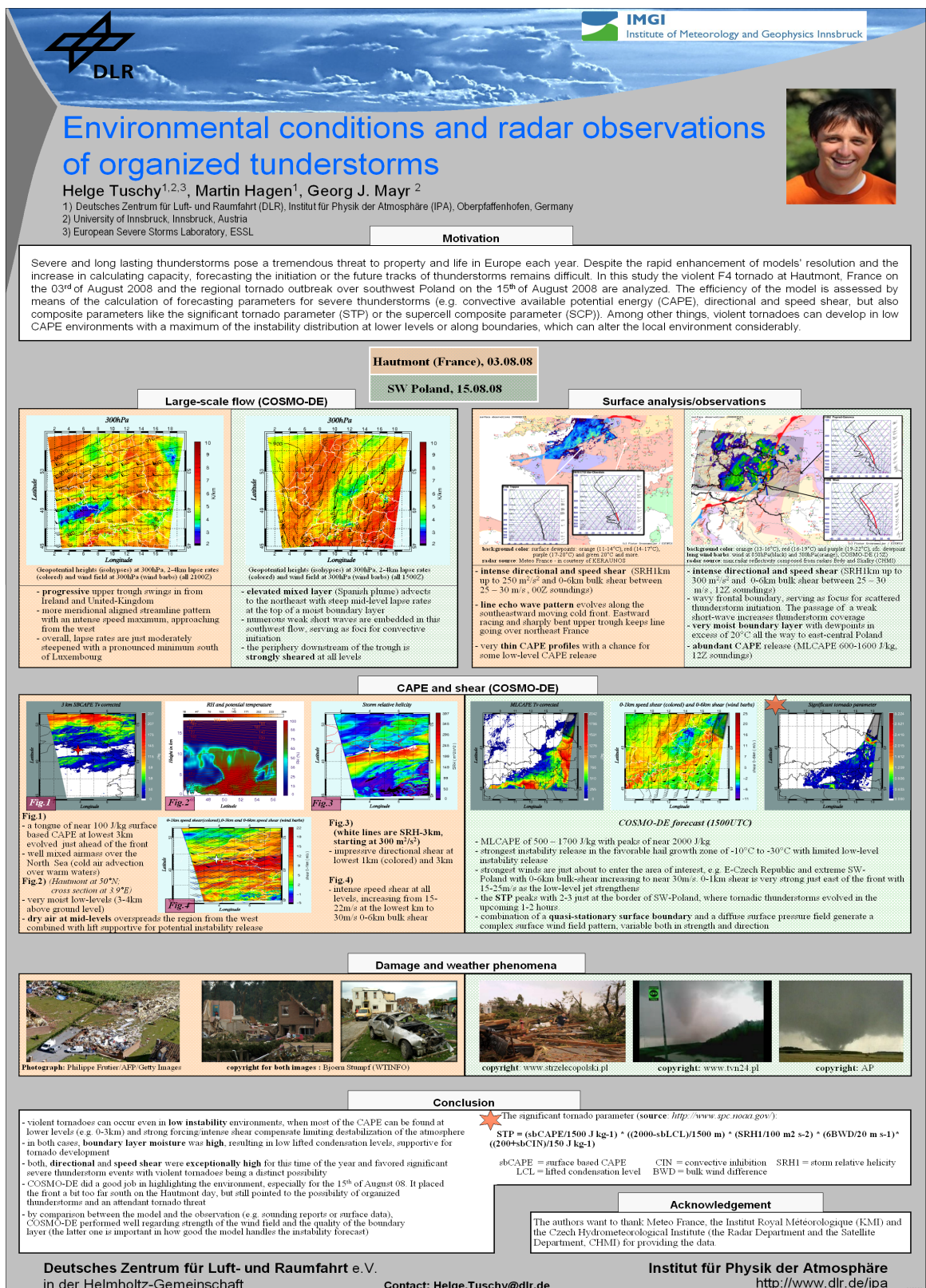


**Figure 5.1:** This poster was presented on the ICAM conference in Rastatt, southwest Germany 2009. It was awarded with the 1<sup>st</sup> prize of the *Young Scientist Poster Award*. Two cases out of the diploma thesis were discussed.



# Curriculum Vitae

## Helge Tuschy

Alte Str.16, D-88427 Bad Schussenried

Born on 21 November 1983 in Bad Waldsee, Germany

---

### EDUCATION AND PROFESSIONAL TRAINING:

**2008–2009** Diploma thesis at the 'Institut für Physik der Atmosphäre' of the 'Deutsches Zentrum für Luft- und Raumfahrt, DLR', under the guidance of Ao. Univ.-Prof. Dr. Georg Mayr, Institute of Meteorology and Geophysics, University of Innsbruck: "*Organized severe thunderstorm events in parts of central Europe*".

**2004–2008** Diploma study at the University of Innsbruck. *Master of Natural Science (Magister rerum naturalium)* in Meteorology.

**1994–2003** Secondary school, St. Johann, Blönried. *Abitur*, July 2003.

**1990–1994** Basic school, Bad Schussenried.

---

### COMPUTER LANGUAGE

Courses in FORTRAN and impropriating Matlab/IDL and Latex

---

### FOREIGN LANGUAGE

French (intensive course), English (amongst others a participation at a seminar in English at the University of Innsbruck [Englisch Basisstufe III]) and Latin.

---

**INTERNSHIPS<sup>1</sup>:****End of July to end of August 2007**

Training and internship for 1 month at the National Weather Service Amarillo, Texas (USA), including an one-day training at the Storm Prediction Center, how to create outlooks

**Mid to end of July 2006**

Internship for 2 weeks at the private Weather Service Meteomedia, Vienna (Austria)

**August 2002**

A stay for 3 weeks at the National Weather Service in Amarillo, Texas (USA), working in day-/ night-shifts

---

**TALKS****27 March 2009**

Discoursing about a severe thunderstorm outbreak in Poland (15 August 2008) at the Czech Hydrometeorological Institute.

**24 March 2009**

Discoursing on the use and handling of severe thunderstorm forecast parameters at the Swiss radio and TV station (SFDRS).

**July 2007**

Making a speech on the forecasting strategy for severe thunderstorm forecasts and another one about the dynamics of organized convection at the TV station RTL. This instruction lasted for 3 days with the emphasis on how to forecast those phenomena correctly.

**24 March 2006**

Giving a talk to the topic: 'Hurricanes and tornadoes', where an animation for the TV weather at RTL was prepared and showed in the following hurricane season.

---

<sup>1</sup>See attachments

---

PUBLICATIONS**April 2005**

Publication of an article in the book:” *Entfesselte Elemente*”, redaktion et agentur

---

POSTERS

” *Environmental conditions and radar observations of organized thunderstorms*”

The International Conference on Alpine Meteorology (ICAM), Rastatt, Germany, 11-15 May 2009.

Receiving the 1<sup>st</sup> prize of the *Young Scientist Poster Award*

” *A case study of two severe hailstorm events over southern and eastern Germany*”

4<sup>th</sup> European Conference on Severe Storms 10 - 14 September 2007 - Trieste - ITALY

---

CO-AUTHOR FOR ORAL PRESENTATIONS:

” *Verification of dichotomous lightning forecasts at the European Storm Forecasting Experiment*”

4<sup>th</sup> European Conference on Severe Storms 10 - 14 September 2007 - Trieste - ITALY

” *A close look at a severe mesoscale convective system during the 'Kyrill'-winter storm over central Europe*”

4<sup>th</sup> European Conference on Severe Storms 10 - 14 September 2007 - Trieste - ITALY

---

MUSIC

- Playing clarinet since 1992; member of a band.
- Participation at divers contests, called ”Jugend-kritik” with the result ”sehr gut”.
- Participation at divers contests, called ”Jugend-musiziert” with the results:  
2nd place as a soloist ( Landeswettbewerb )  
2nd place in a quintet ( Bundeswettbewerb )

---

**OTHERS**

Technical assistant during the International Conference on Alpine Meteorology (ICAM) in Rastatt, Germany, 11-15 May 2009.

**Since 2005**

Participating as a forecaster at the European Storm Forecast Experiment (ESTOFEX), [www.estofex.org](http://www.estofex.org)

**March to June 2004**

Staying in Norman, Oklahoma (USA) with a forecaster of the Storm Prediction Center, SPC. Working with the forecaster on a tornado climatology project

**Oktober 2003 until March 2004**

Jobbing for example in a brewery or at the Kurpark-Klinik.

Holding a 60 minute lesson about thunderstorms: Their genesis, organization and decay. (University of Innsbruck)